

Development of Metamaterial Lenslet Arrays for Cosmic Microwave Background Experiments

Jonathan Andrew Thompson

Thesis submitted in partial fulfilment of the requirements for the degree of
Doctor of Philosophy

January 2021

School of Physics and Astronomy
Cardiff University

Summary

The use of sub-wavelength meshes consisting of square metallic patches (and their complement) embedded in a dielectric substrate for the implementation of optical devices in the millimetre wave bands is well established. Many millimetre wave astronomical instruments incorporate low-pass filters and dichroics using this technology while wave plates and graded index lenses are starting to appear. Combining many lenses into a lenslet array as a method for collecting light onto a focal plane sensor matrix for cosmic microwave background instruments is an active area of research. Reported here is work carried out with the aim of improving the properties of graded index lenses constructed using the mesh technology in lenslet arrays.

A genetic algorithm was developed to search for patch shapes that would improve the basic low-pass filter. It was discovered that square patches with rounded corners could slightly improve the passband performance of Chebyshev response filters. Deliberately designing a new shape that increases the capacitance of the mesh did lead to a patch with useful characteristics. A patch that starts as a square and then grows fingers into the adjacent patch was proposed. It was shown that this super-capacitive patch could be used to create a low-pass filter with an extended stopband before the diffraction limit and an artificial dielectric with an increased refractive index.

Use of the super-capacitive patch in graded index lenslets reduced the number of mesh layers in a polypropylene lens but did not work for a silicon substrate due to the cut-off frequency of the resulting artificial dielectric. A novel curved column design was proposed that better matches the path of light through the lens. This allowed another saving in layers along with the ability to accurately account for the effect of non-normal incidence of waves on the artificial dielectrics and was applicable to silicon.

Contents

Summary	i
List of tables	vi
List of figures	vii
Acknowledgements	xi
Publications	xii
Chapter 1 Introduction.....	1
1.1 Filters	3
1.2 Artificial dielectrics	8
1.3 Lenses	9
1.4 Lenslet arrays	11
1.5 Modelling	13
1.6 Genetic algorithms.....	14
1.7 Thesis structure	14
Chapter 2 The modelling tools	16
2.1 The propagation matrix method.....	17
2.1.1 The propagation matrix for a dielectric	17
2.1.2 The matching matrix for the interface between two dielectrics	18
2.1.3 Matching matrices for capacitive and inductive grids	18
2.1.4 Using the method.....	21
2.2 The finite difference, time domain method	22
2.2.1 The basic method	22
2.2.2 Incident plane waves	26
2.2.3 Absorbing waves at the model boundary.....	28
2.2.4 Thin layers	32
2.3 The Ansys HFSS Package	35
2.4 The genetic algorithm	37
2.4.1 The genome.....	39
2.4.2 Fitness assessment	40
2.4.3 Breeding	43
2.4.4 Completeness.....	44
2.5 The modelling application	45
2.5.1 The Modelling Grid	47
2.5.2 The Modelling Scene	48
2.5.3 Excitation Sources	50

2.5.4	Sensors.....	51
2.5.5	Variables.....	52
2.5.6	Sequencers.....	53
2.5.7	Node Manager.....	55
2.5.8	Designers.....	55
2.5.9	Propagation matrix verification.....	56
2.5.10	FDTD verification.....	58
2.5.11	Effect of FDTD cell size.....	59
2.5.12	FDTD thin layer feature.....	62
2.5.13	The propagation matrix method and layer spacing.....	63
Chapter 3 Beyond the square.....		66
3.1	Searching with the genetic algorithm.....	66
3.1.1	Step 1. Finding initial filter designs.....	67
3.1.2	Step 2. Improving the square patch.....	69
3.1.3	Step 3. Decompose the results.....	70
3.1.4	The Chebyshev filter.....	71
3.1.5	The Butterworth filter.....	74
3.1.6	Conclusions.....	77
3.2	The super-capacitive patch.....	78
3.2.1	Increasing the capacitance of a patch.....	78
3.2.2	Extending the progression.....	82
3.2.3	Making a filter.....	85
3.2.4	Conclusions.....	87
3.3	Pattern catalogues.....	88
3.3.1	Symmetries.....	88
3.3.2	A 10x10 four-fold symmetrical catalogue.....	90
3.3.3	Classifying the patterns in a catalogue.....	91
3.3.4	Corner-to-corner pixels.....	93
3.3.5	A 10x10 two-fold symmetric catalogue.....	95
3.3.6	Using the catalogue data.....	97
3.3.7	Conclusions.....	98
Chapter 4 Lenslet design.....		99
4.1	Simple path length lenslet design method.....	100
4.1.1	Focal length compensation factor.....	103
4.2	A note on HFSS modelling.....	104
4.2.1	Gaussian beams.....	106
4.3	Artificial dielectrics.....	108
4.3.1	Measuring the phase velocity.....	108

4.3.2	Matching with a test dielectric.....	110
4.3.3	Extraction from two port S-parameters	111
4.3.4	The refractive index of a polypropylene block	117
4.3.5	Refractive index of the super-capacitive patch	118
4.3.6	Super-capacitive patches and lenslet designs.....	121
4.4	Choosing the column width	123
4.4.1	Spatial resolution	123
4.4.2	Cut-off frequency	127
4.4.3	Making the choice.....	130
4.5	Choosing the layer spacing.	130
4.5.1	Polypropylene	130
4.5.2	Silicon	133
4.6	Refractive index catalogues	134
4.7	Anti-reflection layers	135
4.7.1	Possible structures	137
4.7.2	The effects	139
4.8	Complete lenslet designs	143
4.8.1	Polypropylene	143
4.8.2	Silicon	150
4.9	Improving the simple path length model.....	153
4.9.1	Bending at the lenslet structure boundary	153
4.9.2	Metamaterial artificial dielectrics incidence angle.....	155
4.9.3	Following the rays.....	157
4.9.4	Following the rays in three dimensions.....	165
4.9.5	The full silicon lenslet.....	166
4.9.6	Final thoughts on 3D.....	170
4.10	Conclusions	172
	Chapter 5 Summary	175
	Bibliography.....	179
	Appendix A Propagation matrix derivation	194
A.1	One dimensional plane waves.....	194
A.2	The propagation matrix.....	198
A.3	The matching matrix for two dielectrics	199
A.4	Matching matrices for capacitive and inductive grids	200
	Appendix B Derivation of FDTD stepping equations.....	202
B.1	Derivation of the basic FDTD equations.....	202
B.2	Incident plane waves	209
B.3	1D plane wave incident on a lossy region	214

Contents

B.4	Berenger's split coordinate perfectly matched layer	218
B.5	The convolutional perfectly matched layer	221
B.6	Thin layers	225
Appendix C The 10x10 pixelated pattern catalogues		232
Appendix D Modelling tool source code		234

List of tables

Table 2.1. Yee grid offsets	23
Table 2.2. Shapes available for scene building.....	50
Table 2.3. Some of the genes available	55
Table 3.1. The search parameters for step 1	69
Table 3.2. Pattern symmetries	89
Table 3.3. Two example fitted polynomial classification bins	92
Table 4.1. The specifications of the example lenses.....	99
Table 4.2. Anti-reflection layer formulae.....	136
Table 4.3. Polypropylene trial centre column structure details.....	140
Table 4.4. Silicon trial centre column structure details	142
Table 4.5. Lenslet design details.....	143
Table 4.6. Square patch polypropylene lenslet, refractive indices	144
Table 4.7. Square patch polypropylene lenslet, patch ratios.....	145
Table 4.8. FWHM for the square patch polypropylene design	147
Table 4.9. FWHM for the super-capacitive patch polypropylene design	147
Table 4.10. Super-capacitive patch polypropylene lenslet, refractive indices ..	149
Table 4.11. Example polypropylene lenslet, super-capacitive patches.....	149
Table 4.12. Example silicon lenslet, square patches	151
Table 4.13. Example silicon lenslet, square patches, refractive indices	151
Table 4.14. Full width, half maximum for the square patch silicon design	153
Table 4.15. Refractive index catalogue contents	163
Table 4.16. Curved column widths	164
Table 4.17. Curved column Silicon lenslet design details	167
Table 4.18. Full width, half maximum for the curved column silicon design.....	168
Table 4.19. Curved column patch ratios.....	169
Table 4.20. Curved column, refractive indices	169

List of figures

Figure 1.1. Air gap two-layer filter.....	4
Figure 1.2. Commonly used mesh layouts (metal is in blue).....	5
Figure 1.3. Combination mesh layouts (metal is in blue).....	6
Figure 1.4. The split ring resonator (metal is in blue).	6
Figure 1.5. A 4x4 pixelated pattern with corner-to-corner pixels.	7
Figure 1.6. The general Luneburg lens	10
Figure 1.7. Baghel et al's S shape.....	10
Figure 1.8. Flat GRIN lens concept	11
Figure 1.9. Slot and horn antenna beam pattern sketches.....	12
Figure 1.10. Silicon hemispherical lens with antenna.....	12
Figure 2.1. 1D propagation in a dielectric.....	17
Figure 2.2. 1D propagation across a boundary	18
Figure 2.3. Square metallic mesh grid dimensions.....	19
Figure 2.4. 1D propagation through grid.....	19
Figure 2.5. The Yee grid.....	23
Figure 2.6. Total Field/Scattered Field method of inserting a plane wave.....	26
Figure 2.7. A wave encounters a boundary with a lossy region	29
Figure 2.8. The Yee grid with the thin layer modification.....	32
Figure 2.9. HFSS mesh generation example	36
Figure 2.10. Basic operation of the genetic algorithm	37
Figure 2.11. Basic operation of the micro-genetic algorithm	38
Figure 2.12. Genome encoding	39
Figure 2.13. Fitness assessment.....	40
Figure 2.14. Butterworth and Chebyshev filter transmittance functions	42
Figure 2.15. Butterworth and Chebyshev filter phase shift functions	43
Figure 2.16. Tournament selection.....	44
Figure 2.17. Uniform crossover	44
Figure 2.18. Modelling tool main GUI window	45
Figure 2.19. Basic UML symbols.....	46
Figure 2.20. The main components of the modelling application	46
Figure 2.21. The three available boundary conditions for the FDTD domain	47
Figure 2.22. Electric field FDTD update code.....	48
Figure 2.23. The application domain object contents	49
Figure 2.24. Modelling tool GUI, the shapes panel	49

Figure 2.25. Modelling application sources	51
Figure 2.26. Modelling application sensors	52
Figure 2.27. Modelling tool GUI, the variables panel	53
Figure 2.28. Modelling tool sequencer objects.....	53
Figure 2.29. Modelling tool GUI, the genetic search panels.....	54
Figure 2.30. Verification modelling in HFSS and FDTD	56
Figure 2.31. Thin metal patch represented in a Yee grid	57
Figure 2.32. Propagation matrix formulae verification.....	58
Figure 2.33. FDTD algorithm verification.....	58
Figure 2.34. A half wave rectified sine wave encountering a metal mesh.....	59
Figure 2.35. FDTD verification model.....	60
Figure 2.36. FDTD transmittance verification.....	61
Figure 2.37. Effect of mesh coarseness with HFSS.....	61
Figure 2.38. FDTD thin sheet verification.....	63
Figure 2.39. Layer spacing and the propagation matrix method	64
Figure 2.40. Modelling error for the propagation matrix method	64
Figure 3.1. Relationship between the repeat cell and the unit cell	68
Figure 3.2. An 18x18 pixel plate with four-fold symmetry.....	70
Figure 3.3. Chebyshev low-pass filter design from step 1.....	71
Figure 3.4. Chebyshev low-pass filter step 2	72
Figure 3.5. Chebyshev low-pass filter designs.....	72
Figure 3.6. Losses of the Chebyshev low-pass filter designs	73
Figure 3.7. Chebyshev low-pass filter step 3	74
Figure 3.8. Butterworth low-pass filter design from step 1	75
Figure 3.9. Butterworth low-pass filter step 2.....	76
Figure 3.10. The transmittance of the Butterworth low-pass filter	76
Figure 3.11. Losses of the Butterworth low-pass filter designs	77
Figure 3.12. Capacitors and dimensions of a square patch mesh	79
Figure 3.13. Diffraction grating and interference	79
Figure 3.14. Capacitive mash as a diffraction grating	80
Figure 3.15. A super-capacitance patch with two fingers.....	81
Figure 3.16. A birefringent mesh	82
Figure 3.17. Sequence of square and super-capacitive patches	83
Figure 3.18. Transmittance curves of selected steps.....	84
Figure 3.19. Phase shift curves of selected steps.....	84
Figure 3.20. Super-capacitive low-pass filter model.....	86
Figure 3.21. Super-capacitive low-pass filter transmittance.....	87
Figure 3.22. Four-fold and two-fold symmetries.....	89

Figure 3.23. Four-fold 10x10 binary pattern catalogue.....	90
Figure 3.24. A sequence of inductive patterns	91
Figure 3.25. The transmittance curves from classification bin 54.....	92
Figure 3.26. Transmittance curves from classification bin 24.....	93
Figure 3.27. Corner-to-corner pixels.....	93
Figure 3.28. Corner-to-corner pixel test patterns.....	94
Figure 3.29. Transmittances for the corner-to-corner test patterns	94
Figure 3.30. Two-fold 10x10 binary pattern catalogue	96
Figure 3.31. The chosen four-fold patterns for the usage test.....	97
Figure 3.32. Two four-fold pattern verification	98
Figure 4.1. Simple path length design model	101
Figure 4.2. Variation of refractive index across a lens.....	103
Figure 4.3. Initial HFSS modelling of metamaterial lenslet structures	105
Figure 4.4. Extrapolating a lenslet radial stripe	106
Figure 4.5. Gaussian beam at lenslet focal point	107
Figure 4.6. Model for measuring the phase velocity.....	109
Figure 4.7. Matching with a test dielectric	110
Figure 4.8. Signal flows in a two-port network.....	111
Figure 4.9. The test arrangement used by Nicholson and Ross	112
Figure 4.10. Signal flow graph for the Nicholson and Ross setup.....	112
Figure 4.11. Measuring the refractive index using HFSS	113
Figure 4.12. Signal flow graph with a vacuum zone	113
Figure 4.13. The refractive index using the three methods described.....	118
Figure 4.14. The HFSS model for the refractive index survey.....	119
Figure 4.15. Polypropylene artificial dielectric series.....	120
Figure 4.16. Silicon artificial dielectric series.....	120
Figure 4.17. Example polypropylene lenslet designs	121
Figure 4.18. The electric field magnitude for the two lenslet designs.....	122
Figure 4.19. The far-fields of the two example lenses.....	122
Figure 4.20. Calculated refractive index across the diameter	124
Figure 4.21. Effect of GRIN column width on lenslet behaviour	124
Figure 4.22. Effect of GRIN column width on the wavefront.....	125
Figure 4.23. Deviation due to GRIN column width	126
Figure 4.24. Transmittance of 10 layers of a 240 μm square patch	127
Figure 4.25. Polypropylene mean ripple transmittance	128
Figure 4.26. Silicon mean ripple transmittance	128
Figure 4.27. Silicon mean ripple transmittance and patch ratio.....	129
Figure 4.28. Silicon mean ripple transmittance heat map	129

Figure 4.29. Polypropylene refractive index and layer spacing.....	131
Figure 4.30. Polypropylene refractive index against layer spacing	131
Figure 4.31. Polypropylene phase shift per metamaterial layer	132
Figure 4.32. Polypropylene attenuation and layer spacing	133
Figure 4.33. Silicon attenuation and patch size.....	134
Figure 4.34. Polypropylene: refractive index against patch ratio.....	135
Figure 4.35. Silicon: refractive index against patch ratio	135
Figure 4.36. Anti-reflection stages.....	136
Figure 4.37. Lenslet structures with anti-reflection layers	138
Figure 4.38. Silicon lenslet structure with anti-reflection layers.....	139
Figure 4.39. Possible centre columns of the polypropylene lenslet	140
Figure 4.40. Polypropylene centre column attenuation	141
Figure 4.41. Possible centre columns of the silicon lenslet.....	141
Figure 4.42. Silicon centre column attenuation	142
Figure 4.43. Polypropylene lenslet, square patches, E field	146
Figure 4.44. Polypropylene lenslet, square patches, far field.....	146
Figure 4.45. Polypropylene lenslet, super-capacitive, E field.....	148
Figure 4.46. Polypropylene lenslet, super-capacitive, far field	148
Figure 4.47. Silicon lenslet, square patches, E field.....	152
Figure 4.48. Silicon lenslet, square patches, far field.....	152
Figure 4.49. Ray tracing concept	154
Figure 4.50. Polypropylene lenslet ray tracing	155
Figure 4.51. Angle of incidence modelling	156
Figure 4.52. Effect of incidence angle on refractive index.....	157
Figure 4.53. Curved column concept	158
Figure 4.54. Curved column geometry	159
Figure 4.55. Curved column unit cell geometry.....	160
Figure 4.56. Curved column geometry, ray close up.....	161
Figure 4.57. Curved column demonstration E field	164
Figure 4.58. Constant column size with curved columns	165
Figure 4.59. Curved column silicon lenslet, E field magnitude.....	167
Figure 4.60. Curved column lenslet, far field.....	168
Figure 4.61. Possible layer layout for a curved column lenslet.	170
Figure 4.62. A trapezoid patch in a trapezoid unit cell	170
Figure 4.63. HFSS model of trapezoid patches	171
Figure 4.64. Refractive index of a trapezoid patch.....	172
Figure B.1. FDTD plane wave geometry	211

Acknowledgements

I could not have taken the time to fulfil a long-held ambition to ‘do a PhD’ without the unfailing support of my wife, Heather. Thank you for being part of my life for all these years.

Many thanks to my supervisors, Giampaolo Pisano and Carole Tucker, for being happy to take on a (very) mature student and guiding me through this project. Extra thanks go to Giampaolo for naming the Super-Capacitive patch.

Thanks also go to Thomas Gascard for very useful discussions over smoothies in Cardiff city centre.

Finally, I acknowledge the support of the Supercomputing Wales project, which is part-funded by the European Regional Development Fund (ERDF) via Welsh Government, for the provision of the Hawk cluster computer and for foolishly allowing me access.

Publications

The work described by this thesis has been reported in the following publications.

Conference proceeding

Thompson, J. A.; Pisano, G. *Use of Evolutionary Computing Algorithms in the Design of Millimetre-Wave Metamaterial Devices*. In Millimeter, Submillimeter, and Far-Infrared Detectors and Instrumentation for Astronomy IX; International Society for Optics and Photonics, 2018; Vol. 10708, p 107083H

Refereed journals

Thompson, J. A.; Pisano, G.; Tucker, C. *Mesh Low-Pass Filters for Millimeter-Wave Applications: Is the Square Capacitive Shape Optimal?* J. Astron. Telesc. Instrum. Syst. 2020, 6 (3), 036003

Thompson, J. A.; Pisano, G.; Tucker, C. *Super-capacitive patches and their use in low pass filters and artificial dielectrics*. Opt. Eng. 2021, 60 (1), 017106

Chapter 1

Introduction

The Cosmic Microwave Background (CMB) is of great interest to astronomers as it contains information from the early universe. Samtleben et al¹, give a useful review of the phenomenon. The universe immediately after the big bang was dominated by radiation and was hot and opaque. As the universe expanded and cooled, neutral atoms began to form in a period known as the recombination epoch, around 370,000 years after the big bang. This caused the universe to become transparent, and photons began to travel without continual scattering. It is this relic radiation from the surface of last scattering that forms the CMB which manifests today as an almost smooth glow in all directions with the frequency curve of blackbody radiation at 2.725 K, corresponding to a peak frequency of 160 GHz. The radiation was emitted at a temperature of around 3000 K, but the subsequent expansion of the universe has red shifted it to that seen today.

The blackbody temperature observed from all directions is the same (to within one part in 10^{-4}) which implies that the observable universe must have been in thermal equilibrium at this time. This is surprising as the speed of light is such that not all parts of that universe can have been in contact in the time since the big bang. This has led to the proposal that there was a period of faster than light expansion of the universe before it was 10^{-32} seconds old that increased its size by some twenty-one orders of magnitude, a phenomenon known as inflation. The small differences that can be measured in the blackbody temperature across the sky (its anisotropy) are identified with quantum fluctuations that occurred in the pre-inflated universe.

It is the anisotropies in the CMB that are the main interest to astronomers. As these are very small, they are difficult to measure, requiring a sensitive receiver. In addition, the highest frequencies of interest lie on the lower boundary of a region of the electromagnetic spectrum that has been termed the terahertz gap, Sirtori². The gap exists due to the upper frequency range of oscillating electron devices (antennas) and the lower frequency range of semiconductor band gap devices (laser diodes for example) not overlapping. This reduces the sensitivity of antennas designed for these frequencies, raising the importance of light collection devices to compensate.

The sensitivity of a receiver is the smallest signal that produces a specified signal to noise ratio. Part of the noise in the ratio is thermal due to the vibrations of electrons (Nyquist³) which can be reduced by lowering the temperature of the detector. This leads to the trend of cooling CMB detectors to cryogenic temperatures.

A further difficulty arises from how the desired information about the early universe is encoded in the anisotropy and polarisation (Seljak⁴ for example) of the CMB. The polarisation is generated by the last scattering event it encountered during the recombination epoch (assuming light that has subsequently been scattered by foreground objects can be removed). In recent years, attention has been focussed on the prediction that inflation should have generated primordial gravitational waves that could be detected through polarisation anisotropy of the CMB, Seljak and Zaldarriaga⁵. These signals, referred to as B-mode polarisation, are very difficult to detect and require that optical components distort it as little as possible. The atmosphere itself complicates observations, absorbing radiation in a frequency dependent manner (water vapour and carbon dioxide are major absorbers in the frequency range of interest). It is mostly transparent in the “radio window” up to around 30 GHz, becoming increasingly absorbing up to 300 GHz. As a result instruments are now being planned for spacecraft, for example LiteBIRD described by Ishino⁶. This can impose mass limitations on instruments which impact optical processing.

The use of metamaterials in the design of optical components for millimetre wave cosmic microwave background instruments has become almost routine in recent years. Many instruments now contain filters constructed using metamaterials, and other devices such as wave plates and lenses, are starting to appear. In their review paper, Ade et al⁷ describe filters and dichroics manufactured by the Cardiff group for instruments including Planck (Lamarre et al⁸), the Atacama Cosmology Telescope (Kosowsky⁹), Scuba-2 (Audley et al¹⁰), and Herschel (Griffin et al¹¹, Poglitsch et al¹²). Devices constructed using these technologies often offer advantages in robustness, mass, volume, and performance over more conventional approaches. These devices are examples of frequency selective surfaces (FSSs) to which Munk¹³ gives a good introduction.

In general terms, a metamaterial is a sub-wavelength arrangement of physical structures embedded in a dielectric that interact with the radiation in a manner that causes the effective bulk properties (permittivity and permeability) of the combination to take up values not necessarily found in naturally occurring

materials. In the millimetre wave regime, such structures can include holes in a dielectric, metal grains or patches embedded in a dielectric, and even small, printed circuit boards carrying copper tracks. These structures, when repeated in regular arrays, can be viewed as artificial dielectrics with permittivity and permeability characteristics that can be tailored for the application. Perhaps the most famous is the ‘invisibility cloak’ described by Schurig et al¹⁴ which utilises split ring resonators to create a metamaterial that can hide a volume of space, directing electromagnetic radiation around it. Its drawback is that it only works for a restricted range of frequencies. Ergin et al¹⁵ have extended the principles into the optical regime using transformation optics (of which, more in section 1.3 below) to design the arrangement of dielectric bulk properties.

1.1 Filters

The use of metal meshes consisting of arrays of square patches (a capacitive grid) or square holes in a metal sheet (an inductive grid) was described by Ulrich¹⁶. He showed that square patches provided a low-pass response, square holes were complementary with a high-pass response and that both could be modelled as lumped elements in transmission lines. The capacitive devices consisted of metal meshes supported by a thin Mylar film. Where multiple layers were used, they were separated by air, were rather hard to construct and delicate (Figure 1.1). These principles have been used to design bandpass filters using both capacitive and inductive grids, for example Ade¹⁷ and Timusk and Richards¹⁸. Over the years there have been further developments, usefully reviewed by Ade et al⁷ and by Pisano et al¹⁹.

The use of solid dielectrics to fill the gaps between metamaterial mesh layers leading to more robust devices has enabled many applications for the technology. The hot press process using copper patches on polypropylene sheets, described by Ade et al⁷, leads to devices that can be cut into any shape and withstand rough handling. The dielectric keeps the layers fixed relative to each other and makes devices with many layers eminently practical.

Other methods of creating robust devices have been investigated. Sushko et al²⁰ assessed the feasibility of using ink jet printing technologies to create mesh patterns with a silver based conductive ink on polyethylene terephthalate film. They demonstrated single layer bandpass filters at 100 GHz and 300 GHz. They did not investigate combining multiple layers, however.

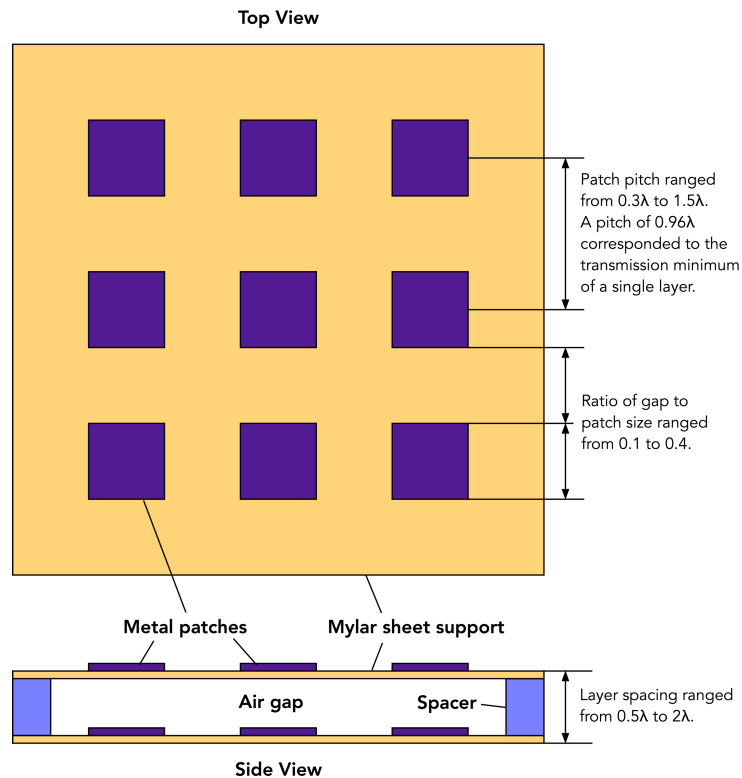


Figure 1.1. Air gap two-layer filter. Arrangement of the two-layer capacitive patch filters constructed by Ulrich. The square metallic patches were deposited on a Mylar film which was then suspended between spacers to form the air gap. The patches are shown here aligned vertically, this is not required in practice, however. Ulrich made measurements over the ranges of dimensions as indicated.

Three-dimensional printing technology has also shown promise. Sun and Hy²¹ review the application of 3D printing for many different devices in the terahertz region. They describe the most important features of several 3D printing technologies and printable materials when used for this kind of application. Finally, they describe instances of various devices including a number of lens variants, some examples of which based on printed nylon metamaterials with air gaps.

Silicon is also often used as the substrate dielectric carrying the meshes; Kundu et al²² describe a band-stop filter using bonded silicon wafers. The choice of silicon as the dielectric is often down to its cryogenic properties and the ease with which chemical processes can be performed on this solid substrate. Due to its extensive use in electronic integrated circuit manufacture, there are many photolithographic manufacturing processes readily available. This is important for the lenslet work reported here which has the ultimate aim of incorporating the antenna and the lenslet arrays into a single device.

The square patches and holes originally described by Ulrich¹⁶ are still the predominant patch shapes used in low and high-pass filter devices, for example Tucker and Ade²³ describe such devices. The behaviour of these meshes is due to the currents and field storage that are induced when they are excited by an incident electromagnetic wave, shown in Figure 1.2. The isolated square patches of the capacitive mesh store the electric field in the gaps between them in the same way as electronic capacitors. In contrast, in the inductive mesh currents are free to flow around the structure, forming an array of one turn inductors.

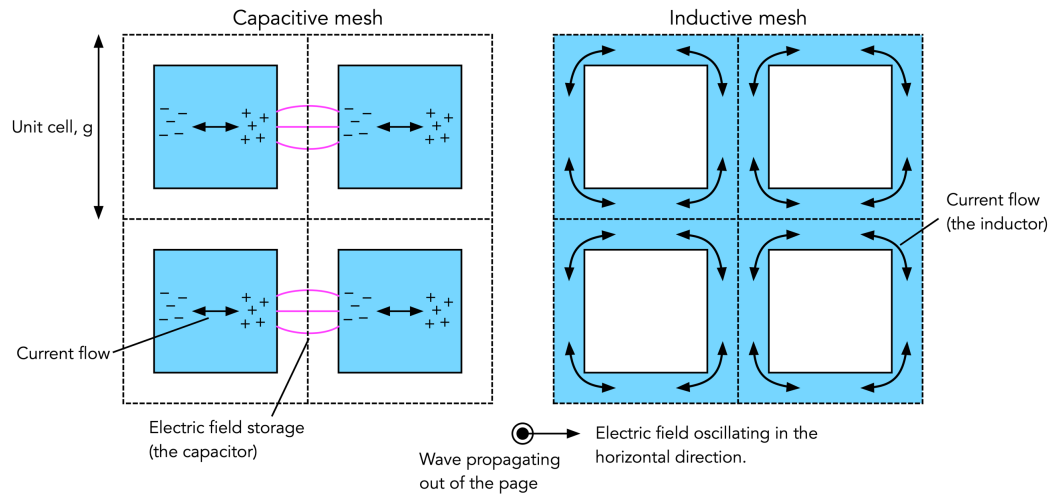


Figure 1.2. Commonly used mesh layouts (metal is in blue). The mesh on the left behaves as an array of capacitors, storing the electric field in the gaps between the plates. Its complement on the right allows currents to flow in essentially single turn inductors. The movement of charge in the metal is mostly induced by the incident wave's electric field.

Combinations of the capacitive and inductive grid shapes have been used to create bandpass and bandstop responses. Moallem and Sarabani²⁴ constructed a bandstop device using the pattern on the right of Figure 1.3, which consists of capacitive squares inside the inductive mesh. Wang et al²⁵ produced machined cross holes in a metal sheet to demonstrate the pattern on the right of Figure 1.3, doing their measurements in reflection mode where it behaves as a bandstop device. Melo et al²⁶ used photo-lithography to make their cross patterns which they measured in transmission.

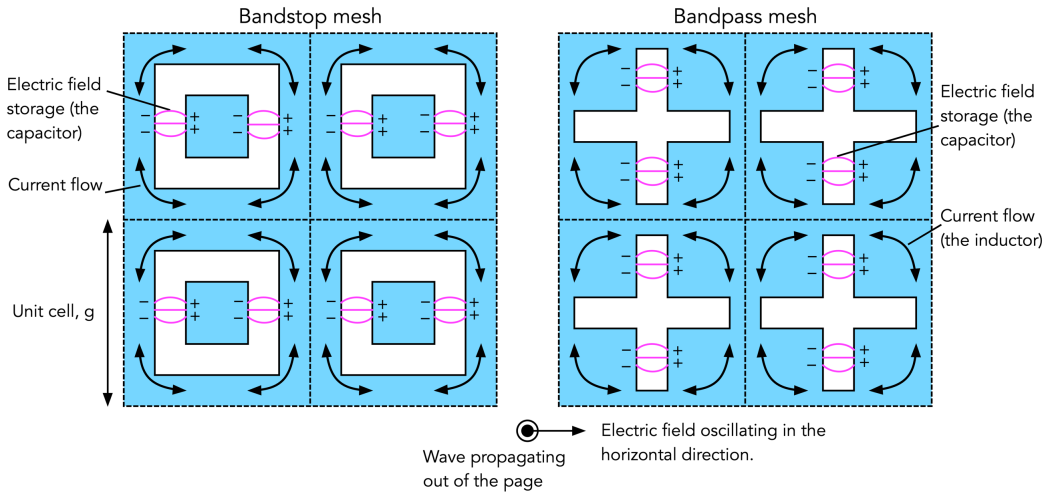


Figure 1.3. Combination mesh layouts (metal is in blue). The mesh on the left behaves as bandstop pattern (in transmission), the inductor is in parallel with the capacitor. The mesh on the right performs the band pass function.

Split ring resonators as shown in Figure 1.4 have been used on occasion. Two examples are the invisibility cloak already discussed (Schurig et al¹⁴) and Kundu et al²² who described a tuneable bandstop filter in the 30 to 70 GHz range. More esoteric patch shapes have also been mentioned: Monacelli et al²⁷ investigated the behaviour of square metallic loops, Navarro-Cia et al²⁸ used nested split ring resonators and Wu²⁹ explored various fractal shapes.

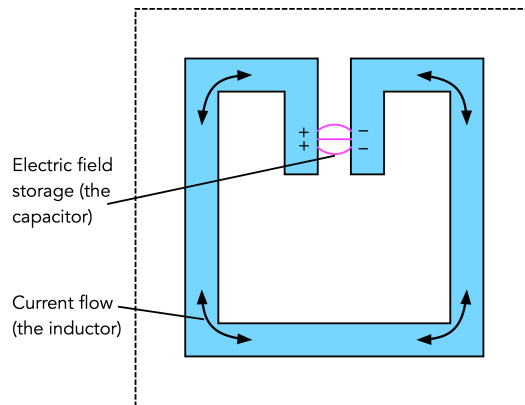


Figure 1.4. The split ring resonator (metal is in blue). This pattern consists of an inductive loop that is cut by a capacitive gap. The resonant frequency is governed by the values of the inductor and capacitor.

The concept of pixelated patterns consisting of regular arrays of square sub-cells (pixels) that may or may not be metal filled, have been used with optimisation algorithms to design novel shapes. Ge and Esselle³⁰ describe combining a genetic algorithm (a optimisation method based on natural evolution, see section 2.4) with

the finite differences time domain (FDTD) modelling method (see section 2.2). They use this to propose a pair of reflective surfaces.

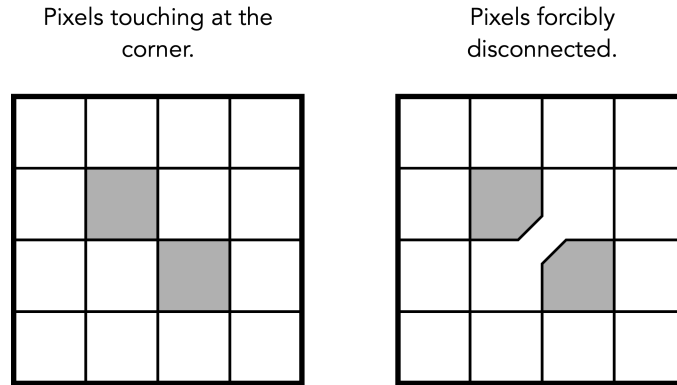


Figure 1.5. A 4x4 pixelated pattern with corner-to-corner pixels. The grey pixels are metal filled, the white pixels are not. On the left, the two grey pixels only touch at their corners. On the right a small gap (exaggerated in the diagram) is introduced to disconnect them.

One problem with the pixelated patterns that the genetic algorithm settles on is that they may contain pixels that are only connected at their corners as shown in Figure 1.5. These pixels will be difficult to manufacture reliably, sometimes the pixels will be connected and sometimes not, possibly causing severe mismatches between modelling and the constructed devices. Sui et al³¹ use the same technique for a reflective surface that they proceed to manufacture and test. It too has a few corner-to-corner pixels, but they do not comment on their impact. Sui et al³² also talk about the resemblance of these patterns to QR codes although this seems a little irrelevant.

Ranjan et al^{33,34} use the same pixelated pattern patches with a wind driven optimisation algorithm, but they note the corner-to-corner issue and forcibly disconnect them by introducing a small gap which makes them easily manufacturable (shown on the right in Figure 1.5). This does, however, require the modelling technique used to have sufficient resolution to represent the gap. The wind driven optimisation algorithm is a nature inspired search method based on the movement of the atmosphere.

Whether there are any other shapes that can be used in metamaterial meshes that lead to filter designs with improved properties is one of the questions that this work investigated. The pixelated pattern along with a search technique inspired by evolution and natural selection (the genetic algorithm) being the chosen methodology. Another approach to finding alternative patterns for capacitive

meshes, by focussing on ways of increasing their capacitance, is a further line of enquiry that was followed.

The genetic algorithm (and similar optimisation methods) are stochastic tools and could easily miss patterns with interesting characteristics. This led to the author investigating the feasibility of cataloguing a complete set of $N \times N$ pixelated patterns that could be rapidly searched for useful features. The problem with this is that there are an exceedingly large number of patterns for useful values of N . However, using symmetry and other arguments, this number can be reduced to a quantity of patterns that is possible to model on a cluster computer and the results are reported here in section 3.3.

1.2 Artificial dielectrics

Kock³⁵ describes using various kinds of metallic shapes, including conductive squares on a foam carrier, to produce a structure with an increased refractive index that is then used to construct a lens operating at frequencies of a few gigahertz. These structures would now be recognised as meta-material based artificial dielectrics.

The use of closely spaced capacitive squares in a hot-pressed polypropylene dielectric in order to create an artificial dielectric is described by Zhang et al³⁶. They show that the effective refractive index of such a structure is dependent on the ratio of the inter-square gap and the unit cell size. They use this to demonstrate an anti-reflection coating for a quartz plate, where they are able to tune one anti-reflection layer to have a refractive index of 1.7. This principle was applied to half-wave plates deployed on the balloon borne instruments, PILOT, Bernard et al³⁷, and BLAST-Pol, Fissel et al³⁸. Zhang et al³⁹ describe a half wave plate that introduces the concept of varying the patch shape to affect the properties of the metamaterial mesh, an idea that is expanded upon in this work.

Another application of an artificial dielectric is described by Syed and Neto⁴⁰. Using the ability to tailor the dielectric properties of the bulk material, they demonstrate the ability to enhance the front to back ratio of a printed planar antenna. Pisano, Ade and Tucker⁴¹ present a magnetic mirror incorporating a graded refractive index layer constructed with metamaterial artificial dielectrics. A reflective half-wave plate implemented using artificial dielectrics is described by Pisano et al⁴².

In a pair of papers Cavello et al^{43,44} present a mathematical analysis of the behaviour of the closely spaced meta-material mesh layers in an artificial dielectric.

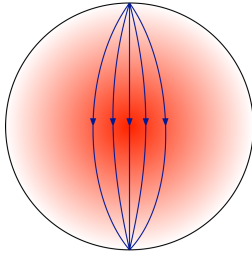
1.3 Lenses

A conventional lens achieves its focussing behaviour by varying the thickness of a dielectric material across its diameter, the bending of the light occurring at the curved boundaries. An alternative concept of creating a lens by varying the refractive index of the dielectric across the diameter of the lenses, causing light to bend within it rather than at its surface, is referred to as a graded index (GRIN) lens.

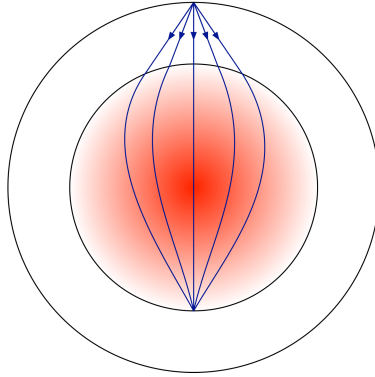
In the middle of the 19th century, Maxwell⁴⁵ mathematically described a GRIN lens which has become known as Maxwell's Fisheye Lens. It consisted of a sphere made of a dielectric material whose refractive index varied along the radius. Luneburg⁴⁶ generalised the treatment which led to a class of devices now called Luneburg Lenses (Figure 1.6) which have found a number of specialist applications. Two examples are; a microwave lens patented by Robinson⁴⁷ and a method of reducing back reflection from a fibre optic termination claimed by Sinclair⁴⁸. Xin and Liang⁴⁹ describe manufacturing millimetre wave Luneburg lenses using 3D printing of a polymer, effectively an air-gapped metamaterial artificial dielectric structure. Kuntz and Smith⁵⁰ describe the use of transformation optics to produce a flattened Luneburg lens, introducing the idea of curved columns in a flat GRIN structure, something that was investigated in this work. Chen et al⁵¹ give a very accessible description of the principles behind transformation optics; basically a method of converting spatial geometry into parameter (permittivity and permeability) geometry, although Pendry et al⁵² and Leonhardt⁵³ both give treatments that predate this. In his PhD thesis, Hunt⁵⁴ discusses the uses of transformation optics in metamaterial lens design in detail.

The most common approach to constructing a flat GRIN lens, varying the refractive index transversely with respect to the propagation of the light (Figure 1.8), is described by a number of authors. In the infra-red, Luque-Gonzalez et al⁵⁵ use a sub-wavelength grating (the grating spacing controls the effective refractive index) to create a spot converter lens. For millimetre waves, split ring resonators (introduced in Figure 1.4) are a common choice for constructing the artificial dielectric, used by Mishra et al⁵⁶ and Kitayama et al⁵⁷. Being resonant structures, the resulting artificial dielectric can be rather frequency dependent which may result in devices with a limited bandwidth.

Maxwell's fish eye lens, rays from the sphere surface are focussed on the surface directly opposite.



General case, rays from one concentric sphere are focussed onto the surface of the other sphere.



Outer sphere at infinity, parallel incident rays are focussed on the opposite sphere surface.

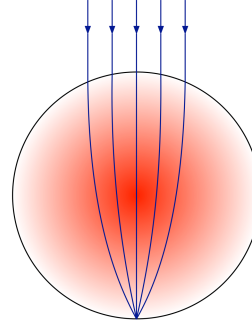


Figure 1.6. The general Luneburg lens is a dielectric sphere with a graded refractive index such that rays from another concentric sphere are focussed onto its surface. Maxwell's fisheye lens is the special case where the two spheres are identical. Darker colour indicates a higher refractive index.

Another resonant pattern variant, 'S' shaped metal patches, was used by Baghel et al⁵⁸. These were printed on both sides of thin dielectric slabs and an array of them arranged edge on to the wave propagation direction, as shown in Figure 1.7. This allows the electrons in the metal that are set in motion by the electric field, to also react to the magnetic field without being constrained to a plane parallel to the magnetic field.

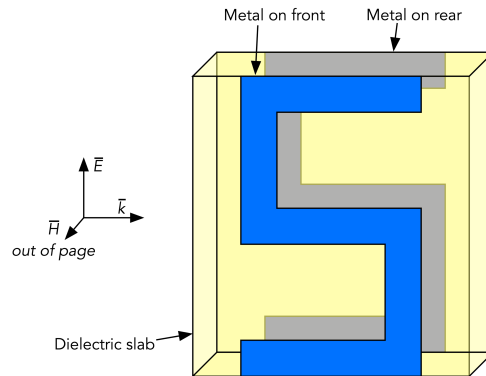


Figure 1.7. Baghel et al's S shape. The waves propagating from left to right encounter the patches edge on.

Chen et al⁵⁹ used closed square rings but more importantly gave a detailed derivation of the design model used to specify the refractive index across the lens. This contains the assumption that all the ray bending happens at the lens surface which becomes less valid with increasing lens thickness, something that was investigated in detail by this work.

Drilled holes are also often used to vary the refractive index of a dielectric. When they repeat at sub-wavelength distances, they reduce the refractive index seen by incident waves in proportion with the amount of material removed. Defrance et al⁶⁰ use this in their lens and He and Eleftheriades^{61,62} also include anti-reflection layers in the structure. The approach studied in the work reported here used square metallic patches, as reported by Nguyen et al⁶³, Savini et al⁶⁴ and Pisano et al⁶⁵.

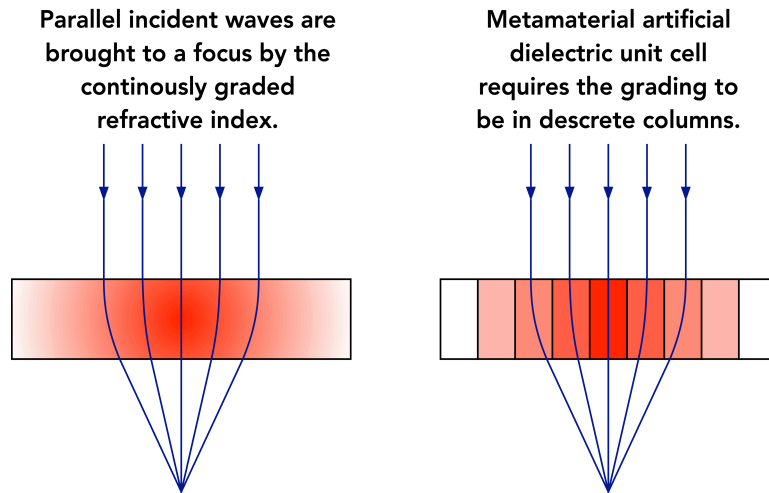


Figure 1.8. Flat GRIN lens concept. Ideal continuously graded refractive index on the left, discretely graded artificial dielectric implementation on the right. Darker colour indicates a higher refractive index.

A number of applications of GRIN lenses have been patented over the years, here are some examples. A method of using longitudinal index grading to improve spherical aberration is claimed by Sukumlyn⁶⁶. A spherical Luneberg lens for a radar system is claimed by Robinson⁴⁷. A GRIN lens array constructed using synthetic resin for use in a fax machine read head is claimed by Yamamoto et al⁶⁷. The use of an optical GRIN lens as the objective in a biological microscope is claimed by Schnitzer⁶⁸. A GRIN lens with a specific transfer function used to couple an antenna array is claimed by Lier⁶⁹.

1.4 Lenslet arrays

The focal planes of some millimetre wave imaging instruments consist of an array of corrugated horn antennas each providing one pixel. While there has been much work done on optimising their design and manufacture, horn antennas still remain hard to construct, especially in larger arrays. Shulwitz and Mortazawi⁷⁰ describe a lithographic technique, Li et al⁷¹ use a 3D printing process. Nibarger et al⁷² describe an 84 pixel array suitable for cosmic microwave background measurements. Chattopadhyay et al⁷³ suggest an array of slot antennas to avoid

the need for horns, but these do not have the same highly directional beam pattern (see Figure 1.9).

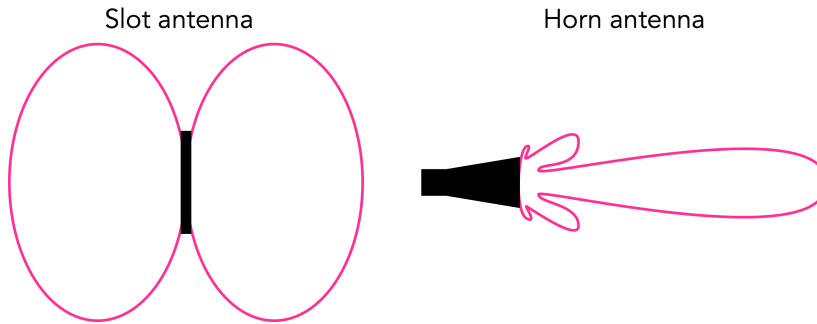


Figure 1.9. Slot and horn antenna beam pattern sketches. The beam formed by a slot antenna is rather non-directional when compared to a horn antenna.

An approach used to emulate a horn array is to form an array of lenslets, in the manner of a compound eye, each one coupling to an antenna. The lens converts the rather isotropic antenna beam into the desired directional beam that allows an image to be constructed. Huo et al⁷⁴ investigate a typical arrangement of an antenna (log-periodic in their case) mounted on the back of a hemispherical lens as in Figure 1.10. Nitta et al⁷⁵ use this arrangement coupled with kinetic induction detectors (KIDs). An array of 271 lenses constructed from silicon hemispheres with a two stage anti-reflection coating is described by Suzuki et al⁷⁶. The CMB instruments POLARBEAR-2 and the Simons Array both use these and are discussed by Suzuki et al⁷⁷.

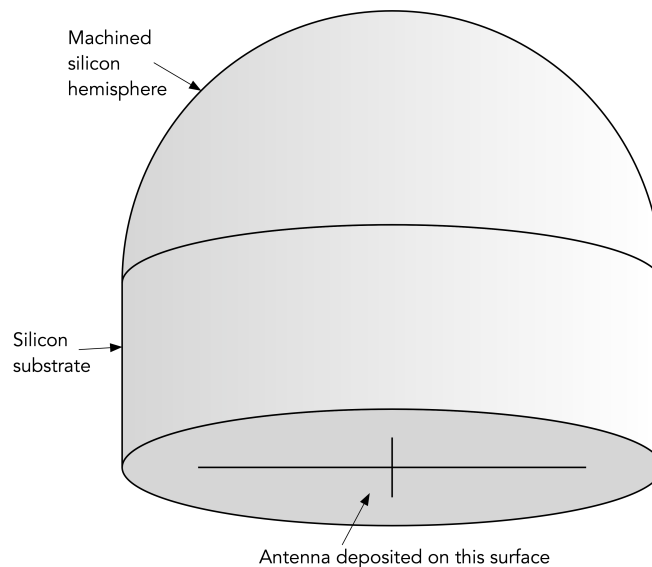


Figure 1.10. Silicon hemispherical lens with antenna.

More recently, replacing the silicon hemispheres (themselves reasonably difficult to manufacture) with flat metamaterial GRIN lenslet arrays has been investigated. Pisano et al⁷⁸ report an array of seven lenses, each 10.3mm in diameter, in a hexagonal tessellation using a polypropylene base dielectric. Trappe et al⁷⁹ combined this with sinuous and dual slot antennae. Pisano et al⁶⁵ describe an extension to an array of nineteen 6.3 mm diameter lenses in a silicon substrate. The main aim of the work reported here was to find ways to improve the performance of the metamaterial lenslets used in such arrays.

1.5 Modelling

Computer modelling of electromagnetic radiation as it passes through and around structures is an important part of the design process of metamaterial devices. It is used to investigate the properties of individual components of designs as well as complete structures. During the course of the work for this thesis, a number of modelling methods were investigated and used.

Firstly, and most straightforward, was the one dimensional forward and reverse fields approach described by Orfanadis⁸⁰. Using the complex admittances of meshes, this method can be used to rapidly model single columns of meshes, so long as constraints on the validity of the admittances used are observed. This method is referred to as the Propagation Matrix Method in this thesis.

Secondly, the Finite Differences, Time Domain (FDTD) algorithm, originally described by Yee⁸¹ and expanded by Taflov and Hagness⁸² and Schneider⁸³ was explored. An implementation of this algorithm was produced that allowed modelling to take place on the Cardiff University cluster. This allowed for the rapid assessment of options, although the shortcomings of the resolution of the underlying cubic grid must always be considered.

Finally, the Finite Element Analysis (FEA) method as implemented by the commercial Ansys HFSS⁸⁴ modelling application was used to validate designs. This tool has a track record of producing accurate results for a wide variety of models and was used in this work as the final authority during the modelling stage and as the reference against which the propagation matrix and FDTD model implementations were verified.

1.6 Genetic algorithms

Ge and Esselle³⁰ described a method of using an evolutionary algorithm alongside FDTD to find meta-material patterns that implement target transfer functions. They encoded the potential patterns as a 16x16 pixel grid, using four-fold symmetry to reduce the number of bits required to represent them to thirty-six. The basic genetic algorithm is described in Holland⁸⁵ and Eiben and Smith⁸⁶. Gi and Esselle used a variant, the micro-genetic algorithm (MGA) described by Krishnakumar⁸⁷.

It was felt that this general approach may be useful in optimising the design of metamaterial devices. An implementation of the MGA was coupled with the FDTD and propagation matrix method implementations to produce a tool capable of working not just on the patterns, but also other parameters that must be optimised in a metamaterial design.

1.7 Thesis structure

This thesis describes the modelling work undertaken to investigate the following.

- The optimisation of the basic square pattern capacitive structures as used by the Cardiff University filter group in the implementation of low pass filters using NxN pixelated patterns and the genetic algorithm.
- Production of catalogues of admittances of complete sets of NxN pixelated patterns for values of N that are feasible.
- A method of increasing the capacitance of such structures beyond that provided by the standard square shape and its possible use in filter designs.
- The design of GRIN lenses and possible improvements using the extended capacitance shape.
- Other performance gains that can be achieved by breaking away from the standard vertical column design of GRIN lenses to embrace columns that follow the paths of rays through the lens.

Chapter 1 is this introduction to the field of metamaterials, some of their applications and a review of the modelling and manufacturing techniques used to date.

Chapter 2 covers the modelling tools that were developed solely by the author, along with an introduction to the commercial Ansys HFSS tool. The mathematics of the implemented modelling techniques are outlined (with greater detail in Appendices A and B), and the evolutionary computing methods used are introduced. Finally, a summary of the functionality available to the user and the software design is given along with some verification results.

Chapter 3 reports on the efforts to improve the implementation of low-pass metamaterial filters using the genetic algorithm. An approach to increasing the capacitance of the patch using finger like modifications is then proposed and analysed. Finally, two catalogues of pixelated 10x10 patterns (four-fold and two-fold symmetric) are described, giving the normalised frequency response for each unique pattern.

Chapter 4 describes the design methods used for the GRIN lenses, bringing the various design points from the literature into a single design process, and shows the results of the optimisation and modelling. The modified capacitive patch from Chapter 3 is used to increase the range of refractive indices available to the artificial dielectrics. Improvements to the design model utilising curved columns are also proposed.

Finally, Chapter 5 contains a summary and suggestions for further work.

Prior to the University shutdown resulting from the Covid-19 pandemic, it had been planned to manufacture a low pass filter made using the increased capacitance patch, as described in section 3.2.3. Unfortunately, the manufacturing facilities at Cardiff were forced to close delaying this work.

The main unique achievements of the work reported in this thesis are:

- The proposal for a patch pattern with finger extensions that may lead to low pass filters with an extended stopband prior to the diffraction limit, and to extending the range of refractive indices available in artificial dielectrics.
- The use of curving columns in the implementation of mesh lenses, which has the potential to improve their performance.
- The production of catalogues of the complex admittances of 10x10 pixelated mesh patterns.

Chapter 2

The modelling tools

Two of the most popular modelling packages used in the investigation of the properties of meta-material devices are HFSS by Ansys⁸⁴ and CST Microwave Studio by Dassault Systemes⁸⁸. HFSS uses Finite Element Analysis (FEA) to numerically solve an equation derived from the time harmonic version of Maxwell's equations. CST uses the Finite Integration Technique (FIT) to solve Maxwell's equations in the time and frequency domains. Much of the modelling work for the lens investigation work reported by this thesis in Chapter 4 used HFSS which was also the mainstay of the group the author worked with.

Neither of these packages were available for use with the Hawk cluster provided by Supercomputing Wales that was used for the genetic algorithm and the cataloguing work, nor was there any custom modelling software maintained by the author's group that could be ported to the cluster. As a result, the cluster was not a resource used by the group. The author therefore developed a cross platform modelling tool that was primarily aimed at enabling the fulfilment of the aims of the work reported in Chapter 3, allowing the inclusion of the desired search and optimisation algorithms. It was also easily extensible for other related purposes and provided a platform for the implementation of the tools for the lens design methods of Chapter 4.

Two well-known modelling methods were selected for implementation. The first was a method outlined by Orfanadis⁸⁰ that is suitable for simple (essentially 1 dimensional) cases, referred to here as the propagation matrix method. The second was a method named Finite Differences, Time Domain (FDTD), as described in Taflov and Hagness⁸² and Schneider⁸³. The propagation matrix method produces a solution very quickly (in the order of seconds) for cases that conform to its limitations whereas the more general FDTD algorithm has much longer calculation times (often hours) that grow rapidly with model size.

This chapter along with Appendix A and Appendix B, expands on the referenced treatments to arrive at mathematical models with sufficient detail to allow their implementation on a modern, Linux based, cluster computer. The code was written in the widely used, general-purpose object-oriented language, C++17 and

structured in such a way that allowed builds to be created for desktop computers running Windows, MacOS or Linux as well as the cluster.

2.1 The propagation matrix method

The propagation matrix method is a means of modelling simple one-dimensional electromagnetic wave propagation (in the z direction, the modelled space is effectively infinitely sized in the x and y directions) by splitting the field into forward and backward components, as described in Orfanadis⁸⁰ chapters 2 and 5. One-dimensional Maxwell's equations are used to deduce propagation and matching matrices that can be used to calculate the effect of a plane wave travelling through homogenous dielectric regions and encountering boundaries between them. Despite being one-dimensional it is applicable to many meta-material designs for microwave optical devices.

This section presents the equations as implemented in the modelling tool. They are derived from the time harmonic version of Maxwell's curl equations (section 7.10 of Huray⁸⁹ for example) for plane waves in one dimension. For a full explanation, see Appendix A.

2.1.1 The propagation matrix for a dielectric

The propagation matrix represents the transmission of a plane wave completely within a dielectric (i.e., without encountering any boundaries) along the z axis as shown in Figure 2.1.

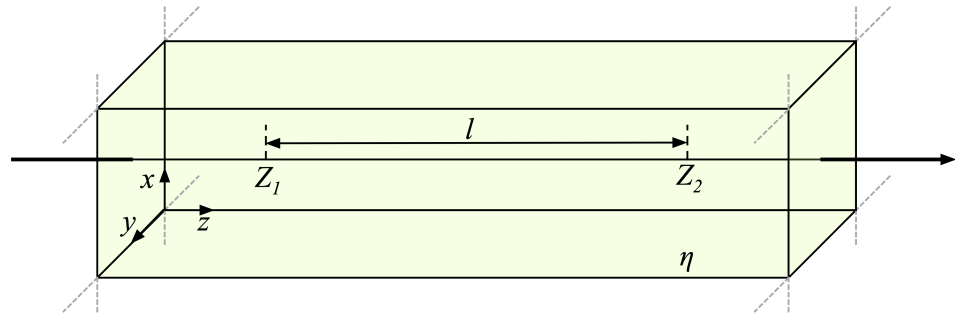


Figure 2.1. 1D propagation in a dielectric. A plane wave polarised in the x direction propagating along the z axis between two positions, z_1 and z_2 within a dielectric with characteristic impedance η that extends to infinity in the x and y directions.

The matrix equation (where the angular wave number $k = \omega/c = \omega\sqrt{\mu\varepsilon}$ and the characteristic impedance $\eta = \sqrt{\mu/\varepsilon}$) is

$$\begin{bmatrix} E_{1+} \\ E_{1-} \end{bmatrix} = \begin{bmatrix} e^{ikl} & 0 \\ 0 & e^{-ikl} \end{bmatrix} \begin{bmatrix} E_{2+} \\ E_{2-} \end{bmatrix} \quad 2-1$$

2.1.2 The matching matrix for the interface between two dielectrics

The matching matrix accounts for a plane wave crossing a boundary between two dielectrics with characteristic impedances η and η' , shown in Figure 2.2. The matrix equation is

$$\begin{bmatrix} E_+ \\ E_- \end{bmatrix} = \frac{1}{\tau} \begin{bmatrix} 1 & \Gamma \\ \Gamma & 1 \end{bmatrix} \begin{bmatrix} E'_+ \\ E'_- \end{bmatrix} \quad 2-2$$

where the reflection and transmission coefficients are

$$\Gamma = \frac{\eta' - \eta}{\eta + \eta'} \quad \tau = \frac{2\eta'}{\eta + \eta'}. \quad 2-3$$

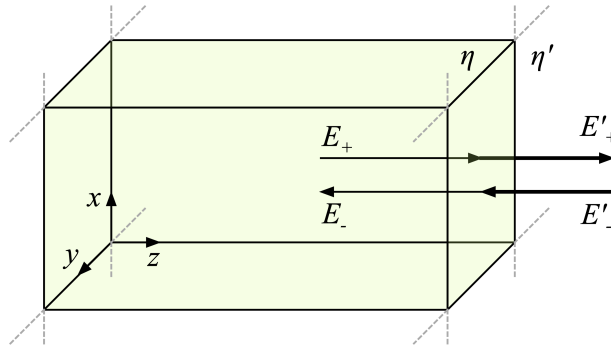


Figure 2.2. 1D propagation across a boundary. A plane wave propagating in the z direction encountering a boundary between two dielectrics. There will be transmitted and reflected components of the wave at the boundary, shown offset here for clarity.

2.1.3 Matching matrices for capacitive and inductive grids

Square capacitive and inductive grids with negligible thickness may be modelled as shunt admittances. Figure 2.3 shows the main characteristics of such a grid. A plane wave encountering this negligibly thin grid embedded in a dielectric is shown in Figure 2.4.

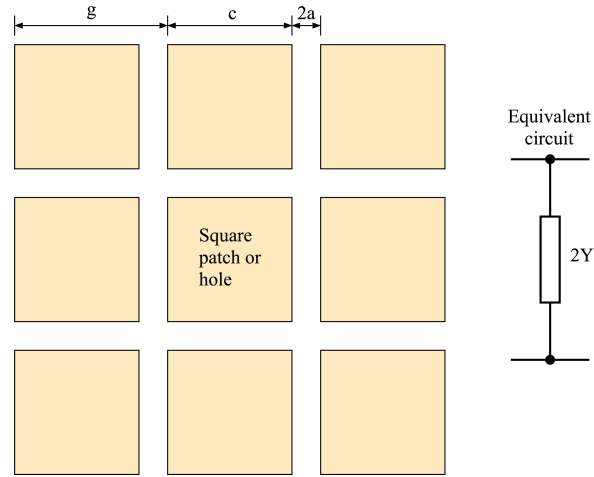


Figure 2.3. Square metallic mesh grid dimensions. Capacitive and inductive grids are made up of square plates and holes respectively. The dimensions are the unit cell size g , the size of the plate or hole c (often expressed as a proportion of the unit cell) and the distance between the plates or holes $2a$. The equivalent circuit is a shunt admittance of value $2Y$.

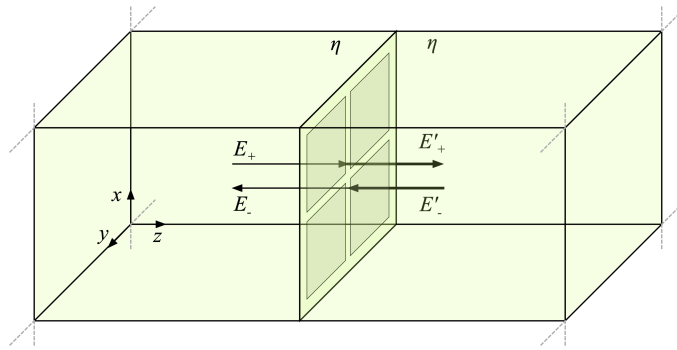


Figure 2.4. 1D propagation through grid. A plane wave encountering a negligibly thin grid embedded in a dielectric of characteristic impedance η .

Lee et al⁹⁰ give the transmission and reflection coefficients in terms of the admittance

$$T = \frac{1}{1 + Y} \quad 2-4$$

$$R = -\frac{1}{1 + \frac{1}{Y}} = T - 1 \quad 2-5$$

and the matching matrix equation for the grid is

$$\begin{bmatrix} E_+ \\ E_- \end{bmatrix} = \begin{bmatrix} 1 + Y & Y \\ -Y & 1 - Y \end{bmatrix} \begin{bmatrix} E'_+ \\ E'_- \end{bmatrix}. \quad 2-6$$

Various formulae for the equivalent admittance are given in the literature for Y_I (inductive grid) and Y_C (capacitive grid). Lee et al⁹⁰ provide their own formula (an approximation of the numerical solution of a double Fourier series that they derive)

$$Y_I = \frac{1}{Y_C} = (-i) \left(\beta - \frac{1}{\beta} \right) \frac{\left(\frac{a}{c} + \frac{a^2}{2\lambda^2} \right)}{\ln \csc \left(\frac{\pi\delta}{2a} \right)} \quad 2-7$$

where

$$\beta = \frac{\left(1 - 0.41 \frac{\delta}{a} \right) \lambda}{a}, \quad \delta = \frac{a - c}{2}. \quad 2-8$$

Lee et al also give a formula credited to Ulrich¹⁶

$$Y_I = \frac{1}{Y_C} = (-i) \left(\beta - \frac{1}{\beta} \right) \frac{1}{\ln \csc \left(\frac{\pi\delta}{2a} \right)} \quad 2-9$$

where

$$\beta = \frac{\left(1 - 0.27 \frac{\delta}{a} \right) \lambda}{a}, \quad \delta = \frac{a - c}{2}. \quad 2-10$$

Another formula that Lee et al credit to Arnaud and Pelow⁹¹ and corrected by Anderson⁹² is

$$Y_I = \frac{1}{Y_C} = (-i) \frac{1}{\left(\frac{a}{\lambda} \right) \ln \csc \left(\frac{\pi\delta}{2a} \right)} \quad 2-11$$

where

$$\delta = \frac{a - c}{2}. \quad 2-12$$

Finally, a complex formula credited to Chen⁹³ by Lee et al is (looking back at Chen's paper, the whole formula should be multiplied by $(-i)$ not just the first term as shown by Lee et al)

$$Y_I = \frac{1}{Y_C} = (-i) \left[2\alpha\gamma - \frac{1}{\alpha}\delta + \left(\beta - \frac{1}{\beta} \right) \gamma\delta \right] \quad 2-13$$

where

$$\alpha = \sqrt{\left(\frac{\lambda}{a}\right)^2 - 1}, \quad \beta = \sqrt{2\left(\frac{\lambda}{a}\right)^2 - 1},$$

$$\delta = \left[\frac{\sin\left(\frac{\pi c}{a}\right)}{\frac{\pi c}{a}} \right]^2, \quad \delta = \left[\frac{\sin\left(\frac{\pi c}{a}\right)}{\frac{\pi c}{a}} \right]^2. \quad 2-14$$

The relative performance of these formulae and a comparison with results from Ansys HFSS were studied during the modelling tool verification process, the results are presented in section 2.5.9.

It is also possible to use admittance data collected for a mesh grid using a full three-dimensional modelling tool, such as Ansys HFSS or FDTD in place of the formulae. This was the usual method of modelling mesh grids using this method in the work reported here; the formulae from the literature were rarely used. This feature was also exploited when using the mesh pattern catalogues described in section 3.3.

The existence of an equivalent electronic circuit was noted in this section. This is useful in the basic understanding of how mesh grids work, but the precise relationship between the mesh geometry and the values of the components in the equivalent circuit was never directly used.

2.1.4 Using the method

The propagation and matching matrices introduced in sections 2.1.1, 2.1.2 and 2.1.3 allow the fields to be calculated at any point along the direction of propagation of a wave. The appropriate propagation matrices for the dielectrics and boundaries the wave encounters between its source and the calculation point are just multiplied together. This determines the transmitted (and the reflected) wave which in turn allows the complex admittance of the assembly to be calculated. Performing the calculation at a range of frequencies allows the full frequency dependent admittance curve to be determined.

There are two shortcomings of this method that the user must be aware of. It takes no account of diffraction effects, so care must be taken to avoid calculations at frequencies that are beyond the diffraction limit for the structures being

investigated. When mesh grids are very closely spaced when compared to the wavelength of the incident radiation, they start affecting each other's admittance. This effect is investigated further in section 2.5.13.

2.2 The finite difference, time domain method

The Finite Difference, Time Domain (FDTD) method is an algorithm for the numerical solution of Maxwell's equations in three dimensions. The basic method using finite differences calculated on a cubic grid with offset electric and magnetic fields was first outlined by Yee⁸¹. Taflov and Hagness⁸² bring many different threads together to describe the complete method. The derivation of many of the equations stated in this section is given in detail in Appendix B.

2.2.1 The basic method

Yee's algorithm divides the modelled space into a regular array of identical cubes and then numerically calculates the three components of the electric field and the three components of the magnetic field for each cube at discrete, regular, time steps. Only the field component values in a cube and its immediately adjacent cubes are involved in the calculation; a localisation of data dependency that can be taken advantage of in the implementation.

The scene being modelled is represented on this grid of cubes by assigning the appropriate material to each cube in much the same way as two-dimensional computer graphics uses pixels. The resolution of the grid therefore directly affects the accuracy of the scene representation. Each material assigned provides the necessary values of electric permittivity, magnetic permeability, and conductivity for the cube.

The algorithm locates the electric and magnetic field components at specific places on the surfaces of the cubes, as shown in Figure 2.5. This arrangement reflects the curl dependencies of each component of one field on the other field. For example, the E_y component is surrounded by exactly the H components necessary to calculate the curl (indicated by the red circle in the diagram). The offsets from the lower left corner of the Yee cube of each component are listed in Table 2.1.

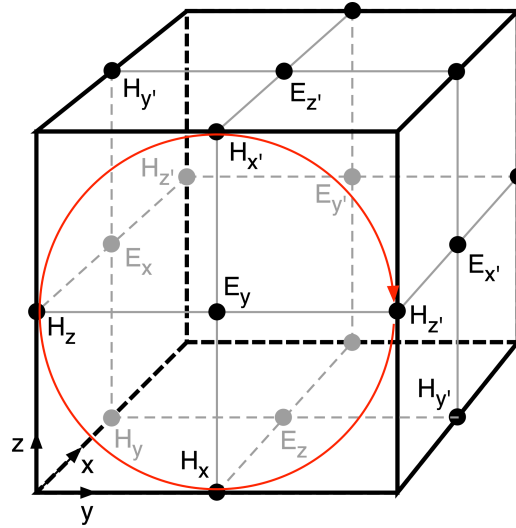


Figure 2.5. The Yee grid. The electric field components are positioned at the centre of the cube's faces, the magnetic components at the centre of the edges. The red circle indicates the H components required for the calculation of E_y . The components marked with a prime (e.g. H_z') belong to an adjacent cube.

Table 2.1. Yee grid offsets. The offsets from the grid point $(i\Delta x, j\Delta y, k\Delta z)$ where i, j, k are integers for each of the electric and magnetic field components on the Yee grid.

E_x	$(0, \frac{1}{2}\Delta y, \frac{1}{2}\Delta z)$
E_y	$(\frac{1}{2}\Delta x, 0, \frac{1}{2}\Delta z)$
E_z	$(\frac{1}{2}\Delta x, \frac{1}{2}\Delta y, 0)$
H_x	$(\frac{1}{2}\Delta x, 0, 0)$
H_y	$(0, \frac{1}{2}\Delta y, 0)$
H_z	$(0, 0, \frac{1}{2}\Delta z)$

Another feature of Yee's algorithm is that the magnetic field is calculated for each time step n , while the electric field is calculated for time steps $n + \frac{1}{2}$. This is often referred to as a leap frogging, time marching, scheme.

A notation is used in the following equations that indicates which cell and time step each electric and magnetic field component is associated with. Here's an example electric field component

$$E_x|_{i,j+\frac{1}{2},k+\frac{1}{2}}^{n+\frac{1}{2}}$$

2-15

where the vertical bar separates the field component, E_x , from the superscript that indicates the time step and the subscript that indicates the grid cell coordinates. In the example, this is the electric field x component at time step $n + \frac{1}{2}$ and location in the grid of $i, j + \frac{1}{2}, k + \frac{1}{2}$. Where a term is time independent, the superscript after the vertical bar is omitted.

Using central difference approximations for the time and space derivatives, the update equations for electric field (a complete derivation is included for reference in appendix B.1) are

$$E_x|_{i,j+\frac{1}{2},k+\frac{1}{2}}^{n+\frac{1}{2}} = C_{ae}|_{i,j+\frac{1}{2},k+\frac{1}{2}} \left(\frac{H_z|_{i,j+1,k+\frac{1}{2}}^n - H_z|_{i,j,k+\frac{1}{2}}^n}{\Delta y} - \frac{H_y|_{i,j+\frac{1}{2},k+1}^n - H_y|_{i,j+\frac{1}{2},k}^n}{\Delta z} - J_x|_{i,j+\frac{1}{2},k+\frac{1}{2}}^n \right) + E_x|_{i,j+\frac{1}{2},k+\frac{1}{2}}^{n-\frac{1}{2}} C_{be}|_{i,j+\frac{1}{2},k+\frac{1}{2}} \quad 2-16$$

$$E_y|_{i+\frac{1}{2},j,k+\frac{1}{2}}^{n+\frac{1}{2}} = C_{ae}|_{i+\frac{1}{2},j,k+\frac{1}{2}} \left(\frac{H_x|_{i+\frac{1}{2},j,k+1}^n - H_x|_{i+\frac{1}{2},j,k}^n}{\Delta z} - \frac{H_z|_{i+1,j,k+\frac{1}{2}}^n - H_z|_{i,j,k+\frac{1}{2}}^n}{\Delta x} - J_y|_{i+\frac{1}{2},j,k+\frac{1}{2}}^n \right) + E_y|_{i+\frac{1}{2},j,k+\frac{1}{2}}^{n-\frac{1}{2}} C_{be}|_{i+\frac{1}{2},j,k+\frac{1}{2}} \quad 2-17$$

$$E_z|_{i+\frac{1}{2},j+\frac{1}{2},k}^{n+\frac{1}{2}} = C_{ae}|_{i+\frac{1}{2},j+\frac{1}{2},k} \left(\frac{H_y|_{i+1,j+\frac{1}{2},k}^n - H_y|_{i,j+\frac{1}{2},k}^n}{\Delta x} - \frac{H_x|_{i+\frac{1}{2},j+1,k}^n - H_x|_{i+\frac{1}{2},j,k}^n}{\Delta y} - J_z|_{i+\frac{1}{2},j+\frac{1}{2},k}^n \right) + E_z|_{i+\frac{1}{2},j+\frac{1}{2},k}^{n-\frac{1}{2}} C_{be}|_{i+\frac{1}{2},j+\frac{1}{2},k} \cdot \quad 2-18$$

For the magnetic field they are

$$\begin{aligned}
 H_x|_{i+\frac{1}{2},j,k}^{n+1} = & C_{ah}|_{i+\frac{1}{2},j,k} \left(-\frac{E_z|_{i+\frac{1}{2},j+\frac{1}{2},k}^{n+\frac{1}{2}} - E_z|_{i+\frac{1}{2},j-\frac{1}{2},k}^{n+\frac{1}{2}}}{\Delta y} \right. \\
 & \left. + \frac{E_y|_{i+\frac{1}{2},j,k+\frac{1}{2}}^{n+\frac{1}{2}} - E_y|_{i+\frac{1}{2},j,k-\frac{1}{2}}^{n+\frac{1}{2}}}{\Delta z} - M_x|_{i+\frac{1}{2},j,k}^{n+\frac{1}{2}} \right) \\
 & + H_x|_{i+\frac{1}{2},j,k}^n C_{bh}|_{i+\frac{1}{2},j,k}
 \end{aligned} \tag{2-19}$$

$$\begin{aligned}
 H_y|_{i,j+\frac{1}{2},k}^{n+1} = & C_{ah}|_{i,j+\frac{1}{2},k} \left(-\frac{E_x|_{i,j+\frac{1}{2},k+\frac{1}{2}}^{n+\frac{1}{2}} - E_x|_{i,j+\frac{1}{2},k-\frac{1}{2}}^{n+\frac{1}{2}}}{\Delta z} \right. \\
 & \left. + \frac{E_z|_{i+\frac{1}{2},j+\frac{1}{2},k}^{n+\frac{1}{2}} - E_z|_{i-\frac{1}{2},j+\frac{1}{2},k}^{n+\frac{1}{2}}}{\Delta x} - M_y|_{i,j+\frac{1}{2},k}^{n+\frac{1}{2}} \right) \\
 & + H_y|_{i,j+\frac{1}{2},k}^n C_{bh}|_{i,j+\frac{1}{2},k}
 \end{aligned} \tag{2-20}$$

$$\begin{aligned}
 H_z|_{i,j,k+\frac{1}{2}}^{n+1} = & C_{ah}|_{i,j,k+\frac{1}{2}} \left(-\frac{E_y|_{i+\frac{1}{2},j,k+\frac{1}{2}}^{n+\frac{1}{2}} - E_y|_{i-\frac{1}{2},j,k+\frac{1}{2}}^{n+\frac{1}{2}}}{\Delta x} \right. \\
 & \left. + \frac{E_x|_{i,j+\frac{1}{2},k+\frac{1}{2}}^{n+\frac{1}{2}} - E_x|_{i,j-\frac{1}{2},k+\frac{1}{2}}^{n+\frac{1}{2}}}{\Delta y} - M_z|_{i,j,k+\frac{1}{2}}^{n+\frac{1}{2}} \right) \\
 & + H_z|_{i,j,k+\frac{1}{2}}^n C_{bh}|_{i,j,k+\frac{1}{2}}.
 \end{aligned} \tag{2-21}$$

The time independent terms that embody the parameters of the dielectric in a cell are

$$C_{ae} = \frac{\frac{\Delta t}{\varepsilon}}{\left(1 + \frac{\sigma \Delta t}{2\varepsilon}\right)} \quad C_{be} = \frac{\left(1 - \frac{\sigma \Delta t}{2\varepsilon}\right)}{\left(1 + \frac{\sigma \Delta t}{2\varepsilon}\right)} \tag{2-22}$$

$$C_{ah} = \frac{\frac{\Delta t}{\mu}}{\left(1 + \frac{\sigma^* \Delta t}{2\mu}\right)} \quad C_{bh} = \frac{\left(1 - \frac{\sigma^* \Delta t}{2\mu}\right)}{\left(1 + \frac{\sigma^* \Delta t}{2\mu}\right)} \tag{2-23}$$

and ε is the permittivity of the material in the cell, μ is the permeability, σ is the conductivity and σ^* is the magnetic conductivity. This latter parameter, the

conductivity of magnetic monopoles, is somewhat non-physical but is included as it is useful when matching the absorbing layers that simulate an unbounded space (section 2.2.3).

2.2.2 Incident plane waves

A method of exciting the model with an incident wave is required. Many applications study the interaction of an incident plane wave with material structures so a method of applying a plane wave is useful. The accepted approach to modelling and experimental characterisation of metamaterial mesh devices utilises both on and off axis plane waves. The Total Field/Scattered Field method is a widely-used such method of applying plane waves in an FDTD algorithm. It is described by Potter and Berenger⁹⁴ and in section 5.8 of Taflove and Hagness⁸².

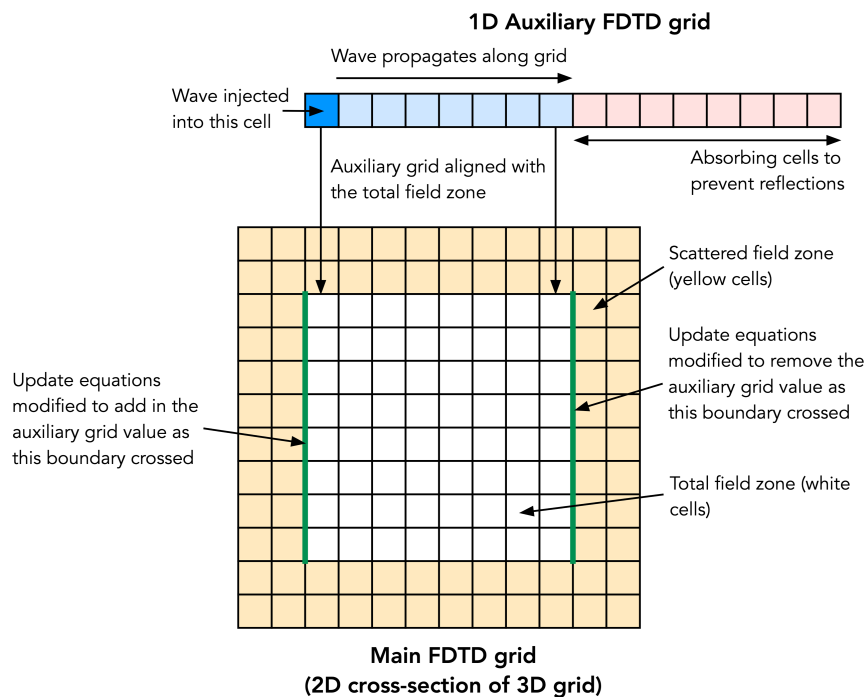


Figure 2.6. Total Field/Scattered Field method of inserting a plane wave. This diagram shows the normal incidence case. An auxiliary 1D FDTD grid is aligned with the main grid and tracks the propagation of the plane wave. The main grid's update equations are adjusted to add and remove the incident wave on the boundaries shown.

The simulation domain is separated into two zones, the Total Field Zone and the Scattered Field Zone. The Yee algorithm is applied normally for all cells except at the boundary between the two zones where the incident wave is accounted for. It is added in at the incident boundary and removed at the opposite boundary. Figure 2.6 demonstrates the method for the normally incident case. The general

case for an arbitrary incidence angle requires the orientation of the auxiliary grid to be rotated appropriately.

The incident wave is calculated using a one-dimensional auxiliary FDTD grid. The E and H field wave magnitudes of the source wave are calculated and set in the origin cell of this grid. One dimensional FDTD is used to propagate the wave down the grid. The origin of the grid is aligned with the corner of the total field zone of the main grid that encounters the incident wave first. The direction of the grid aligns with the direction of the incident wave. The auxiliary grid only needs to record one transverse component for the E and H fields, the polarization is taken care of when the incident field correction is made to the main grid.

The main FDTD grid is extended in all directions by the scattered field zone (two extra cells as shown, in yellow). A set of corrections to the cells each side of the boundary between the scattered field and the total field can then be made to add and remove the incident wave so that it only appears in the total field part of the grid. Using the coordinates indicated in the figure (for example, the total field part of the x axis ranges from i_0 to i_1) for the two boundaries indicated in the diagram, these corrections, ΔE and ΔH , to be added to the electric field (H_{inc} and E_{inc} are the magnetic and electric fields calculated from the auxiliary grid at the specified position) are:

for the $k = k_0 - 1$ face, $i = i_0 \dots i_1, j = j_0 \dots j_1$

$$\Delta E_x|_{i,j+\frac{1}{2},k+\frac{1}{2}}^{n+\frac{1}{2}} = + \frac{\Delta t}{\varepsilon_0 \Delta Z} H_{y,inc}|_{i,j+\frac{1}{2},k+1}^n \quad 2-24$$

$$\Delta E_y|_{i+\frac{1}{2},j,k+\frac{1}{2}}^{n+\frac{1}{2}} = - \frac{\Delta t}{\varepsilon_0 \Delta Z} H_{x,inc}|_{i+\frac{1}{2},j,k+1}^n \quad 2-25$$

the $k = k_0$ face, $i = i_0 \dots i_1, j = j_0 \dots j_1$

$$\Delta H_y|_{i,j+\frac{1}{2},k}^{n+1} = + \frac{\Delta t}{\mu_0 \Delta Z} E_{x,inc}|_{i,j+\frac{1}{2},k-\frac{1}{2}}^{n+\frac{1}{2}} \quad 2-26$$

$$\Delta H_x|_{i+\frac{1}{2},j,k}^{n+1} = - \frac{\Delta t}{\mu_0 \Delta Z} E_{y,inc}|_{i+\frac{1}{2},j,k-\frac{1}{2}}^{n+\frac{1}{2}} \quad 2-27$$

the $k = k_1$ face, $i = i_0 \dots i_1, j = j_0 \dots j_1$

$$\Delta E_x|_{i,j+\frac{1}{2},k+\frac{1}{2}}^{n+\frac{1}{2}} = - \frac{\Delta t}{\varepsilon_0 \Delta Z} H_{y,inc}|_{i,j+\frac{1}{2},k+1}^n \quad 2-28$$

$$\Delta E_y \Big|_{i+\frac{1}{2},j,k+\frac{1}{2}}^{n+\frac{1}{2}} = + \frac{\Delta t}{\epsilon_0 \Delta Z} H_{x,inc} \Big|_{i+\frac{1}{2},j,k+1}^n \quad 2-29$$

the $k = k_1 + 1$ face, $i = i_0 \dots i_1$, $j = j_0 \dots j_1$

$$\Delta H_y \Big|_{i,j+\frac{1}{2},k}^{n+1} = - \frac{\Delta t}{\mu_0 \Delta Z} E_{x,inc} \Big|_{i,j+\frac{1}{2},k-\frac{1}{2}}^{n+\frac{1}{2}} \quad 2-30$$

$$\Delta H_x \Big|_{i+\frac{1}{2},j,k}^{n+1} = + \frac{\Delta t}{\mu_0 \Delta Z} E_{y,inc} \Big|_{i+\frac{1}{2},j,k-\frac{1}{2}}^{n+\frac{1}{2}} \quad 2-31$$

For the complete specification of the total field/scattered field boundary corrections to the update equations, see appendix B.2.

This method of implementing an incident plane wave has two useful features that are taken advantage of in the implementation of the FDTD modelling tool. The first is that since the incident wave is only added at the boundary between the scattered field zone and the total field zone, the measurement of any reflections from structures in the total field zone is made easier, monitoring a cell in the scattered field zone will only see the reflection and not the incident wave. The second is that the auxiliary grid can provide the reference for the determination of any phase shift that may have been induced during the traversal of the main grid by the wave.

2.2.3 Absorbing waves at the model boundary

To emulate a model surrounded by an infinite space, waves that encounter the boundary of the modelled domain must be absorbed. This is true for both the main three-dimensional grid and the one-dimensional auxiliary grid used by the total field/scattered field method of injecting a plane wave.

The auxiliary grid algorithm requires only a simple modification, waves are travelling only in the x direction and always encountering the boundary at right angles. A lossy zone consisting of extra Yee cells is added to the end of the grid as shown in Figure 2.7, the region of space $x < 0$ is lossless (the original auxiliary grid) and the region $x \geq 0$ has electric conductivity σ and magnetic conductivity σ^* .

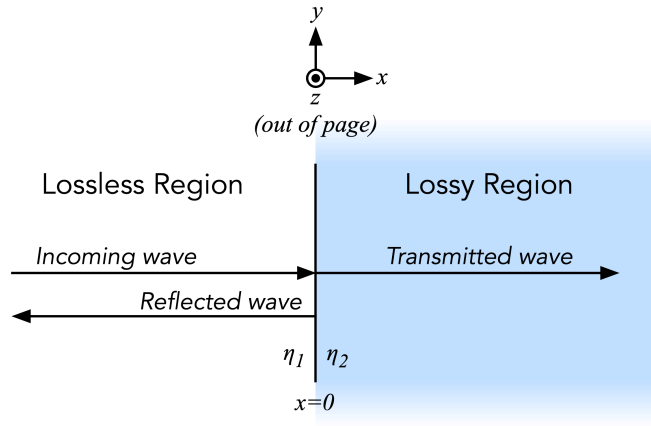


Figure 2.7. A wave encounters a boundary with a lossy region. Part of the wave is transmitted through into that region; the remainder is reflected back into the lossless region.

For the lossy region to match the lossless region (and avoid a reflection at the boundary) the following equation must be met:

$$\frac{\sigma_2^*}{\mu} = \frac{\sigma_2}{\varepsilon}. \quad 2-32$$

It is necessary to increase the loss (represented by σ_2 and σ_2^* which are the electric and magnetic conductivities in the lossy region) slowly to avoid reflections brought about by the discrete nature of the model. The electric permittivity, ε , and magnetic permeability, μ , are kept the same in the two regions. This match is broadband as none of the parameters involved are frequency dependent in the ideal modelling world.

For the main three-dimensional Yee grid, a more elaborate scheme to match the domain to a lossy border region is required as waves can encounter it at any angle. A number of these algorithms have been proposed over the years and are generally referred to as Perfectly Matched Layers (PMLs). An efficient implementation of a stretched field algorithm (see Chew and Weedon⁹⁵) referred to as the Convolutional PML (CPML) described by Roden and Gedney⁹⁶ was used. It utilises a set of discrete unknowns to modify the field update equations, described fully in appendix B.5. The simplified update equations become (new terms in red)

$$\begin{aligned}
 E_x|_{i,j+\frac{1}{2},k+\frac{1}{2}}^{n+\frac{1}{2}} = & C_{aex}|_{i,j+\frac{1}{2},k+\frac{1}{2}} \left(\frac{H_z|_{i,j+1,k+\frac{1}{2}}^n - H_z|_{i,j,k+\frac{1}{2}}^n}{\kappa_y|_{j+\frac{1}{2}}\Delta y} \right. \\
 & - \frac{H_y|_{i,j+\frac{1}{2},k+1}^n - H_y|_{i,j+\frac{1}{2},k}^n}{\kappa_z|_{k+\frac{1}{2}}\Delta z} - J_x|_{i,j+\frac{1}{2},k+\frac{1}{2}}^n + \Psi_{E_{x,y}}|_{i,j+\frac{1}{2},k+\frac{1}{2}}^n \\
 & \left. - \Psi_{E_{x,z}}|_{i,j+\frac{1}{2},k+\frac{1}{2}}^n \right) + E_x|_{i,j+\frac{1}{2},k+\frac{1}{2}}^{n-\frac{1}{2}} C_{bex}|_{i,j+\frac{1}{2},k+\frac{1}{2}}
 \end{aligned} \tag{2-33}$$

$$\begin{aligned}
 E_y|_{i+\frac{1}{2},j,k+\frac{1}{2}}^{n+\frac{1}{2}} = & C_{aey}|_{i+\frac{1}{2},j,k+\frac{1}{2}} \left(\frac{H_x|_{i+\frac{1}{2},j,k+1}^n - H_x|_{i+\frac{1}{2},j,k}^n}{\kappa_z|_{k+\frac{1}{2}}\Delta z} \right. \\
 & - \frac{H_z|_{i+1,j,k+\frac{1}{2}}^n - H_z|_{i,j,k+\frac{1}{2}}^n}{\kappa_x|_{i+\frac{1}{2}}\Delta x} - J_y|_{i+\frac{1}{2},j,k+\frac{1}{2}}^n + \Psi_{E_{y,z}}|_{i+\frac{1}{2},j,k+\frac{1}{2}}^n \\
 & \left. - \Psi_{E_{y,x}}|_{i+\frac{1}{2},j,k+\frac{1}{2}}^n \right) + E_y|_{i+\frac{1}{2},j,k+\frac{1}{2}}^{n-\frac{1}{2}} C_{bey}|_{i+\frac{1}{2},j,k+\frac{1}{2}}
 \end{aligned} \tag{2-34}$$

$$\begin{aligned}
 E_z|_{i+\frac{1}{2},j+\frac{1}{2},k}^{n+\frac{1}{2}} = & C_{aez}|_{i+\frac{1}{2},j+\frac{1}{2},k} \left(\frac{H_y|_{i+1,j+\frac{1}{2},k}^n - H_y|_{i,j+\frac{1}{2},k}^n}{\kappa_x|_{i+\frac{1}{2}}\Delta x} \right. \\
 & - \frac{H_x|_{i+\frac{1}{2},j+1,k}^n - H_x|_{i+\frac{1}{2},j,k}^n}{\kappa_y|_{j+\frac{1}{2}}\Delta y} - J_z|_{i+\frac{1}{2},j+\frac{1}{2},k}^n + \Psi_{E_{z,x}}|_{i+\frac{1}{2},j+\frac{1}{2},k}^n \\
 & \left. - \Psi_{E_{z,y}}|_{i+\frac{1}{2},j+\frac{1}{2},k}^n \right) + E_z|_{i+\frac{1}{2},j+\frac{1}{2},k}^{n-\frac{1}{2}} C_{bez}|_{i+\frac{1}{2},j+\frac{1}{2},k}
 \end{aligned} \tag{2-35}$$

where

$$C_{aew} = \frac{\frac{\Delta t}{\varepsilon}}{\left(1 + \frac{\sigma_w \Delta t}{2\varepsilon}\right)} \quad C_{bew} = \frac{\left(1 - \frac{\sigma_w \Delta t}{2\varepsilon}\right)}{\left(1 + \frac{\sigma_w \Delta t}{2\varepsilon}\right)} \quad w = x, y, z. \tag{2-36}$$

The magnetic equations become:

$$E_z|_{i+\frac{1}{2},j+\frac{1}{2},k}^{n+\frac{1}{2}} = C_{aez}|_{i+\frac{1}{2},j+\frac{1}{2},k} \left(\frac{H_y|_{i+1,j+\frac{1}{2},k}^n - H_y|_{i,j+\frac{1}{2},k}^n}{\kappa_x|_{i+\frac{1}{2}}\Delta x} - \frac{H_x|_{i+\frac{1}{2},j+1,k}^n - H_x|_{i+\frac{1}{2},j,k}^n}{\kappa_y|_{j+\frac{1}{2}}\Delta y} - J_z|_{i+\frac{1}{2},j+\frac{1}{2},k}^n + \Psi_{Ez,x}|_{i+\frac{1}{2},j+\frac{1}{2},k}^n - \Psi_{Ez,y}|_{i+\frac{1}{2},j+\frac{1}{2},k}^n \right) + E_z|_{i+\frac{1}{2},j+\frac{1}{2},k}^{n-\frac{1}{2}} C_{bez}|_{i+\frac{1}{2},j+\frac{1}{2},k} \quad 2-37$$

$$H_y|_{i,j+\frac{1}{2},k}^{n+1} = C_{ah}|_{i,j+\frac{1}{2},k} \left(-\frac{E_x|_{i,j+\frac{1}{2},k+\frac{1}{2}}^{n+\frac{1}{2}} - E_x|_{i,j+\frac{1}{2},k-\frac{1}{2}}^{n+\frac{1}{2}}}{\kappa_z|_k\Delta z} + \frac{E_z|_{i+\frac{1}{2},j+\frac{1}{2},k}^{n+\frac{1}{2}} - E_z|_{i-\frac{1}{2},j+\frac{1}{2},k}^{n+\frac{1}{2}}}{\kappa_x|_i\Delta x} - M_y|_{i,j+\frac{1}{2},k}^{n+\frac{1}{2}} + \Psi_{Hy,x}|_{i,j+\frac{1}{2},k}^{n+\frac{1}{2}} - \Psi_{Hy,z}|_{i,j+\frac{1}{2},k}^{n+\frac{1}{2}} \right) + H_y|_{i,j+\frac{1}{2},k}^n C_{bh}|_{i,j+\frac{1}{2},k} \quad 2-38$$

$$H_y|_{i,j+\frac{1}{2},k}^{n+1} = C_{ah}|_{i,j+\frac{1}{2},k} \left(-\frac{E_x|_{i,j+\frac{1}{2},k+\frac{1}{2}}^{n+\frac{1}{2}} - E_x|_{i,j+\frac{1}{2},k-\frac{1}{2}}^{n+\frac{1}{2}}}{\kappa_z|_k\Delta z} + \frac{E_z|_{i+\frac{1}{2},j+\frac{1}{2},k}^{n+\frac{1}{2}} - E_z|_{i-\frac{1}{2},j+\frac{1}{2},k}^{n+\frac{1}{2}}}{\kappa_x|_i\Delta x} - M_y|_{i,j+\frac{1}{2},k}^{n+\frac{1}{2}} + \Psi_{Hy,x}|_{i,j+\frac{1}{2},k}^{n+\frac{1}{2}} - \Psi_{Hy,z}|_{i,j+\frac{1}{2},k}^{n+\frac{1}{2}} \right) + H_y|_{i,j+\frac{1}{2},k}^n C_{bh}|_{i,j+\frac{1}{2},k} \quad 2-39$$

where

$$C_{ahw} = \frac{\frac{\Delta t}{\mu}}{\left(1 + \frac{\sigma_w^* \Delta t}{2\mu}\right)} \quad C_{bhw} = \frac{\left(1 - \frac{\sigma_w^* \Delta t}{2\mu}\right)}{\left(1 + \frac{\sigma_w^* \Delta t}{2\mu}\right)} \quad w = x, y, z. \quad 2-40$$

Inside the PML, due to the matching condition $\sigma_w^* = \frac{\sigma_w \mu}{\varepsilon}$, this leads to

$$c_{ahw} = \frac{\frac{\Delta t}{\mu}}{\left(1 + \frac{\sigma_w \Delta t}{2\varepsilon}\right)} \quad c_{bhw} = \frac{\left(1 - \frac{\sigma_w \Delta t}{2\varepsilon}\right)}{\left(1 + \frac{\sigma_w \Delta t}{2\varepsilon}\right)} \quad w = x, y, z. \quad 2-41$$

The discrete unknowns, Ψ , are also updated on each time step, for example (the full set of update equations is given in appendix B.5):

$$\Psi_{E_{x,y}} \Big|_{i,j+\frac{1}{2},k+\frac{1}{2}}^n = b_y \Big|_{j+\frac{1}{2}} \Psi_{E_{x,y}} \Big|_{i,j+\frac{1}{2},k+\frac{1}{2}}^{n-1} + c_y \Big|_{j+\frac{1}{2}} \left(\frac{H_z \Big|_{i,j+1,k+\frac{1}{2}}^n - H_z \Big|_{i,j,k+\frac{1}{2}}^n}{\Delta y} \right) \quad 2-42$$

2.2.4 Thin layers

Many uses of the FDTD model involve a thin layer of material perpendicular to the z axis. The standard Yee grid can only represent this as a layer of cells one cube thick. Generally, the size of an FDTD cube is much bigger than the thickness of the thin layer to keep the memory usage of the model within the limits of the target computer, especially as a halving of the cell size leads to eight times more memory required. Thin layers can be modelled more accurately by using a special grid cell in place of the standard Yee grid cell wherever the layer resides. The technique was first described by Maloney and Smith⁹⁷.

In Figure 2.8 the thin material layer of thickness d , conductivity σ_s , electric permittivity ε_s and unchanged magnetic permeability resides at z location k^* . In the Yee cells that contain this layer, the electric field z component is split into two parts, one outside the layer, E_z and one inside, E_{zin} , as shown.

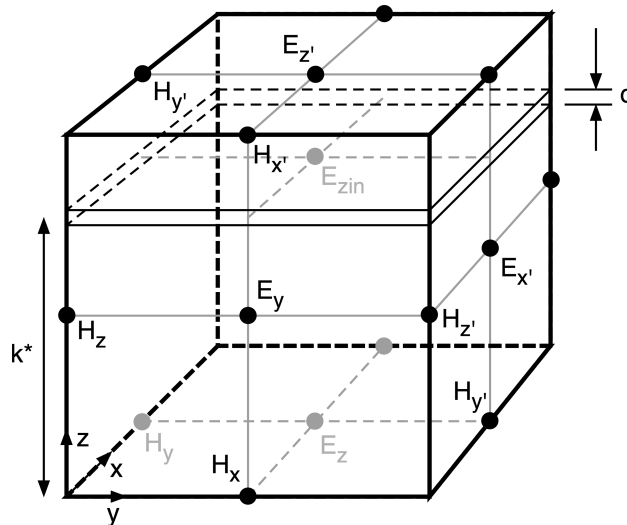


Figure 2.8. The Yee grid with the thin layer modification.

The electric field update equations (for full details see appendix B.6), including the extra component E_{zin} , become:

$$E_z|_{i+\frac{1}{2},j+\frac{1}{2},k}^{n+\frac{1}{2}} = C_{ae}|_{i+\frac{1}{2},j+\frac{1}{2},k} \left(\frac{H_y|_{i+1,j+\frac{1}{2},k}^n - H_y|_{i,j+\frac{1}{2},k}^n}{\Delta x} - \frac{H_x|_{i+\frac{1}{2},j+1,k}^n - H_x|_{i+\frac{1}{2},j,k}^n}{\Delta y} - J_z|_{i+\frac{1}{2},j+\frac{1}{2},k}^n \right) + E_z|_{i+\frac{1}{2},j+\frac{1}{2},k}^{n-\frac{1}{2}} C_{be}|_{i+\frac{1}{2},j+\frac{1}{2},k} \quad 2-43$$

$$E_{zin}|_{i+\frac{1}{2},j+\frac{1}{2},k}^{n+\frac{1}{2}} = C_{aein}|_{i+\frac{1}{2},j+\frac{1}{2},k}^* \left(\frac{H_y|_{i+1,j+\frac{1}{2},k}^n - H_y|_{i,j+\frac{1}{2},k}^n}{\Delta x} - \frac{H_x|_{i+\frac{1}{2},j+1,k}^n - H_x|_{i+\frac{1}{2},j,k}^n}{\Delta y} - J_z|_{i+\frac{1}{2},j+\frac{1}{2},k}^n \right) + E_{zin}|_{i+\frac{1}{2},j+\frac{1}{2},k}^{n-\frac{1}{2}} C_{bein}|_{i+\frac{1}{2},j+\frac{1}{2},k}^* \quad 2-44$$

$$E_x|_{i,j+\frac{1}{2},k+\frac{1}{2}}^{n+\frac{1}{2}} = C_{aeav}|_{i,j+\frac{1}{2},k+\frac{1}{2}} \left(\frac{H_z|_{i,j+1,k+\frac{1}{2}}^n - H_z|_{i,j,k+\frac{1}{2}}^n}{\Delta y} - \frac{H_y|_{i,j+\frac{1}{2},k+1}^n - H_y|_{i,j+\frac{1}{2},k}^n}{\Delta z} - J_x|_{i,j+\frac{1}{2},k+\frac{1}{2}}^n \right) + E_x|_{i,j+\frac{1}{2},k+\frac{1}{2}}^{n-\frac{1}{2}} C_{beav}|_{i,j+\frac{1}{2},k+\frac{1}{2}} \quad 2-45$$

$$E_y|_{i+\frac{1}{2},j,k+\frac{1}{2}}^{n+\frac{1}{2}} = C_{aeav}|_{i+\frac{1}{2},j,k+\frac{1}{2}} \left(\frac{H_x|_{i+\frac{1}{2},j,k+1}^n - H_x|_{i+\frac{1}{2},j,k}^n}{\Delta z} - \frac{H_z|_{i+1,j,k+\frac{1}{2}}^n - H_z|_{i,j,k+\frac{1}{2}}^n}{\Delta x} - J_y|_{i+\frac{1}{2},j,k+\frac{1}{2}}^n \right) + E_y|_{i+\frac{1}{2},j,k+\frac{1}{2}}^{n-\frac{1}{2}} C_{beav}|_{i+\frac{1}{2},j,k+\frac{1}{2}} \quad 2-46$$

where

$$C_{ae} = \frac{\frac{\Delta t}{\varepsilon}}{\left(1 + \frac{\sigma \Delta t}{2\varepsilon}\right)} \quad C_{be} = \frac{\left(1 - \frac{\sigma \Delta t}{2\varepsilon}\right)}{\left(1 + \frac{\sigma \Delta t}{2\varepsilon}\right)} \quad 2-47$$

$$C_{aein} = \frac{\frac{\Delta t}{\varepsilon_s}}{\left(1 + \frac{\sigma_s \Delta t}{2\varepsilon_s}\right)} \quad C_{bein} = \frac{\left(1 - \frac{\sigma_s \Delta t}{2\varepsilon_s}\right)}{\left(1 + \frac{\sigma_s \Delta t}{2\varepsilon_s}\right)} \quad 2-48$$

$$C_{aeav} = \frac{\frac{\Delta t}{\varepsilon_{av}}}{\left(1 + \frac{\sigma_{av} \Delta t}{2\varepsilon_{av}}\right)} \quad C_{beav} = \frac{\left(1 - \frac{\sigma_{av} \Delta t}{2\varepsilon_{av}}\right)}{\left(1 + \frac{\sigma_{av} \Delta t}{2\varepsilon_{av}}\right)} \quad 2-49$$

$$\varepsilon_{av} = \left(1 - \frac{d}{\Delta Z}\right) \varepsilon + \frac{d}{\Delta Z} \varepsilon_s \quad \sigma_{av} = \left(1 - \frac{d}{\Delta Z}\right) \sigma + \frac{d}{\Delta Z} \sigma_s. \quad 2-50$$

The magnetic field update equations become:

$$\begin{aligned} H_z|_{i,j,k+\frac{1}{2}}^{n+1} = & C_{ah}|_{i,j,k+\frac{1}{2}} \left(- \frac{E_y|_{i+\frac{1}{2},j,k+\frac{1}{2}}^{n+\frac{1}{2}} - E_y|_{i-\frac{1}{2},j,k+\frac{1}{2}}^{n+\frac{1}{2}}}{\Delta x} \right. \\ & \left. + \frac{E_x|_{i,j+\frac{1}{2},k+\frac{1}{2}}^{n+\frac{1}{2}} - E_x|_{i,j-\frac{1}{2},k+\frac{1}{2}}^{n+\frac{1}{2}}}{\Delta y} - M_z|_{i,j,k+\frac{1}{2}}^{n+\frac{1}{2}} \right) \\ & + H_z|_{i,j,k+\frac{1}{2}}^n C_{bh}|_{i,j,k+\frac{1}{2}} \end{aligned} \quad 2-51$$

$$\begin{aligned} H_x|_{i+\frac{1}{2},j,k}^{n+1} = & C_{ah}|_{i+\frac{1}{2},j,k} \left(- \frac{\left(1 - \frac{d}{\Delta Z}\right) \left(E_z|_{i+\frac{1}{2},j+\frac{1}{2},k}^{n+\frac{1}{2}} - E_z|_{i+\frac{1}{2},j-\frac{1}{2},k}^{n+\frac{1}{2}}\right)}{\Delta y} \right. \\ & - \frac{\frac{d}{\Delta Z} \left(E_{zin}|_{i+\frac{1}{2},j+\frac{1}{2},k}^{n+\frac{1}{2}} - E_{zin}|_{i+\frac{1}{2},j-\frac{1}{2},k}^{n+\frac{1}{2}}\right)}{\Delta y} \\ & \left. + \frac{E_y|_{i+\frac{1}{2},j,k+\frac{1}{2}}^{n+\frac{1}{2}} - E_y|_{i+\frac{1}{2},j,k-\frac{1}{2}}^{n+\frac{1}{2}}}{\Delta z} - M_x|_{i+\frac{1}{2},j,k}^{n+\frac{1}{2}} \right) \\ & + H_x|_{i+\frac{1}{2},j,k}^n C_{bh}|_{i+\frac{1}{2},j,k} \end{aligned} \quad 2-52$$

$$\begin{aligned}
 H_y|_{i,j+\frac{1}{2},k}^{n+1} = & C_{ah}|_{i,j+\frac{1}{2},k} \left(-\frac{E_x|_{i,j+\frac{1}{2},k+\frac{1}{2}}^{n+\frac{1}{2}} - E_x|_{i,j+\frac{1}{2},k-\frac{1}{2}}^{n+\frac{1}{2}}}{\Delta z} \right. \\
 & + \frac{\left(1 - \frac{d}{\Delta z}\right) \left(E_z|_{i+\frac{1}{2},j+\frac{1}{2},k}^{n+\frac{1}{2}} - E_z|_{i-\frac{1}{2},j+\frac{1}{2},k}^{n+\frac{1}{2}}\right)}{\Delta x} \\
 & + \frac{\frac{d}{\Delta z} \left(E_{zin}|_{i+\frac{1}{2},j+\frac{1}{2},k}^{n+\frac{1}{2}} - E_{zin}|_{i-\frac{1}{2},j+\frac{1}{2},k}^{n+\frac{1}{2}}\right)}{\Delta x} - M_y|_{i,j+\frac{1}{2},k}^{n+\frac{1}{2}} \Bigg) \\
 & + H_y|_{i,j+\frac{1}{2},k}^n C_{bh}|_{i,j+\frac{1}{2},k}
 \end{aligned} \tag{2-53}$$

where

$$C_{ah} = \frac{\frac{\Delta t}{\mu}}{\left(1 + \frac{\sigma^* \Delta t}{2\mu}\right)} \quad C_{bh} = \frac{\left(1 - \frac{\sigma^* \Delta t}{2\mu}\right)}{\left(1 + \frac{\sigma^* \Delta t}{2\mu}\right)}. \tag{2-54}$$

An implementation of this method will need to provide extra storage for the E_{zin} component in each of the special cells. In the implementation described here, a special material object provides these cells and the sheet's electric permittivity and conductivity parameters in addition to referring to the normal material object that represents the rest of the cell. This material object is given the opportunity to perform the necessary modifications to the standard FDTD operating procedure.

2.3 The Ansys HFSS Package

The mainstay modelling tool of the authors groups was Ansys HFSS⁸⁴. This commercial tool is an implementation of the well-known finite element analysis (FEA) method (see, for example, Bhavikatti⁹⁸) configured to solve an equation that is derived from the time harmonic form of Maxwell's equations

$$\nabla \times \left(\frac{1}{\mu} \nabla \times \mathbf{E} \right) - \omega^2 \epsilon \mathbf{E} = -i\omega \mathbf{j}. \tag{2-55}$$

The equation is solved for all the cells of a mesh that is generated to represent the domain and the scene in an adaptive manner. The creation of the mesh is an important step as the success of the FEA is critically dependent on the mesh. The creation process is iterative, successively refining the mesh in regions of the domain where the fields are likely to vary fastest, controlled by a parameter named "maximum delta energy". The smaller the value of this parameter, the finer the mesh generated. There is a trade-off, however, as the finer the mesh is, the more

computer memory is required and the longer it takes to create it. The results of mesh generation for a simple example scene are shown in Figure 2.9. The mesh plays a similar role to the regular cubic grid of the FDTD method.

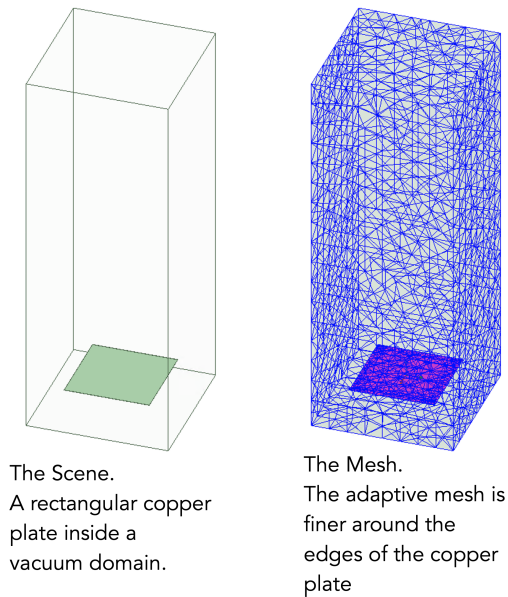


Figure 2.9. HFSS mesh generation example. A finer mesh has been made around the edges of the copper plate where the fields can be expected to change the fastest.

When used for modelling repetitive unit cell-based structures (like that in the example), periodic boundary conditions (named master/slave boundaries in HFSS) are applied on pairs of opposite sides. The top and bottom boundaries are designated as Floquet ports, these are special excitation/sensor ports in HFSS used for periodic structures that use Floquet modes⁹⁹ to represent the fields on the boundary. This allows the S parameters between two ports to be determined by the modelling, from which the complex admittance of the periodic structure can be derived.

HFSS also has a method of applying a Gaussian beam at a specific point in the scene. This feature was used with the field visualisation and far field measurement features during the study of the lenslets described in Chapter 4. The Gaussian beam was placed at the focus of the lens structure and allowed to propagate through it.

The HFSS tool was used as the reference against which the validity of the FDTD and propagation matrix implementations were assessed. The authors group has extensive experience with this tool, using it to model many devices that were subsequently built and measured and discovered to match its predictions well. Its

adaptive mesh technology makes it more efficient, in general, than the FDTD algorithm both in terms of memory usage and processing demands. As a result, the FDTD tool was used by the author where HFSS was not available and when its other features (propagation matrix method and genetic algorithm searching) were required. In most other circumstances, HFSS was preferred.

2.4 The genetic algorithm

The Genetic Algorithm (GA) is an optimisation method modelled on natural evolution. It is one of a number of algorithms from the field of evolutionary computing, first described by Holland⁸⁵ and in a more accessible fashion by Goldberg¹⁰⁰. The use of the GA in the field of electromagnetics is described by Haupt and Werner¹⁰¹. It was used in this work to attempt to optimise metamaterial patch shapes for low pass filters (see section 3.1), an application it is well suited to. The method maintains a population of possible solutions (referred to as individuals) that are gradually improved using an iterative process of evaluation and parameter modification, as summarised in Figure 2.10.

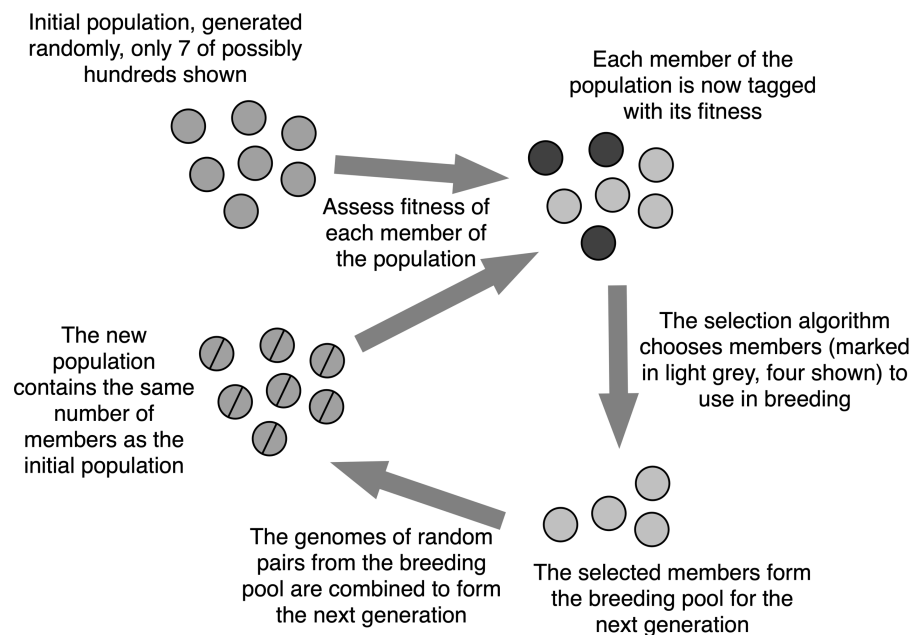


Figure 2.10. Basic operation of the genetic algorithm.

The initial population is generated randomly; each of the parameters that define an individual solution being assigned a value within their defined ranges. Deciding on the set of parameters to be optimised and their range of values is a critical step in the preparation of the data for the algorithm.

The fitness of each individual in the population is then assessed. This process involves running the modelling using the individual's parameters and comparing the output with a desired target. The difference between the model output and the target represents a measure of the unfitness of the solution.

A number of the individuals that best match the target (the fittest) are then selected to form the breeding pool for the next generation. The size of the breeding pool is decided during algorithm set up. Random pairs from the pool are then mated; their parameters being used to generate a new set of (related) parameters for the child. Enough children are generated to create a population of the same size as the previous generation.

This new population is then assessed for fitness and the cycle repeats. Generations are processed in this way until an individual emerges that matches the target closely enough.

The basic algorithm described above requires a large population of individuals (often in the hundreds), each of which must be assessed for fitness on every cycle. When combined with the FDTD method used to model the individuals generally requiring a non-trivial execution time, the computer run time required can become excessive. A variation, called the Micro-Genetic Algorithm (MGA), described by Krishnakumar⁸⁷ alleviates this by limiting the population to exactly five individuals, see Figure 2.11.

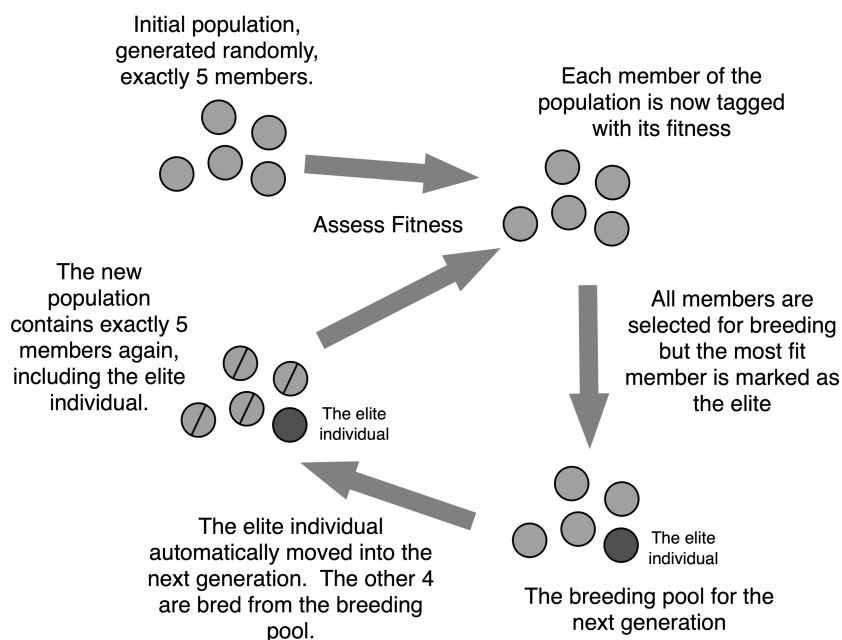


Figure 2.11. Basic operation of the micro-genetic algorithm.

The MGA also modifies the selection and breeding processes. During selection, the most fit individual is marked as the elite, and all then form the breeding pool. During breeding, the elite individual is automatically included in the next generation without modification while the other four children are bred normally. At the end of breeding, a check on the genetic diversity of the population is made; if less than 5% of the genome bits vary among the children, the four non-elite children are replaced by new children with completely random genomes (just like the initial population). Without this step, the population can become full of identical twins very quickly.

2.4.1 The genome

An individual solution within the population is defined by a set of parameters. It is the purpose of the algorithm to optimise the value of these parameters to meet the target. In the most common implementation of the genetic algorithm, the parameters are encoded into a bit string form referred to as the genome, an example is shown in Figure 2.12

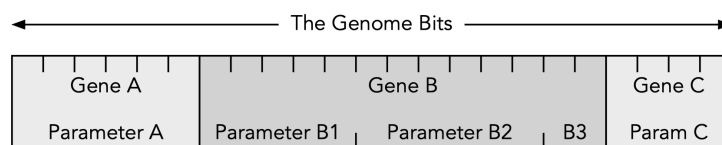


Figure 2.12. Genome encoding.

The parameters are often grouped together into genes, each consisting of one or more related values. They are then encoded into a number of binary bits. The genome is formed by laying the bits end to end to form the bit string.

The number of bits used to represent the genome (N) is a critical part of the set-up process of the genetic algorithm. The size of the search space grows as 2^N ; too many bits will vastly increase the time required for the search. However, using too few bits for each parameter will affect the quality of the result and may lead to an acceptable solution being impossible to find.

Boolean parameters are the easiest to encode. They are represented by a single binary bit encoding the two states.

Integer parameters can be coded directly in binary form. The number of bits required depends on the range of value to be represented. The range must be a power of two to match the binary coding. If the underlying parameter cannot meet

this requirement, the coded values are often wrapped around so that some parameter values are represented by two coded values.

Floating point number parameters must be considered more carefully. The range of valid values is divided by 2^M where M is the number of bits to be used for the parameter. Each binary step then represents this quantity of the parameter, starting from the minimum valid value. Care must be taken to ensure the desired solutions lie within the defined range and that there is enough resolution available to be able to find a good optimisation.

2.4.2 Fitness assessment

The process of assessing the fitness of an individual consists of two steps. First, the execution of a model using the individual's parameters. Secondly, the extraction of results from the model and a comparison with a target.

In this work, the model run was either FDTD or the propagation matrix method, as described in sections 2.2 and 2.1 respectively. The individual's parameters defined things like the shapes that were placed in the model domain and the materials they were made of. For the work described in Chapter 3, the transmittance data against frequency was collected. The target was expressed as minimum and maximum curves (which could be identical) to define an allowed zone. The unfitness corresponds to the area between the boundary of the allowed zone and the modelled curve as shown in Figure 2.13. The fitness, the parameter the genetic algorithm maximises, is therefore the complement of this. The ability to use phase shift data for the unfitness evaluation was also included in the tool but was not used in the studies reported here.

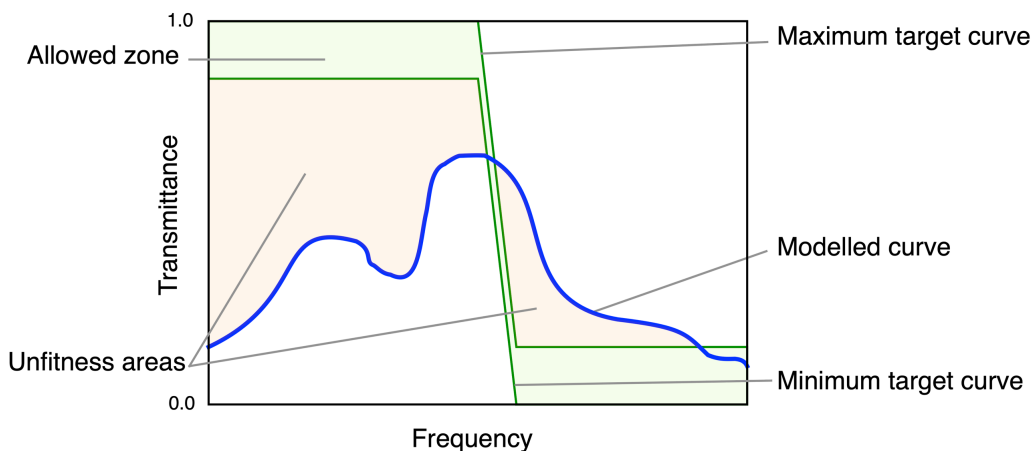


Figure 2.13. Fitness assessment. The area (in pink) between the modelled curve (in blue) and the allowed zone (in green) is a measure of an individual's unfitness. This example would search for a low pass filter style device.

In addition to the arbitrary fitness assessment target curves just described, curves generated from two standard filter functions were also used: Butterworth and Chebyshev. The basics of filter nomenclature and design are described by many authors (albeit usually from an electronics perspective), for example, Winder¹⁰². The Butterworth¹⁰³ filter is designed to have a response in the passband that is as flat as possible with smooth roll-off. It is named after Simon Butterworth who first described the mathematics. In contrast, the Chebyshev filter (based on Chebyshev polynomials, Weinberg and Slepian¹⁰⁴) trades off some ripple in the passband for a steeper cut off and a sharper 'knee' (the transition from passband to roll-off). The transfer functions of these filters are introduced below. Figure 2.14 shows an example of each annotated with their salient features.

The steepness of the roll-off from the passband to the stopband of both filter types can be summarised by a number called the 'order' which also represents the number of poles a filter has (the equations below are subtly different for odd and even order). A pole is a singularity in the transfer function which, along with the related concept of zeroes, is used in filter analysis. For a complete description of filter mathematics Winder¹⁰² is a good source. The higher the order, the steeper the roll-off. In electronics, a simple resistor-capacitor or inductor-capacitor network can implement one or two poles, so higher order filters can be achieved by cascading multiple instances (arranging for appropriate impedance matching between stages). With millimetre wave filters there is a similar relationship, albeit looser, between filter order and the number of mesh layers.

The Butterworth low-pass filter transfer function, $H_n(\omega)$, can be written as

$$H_n(\omega) = \begin{cases} \left[\prod_{k=1}^{\frac{n}{2}} \left[a^2 - 2a \cos\left(\frac{2k+n-1}{2n}\pi\right) + 1 \right] \right]^{-1} & \text{even } n \\ (a+1) \left[\prod_{k=1}^{\frac{n-1}{2}} \left[a^2 - 2a \cos\left(\frac{2k+n-1}{2n}\pi\right) + 1 \right] \right]^{-1} & \text{odd } n \end{cases} \quad 2-56$$

where n is the order of the filter, ω_c is the cut-off angular frequency and $a = j\omega/\omega_c$.

The transfer function, $H_n(\omega)$, for the Chebyshev low-pass filter is

$$H_n(\omega) = \begin{cases} \left[\prod_{k=1}^{\frac{n}{2}} \left[\left(\frac{a}{\alpha_k} \right)^2 + \frac{a}{\beta_k \alpha_k} + 1 \right] \right]^{-1} & \text{even } n \\ \left[\left(\frac{a\sqrt{1-h^2}}{h} + 1 \right) \prod_{k=1}^{\frac{n-1}{2}} \left[\left(\frac{a}{\alpha_k} \right)^2 + \frac{a}{\beta_k \alpha_k} + 1 \right] \right]^{-1} & \text{odd } n \end{cases} \quad 2-57$$

Again, n is the order of the filter, ω_c is the cut-off angular frequency and $a = j\omega/\omega_c$. In addition, r is the passband ripple in dB and α_k and β_k are given by

$$\alpha_k = \sqrt{\frac{1}{1-h^2} - \sin^2 \theta_k}, \quad \beta_k = \frac{1}{2} \sqrt{1 + \frac{1}{h^2 \tan^2 \theta_k}}, \quad 2-58$$

where

$$\theta_k = \frac{2k-1}{2n} \pi, \quad h = \tanh \left(\frac{1}{n} \sinh^{-1} \frac{1}{\sqrt{10^{\frac{r}{10}} - 1}} \right). \quad 2-59$$

Both these filters can be transformed into high-pass filters by using $a = j\omega_c/\omega$ rather than $a = j\omega/\omega_c$.

The transfer functions, $H_n(\omega)$, are complex and are converted to transmittance, $\tau_n(\omega)$, and phase shift, $\varphi_n(\omega)$, by:

$$\tau_n(\omega) = |H_n(\omega)|^2, \quad \varphi_n(\omega) = \arg(H_n(\omega)). \quad 2-60$$

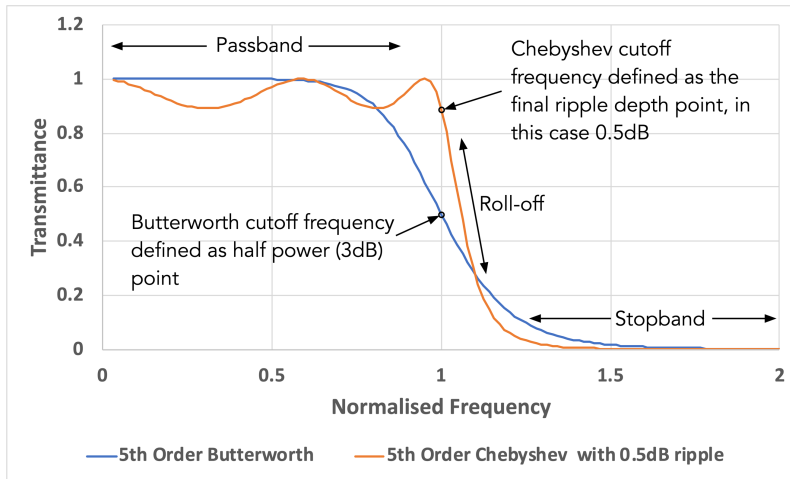


Figure 2.14. Butterworth and Chebyshev filter transmittance functions annotated with their significant features. The theoretical transmittance of the two standard filter types against frequency normalised to the cut-off frequency. Notice the differing definition of the cut-off frequency for the two types.

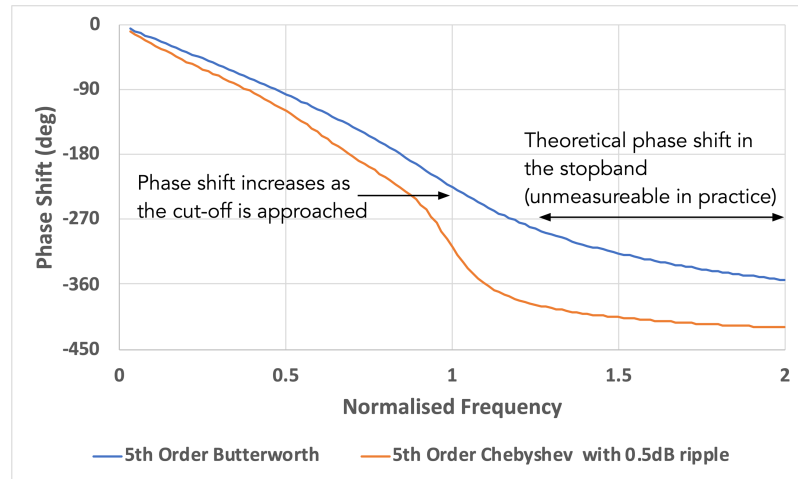


Figure 2.15. Butterworth and Chebyshev filter phase shift functions annotated with their significant features. The theoretical phase shift of the two standard filter types against frequency normalised to the cut-off frequency. Notice how the delay to the signal (indicating by the negative phase shift) increases as the filter cut-off is approached. This feature is used by the lens designs of Chapter 4.

The theoretical transmittance and phase shift functions for an example of each are plotted in Figure 2.14 and Figure 2.15 respectively.

These filter fitness functions assume equal weighting for the passbands and stopbands. In general, it was felt that this is what is required, after all, a stopband in transmission is a passband in reflection. However, the implementation did allow the specification of multiple fitness functions that could be combined using specified weighting factors. This feature could be used to create a fitness test with different weightings for different parts of the bandwidth.

2.4.3 Breeding

The process of breeding is used to generate a new child solution from two parent solutions. There are two steps; firstly, the parents are chosen, then the child is created by mixing the parents' genomes to form the child's genome.

Several methods are described in the literature for choosing the parents from the breeding pool. For this work, the tournament method described in Eiben and Smith⁸⁶ was used due to its ease of implementation while still being fair, see Figure 2.16. In this method, a number of individuals are chosen randomly from the breeding pool; the individual with the best fitness from these then becomes a parent. This is repeated once more for the second parent. The number of individuals chosen is configured during the setting up of the genetic algorithm.

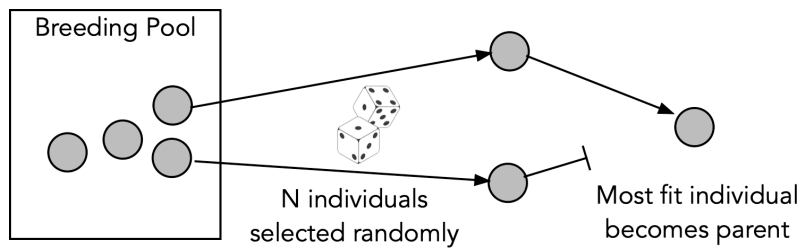


Figure 2.16. Tournament selection.

Eiben and Smith also introduce a few methods of combining the parents' genomes. In this work a method called uniform crossover was used, see Figure 2.17. To generate the child genome, each bit is considered separately; it is set by the equivalent bit from one of the parents selected by a coin flip. This has the effect of keeping parts of the genome that are identical between the two parents while randomly choosing the rest.

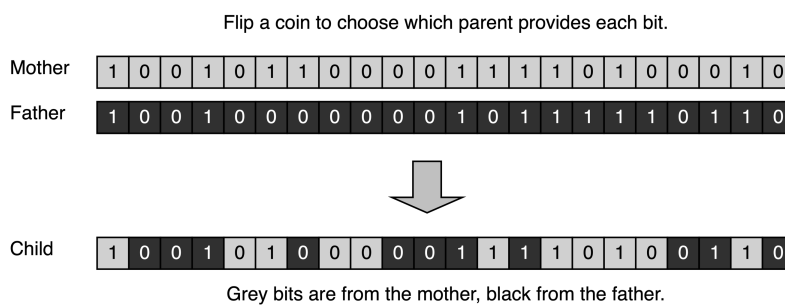


Figure 2.17. Uniform crossover, a method of combining the parental genomes. One of the parents provides each bit of the child's genome, chosen randomly.

A mutation phase is then often applied to the child genome by randomly flipping each bit according to a programmed probability. This step was omitted in the work as the combination of the Micro-Genetic Algorithm, tournament parent selection and uniform crossover already provides enough randomness.

2.4.4 Completeness

As the genetic algorithm does not have a natural end point, a way of deciding when to stop is required. The main method used in this work was by inspecting how many generations a solution has remained stable. Typically, solutions will change rapidly at the beginning of a run with modifications tailing off the more generations are executed. If a solution has been unchanged for more than half the generations of a run, it was taken to be a reasonable solution.

Where the compute time for a generation was short, such as when using the propagation matrix modelling method, the whole algorithm was run multiple times and the best solution taken. However, when using FDTD on the Hawk cluster computer this was not done due to the restricted runtime available to the author.

2.5 The modelling application

This section presents an outline of the capabilities and design of the modelling tool. It was intended to support the modelling of the interaction of electromagnetic waves with the specific kinds of structures the project concentrated on. Its abilities can be divided into several categories described here. It was implemented by the author in C++17 as several library modules. This allowed the tool to be built in a few different ways depending on the application. For example, a Linux command line application was made for use with the Hawk cluster and its batch job system.

An application with a graphical user interface (GUI) using the cross-platform GTK+ 3.0 open source toolkit¹⁰⁵ allowed for its use in an interactive way. A screenshot of the main GUI window showing the general configuration panel is shown in Figure 2.18. This allowed all aspects of the modelling tool to be configured and monitored. When using the cluster, the GUI was used to create the configuration which was stored in a file that the command line application read when it was run.

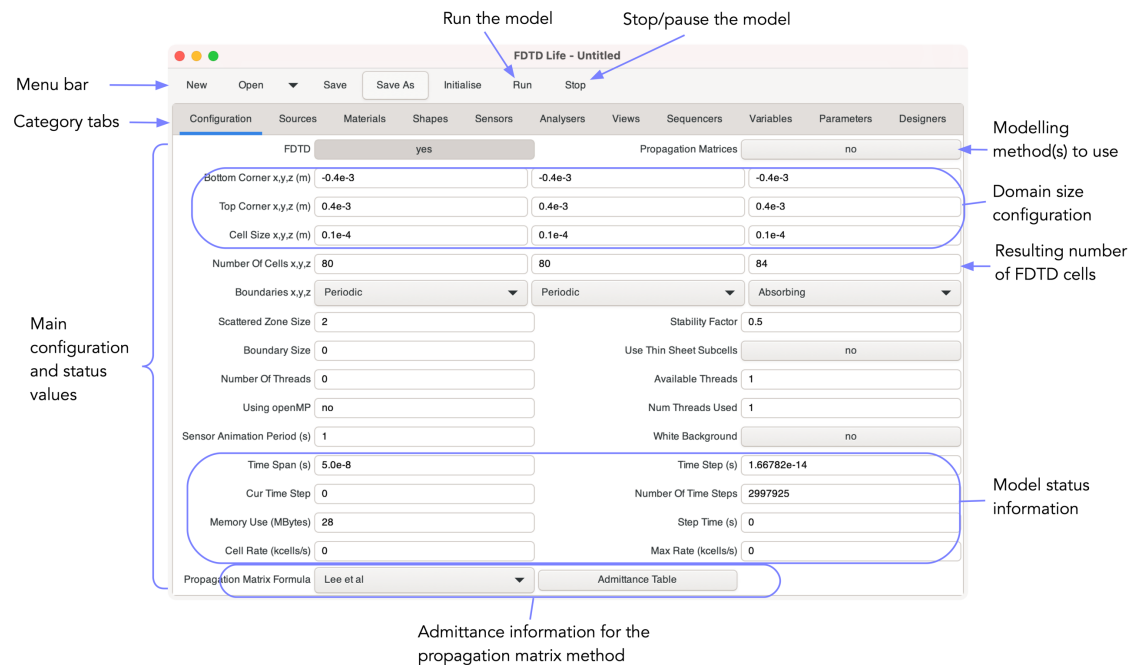


Figure 2.18. Modelling tool main GUI window. The category tabs select which part of the configuration of the tool appears in the area below, this snapshot shows the general configuration and status panel.

The implementation of the modelling methods was verified against Ansys HFSS using a few modelled scenes. The verification also led to the specification of some guidelines for the use of the modelling methods in order to produce accurate results, the most significant of which are also detailed here.

The tool was designed using an object-oriented methodology. A graphical notation called the Unified Modelling Language (UML) is used in this section. UML has been described by many authors; Booch, Jacobson and Rumbaugh¹⁰⁶ and Pilone¹⁰⁷ are two examples. This work uses a very small subset of UML to present concepts in a sketch form. A summary of the symbols used is shown in Figure 2.19.

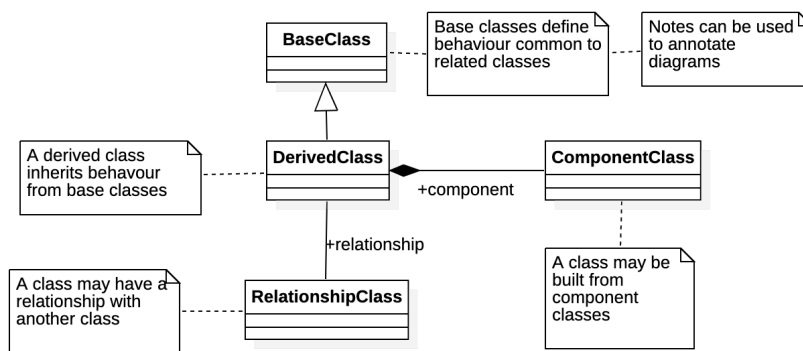


Figure 2.19. Basic UML symbols. The symbols used in the sketch diagrams of this section.

The top-level class of the modelling part of the application (named Model) is shown in Figure 2.20. It contains several components whose responsibilities are described in the following sections.

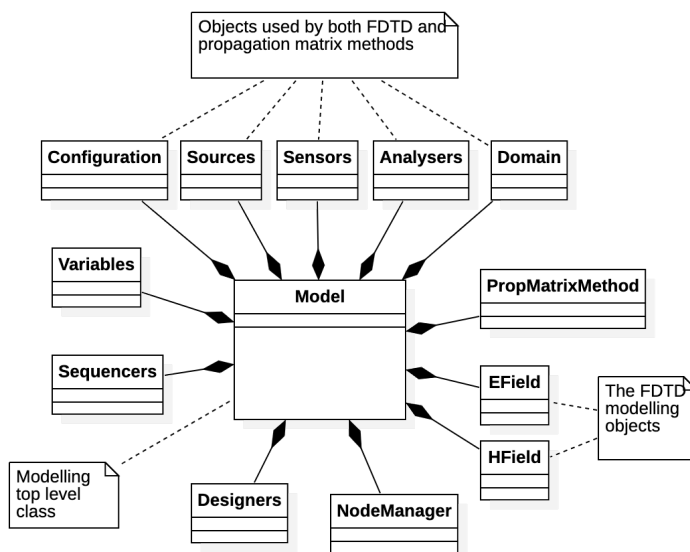


Figure 2.20. The main components of the modelling application.

2.5.1 The Modelling Grid

The FDTD modelling grid consists of a three-dimensional regular array of cells that cover the modelled domain and is used by the FDTD method. The extent of the domain and the size of the individual cells are configurable. Each cell contains values for the three components of the electric field and the three components of the magnetic field along with a reference to the material that fills the cell. These data structures are implemented in the top-level components named EField, HField and Domain in Figure 2.20.

The grid boundary pairs (x, y, and z) can each be set into one of three modes, reflective, periodic, and absorbing (see Figure 2.21). The reflective mode is the easiest to implement but least useful, waves encountering boundaries set to this mode are reflected back into the domain. In periodic mode the boundary pair acts as though the grid loops back on itself, waves that encounter one of the pair reappear at the equivalent place on the other and continue onwards in the same direction. Finally, absorbing mode surrounds the domain with a layer of extra FDTD cells in which to implement the CPML algorithm (see section 2.2.3). Waves encountering these boundaries are absorbed, thus simulating an infinitely large space.

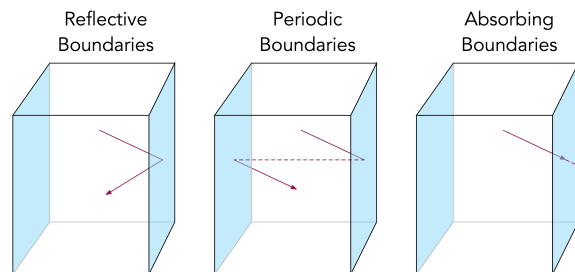


Figure 2.21. The three available boundary conditions for the FDTD domain. Reflective boundaries are naturally produced by the FDTD algorithm but are the least useful. Periodic boundaries can be used to model repeating structures. Absorbing boundaries simulate an infinite space surrounding the domain.

The set of materials that may be placed into the grid is also configurable. The electric permittivity, magnetic permeability and electric conductivity may be specified for each user defined material. In addition, a special material is automatically created that is used to fill the cells that implement the perfectly matched layers at the boundaries. The current set of materials is maintained by the Domain object, as shown in Figure 2.23.

The FDTD update equations detailed in section 2.2.1 are used to modify the electric and magnetic field values of each cell on each time step. The core of the update code itself, when stripped of all the boundary conditions, is rather simple and the electric field version is shown in Figure 2.22. The 3D array of cells in the modelling grid is represented in a one-dimensional array for efficiency reasons. The `g->index()` function calculates the index into this array from the cell's x,y,z coordinates. Firstly, the magnetic field differences are calculated, accessing the appropriate adjacent cells. Then the terms that depend on the material that fills the cell are retrieved from the material's data structure (they are time independent and were pre-calculated during initialisation). Finally, the updates to the electric field components are made.

```
// Precalculate the index of this cell
size_t idx = g->index(i, j, k);
// Calculate the H field differences
double dhxj = h->x_[g->index(i, j + 1, k)] - h->x_[idx];
double dhxk = h->x_[g->index(i, j, k + 1)] - h->x_[idx];
double dhyi = h->y_[g->index(i + 1, j, k)] - h->y_[idx];
double dhyk = h->y_[g->index(i, j, k + 1)] - h->y_[idx];
double dhzj = h->z_[g->index(i, j + 1, k)] - h->z_[idx];
double dhzi = h->z_[g->index(i + 1, j, k)] - h->z_[idx];
// Get the time independent terms for this cell's material
double caex, caey, caez;
double cbex, cbey, cbez;
Material* mat = getMaterialAt(i, j, k);
mat->cae(caex, caey, caez);
mat->cbe(cbex, cbey, cbez);
// Update the electric field cell
e->x_[idx] =
    (dhzj / dr.y() - dhyk / dr.z()) * caex +
    e->x_[idx] * cbex;
e->y_[idx] =
    (dhxk / dr.z() - dhzi / dr.x()) * caey +
    e->y_[idx] * cbey;
e->z_[idx] =
    (dhyi / dr.x() - dhxj / dr.y()) * caez +
    e->z_[idx] * cbez;
```

Figure 2.22. Electric field FDTD update code. This is the C++ code that updates electric field components for cell i,j,k in the modelling grid, stripped of boundary condition complications. It implements the update equations described in section 2.2.1 and is structured to be as efficient as possible. The magnetic field update code is similar.

2.5.2 The Modelling Scene

The scene that is used to fill the modelling grid with material references during the run initialisation phase consists of a list of shapes of various types that can be configured by the user. There are two major types of object, those that are understood by the propagation matrix method (these have an inherent one-dimensional nature, representing layers of material) and those that are not. Both types cause the placement of materials in the FDTD grid to represent the shape

as best it can, given the resolution of the grid. The list of shapes is maintained by the Domain component, see Figure 2.23.

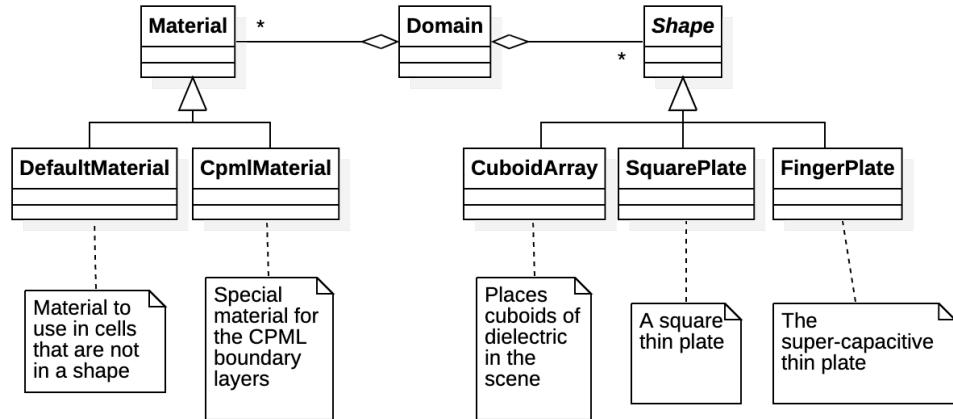


Figure 2.23. The application domain object contents.

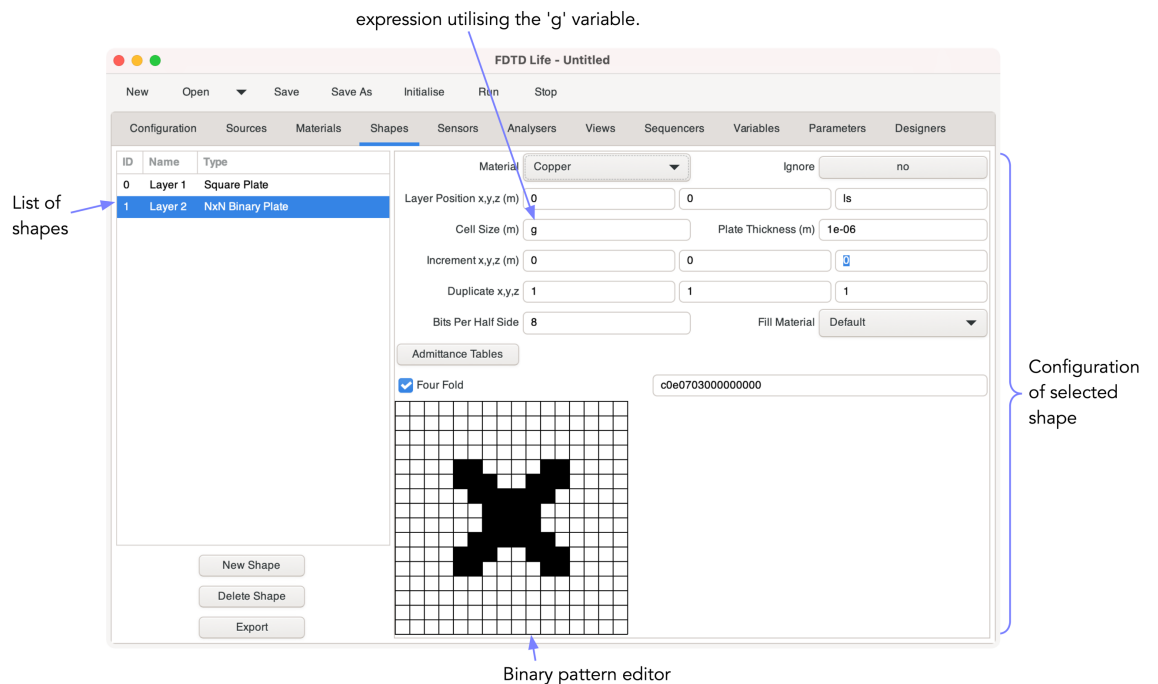


Figure 2.24. Modelling tool GUI, the shapes panel. This example contains two shapes, a square plate and an NxN binary plate. The binary plate is selected, displaying its configuration on the right.

The propagation matrix method does not use the modelling grid, rather it operates directly on shapes in the scene. Only those shapes that represent layers are considered, others are ignored. Layer shapes may contain complex admittance data (or equations that generate the data) that the propagation matrix method can use to model inhomogeneous layers. It is possible to capture admittance data with

FDTD modelling of a particular layer and then use that for subsequent propagation matrix modelling.

The shapes available to the user of the tool are summarised in Table 2.2. The tool allows the scene to be made up of any number of them. A snapshot of the GUI configuration panel for the management of the shapes is shown in Figure 2.24.

Table 2.2. Shapes available for scene building.

Shape	Layer	Configurable Parameters
Dielectric layer in the x/y plane	Yes	Position, unit cell size, thickness, material
Arbitrary cuboid	No	Center (x,y,z), size (x,y,z), duplication count and offset, material
Square plate in the x/y plane	Yes	Position, unit cell size, thickness, duplication count and offset, material, plate size, admittance equation or data.
Square hole in the x/y plane	Yes	Position, unit cell size, thickness, duplication count and offset, material, hole size, admittance equation or data.
NxN binary plate in the x/y plane	Yes	Position, unit cell size, thickness, duplication count and offset, material, size of N, pixel pattern, admittance data.
Super-capacitive plate in the x/y plane	Yes	Position, unit cell size, thickness, duplication count and offset, material, patch ration, admittance data.

2.5.3 Excitation Sources

The tool provides two ways of exciting the model, a plane wave source and a source that emulates the aperture of a rectangular waveguide (named the zone source). The Sources component contains the list of sources set up by the user (see Figure 2.25).

The plane wave source was used with much of the modelling the FDTD tool was applied to. Its implementation followed the algorithm outlined in section 2.2.2. The signal applied could be defined by specifying any number of sine waves of different frequencies and polarisations. The angle of incidence onto the domain could also be configured, although most uses were with normally incident plane waves. The wave could be continuous or applied only for a predefined time.

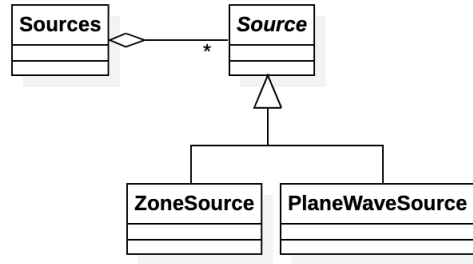


Figure 2.25. Modelling application sources.

The waveguide like source was implemented by superimposing the signal (defined in the same way as for plane waves as a set of plane waves) onto a configurable rectangular patch anywhere in the modelling domain. This source was used for the small amount of lens modelling performed in FDTD.

Any number of these excitation sources could be configured in the model, although the vast majority of the modelling performed for this work used just one. The propagation matrix modelling method could only use the plane wave source, and in addition it was always applied with normal incidence.

2.5.4 Sensors

To allow information regarding the behaviour of waves in the model to be extracted for visualisation and data capture, three types of sensor were provided. The Sensors component maintains the list of configured sensors, shown in Figure 2.26.

The first sensor type captured a two-dimensional slice of instantaneous wave data. This was mostly used for visualising the electric or magnetic fields as they change through simulated time. Each such sensor could capture one component of, or the magnitude of, the electric or magnetic field from one of the planes through the model (x/y, y/z or z/x).

The second sensor type was a variant of the first that captured the material information on the plane. This was typically used for verifying the material layout generated from the scene information described in section 2.5.2 and was not time varying.

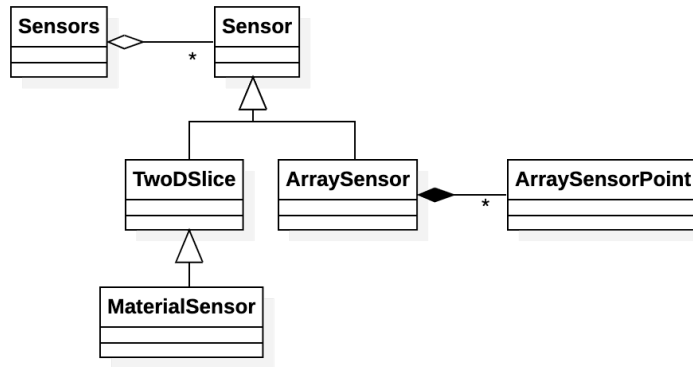


Figure 2.26. Modelling application sensors.

The third sensor type was designed for capturing time series information from the domain. It is configured to define an array of points within the domain from which time series data is collected during the modelling run. The ability to perform spectrum analysis on each of these time series was provided to allow the derivation of complex admittance information for a scene.

2.5.5 Variables

A system of user defined variables allows the parameterisation of various aspects of the model. Many of the tool's numerical configuration parameters accept an expression to define their value rather than just a number. Expressions may consist of mathematical operations involving number constants and variables using a syntax summarised as follows, using an Extended Backus-Naur form (EBNF) notation (see Quinlan¹⁰⁸).

```

expression ::= sumterm, { ('+' | '-'), sumterm };
sumterm    ::= multterm, { ('*' | '/'), multterm };
multterm   ::= ( ('+' | '-'), multterm ) | powerterm;
powerterm  ::= term, { '^', multterm };
term       ::= constant | variable |
              function, '(', expression, { ',', expression }, ')' |
              '(', expression, ')';
  
```

This syntax allows the writing of expressions containing simple maths (with the usual operator priorities) using plus, minus, multiply, divide and raise to the power. A small number of mathematical functions were also provided: sqrt, sin, cos, tan, exp, round, min and max, all implemented by the equivalent C++ functions. The variables tab of the GUI allows the user to give names to constants and other expressions (Figure 2.27).

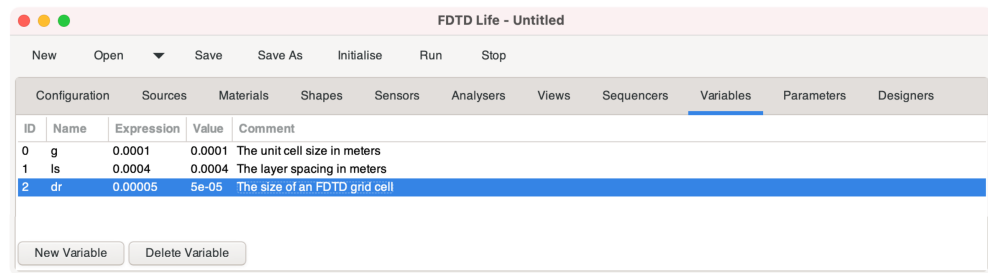


Figure 2.27. Modelling tool GUI, the variables panel. This example shows three variables. The configuration of various parts of a model can use expressions that reference these variables, the advantage being that if, for example, g is changed, only the variable needs editing.

2.5.6 Sequencers

Sequencer components control the creation of modelling tasks that the node manager arranges to run. Three sequencers were implemented (Figure 2.28), and their configuration is controlled by the sequencers tab panel of the main GUI window.

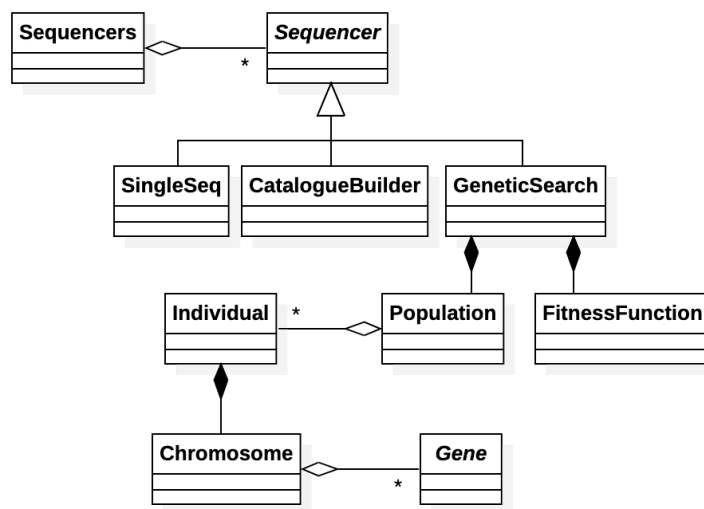


Figure 2.28. Modelling tool sequencer objects.

The simplest, the single job sequencer, creates a single modelling task using the current configuration defined by the other component panels. It is useful for running modelling on manually created scenes in an interactive environment.

The genetic search sequencer implements the genetic algorithm described in section 2.3. Its GUI panel allows the definition of the genome format, the population sizes, and the fitness functions for a search. The genome options available are summarised in Table 2.3. When the search is running, it

automatically creates jobs that model (configurable for either the propagation matrix method or FDTD) the individuals in a generation, collects the results, calculates the fitness values and breeds the next generation. This sequence is repeated until the fitness criteria is matched or until the user stops the run. The node manager is responsible for running the jobs which, in the cluster environment, may occur in parallel. When run interactively, the GUI panel also displays generation information as it happens. Figure 2.29 shows an example of the GUI from a genetic search for a Chebyshev filter.

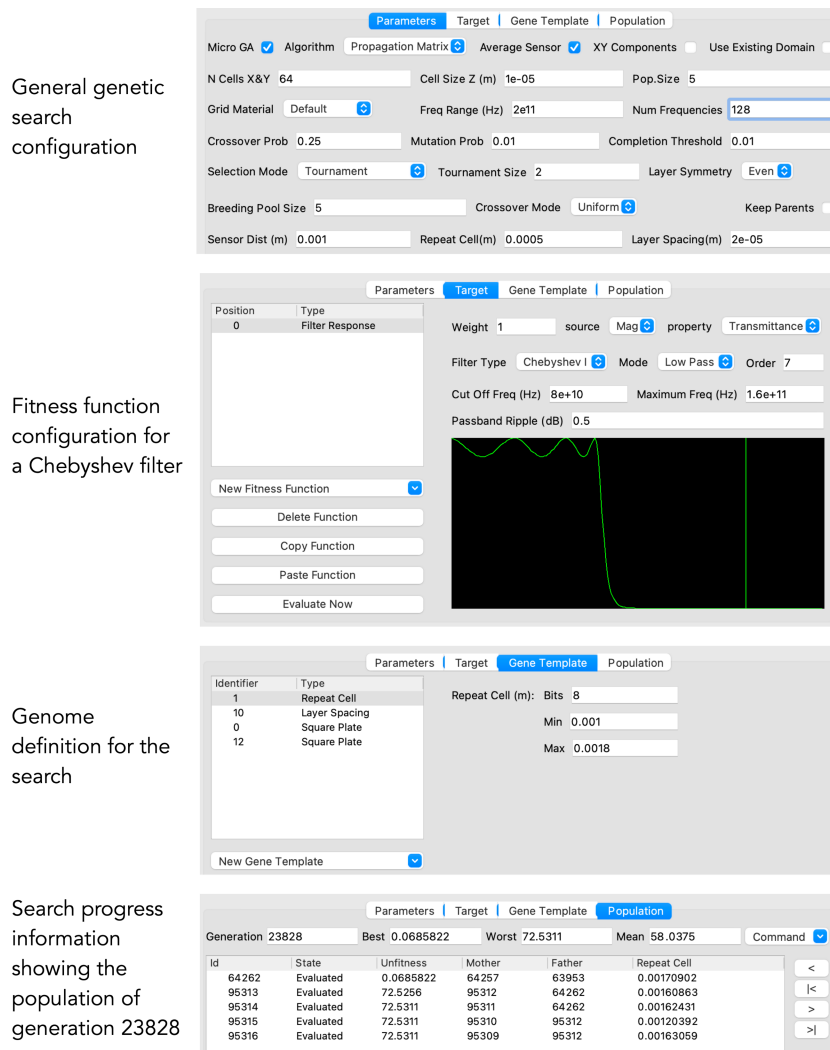


Figure 2.29. Modelling tool GUI, the genetic search panels. The genetic search panel is split into four sub-panels, shown here. Displayed at the top is the general configuration which selects the modelling algorithm, genetic algorithm settings, etc. Next is the fitness function definition, set for a Chebyshev filter. Then there is the genome definition that governs the search space, the example sets up two layers with square plates. At the bottom is a typical generation.

Table 2.3. Some of the genes available for building the genome of members in the population of a genetic search.

Name	Evolving Parameter
Repeat cell	The size of the repeat cell.
Layer spacing	The spacing between layers.
Square plate	The plate size (as a percentage of the unit cell) The repeat count (number of unit cells in the repeat cell) Whether it is a plate or a hole.
NxN pixelated plate	The repeat count (number of unit cells in the repeat cell) The pixel pattern.

The last sequencer was the catalogue builder. This was designed to generate jobs to model all the different patterns available in a NxN binary plate and was used in section 3.3. It was therefore rather specific to the requirements of the desired catalogues.

Associated with the sequencers are the analyser components. These take results from the sensors and provide feedback to the sequencers that require it. With the genetic algorithm they are responsible for the selection of a sensor and the processing of its data into the form required by the fitness functions.

2.5.7 Node Manager

The node manager controls the allocation of modelling tasks generated by the sequencers to processing nodes and handles the collection of results. Important in the cluster environment where it uses the Open MPI library to communicate between nodes. There is no user interaction with this component, but it is important to understand its presence when creating the run control files in the cluster environment.

2.5.8 Designers

The designers tab provides access to tools with specific purposes that can be used to set up models. At the time of writing there were two of these, lens designer and parameter extractor, both associated with the needs of the lenslet design work described in Chapter 4.

The lens designer tool creates the modelling scene for a lenslet given a set of design parameters, following the design models of sections 4.1 and 4.9. An export

feature also allows the lens scene to be written to a file suitable for import into the HFSS commercial tool.

The parameter extractor tool processes S-parameter data to generate tables of refractive index that can be used by the lens designer to choose the shapes that form the lenslets. This implements the method of refractive index determination described in 4.3.3 using data that can be gathered from either the HFSS tool or from previous FDTD modelling.

2.5.9 Propagation matrix verification

The propagation matrix implementation and the accuracy of the admittance formulae given by Lee et al¹⁰⁹ were verified by comparing with HFSS. A single layer of a capacitive square patch mesh in vacuum was modelled. The square patch was $480\text{ }\mu\text{m}$ in a unit cell of $800\text{ }\mu\text{m}$. This arrangement was expected to implement a Butterworth-style low pass filter with a slow roll-off and a minimum at around 340 GHz (a wavelength of nine tenths of the unit cell), as described by Ulrich¹¹⁰. Beyond 375 GHz (where the wavelength is less than the unit cell), diffraction effects begin to dominate, and the propagation matrix method breaks down.

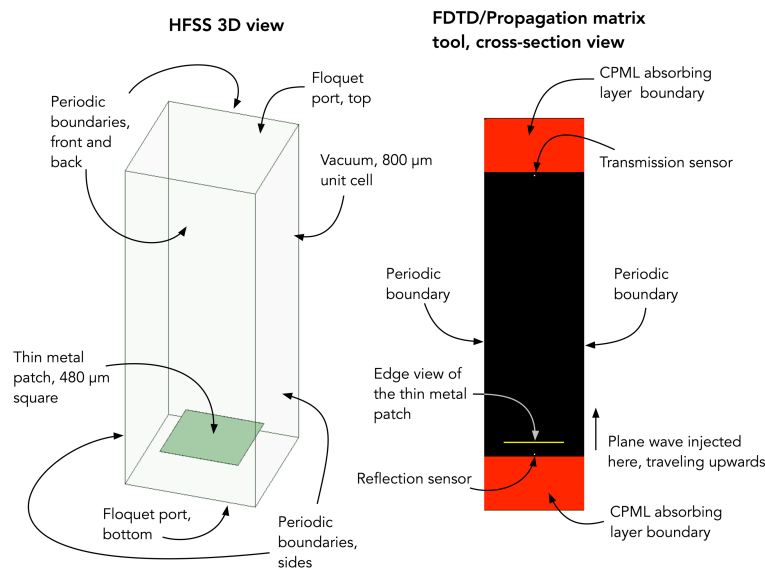


Figure 2.30. Verification modelling in HFSS and FDTD. The scene consisting of a single metal plate was modelled in both HFSS and the FDTD tool. Shown is the 3D view provided by HFSS alongside the equivalent cross-sectional view provided by the FDTD tool. Important features of the scene are labelled.

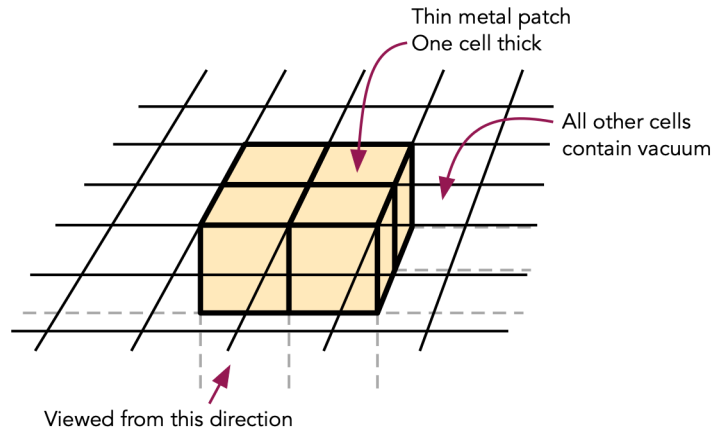


Figure 2.31. Thin metal patch represented in a Yee grid. The cells that represent the metal patch (in salmon) are configured with appropriate permittivity, permeability, and conductivity. All other cells contain the parameters for vacuum. One patch is shown here at a rather low Yee cell resolution for clarity.

Figure 2.30 shows the scene as displayed by the 3D view provided by HFSS on the left. The pairs of sides of the vacuum unit cell were configured with periodic boundaries, effectively making the scene an infinite array of square patches in those two directions. The top and bottom sides of the domain were configured with Floquet ports, HFSS's method of exciting and measuring a unit cell based repetitive structure such as this. The FDTD/propagation matrix tool was configured with the same scene. It could only display a 2D cross-section of the scene (the full 3D scene was modelled however), shown on the right. The pairs of sides were again configured with periodic boundaries but the top and bottom set to CPML absorbing boundaries. A plane wave excitation signal was introduced between the lower CPML boundary and the metal patch travelling in an upwards direction. Sensors were placed (the small white dots) to capture the reflected and transmitted signals. Figure 2.31 shows a simplified view of how the patch is represented in FDTD by a square cluster of cells, one cell thick.

Figure 2.32 shows the resulting transmittance curves. The Ulrich formula captures the minimum quite well, but the roll off is a poor match compared to the reference provided by the Ansys HFSS tool. The formula credited to Arnaud et al also does not appear to be a good match with the reference; in addition, there was some confusion in the literature regarding this formula, so it is not explored further. Both the Lee et al and the Chen formulae, however, are good matches to the HFSS curve although both deviate beyond the minimum. The modelling for all four admittance formulae took less than a second of time on a desktop computer.

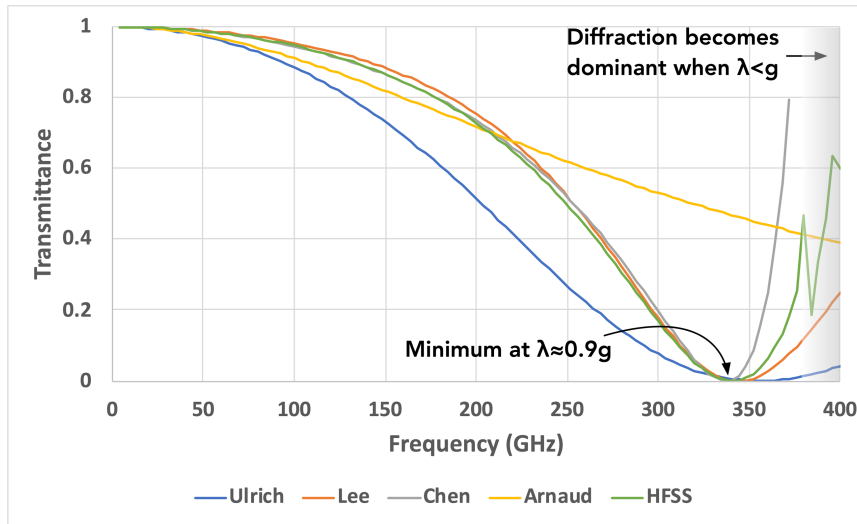


Figure 2.32. Propagation matrix formulae verification. Various admittance formulae compared with the results from HFSS.

2.5.10 FDTD verification

To verify the basic operation of the FDTD algorithm, the same square patch used in the propagation matrix verification (section 2.5.9 and Figure 2.30) was modelled. This test layout was settled on very early in the development of the tool as this kind of scene was intended to be its main use. The verification was repeated regularly during development of the code surrounding the FDTD. The transmittance results are shown compared to Ansys HFSS in Figure 2.33 demonstrating a good consistency with the commercial tool, even into the start of the diffraction zone. The phase shift is a good match until the transmitted signal becomes small, this is due to the arctangent in the FDTD calculation being applied to the ratio of two increasingly small numbers leading to larger errors.

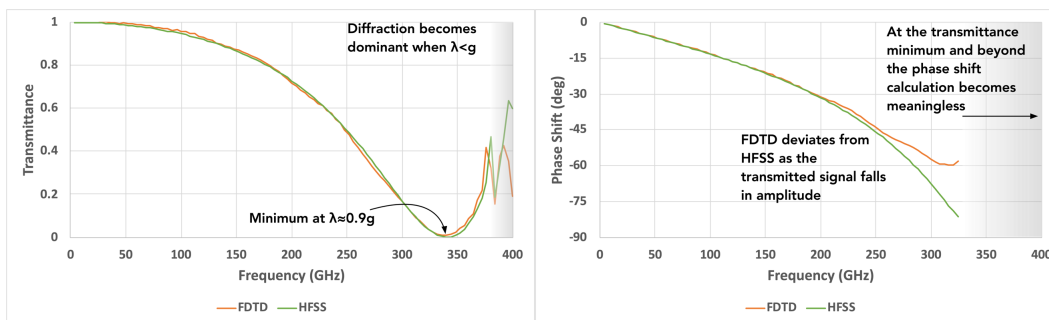


Figure 2.33. FDTD algorithm verification. Transmittance and phase shift results for a single square patch compared with HFSS. The FDTD phase shift calculation becomes unreliable when the transmitted signal is small and meaningless once diffraction occurs.

With a grid cell size of $20\ \mu\text{m}$ the FDTD verification took nearly 10 minutes to run on a desktop computer. If the cell size was halved to $10\ \mu\text{m}$, the run time would be eight times longer at 80 minutes. Comparing these times with the less than one second run time reported for the propagation matrix method in section 2.5.9 distinctly shows the advantage of using that method where it is applicable. This is especially true when used in conjunction with the genetic algorithm which requires many runs of the modelling method.

A nice feature of the FDTD algorithm is the ability to see the behaviour of waves during the execution of the model. Figure 2.34 shows a series of snapshots of a cross section of the electric field magnitude as the first cycle of a 150 GHz half-wave rectified sine wave travels downwards through the same square patch mesh ($800\ \mu\text{m}$ unit cell, $480\ \mu\text{m}$ patch size). Two instances of the unit cell are shown in each snapshot, the horizontal yellow lines are the edges of two adjacent patches. The half cycle is stored on the capacitors formed by adjacent patches before being transmitted and reflected. Notice how the first harmonic (a 150 GHz half wave rectified sine wave consists mostly of the fundamental and the first harmonic at 300 GHz) is stored for longer before being mostly reflected (at 300 GHz not much gets transmitted), indicating the higher frequency receives a larger phase shift (compare the phase shifts at 150 GHz and 300 GHz in Figure 2.33) .

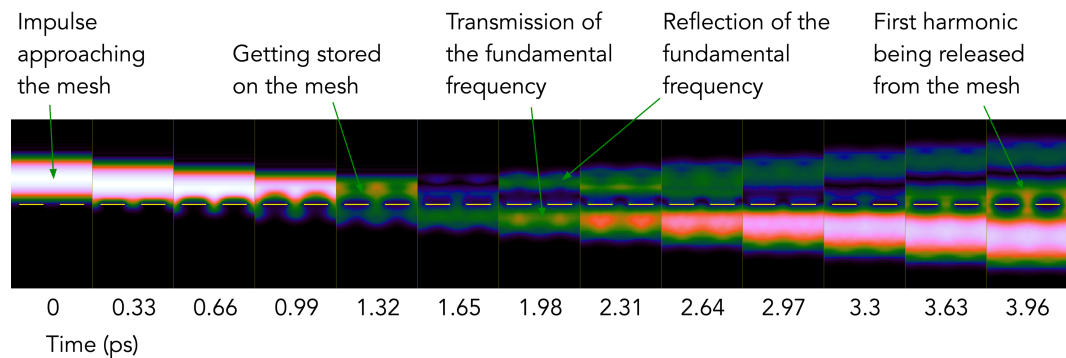


Figure 2.34. A half wave rectified sine wave encountering a metal mesh. Each snapshot of the electric field magnitude is advanced 0.33 ps from the previous. The horizontal yellow lines are the edges of the patches forming the mesh, two shown in each snapshot. The wave is travelling downwards.

2.5.11 Effect of FDTD cell size

The size of the Yee cell in the FDTD model governs the accuracy of the results obtained from it, the smaller the cell, the higher the accuracy. Smaller cells, however, lead to higher memory usage and increased processing time. A halving of the Yee cell increases the memory usage by a factor of eight (three spatial

dimensions) and processing time by a factor of sixteen (three spatial dimensions plus time). It is important therefore to understand the effects that the resolution of the FDTD grid has.

Two layers of a metamaterial mesh in vacuum were modelled using FDTD and HFSS. The mesh consisted of a $480\text{ }\mu\text{m}$ square patch in a unit cell of $800\text{ }\mu\text{m}$ and thickness of $1\text{ }\mu\text{m}$. The layers were spaced apart by $400\text{ }\mu\text{m}$ forming a crude low-pass filter, see Figure 2.35. This was modelled in FDTD using Yee cell sizes of $10\text{ }\mu\text{m}$, $20\text{ }\mu\text{m}$, and $40\text{ }\mu\text{m}$ (corresponding to 80, 40 and 20 Yee cells per unit cell).

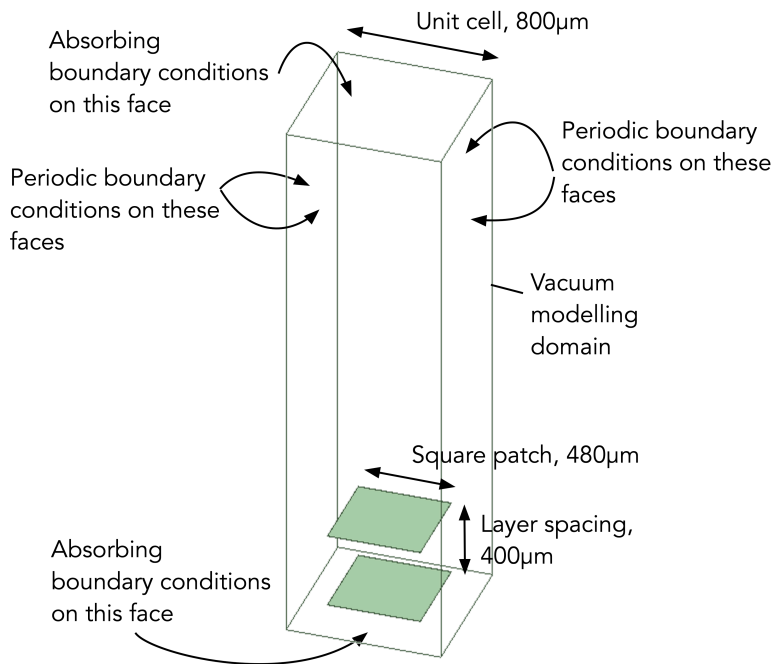


Figure 2.35. FDTD verification model. Metamaterial mesh arrangement used to investigate the effect of the FDTD Yee cell resolution on modelling accuracy.

There are two aspects to the influence of the Yee grid resolution on the modelling accuracy. One is the precision with which the physical dimensions of the parts being modelled can be represented on the grid. For example, a grid that is too coarse will distort the shape of the metallic shapes forming the mesh and in extreme cases small features may be lost altogether. The second is the spatial (and temporal) precision of the electric and magnetic fields. Too coarse a grid will be unable to represent rapidly varying fields properly, detrimentally affecting the results at higher frequencies.

The transmittance results are shown in Figure 2.36. It is clear that as the resolution of the Yee grid increases, the curves approach the HFSS result. At low resolutions there is a shift of the cut-off frequency towards longer wavelengths along with extra

attenuation in the passband. At 80 Yee cells to the unit cell, the match with HFSS is good.

Ansys HFSS itself shows a similar phenomenon when its FEA mesh is too coarse. The mesh is refined by an iterative algorithm that tries to increase its resolution in the regions of the model that need it. The termination of this process is controlled by a parameter named “Maximum Delta S”. The smaller the value of this parameter is, the finer is the resulting mesh. Figure 2.37 shows data collected for the low pass filter for three different values, clearly showing a shift of the cut-off frequency towards the longer wavelengths when the mesh is too coarse.

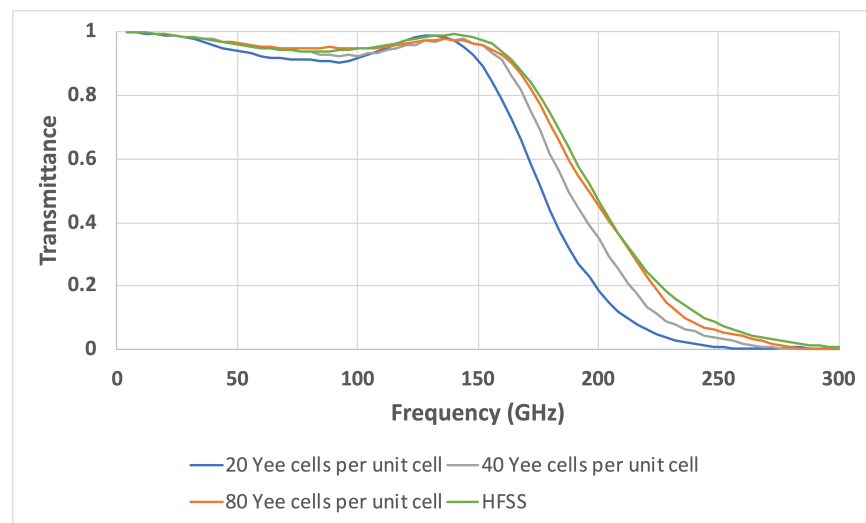


Figure 2.36. FDTD transmittance verification. Transmittance curves for the low-pass filter at three FDTD model resolutions and HFSS.

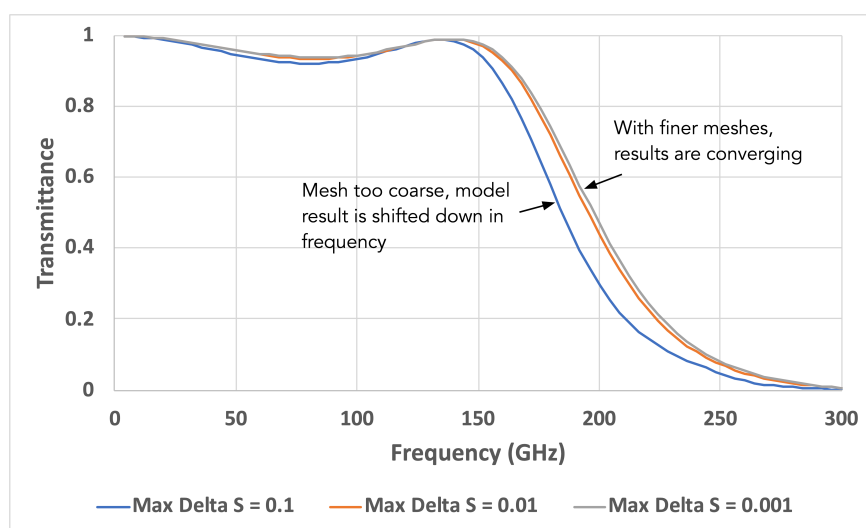


Figure 2.37. Effect of mesh coarseness with HFSS. The mesh must be fine enough for the modelling results to converge.

The reason for these effects is the discretisation of modelled space interacting with the waves travelling through it. As previously discussed, a coarse mesh or FDTD grid will be unable to accurately represent higher frequencies properly, introducing an extra impedance effect into the modelling. It is therefore as important that the FDTD cell size is chosen appropriately as it is that the HFSS maximum delta S is set to a value that allows the mesh to converge.

Some basic guidelines for both FDTD and HFSS modelling may therefore be stated. With FDTD when modelling unit cell bases structures use between 40 and 80 Yee cells per unit cell. A value between these two limits that is best able to represent the dimensions of the scene should be chosen. In principle, this choice also affects the maximum frequency that the FDTD model can represent, but in practice, the diffraction limit of the unit cell (generally the interest is in the behaviour without diffraction) occurs before this is reached. The choice of maximum delta S with HFSS is a little more complicated as it controls the convergence of the mesh refinement, but it should be less than 0.01. The smaller it is, the more memory HFSS requires, so choosing a value that fits in the available memory is usually the aim when running on a standard desktop computer.

2.5.12 FDTD thin layer feature

The thin layer feature of FDTD that was described in section 2.2.4 effectively increases the resolution of the FDTD grid in the z direction. Since the z direction is usually normal to the plane of the metamaterial mesh layers, this allows the thickness of the patches in the mesh to be more closely represented by the model. To verify the operation of the feature and to quantify the effect on the accuracy of the results, the investigation of the previous section, 2.5.10, was repeated with the thin layer feature enabled.

Figure 2.38 compares the normal FDTD 80 Yee cell per unit cell curve with that for thin sheet 40 Yee cell per unit cell; the two curves are very close together and both are a good match with HFSS. The thin sheet modification can be thought of as effectively doubling the FDTD resolution in models where it is appropriate. This is important from the modelling run time point of view. The 40 Yee cell per unit cell thin sheet version took 5 minutes to run on a typical desktop PC. The 80 Yee cell per unit cell version without the thin sheet modification took more than 90 minutes. The fact that the same results can be achieved at half the resolution in $1/16^{\text{th}}$ of the modelling time (a doubling in Yee cell resolution leads to a 2^4 time increase in modelling time, due to 3 spatial dimensions plus time) is rather useful.

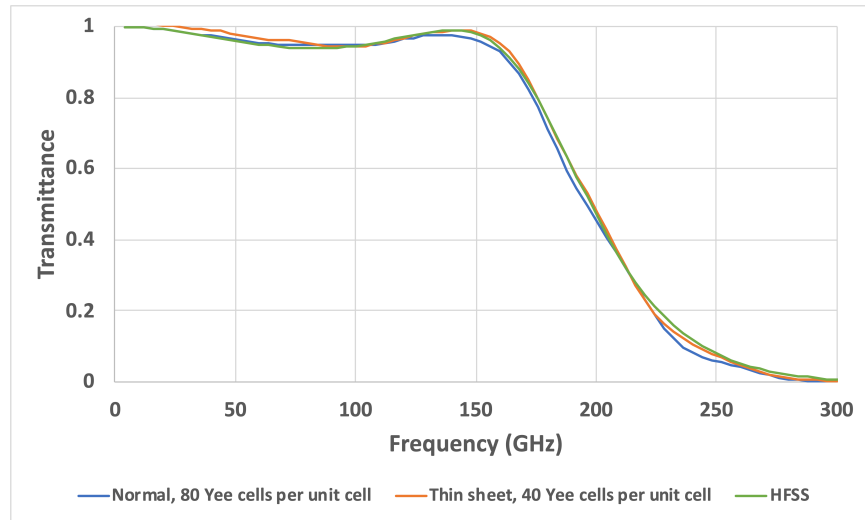


Figure 2.38. FDTD thin sheet verification. Transmittance curves for the low-pass filter showing the thin sheet modification can be like doubling the Yee cell resolution.

2.5.13 The propagation matrix method and layer spacing

The propagation matrix modelling method treats every boundary between dielectrics and, since they are considered special boundaries, every metamaterial mesh, individually. When the propagating wave encounters a boundary, the associated matrix is used without any reference to other boundaries that may be nearby. This approximation is fine when the boundaries are far apart but can break down as they get closer and enter each other's near field at the frequencies of interest. This is especially true of metamaterial mesh boundaries that can affect each other's admittance characteristics drastically when they are close together.

During the verification of the propagation matrix method, how the spacing between a pair of metamaterial meshes affected the results was investigated. The metamaterial mesh used was a square patch of size $480\text{ }\mu\text{m}$ in a unit cell of $800\text{ }\mu\text{m}$. The admittance data for this patch was collected using FDTD modelling. Two layers of this metamaterial at various layer spacings were then modelled using the propagation matrix method and FDTD, see Figure 2.39. It is apparent that as the layer spacing is reduced, the propagation matrix method results deviate from those of FDTD.

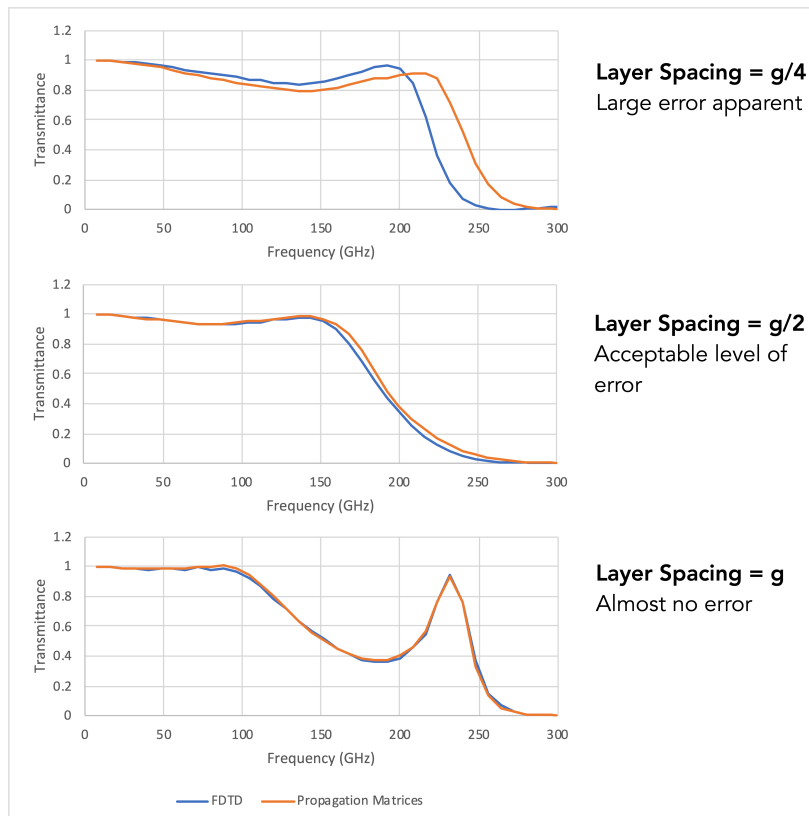


Figure 2.39. Layer spacing and the propagation matrix method. Comparing FDTD and the propagation matrix modelling methods for two metamaterial mesh layers consisting of $480\text{ }\mu\text{m}$ square patches in a unit cell, g , of $800\text{ }\mu\text{m}$, as the spacing between the layers is varied.

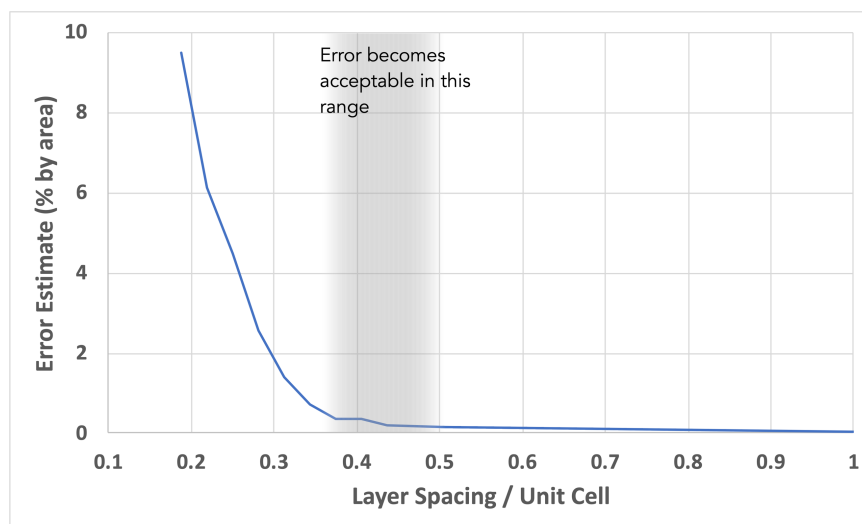


Figure 2.40. Modelling error for the propagation matrix method when metamaterial layers get too close together. A safe limit for accurate results (error $< 0.5\%$) is half the unit cell.

To quantify this effect, an error value was calculated from the area between the propagation matrix transmittance and the FDTD transmittance curves compared with the total area under the FDTD curve. This value was found for a range of layer spacings and the results are shown in Figure 2.40 plotted against the layer spacing as a fraction of the unit cell. The modelling error becomes acceptable with a layer spacing above about one third of the unit cell. In this work, a value of one half the unit cell is used for safety (where the error is rather less than 0.5%).

Chapter 3

Beyond the square

Millimetre wave filter devices using metal mesh metamaterials have been developed for many years. Ade et al⁷ describe the use of meshes consisting of square patches for low-pass filters, square holes for high-pass filters and a hybrid pattern for band pass filters. This chapter reports on work exploring the possibility of making changes to the conventional square patch shape to better match the theoretical transmittance curves for low-pass filters and to increase the range of refractive index available from artificial dielectrics.

Two basic types of filter response were considered in the work reported here: the Butterworth and the Chebyshev. These standard filter types were introduced in section 2.4.2 during the discussion of genetic algorithm fitness functions. There are other types of filter (Elliptic, Bessel, etc.) but these two were chosen for the purposes of exploring non-square patches as they have reasonably straightforward math and are well known. The exact type of filter was not important when looking at what difference the patch shape could make.

3.1 Searching with the genetic algorithm

The genetic algorithm and modelling methods described in Chapter 2 were used to investigate whether an improvement could be found on the square patch for a low-pass filter. The work described in this section was published in Thompson and Pisano¹¹¹ and Thompson et al¹¹².

The author's group at Cardiff have experience in providing low pass filters for various instruments (see section 1.1), one of which, with six layers, is introduced in section 3.2.3. The searches reported in this section were, however, restricted to four layers to keep the runtime required by step 2 (section 3.1.2) manageable. They are also all air-gapped filters (no solid dielectric fills the space between the layers). Direct comparisons with the existing Cardiff filter design were therefore not possible, rather the intention was to establish if there were any patch pattern variations that might be applicable generally.

The investigation procedure followed these steps, which are detailed in the following sections:

1. Find an initial filter design using conventional copper square patches.
2. Attempt to improve the performance of the design by varying the copper patches away from the square shape.
3. Analyse the resulting patterns.

Two low-pass filters with cut-off frequencies of 80 GHz were used as examples: a seventh order Chebyshev with 0.5 dB passband ripple and a fifth order Butterworth.

3.1.1 Step 1. Finding initial filter designs

The initial filter designs using conventional square patches were found using the genetic algorithm applied to the propagation matrix modelling method. The standard filter fitness functions described in section 2.4.2 were used. These calculated the area between the measured transmittance curve and the ideal filter response, allowing the genetic algorithm to minimise this difference. The effect of step 1 was therefore to find a square patch layout that had a transmittance curve that was close to the theoretical.

The number of layers used in the filters was fixed at four. The accepted practice for filter design in the Cardiff group is to produce a stack of layers that are identical when viewed from either side. This means that for four layers, the outer two layers were required to be identical as were the inner two layers. This helps the genetic algorithm as it is only searching for two layers, keeping the dimensions of the parameter search space down (the full set of search parameters for step 1 are summarised in Table 3.1). This is not so important for step 1 (due to the propagation matrix modelling method being fast) but for step 2, the extra sets of pixel pattern bits for more layers would cause the search space to rapidly become infeasible for FDTD modelling.

The propagation matrix modelling method is capable of handling designs with arbitrarily different unit cells on each layer. However, the second step will use the FDTD modelling technique with periodic boundary conditions which requires all the layers to have the same periodicity. Figure 3.1 shows how this requirement was enforced while still allowing layers to have different (albeit somewhat constrained) unit cells. The overall periodicity (termed the repeat cell, the same value used for all layers) was allowed to vary from 1 mm to 1.8 mm in 256 steps. This range of values was chosen as it covers the values of repeat cell expected for an 80 GHz filter; a demonstration of how it is necessary to know something about the expected

solution in order to utilise the genetic algorithm effectively. How many unit cells the repeat cell was divided into was then allowed to vary independently for each pair of layers. This parameter, called the ‘repeat factor’, was limited to values of 1, 2, 3 or 4 (i.e., one-, two-, three- or four-unit cells respectively in the repeat cell, the diagram shows three).

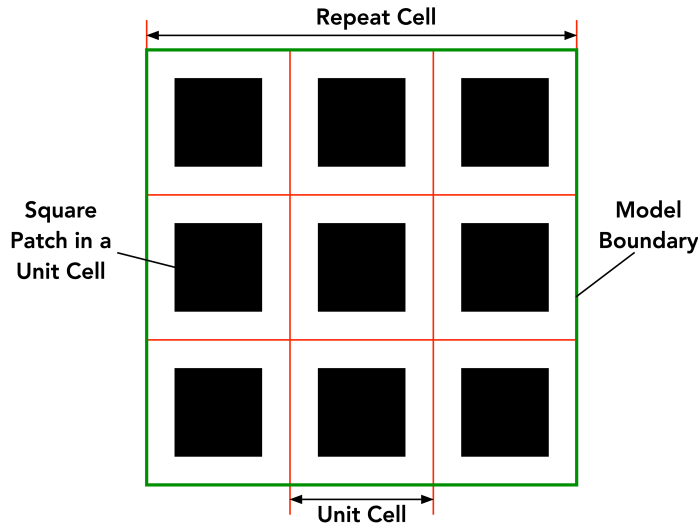


Figure 3.1. Relationship between the repeat cell and the unit cell. To demonstrate how the repeat cell is divided into unit cells this example shows a repeat factor of 3; i.e., the repeat cell is divided into a three-by-three array of unit cells (each containing a square patch).

The genetic algorithm also varied the patch size for each pair of layers. The range of values allowed was from 15% to 95% of the unit cell in steps of 5%. The admittances for these patch sizes for a standard unit cell were captured using FDTD. This data was then used by the propagation matrix method in the modelling for this step, scaling according to the unit cell as appropriate.

The layer spacing was another parameter the genetic algorithm was configured to modify. This was allowed to vary from 0.5 to 1 mm in sixteen steps. This range was selected so that the layers did not get too close together and cause the propagation matrix modelling to fail (see section 2.5.13) but still covered the values expected for an 80 GHz filter.

This set of search parameters required a genome size of 24 bits for the genetic algorithm. As the modelling used was the propagation matrix method, the genetic algorithm could run a thousand generations in around 5 minutes on a regular desktop computer, rapidly finding conventional square patch solutions where typically 3000 generations were required before no further progress was observed.

These runs were executed a few times and the best solution chosen from among them.

Table 3.1. The search parameters for step 1 .

Parameter	Range	Bits
Repeat cell	1 to 1.8 mm	8
Layer spacing	0.5 to 1 mm	4
Patch size layer 1 & 4	15% to 95%	4
Patch size layer 2 & 3	15% to 95%	4
Repeat factor layers 1 & 4	1, 2, 3 or 4	2
Repeat factor layers 2 & 3	1, 2, 3 or 4	2

3.1.2 Step 2. Improving the square patch

In step 2, attempts were made to improve the performance of the designs by converting the square patches from the step 1 solution to NxN pixelated patterns. The FDTD modelling method was then used with the genetic algorithm to vary the patches away from square keeping the repeat cell size, repeat factor and layer spacing fixed at the values discovered by step 1. These parameters were not included in step 2 to avoid inflating the search space beyond that which is feasible with FDTD modelling. This may have caused possible better solutions to be missed, but the time required for the patterns only search was at the boundary of the cluster compute time available to the author. The genetic algorithm's fitness function was also kept the same as step 1, the effect being to try to increase the conformance of the filter to the theoretical transmittance curve by varying the patch shapes.

The NxN pixel patterns used were based on those described by Ge and Esselle¹¹³. An 18x18 example is shown in Figure 3.2. The method of encoding the binary data imposes four-fold symmetry on the patterns. The whole of the repeat cell is encoded into a single NxN pixel pattern, the value of N being chosen so that the pattern accurately represents the starting square patches without getting too large that the FDTD model becomes unusable (there must be at least one FDTD cell per binary pattern pixel, preferably two or more).

As the only parameters the genetic algorithm searches through in this step are the two NxN pixel patterns, the genome consists solely of the bits representing them. This is still generally larger than the number of bits in the genome of step 1. The number of bits required to represent the patch on a layer was also the main reason

for restricting these searches to four layers; any further layers would take the required computer runtime beyond that available to the author. The modelling method is also FDTD which requires much more computing power than the propagation matrix method. As a result, it was not feasible to run this step on a desktop computer, instead it was run on the Hawk cluster provided by the Supercomputing Wales project. The genetic algorithm was typically run for three days (the limit on runtime for a single job, it was theoretically possible to continue the search with another run, but this was not practical for this work) using four nodes of the cluster, each node containing 40 CPU cores. Due to the computer time required, this genetic algorithm run was only executed once.

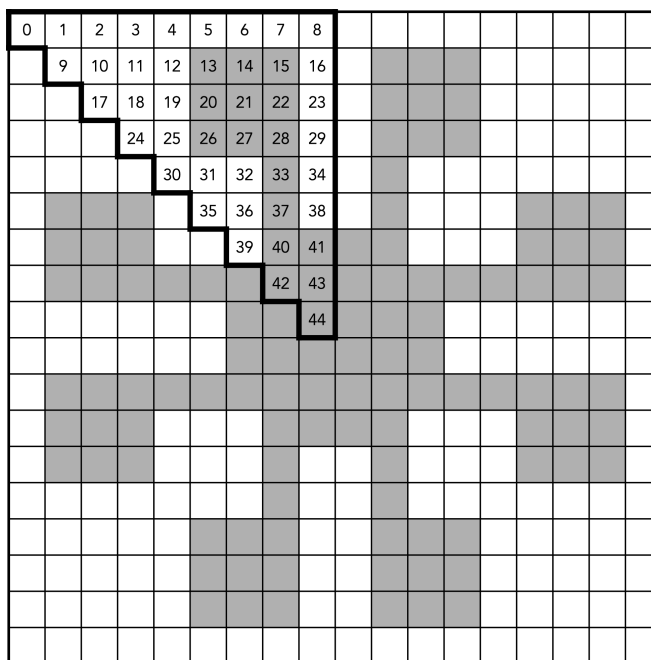


Figure 3.2. An 18x18 pixel plate with four-fold symmetry. The pattern was represented in the genetic algorithm by the binary code indicated in the triangle at the top left, the numbers being the bit position in the code.

The individuals making up the starting step for a genetic algorithm search normally have randomly generated genomes. In this case however, one of the individuals was initialised to contain the square patches discovered in step 1. As a result, the genetic algorithm starts from these shapes and slowly improves the result by evolving the patterns away from the squares.

3.1.3 Step 3. Decompose the results

The patterns resulting from step 2 typically showed the basic outline of the starting square patches with fairly minor changes, for example corners rounded off, extra protrusions, holes, etc. The changes were classified into a number of small groups

and removed from the pattern one at a time, using FDTD to acquire the transmittance response each time. An error value was calculated by measuring the area between the desired and modelled curves. Using this, a numerical estimate of the effect of each group of changes could be made.

3.1.4 The Chebyshev filter

The first example to which this improvement procedure was applied was a seventh order Chebyshev with 0.5 dB of passband ripple, cut-off frequency of 80 GHz and a stopband running to at least 140 GHz (see Figure 3.5). The genetic algorithm of step 1 was allowed to run for more than 3500 generations. The best (according to the chosen fitness criteria) design discovered was stable for the last 2000 generations; a good indication that it is a reasonable solution. It is shown in Figure 3.3. Layers 1 and 4 used an 80% square patch with repeat factor of two, layers 2 and 3 a 70% square patch with a repeat factor of 1. The repeat cell size was 1.716 mm, implying a unit cell size of 0.858 mm for layers 1 and 4, 1.716 mm for layers 2 and 3. The layer spacing was 0.875 mm.

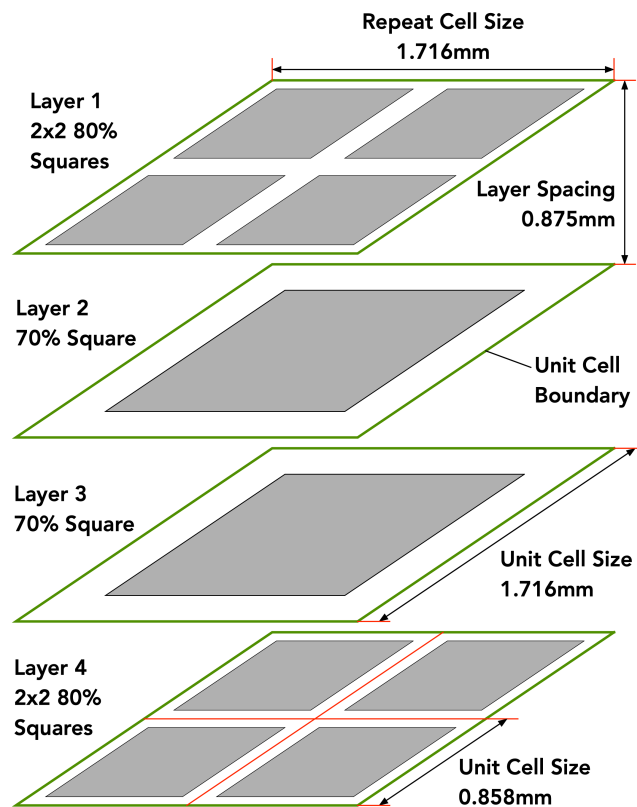


Figure 3.3. Chebyshev low-pass filter design from step 1 of the improvement procedure.

The design from step 1 was then used to initialise the genetic algorithm in step 2 and run for three days on the Hawk compute cluster. This was long enough for

1172 generations to be processed with the result shown in Figure 3.4. As the result was only the best for roughly the last 150 generations there may be further improvements possible given more time on the cluster. For the purposes of this study however, the changes that make most difference to the match with the desired response are likely to already be present.

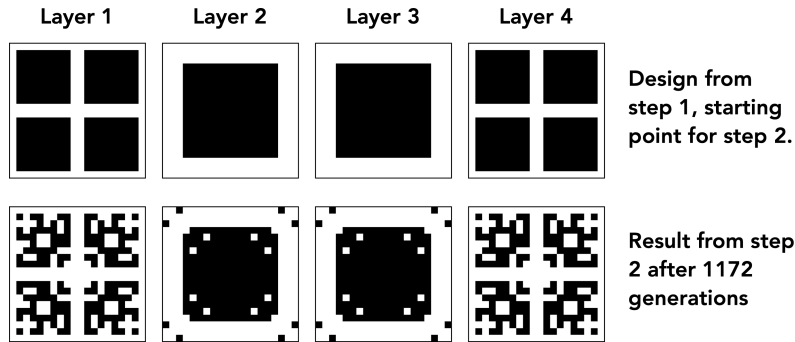


Figure 3.4. Chebyshev low-pass filter step 2. The starting pattern in the top row and the evolved pattern in the bottom.

The transmittance of the designs from step 1 and step 2 along with the ideal Chebyshev low-pass filter response is shown in Figure 3.5. The response of the solution with the patterns improved during step 2 is closer to the ideal Chebyshev response in both the passband ripples and the cut-off.

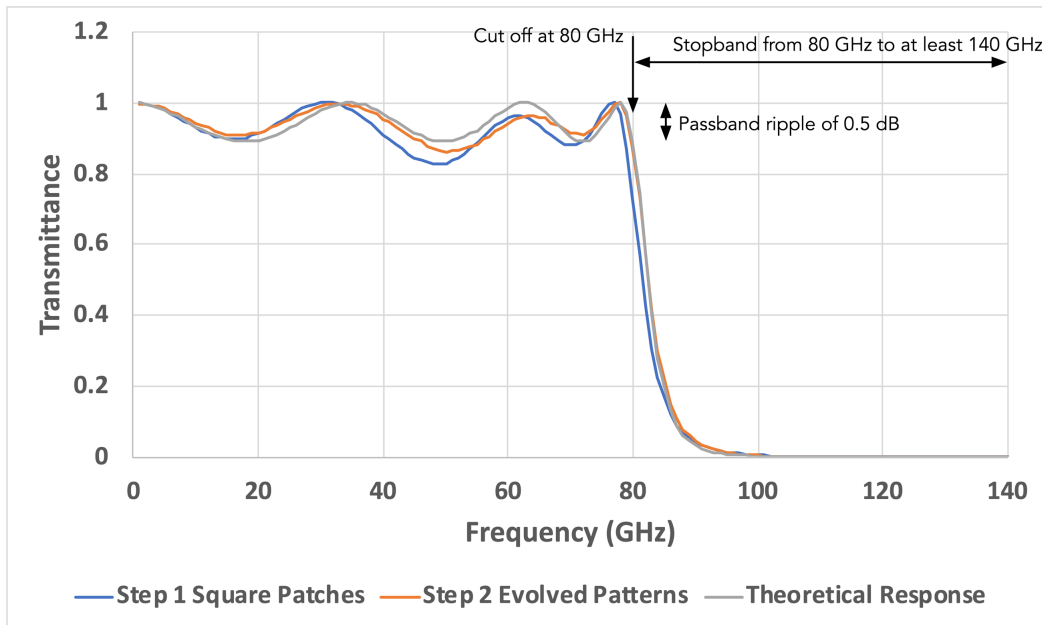


Figure 3.5. Chebyshev low-pass filter designs. The transmittance of the designs from steps 1 and 2 along with the theoretical Chebyshev response and the cut off, stopband and ripple requirements.

A look at the losses, as represented by the power that is neither transmitted nor reflected, is shown in Figure 3.6. The losses of the designs from step 1 and step 2 are the same (certainly within the limits of the accuracy of the FDTD modelling) except for a spike in loss in the stopband of the step 2 solution. The step 2 changes have introduced small inductive elements to the layer 1 and 4 patterns in which currents can flow dissipating power, especially at high frequencies. These are combining with the capacitance of the patches to produce a resonant circuit at around 125 GHz. Since this is in the stopband of the low pass filter, it won't have much effect on its use as a transmission filter. However, it will reduce the usefulness of the device operating in reflection as a high pass filter as it will put a notch in what becomes the passband.

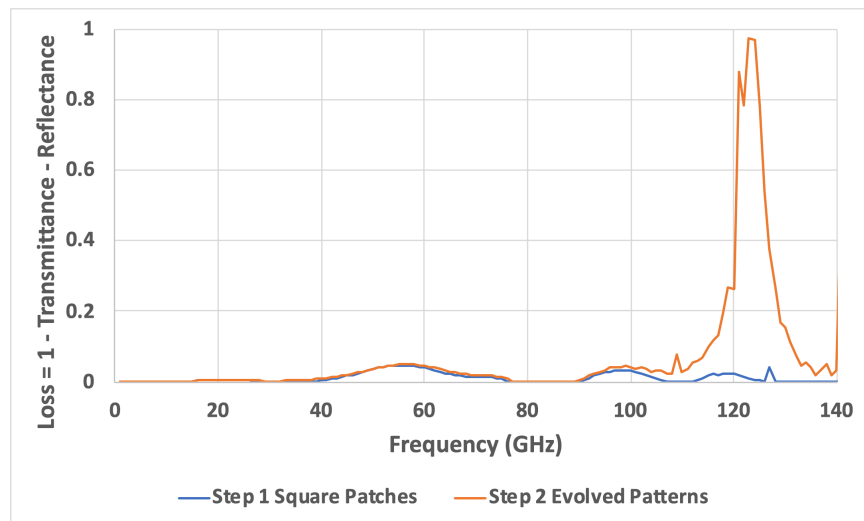


Figure 3.6. Losses of the Chebyshev low-pass filter designs. There is an increase in loss in the stopband of the design using evolved patterns.

In step 3 the changes made to the layer patterns by step 2 were removed one by one. At each stage the effect on the transmittance characteristic compared to the ideal was quantified. This was achieved by measuring the area between the measured curve and the theoretical response, expressed as a percentage of the total area under the theoretical response. The patterns and errors are summarised in Figure 3.7. These results indicate that the changes made to the square patches by step 2 led to an almost halving of the error in the transmittance curve compared with the ideal Chebyshev response. Bear in mind, however, that the step 1 error was already quite small (at 4.08%) so the improvement (to 2.15%) itself is small and is mostly in the match with the passband ripples. They go on to show that the majority of the improvement comes from the rounding of the corners of the large square patches of layers 2 and 3. A further useful improvement comes from the

changes made to the outer corners of the smaller squares of layers 1 and 4. Other changes only make small contributions.

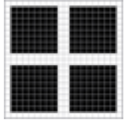
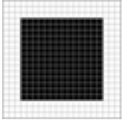

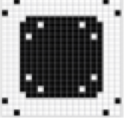

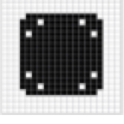

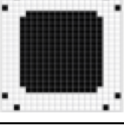

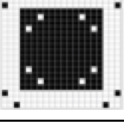
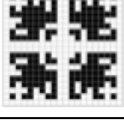
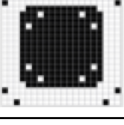
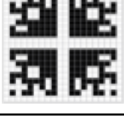
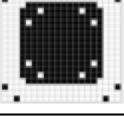
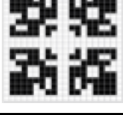
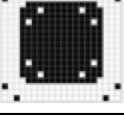
Description	Layers 1&4	Layers 2&3	Comments
Stage 1 result Error: 4.08%			The conventional square capacitive plates result
Stage 2 result Error: 2.15%			The solution evolved from the conventional result
Layers 2&3 corner dots Error: 2.43%			The dots only make a small difference to the error
Layers 2&3 plate holes Error: 2.19%			These plate holes make even less difference
Layers 2&3 plate corners not cut off Error: 3.51%			This change makes the biggest difference of all the changes made to layers 2&3
Layers 1&4 plate center holes Error: 2.35%			The holes in the center of the layer 1&4 plates make only a small difference
Layers 1&4 middle corners Error: 2.52%			Only a small difference made by this feature
Layers 1&4 outer corners Error: 2.82%			The rounding of the outer corners of layers 1&4 do make a difference

Figure 3.7. Chebyshev low-pass filter step 3. The effect of each change to the patterns as indicated by the error calculated from the area between the ideal transmittance curve and transmittance curve of the pattern.

3.1.5 The Butterworth filter

The improvement procedure was applied to a second example; a fifth order Butterworth low-pass filter, again with a cut-off frequency of 80 GHz, see Figure 3.10. In order to get a reasonable response from only four layers, it was found necessary to bring the stopband limit down to 120 GHz (cf. the Chebyshev low-pass first example where the stopband extended to 140 GHz). It turned out to be

quite difficult for the genetic algorithm to achieve a Butterworth response with minimal ripple in the passband.

Step 1 of the procedure settled on the design shown in Figure 3.8. This consisted of four layers all with the same unit cell of 1.789 mm with a layer spacing of 1.167 mm. Layers 1 and 4 contained square patches occupying 30% of the unit cell, while layers 2 and 3 contained 60% squares. The genetic algorithm was run for more than 5400 generations with the solution appearing around generation 4000 and remaining stable thereafter.

The layers were converted to 20x20 pixelated plates to initialise the genetic algorithm of step 2. This was then run for three days on the Hawk cluster managing 2048 generations. The improved solution, which had only been discovered a few generations from the end of the run, is shown in Figure 3.9. The small square patch of layers 1 and 4 has been evolved almost to nothing replaced by a scattering of small dots. This implies that the small squares are having very little effect on the transmittance curve. The larger squares of layers 2 and 3 have had their corners modified.

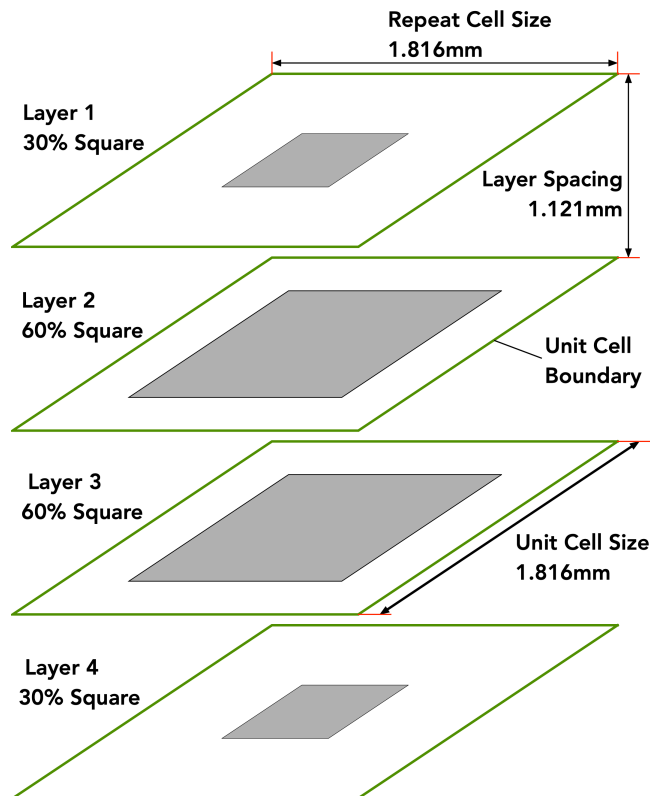


Figure 3.8. Butterworth low-pass filter design from step 1 of the improvement procedure.

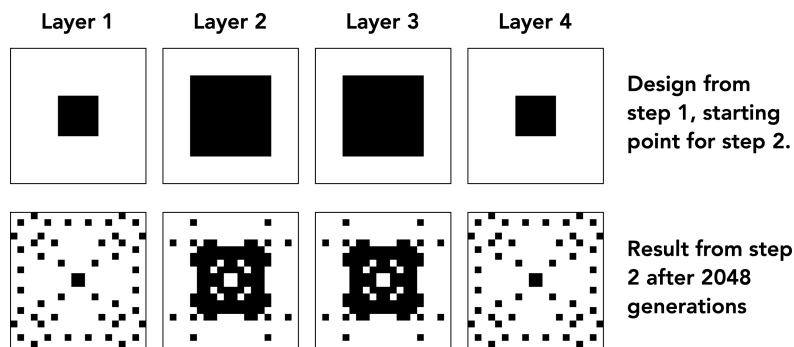


Figure 3.9. Butterworth low-pass filter step 2. The starting pattern in the top row and the evolved pattern in the bottom.

The transmittance curves for the solutions of stage 1 and stage 2, along with the ideal response, are shown in Figure 3.10. This shows that the improvement made by stage 2 is marginal. Using the area between a transmittance curve and the ideal response as a measure of the error once more, the evolved solution manages to reduce the error by just 8%. In addition, most of the improvement comes about from better conformance to the ideal curve on the approach to the stopband, arguably a region that is of lesser importance, at the expense of a little more attenuation in the passband.

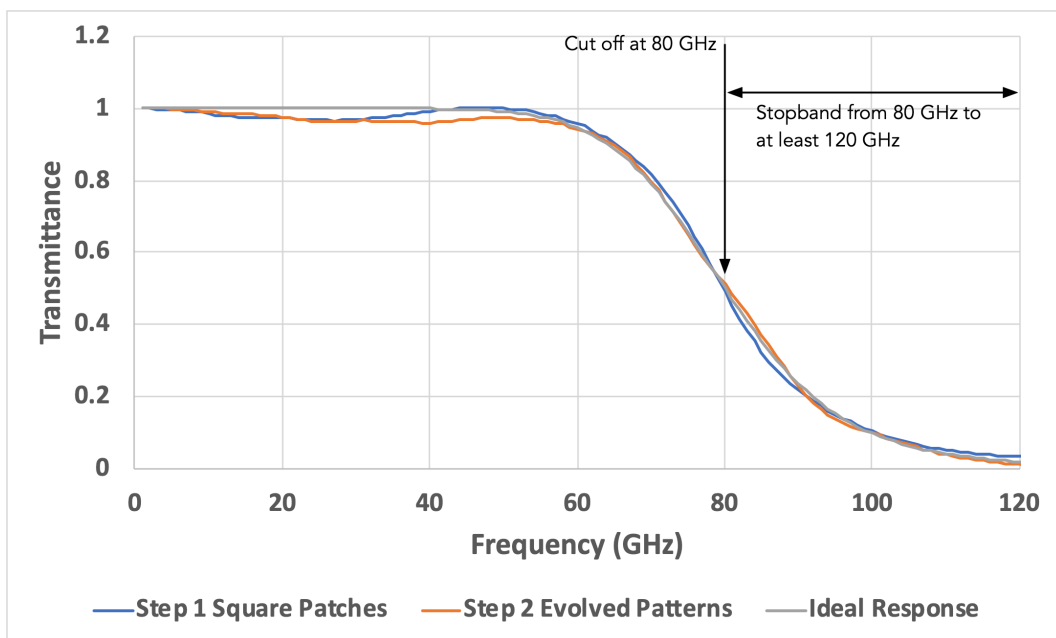


Figure 3.10. The transmittance of the Butterworth low-pass filter designs from steps 1 and 2 along with the theoretical response. The cut off and stopband requirements are also shown.

It was felt that the changes made to the square patches by step 2 affected the performance so marginally it was not worth proceeding to step 3. However, the

losses were measured and are shown in Figure 3.11. There is a slightly raised loss around the cut-off frequency but nothing that can be regarded as significant.

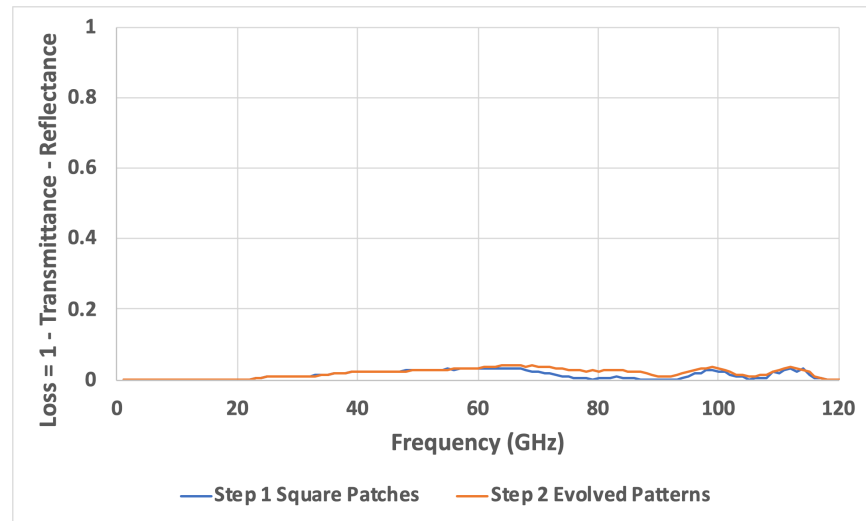


Figure 3.11. Losses of the Butterworth low-pass filter designs. There is no significant difference in the loss between the step 1 and step 2 designs.

3.1.6 Conclusions

The success of the genetic algorithm search for patterns that might improve on the conventional square patch was mixed.

In the Chebyshev case, which accepts some passband ripple in exchange for a steeper cut-off, there were measurable gains made. It proved possible to improve the performance in the passband, reducing the ripple and making it conform more to the theoretical response. The error was reduced from 4.08% to 2.15% (the error was calculated as the area between the measured curve and the theoretical curve expressed as a percentage of the total area under the theoretical). The best change being the rounding of the corners of the square patches. Due to the Covid-19 pandemic, it was not possible to construct the improved design and verify the modelling, this must remain as further work. The new design's rounded corners may ease the manufacturability a little, although this is likely offset by the fine detail of the patches.

Improvements to the Butterworth response were a lot harder to come by. No improvement in the passband was managed, the only effect achieved being a slightly better match with the theoretical response at the entry to the stopband. The conclusion for this filter response is to stay with square patches. The vast majority (if not all) of low pass filters designed and manufactured by the Cardiff team have a maximally flat, Butterworth style, response. These results indicate

that the current practice of keeping the patch corners as sharp as possible should not be changed.

The nature of the genetic algorithm, being a method driven by random numbers, does not guarantee that the optimal solution is found. Nor does it provide an indication whether any given solution is optimal. If the search space is visualised as a two-dimensional surface with hills, the aim being to find the top of the highest hill, the algorithm is good at finding the top of a hill. It also can jump between hills to avoid getting stuck on a local maximum although this effectively gets harder the nearer to the top of the highest hill the current hill is. But it can never know if it is on the highest hill. Running the algorithm multiple times can indicate the possibility of an optimal solution if the same solution is found each time. In the work reported here, the results were not significant enough to pursue multiple runs given the scarcity of compute cluster runtime available to the author.

3.2 The super-capacitive patch

The genetic algorithm is a reasonably effective method of searching a multi-dimensional parameter space. The search itself is not directed by any knowledge of the physical realities embodied by the genomes; only in the evaluation of the fitness function for each individual does this become relevant. Having obtained mixed results using this blind search method, the underlying physics of the operation of a low-pass filter using square patches was considered instead and a reasoned approach to improvements was tried. The work described in this section was published in Thompson et al¹¹⁴.

3.2.1 Increasing the capacitance of a patch

The property of the regular array of square patterns that controls the behaviour of the low-pass filter is the capacitance between adjacent patches, C , shown in Figure 3.12. Much like an electronics parallel plate capacitor, this capacitance is proportional to the length of the patch edges that run next to each other and inversely proportional to the gap between the edges. The manufacturing process used to produce the patches imposes a minimum feature size which defines a lower limit for the gap (this ranged from 1 to 10 μm for the processes available at Cardiff University). There is, therefore, a maximum possible capacitance for any chosen unit cell, g . Another way to increase the capacitance is to increase the size of the unit cell and thus the square patch, but this will tend to lower the frequency at which diffraction occurs.

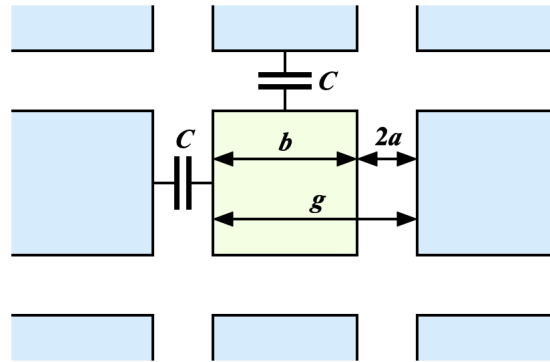


Figure 3.12. Capacitors and dimensions of a square patch mesh. The capacitances, C , between adjacent patches affect filter performance, the unit cell, g controls the diffraction limit.

A diffraction grating consists of a series of narrow slits at regular intervals, see Figure 3.13. A diffraction pattern appears on the right of the grating with peaks at angles θ_m (where m is an integer) given by the well know diffraction grating equation (for example Harvey and Pfisterer¹¹⁵)

$$\sin \theta_m = \frac{m\lambda}{d} \quad 3-1$$

where θ_m is the m th diffraction peak, λ is the wavelength and d is grating spacing. It can be shown that the first diffraction peak ($m = 1$, the main undiffracted peak is $m = 0$) appears when $\sin \theta_1 \leq 1$ and therefore when

$$\lambda \leq d. \quad 3-2$$

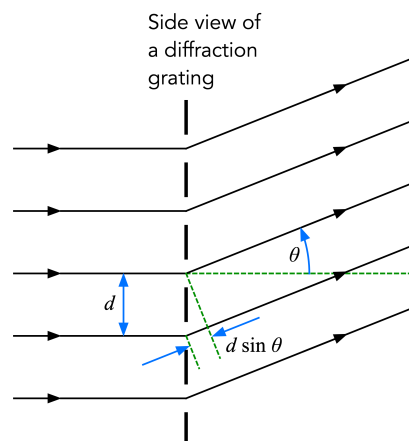


Figure 3.13. Diffraction grating and interference. Interference occurs between adjacent rays after the grating due to their differing path lengths ($d \sin \theta$). Maxima occur when the path length difference is an integer number of wavelengths.

The capacitive square mesh can be thought of as a pair of diffraction gratings one horizontal, one vertical (Figure 3.14). The unit cell, g , of the capacitive mesh therefore corresponds to the diffraction grating spacing parameter d . It follows that to avoid diffraction effects becoming significant, we must keep $\lambda \leq g$. Therefore, increasing the unit cell will consequently reduce the frequency at which diffraction causes problems.

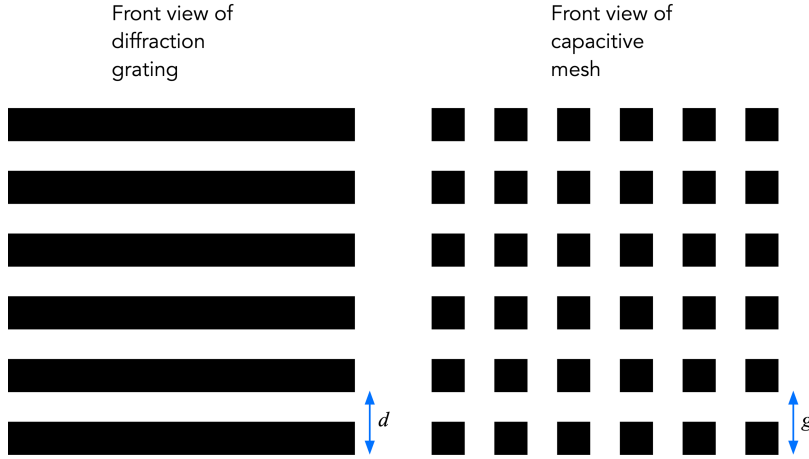


Figure 3.14. Capacitive mesh as a diffraction grating. The mesh acts as a diffraction grating both vertically and horizontally. The unit cell, g , is the equivalent of the diffraction grating's d parameter.

If the conventional shape is abandoned, the length of the adjacent sides can be increased, without changing the unit cell, by allowing finger-like protrusions to grow out of the square patch into sockets in the adjacent patch, a pattern that was named the super-capacitive patch, as shown in Figure 3.15. A version of this approach using a short finger was described by Zhang et al³⁹. The minimum feature size of the manufacturing process, d , defines the width of the fingers and the sockets into which they fit. Multiple fingers are possible, their maximum length diminishing as the socket into which they fit cannot be allowed to collide with a socket in the other direction.

The maximum length of the n th finger for a given unit cell, g , and minimum feature size, d , is given by

$$l_{n(max)} = g - (4n + 1)d . \quad 3-3$$

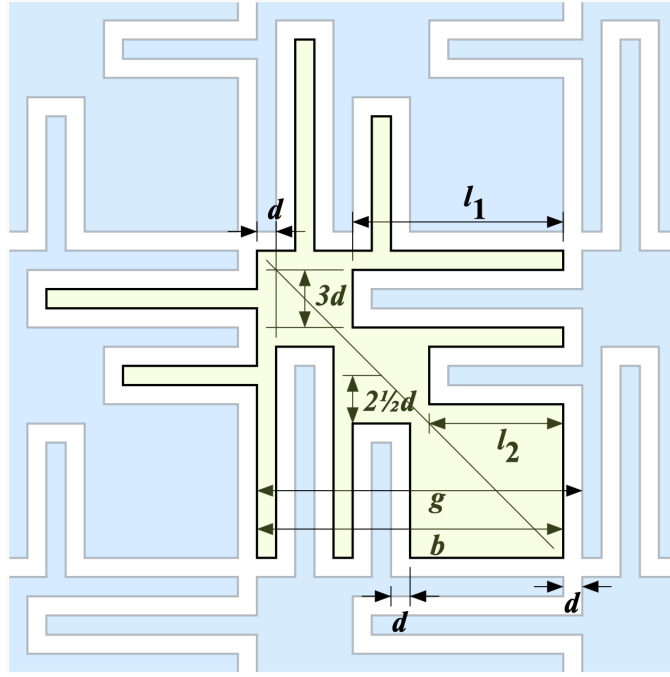


Figure 3.15. A super-capacitance patch with two fingers, horizontally and vertically, shown at their maximum extent to increase the capacitance between adjacent patches.

At this point it is noted that the pattern is no longer fourfold symmetric which can lead to the mesh behaving differently for different polarisations of incident light; an effect called birefringence. In a capacitive mesh, this comes about due to the capacitance encountered by different polarisations being different. Figure 3.16 shows a mesh with a square unit cell, g , containing rectangles with sides $b_x = 4g/12$ and $b_y = 10g/12$ and spacing between rectangles of $2a_x = 8g/12$ and $2a_y = 4g/12$. As explained previously, the capacitances are proportional to the length of adjacent patch edges and inversely proportional to the spacing between the edges. The capacitances (in arbitrary units) are therefore $C_x \propto b_x/a_y = 1$ and $C_y \propto b_y/a_x = 5/4$. A wave travelling in the z direction (out of the page) with x polarisation (its electric field oscillating in the x direction) will only see the C_x capacitors while a y polarised wave will only see the C_y capacitors. These effects are avoided with the super-capacitive patch because the capacitances in the two polarisations are identical due to the lengths of the adjacent patches in each direction being equal.

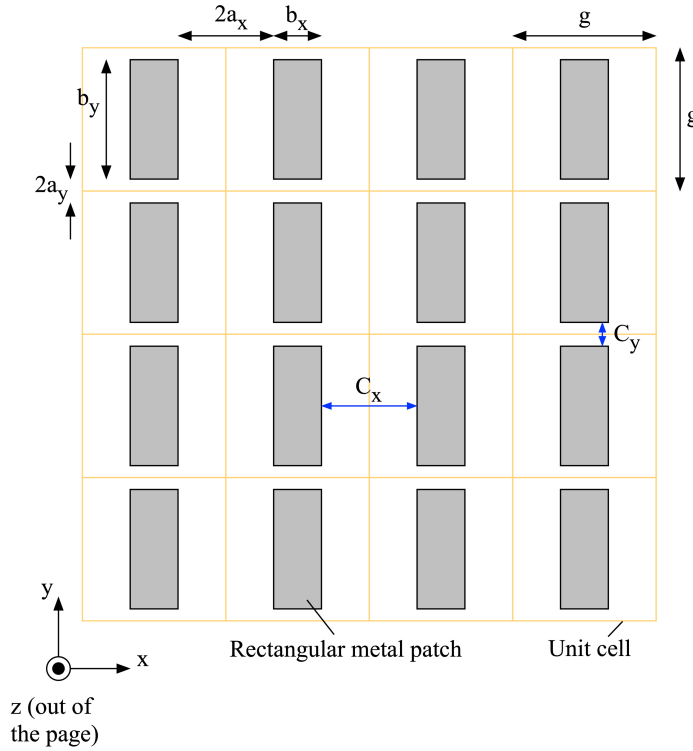


Figure 3.16. A birefringent mesh. The capacitance between the patches in the x and y directions (C_x and C_y) are different. This leads to the differing effects on waves (travelling in the z direction) polarised in the x and y directions.

3.2.2 Extending the progression

The super-capacitive patch can be used to extend the sequence of conventional capacitive square patches, see Figure 3.17. In a given unit cell, the sequence starts with a square patch of the minimum feature size (step 1 in the figure) and grows to a maximum square patch of unit cell size minus the minimum feature size (through step 2 to step 3). The first finger then starts to extend into the adjacent unit cell (step 4) and grows to its maximum size (step 5) when the neck between sockets falls to the minimum feature size. The second finger then starts to grow (step 6) up to its maximum length (step 7). Further fingers can then grow in turn (step 8), limited by the number of fingers that can be fitted in.

In order to make referring to patterns in this sequence easier, a parameter called the *patch ratio* was defined. It can be regarded as an extension of the method of identifying conventional square patches by the percentage of the unit cell they cover. It is given by

$$p = 100 \frac{b + \sum_{n=1}^N l_n}{g} \quad 3-4$$

where b is the size of the square part of the patch, N is the number of fingers, g is the unit cell size and l_n is the length of the n th finger. The patch ratio is roughly proportional to the capacitance between adjacent patches.

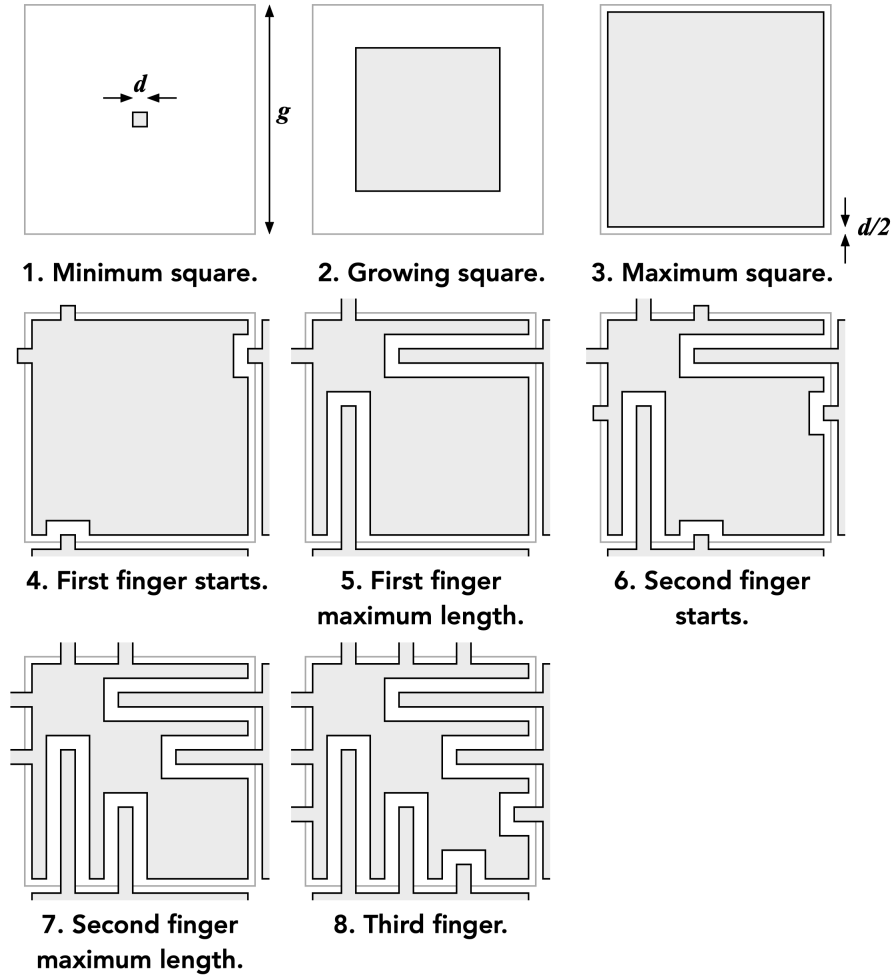


Figure 3.17. Sequence of square and super-capacitive patches.

The properties of an example set of these patterns with unit cell $g = 160 \mu\text{m}$ and minimum feature size of $d = 10 \mu\text{m}$ was investigated by modelling them using HFSS. This sequence starts with the minimum conventional square patch of $10 \mu\text{m}$ (patch ratio $p = 6$) rising to the maximum square patch of $150 \mu\text{m}$ ($p = 94$). The first finger then grows from its minimum length of $10 \mu\text{m}$ ($p = 100$) to a maximum of $100 \mu\text{m}$ ($p = 156$) followed by the second finger to $60 \mu\text{m}$ ($p = 194$). Finally, a third finger up to $20 \mu\text{m}$ ($p = 206$) can also be fitted in.

A selection of the transmittance and phase shift curves for this example sequence, embedded in polypropylene, are shown in Figure 3.18 and Figure 3.19 respectively. The diagrams mark four regions of interest.

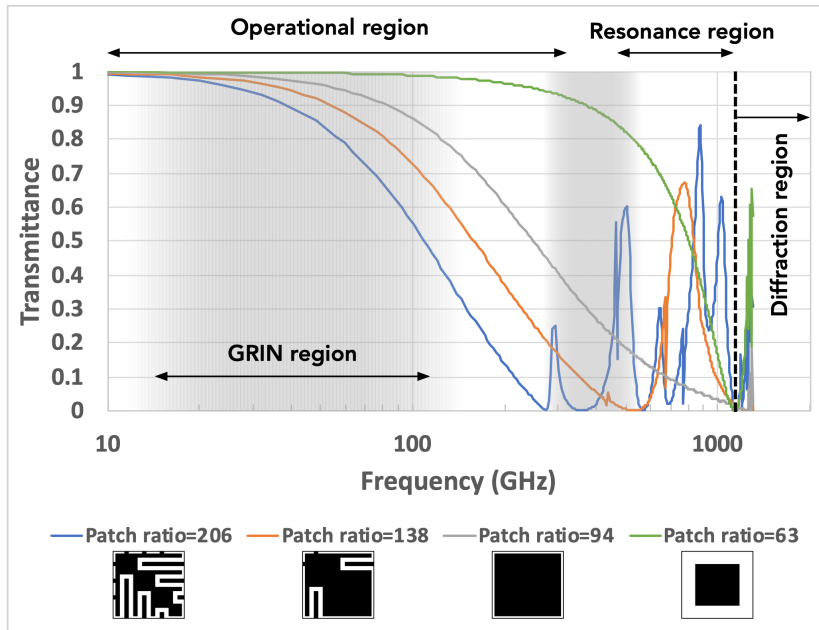


Figure 3.18. Transmittance curves of selected steps from the $g = 160 \mu\text{m}$ super-capacitive patch sequence.

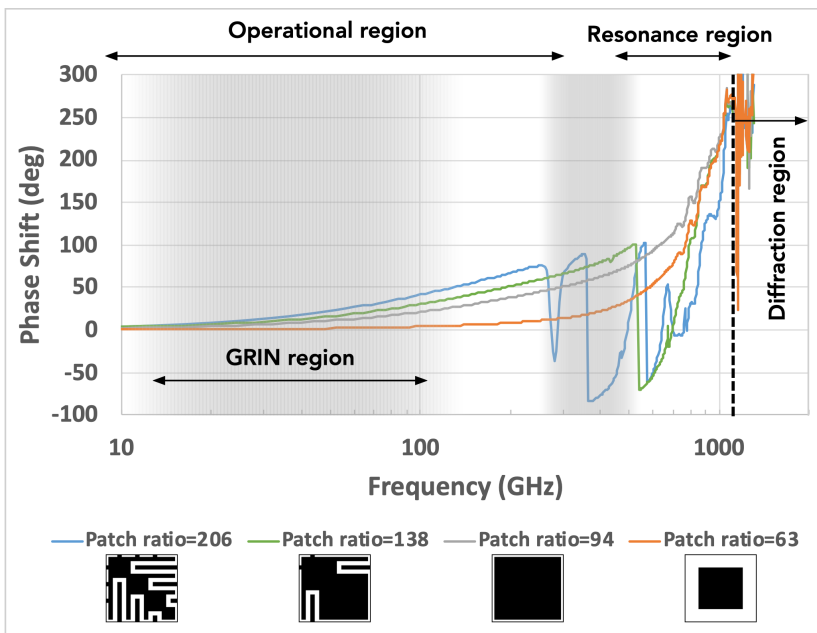


Figure 3.19. Phase shift curves of selected steps from the $g = 160 \mu\text{m}$ super-capacitive patch sequence.

The operational region covers the first part of the transmittance curve as it descends towards zero. The upper boundary of this region therefore varies with patch ratio. It can be seen that the curves for the patch ratio 138 and 206 super-capacitive patches in the operational region nicely extend the sequence that ends with the patch ratio 94 conventional square.

Between the operational region and the diffraction limit (around 1250 GHz for this example) is the resonance region. This region does not exist for the conventional square patches, the super-capacitive patch curves however display various transmittance peaks. This is not surprising as the patch pattern contains embedded features that are similar to shapes well known for resonant behaviour, the split ring resonators of Schurig et al¹⁴ for example. The precise details of these peaks appear to vary quite rapidly with the exact dimensions of the fingers, as a result, it will be shown that it is reasonably easy to suppress them in filter designs.

The diffraction region is the zone beyond the diffraction limit. This is the effective limit of the proper operation of devices made with these meshes. It is dependent only on the unit cell size as expressed in Equation 3-2.

In addition, a GRIN region is marked. This is generally the zone utilised for making the artificial dielectrics used in graded index lenses. A subject that will be returned to in section 4.3.5.

3.2.3 Making a filter

The observation that the super-capacitive patch can be regarded as an extension of a sequence of conventional capacitive square patches from a transmittance point of view raises the question of using them in filter designs. Will the super-capacitive patch characteristic have any useful properties that a filter can take advantage of?

The most apparent property is that the diffraction limit is at a much higher frequency than the first minimum in the transmittance curve. With a conventional square patch, the diffraction limit is reached shortly after this minimum. If a suitable set of patterns can be arranged to suppress the various resonances between the first transmittance minimum and the diffraction limit can be found, a low-pass filter with a large stopband may be possible.

Somewhat less obviously, the extended range of characteristics available may make it less necessary to use layers with differing unit cells. This is advantageous from an HFSS modelling point of view as it keeps the necessary model dimensions small. For example, consider a design that consists of two layers, one with a 400 μm unit cell the other with 500 μm . To model this in HFSS using periodic boundary conditions, a periodicity must be found that contains an integer number of unit cells for both layers. In this case, a 2000 μm period with the layers containing five and

four unit cells respectively. This leads to a much bigger model than might be otherwise expected, with increased computer memory requirements and run time.

To investigate, an existing low-pass filter following a standard design was chosen. Amongst other uses, this filter was employed in instrumentation mounted on the Atacama Cosmology Telescope, described by Fowler et al¹¹⁶ and by Swetz et al¹¹⁷. It consisted of six layers of square patch meshes embedded in polypropylene. The specification was for a low pass edge filter operating at 1 K for the 148 GHz telescope tube, with a cut off at 186 GHz, 200 dB/octave roll off and less than 0.2 dB ripple in the ultimate passband (138 to 158 GHz, defined by a subsequent bandpass filter). The resulting design was modelled here at ambient temperatures at which it has a cut off at 200 GHz. This is a real-world millimetre wave low pass filter design that is Butterworth like in the desired part of the passband but has significant ripple (cf. Chebyshev characteristics) at lower frequencies.

The genetic algorithm was used with the propagation matrix modelling method to search for solutions using super-capacitive patches with a minimum feature size of 12.5% of the unit cell in order to reduce attenuation in the passband. The admittance data used by the modelling method was derived from transmittance and phase shift data collected through HFSS modelling. The search was limited to three pairs of identical layers (six layers in total), all with the same unit cell size. The unit cell size itself, along with the three patch ratios and the layer spacing made up the dimensions of the search space. Like the existing filter, the layers were separated by polypropylene sheets of appropriate thickness.

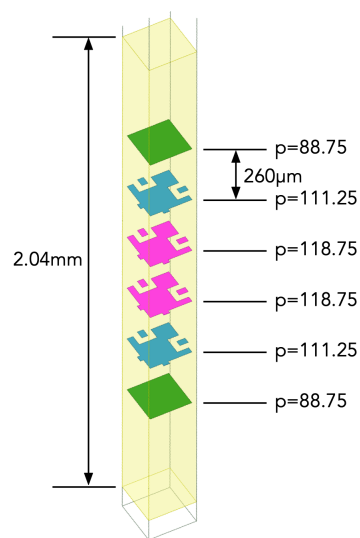


Figure 3.20. Super-capacitive low-pass filter model. A single unit cell of a super-capacitive patch design for a low-pass filter to reproduce the behaviour of the standard filter.

After more than 4300 generations, the genetic algorithm settled on the solution shown in Figure 3.20. This solution had been unchanged for the last 1500 generations so should be a reasonable design given the search constraints used. It consisted of layers with patch ratios of 88.75 (layers 1 and 6), 111.25 (layers 2 and 5) and 118.75 (layers 3 and 4) on a unit cell of $198\ \mu\text{m}$ with a layer spacing of $260\ \mu\text{m}$ (compared with the existing design's $400\ \mu\text{m}$ and $500\ \mu\text{m}$ unit cells and $240\ \mu\text{m}$ layer spacing). The polypropylene dielectric slab that the layers were embedded in was $2.04\ \text{mm}$ thick.

The resulting filter design was then modelled in HFSS. The transmittance characteristic, along with that of the standard low-pass filter, is shown in Figure 3.21. The conventional design has a stopband that goes to roughly $400\ \text{GHz}$ which corresponds to the diffraction limit. In contrast, the theoretical diffraction limit of the new design is beyond $1000\ \text{GHz}$ allowing a much larger stopband, although there is a small burst inside it where the resonance region is incompletely suppressed. Further work is necessary to confirm the diffraction limit is at the frequency expected from the unit cell size. However, the shape of the passband of the new design is a little compromised when compared with the standard design.

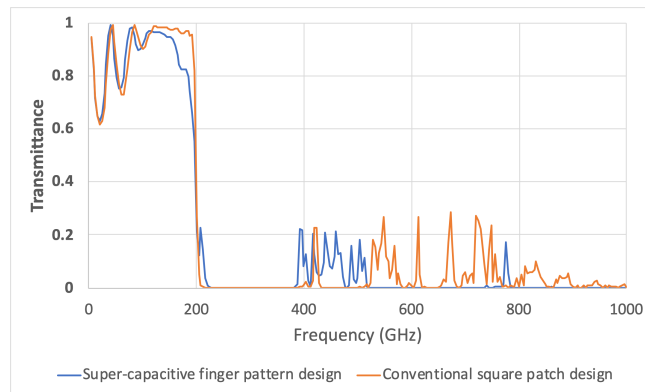


Figure 3.21. Super-capacitive low-pass filter transmittance. Transmittance curves of low-pass filters implemented using square patches and super-capacitive patches. The peaks in the stop band from around $400\ \text{GHz}$ upwards are due to resonances that have not been completely suppressed for the super-capacitive patch filter as opposed to diffraction for the square patch filter.

3.2.4 Conclusions

It was shown that growing fingers into the adjacent cell does indeed increase the capacitance of the pattern beyond that available from a conventional square patch. The resulting transmittance and phase shift curves raised the possibility of building a low-pass filter with a diffraction limit much further away from the filter roll off than

is usual with a square patch filter (for example, a diffraction frequency limit at more than twice that of an established conventional filter). Such an example filter was modelled and compared with an equivalent conventional filter and shown to be feasible. Further work is necessary to improve the roll off and suppress more signal in the stopband as well as to build and test an implementation. The approach shows promise as a method of increasing the useful frequency range of lowpass filters.

The super-capacitive patch is a much more complex shape than the squares that are normally made by the Cardiff group. However, the dimensional accuracy of the process used is easily sufficient to accurately create the examples that have been modelled, so there's a reasonable level of confidence that manufacturing won't significantly compromise their performance. The sharpness of the corners of square patches is something the group knows to be important to the performance of conventional filters and the manufacturing process is already geared towards achieving this. The further work of demonstrating the performance of a real-life device is still important though, to prove this confidence is not misplaced.

3.3 Pattern catalogues

The complete set of $N \times N$ binary plates used by the genetic algorithm in section 3.1 may be hiding some interesting characteristics and a searchable catalogue would be useful. However, the total number of patterns for useful values of N is rather large. Various strategies can be used to reduce this number to a manageable size to allow the FDTD modelling to be performed on a cluster computer in a sensible amount of time.

3.3.1 Symmetries

The most obvious method of reducing the number of patterns needing modelling to produce a catalogue is to employ symmetries, of which there are two broad kinds. The first symmetries discussed constrain the patterns that make up the catalogue. The second type avoid remodelling patterns whose characteristics can be inferred from an already modelled pattern.

The set of binary patterns evolved by the genetic algorithm in section 3.1 are required to be four-fold symmetric. For a 10×10 catalogue, this reduces the number of patterns to 32768. A more interesting set of patterns would be those that only have two-fold symmetry, which would include many with birefringent

characteristics. A 10x10 catalogue with this symmetry would contain $2^{25} = 33,554,432$ patterns. These two symmetries are shown for 10x10 patterns in Figure 3.22.

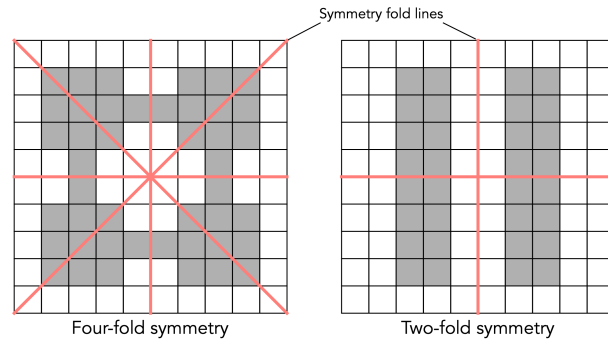


Figure 3.22. Four-fold and two-fold symmetries. Four-fold symmetries prevent any birefringent patterns.

Table 3.2. Pattern symmetries. Seven symmetries that can be used to avoid duplicate modelling of patterns that are equivalent.

	Symmetry	Example		Admittance Modification
a	Half a unit cell translation in the x direction			None
b	Half a unit cell translation in the y direction			None
c	Half a unit cell translation in both directions			None
d	90 degree rotation			Swap the x and y components
e	Half a unit cell x translation and a 90 degree rotation			Swap the x and y components
f	Half a unit cell y translation and a 90 degree rotation			Swap the x and y components
g	Half a unit cell translation in both directions and a 90 degree rotation			Swap the x and y components

Seven other symmetries were identified that can be used to avoid redundant modelling runs, detailed in Table 3.2. To a first approximation, they each reduce the number of unique patterns by nearly a factor of 2 (some patterns when translated remain unchanged). The first three symmetries (a, b and c) are pure translations that do not affect the characteristics of the patterns. The remaining four (d, e, f and g) involve a rotation that requires the x and y components of the complex admittance to be swapped.

3.3.2 A 10x10 four-fold symmetrical catalogue

As a proof of concept, a catalogue of the 32768 10x10 binary patterns with four-fold symmetry was created using the Hawk cluster, taking approximately 5½ days using 16 nodes each with 40 cores. The FDTD model was run using four FDTD cells per binary pattern pixel and an 800 μm unit cell. The complex admittance was recorded for each pattern in the frequency range 2 to 400 GHz at 2 GHz steps. The transmittance and phase shift data derived from this is presented in Figure 3.23 for four of the patterns. The frequency axis has been generalised by expressing the wavelength as a fraction of the unit cell.

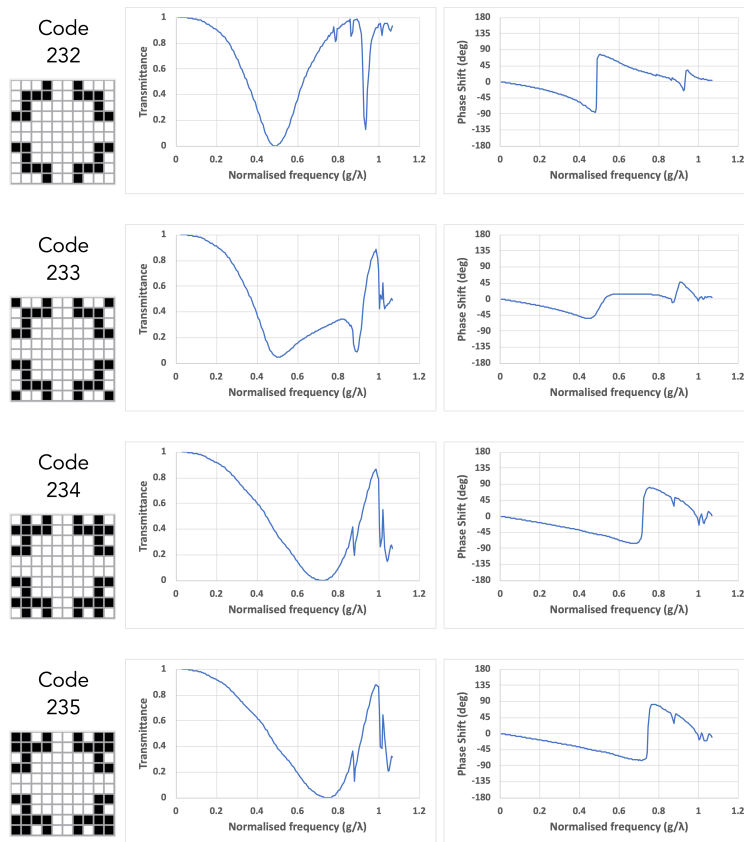


Figure 3.23. Four-fold 10x10 binary pattern catalogue, four consecutive patterns. The transmittance information can help with the choice of patterns for filters while the phase shift indicates how waves are delayed.

For access information and the details of the format of the full catalogue see Appendix C.

3.3.3 Classifying the patterns in a catalogue

Making sense of the behaviour of the patterns within a catalogue is an issue given the number of entries. Some method of sorting the patterns according to the shapes of the admittance curves could make the catalogue more useful by making it easier to browse. Figure 3.24 shows the transmittance for a set of inductive patterns that provide a progressive sequence of curves that was assembled by hand. Manually sorting a whole catalogue (32768 patterns in the four-fold 10x10 catalogue for example) would be quite a task; an automated approach would be better.

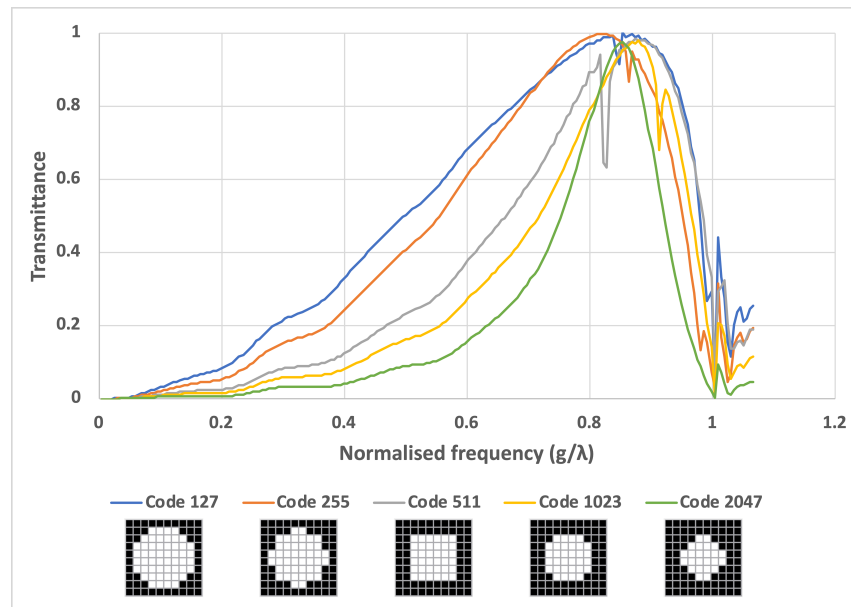


Figure 3.24. A sequence of inductive patterns from the four-fold 10x10 binary pattern catalogue. These patterns are small variations on the conventional square hole inductive grid that provide a reasonable progression of transmittances.

An attempt at an automated classification involved fitting the fifth order polynomial

$$y = fx^5 + ex^4 + dx^3 + cx^2 + bx + a \quad 3-5$$

to each transmittance curve and using the resulting coefficients (a to f) to sort the patterns into bins. The method employed for splitting the six-dimensional coefficient space into bins was quite crude. The space was initially linearly split into $4 \times 4 \times 4 \times 4 \times 4 \times 4$ hypercubes. Bins that were then found to be empty were discarded while those that had more than 3000 entries were further split into

4x4x4x4x4 smaller hypercubes. This was repeated until no bin had more than 3000 entries. This resulted in the 32768 patterns of the four-fold 10x10 catalogue being sorted into 117 bins.

The results of the sorting were a little mixed but showed promise. Two example bins are listed in Table 3.3 both containing eight patterns. The transmittance curves of the patterns in bin 54 all conform to the same basic shape consisting of two maxima, shown in Figure 3.25. In an ideal scenario, pattern codes 14885 and 23078 should maybe not be classified in this bin.

Table 3.3. Two example fitted polynomial classification bins.

Id		a	b	c	d	e	f
24	min	-1	0	0	0	0	-5×10^{-51}
	max	0	5×10^{-11}	5×10^{-21}	1×10^{-30}	5×10^{-41}	0
54	min	0.5	-5.10^{11}	0	1.25×10^{-21}	0	-1.25×10^{-51}
	max	0.75	-3.75×10^{-11}	1.25×10^{-21}	7.96×10^{-22}	1.25×10^{-41}	2.97×10^{-67}

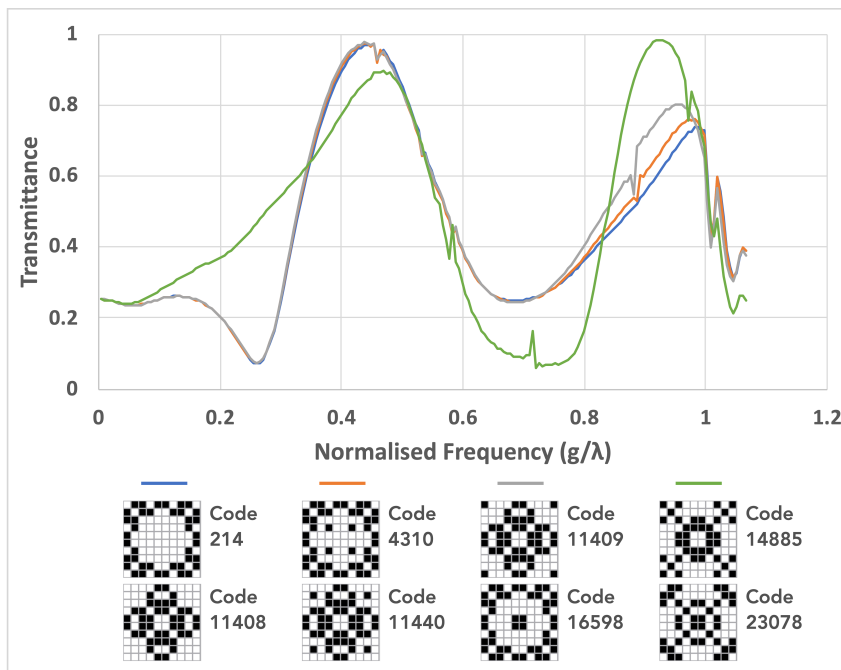


Figure 3.25. The transmittance curves from classification bin 54 containing eight four-fold 10x10 patterns. In this bin pairs of patterns have transmittance curves that completely overlay each other and are therefore plotted as single curves.

Figure 3.26 shows the transmittance curves for four patterns assigned to classification bin 24. This collection is somewhat less coherent; pattern codes 13938 and 18393 are very similar, code 127 is less so but could still belong with them, however pattern code 3450 is very different.

Fitted polynomials do show promise as a method of classification but the boundaries between the bins requires more investigation which remains as further work.

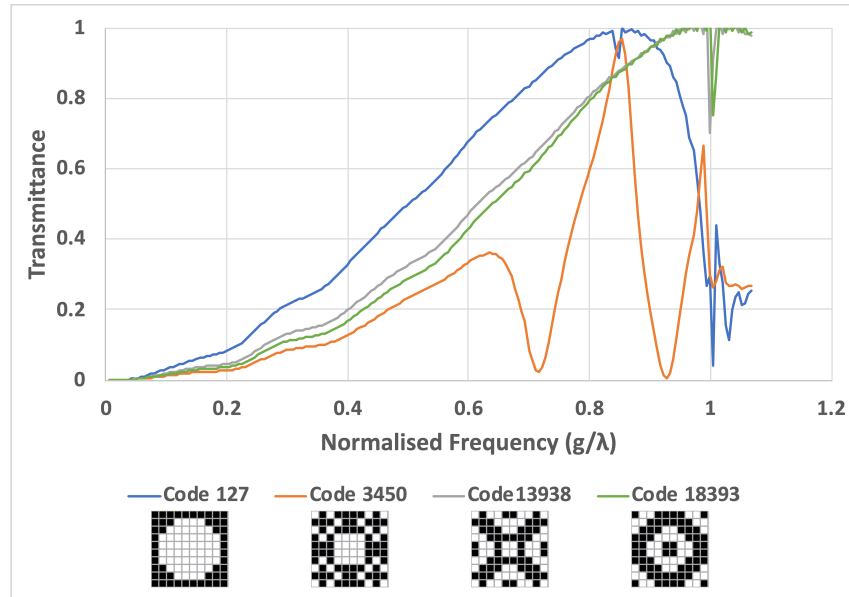


Figure 3.26. Transmittance curves from classification bin 24 containing four four-fold 10x10 patterns.

3.3.4 Corner-to-corner pixels

The four-fold 10x10 catalogue described above contains many patterns with pixels that are only touching at their corners, one such is shown in Figure 3.27. The question is: are these pixels touching or not? The answer critically affects any currents that may be flowing and, in some cases, could change the overall nature of the pattern between inductive and capacitive.

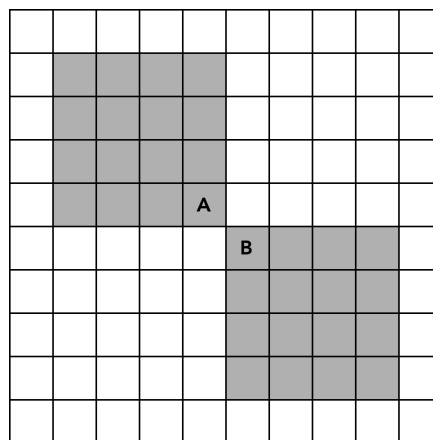


Figure 3.27. Corner-to-corner pixels. A 10x10 binary pattern containing two pixels (marked A and B) that are touching only at their corners.

To investigate how different modelling methods treat corner-to-corner pixels, the patterns shown in Figure 3.28 were modelled in both FDTD and HFSS. In (a), the figure shows the large black squares touching corner-to-corner. In (b) the squares have corners removed so that they clearly do not touch. Finally, in (c) the squares are made to connect with little bulges at their corners. The patterns were modelled using periodic boundary conditions in a $960\ \mu\text{m}$ unit cell.

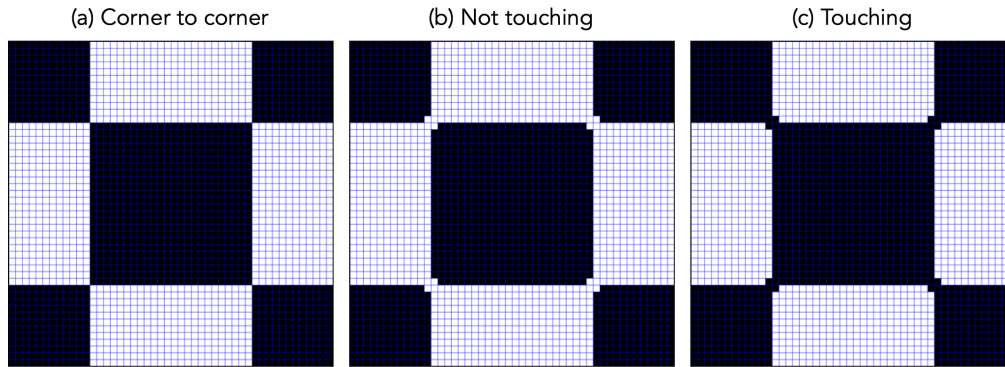


Figure 3.28. Corner-to-corner pixel test patterns used in the investigation. The large squares are touching or not depending on pixels added or removed from the pattern.

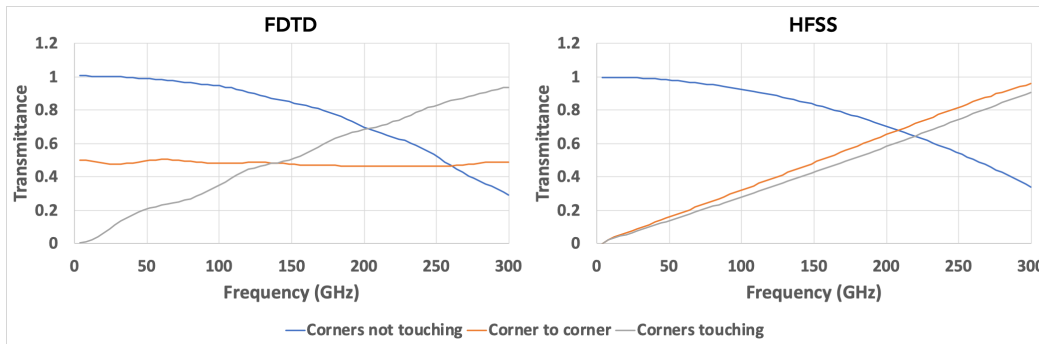


Figure 3.29. Transmittances for the corner-to-corner test patterns calculated by FDTD and HFSS.

The transmittances calculated from the two modelling methods are shown in Figure 3.29. The touching and not touching cases show obvious inductive and capacitive curves in both FDTD and HFSS. The corner-to-corner pattern is, however, treated differently by the two methods. In HFSS the two squares are considered to be touching; the curve has the characteristics of an inductive pattern. The FDTD method has produced a curve that is halfway between capacitive and inductive, it has made an attempt at handling the corner-to-corner case that is neither connected nor disconnected.

Considering the manufacture of metamaterial meshes incorporating corner-to-corner pixels like this, a problem is immediately apparent. It is going to be pretty much impossible to reliably reproduce the exact corner-to-corner effect. In all cases, the corners will be completely connected or completely disconnected; probably pseudo-randomly depending on the exact details of the manufacturing process. Measuring real devices will therefore always produce curves corresponding to connected or disconnected corners and never the corner-to-corner curve that FDTD reports. In addition, to achieve consistent results it is important to either deliberately connect or disconnect the corners during modelling and manufacturing.

Manufacturing limitations, combined with the modelling uncertainty, is leading to the conclusion that patterns with corner-to-corner pixels can be omitted from the catalogue. This will have an enormous effect on the number of patterns that need to be modelled to complete a catalogue as there will be large numbers of corner-to-corner cases.

3.3.5 A 10x10 two-fold symmetric catalogue

Taking the symmetries of Table 3.2 and the corner-to-corner pixel conclusion into account, a catalogue of 10x10 binary patterns with two-fold symmetry becomes feasible. The total number of patterns would be $2^{25}=33,554,432$. Removing all the patterns with corner-to-corner pixels reduces this to 5,735,478. Using the symmetries will leave approximately 45,000 unique patterns that require modelling. The FDTD models were again run on the Hawk cluster computer provided by the Supercomputing Wales project.

Figure 3.30 shows the transmittance and phase shift curves for three of four consecutive patterns. Due to the two-fold symmetry, these patterns will generally have a birefringent response, the x and y components of the complex admittance have therefore been recorded. The fourth pattern (code 221) has not been modelled due to having corner-to-corner pixels.

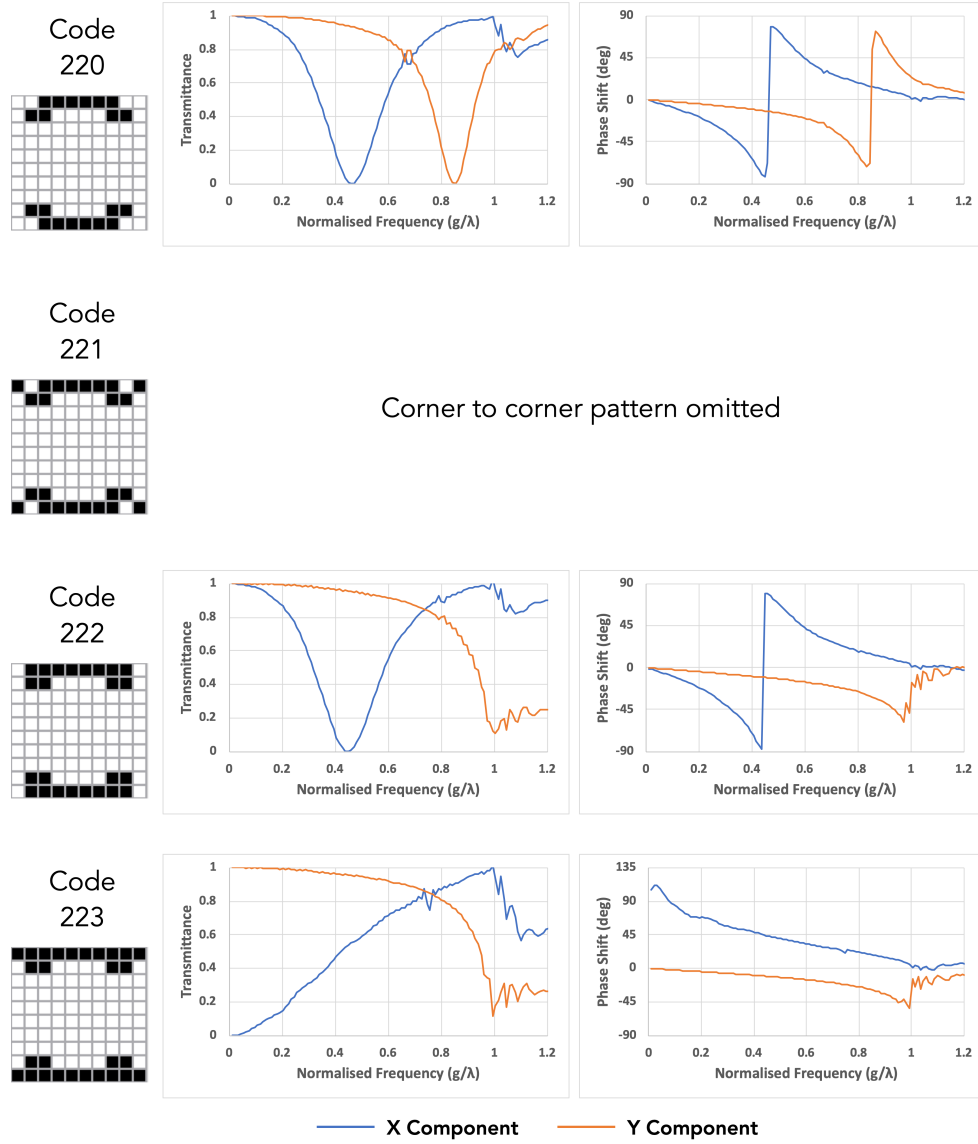


Figure 3.30. Two-fold 10x10 binary pattern catalogue, four consecutive patterns. Patterns with corner-to-corner pixels were not modelled.

One question that occurs is whether the two components of birefringent patterns could be modelled separately by converting each two-fold pattern into a pair of four-fold patterns. This would drastically reduce the number of patterns that would need to be modelled to generate a catalogue ($2m$ rather than m^2 , where m is the number of patterns visible to one component). It is not obvious to this author how this could be done, so it will remain as further work.

For access information and the details of the format of the full catalogue see Appendix C.

3.3.6 Using the catalogue data

The catalogues described in sections 3.3.2 and 3.3.5 provide complex admittance data for each pattern in the set. This data is suitable for use with the propagation matrix method which can therefore be used to investigate the properties of multi-layer structures made from these patterns.

As a demonstration, a pair of layers were chosen from the four-fold symmetric catalogue, the catalogue entries shown in Figure 3.31. These patterns and their associated complex admittance data were loaded into the FDTD modelling tool as two layers on an 800 μm unit cell with a layer spacing of 400 μm . The same model was also constructed in HFSS. All three modelling methods were then run: propagation matrix method, FDTD and HFSS.

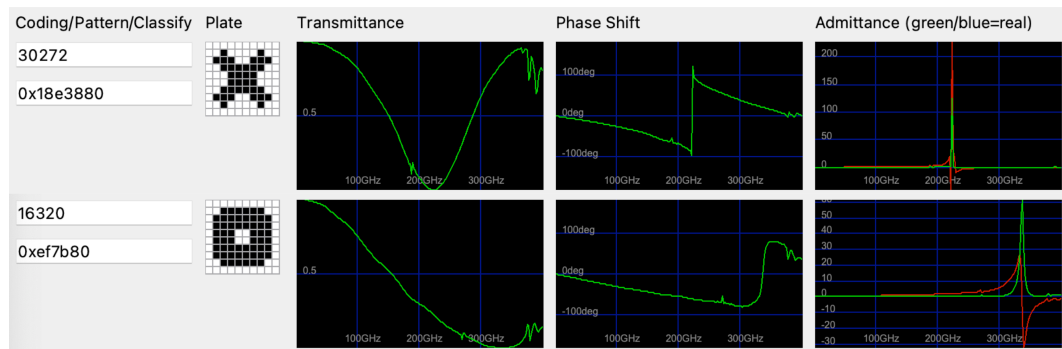


Figure 3.31. The chosen four-fold patterns for the usage test. Patterns without corner-to-corner pixels were chosen to avoid modelling comparison difficulties.

The results are shown in Figure 3.32 (alongside a view of the layers in HFSS). The propagation matrix method ran in less than one second, the FDTD and HFSS run times were both around 10 minutes. The results, both for transmittance and phase shift, are all remarkably similar clearly indicating the usefulness of the catalogue in the rapid assessment of potential pattern combinations with the propagation matrix method.

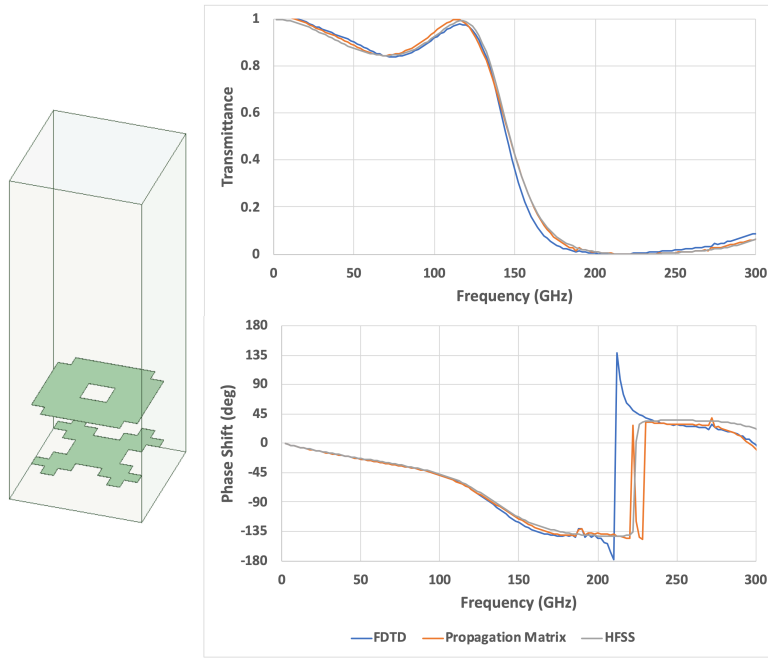


Figure 3.32. Two four-fold pattern verification. The three modelling methods agree except for the phase shift from 200 to 250 GHz where the transmittance is around zero. A view of the model in HFSS is shown on the left.

3.3.7 Conclusions

Using the Hawk cluster provided by Supercomputing Wales, catalogues of 10x10 binary patterns with both four-fold and two-fold symmetry were produced and are available for use (see Appendix C). In the two-fold case, this was made feasible by omitting all patterns containing pixels that only touched at their corners; patterns that are extremely difficult, if not impossible, to manufacture. A method of classifying patterns by their response was attempted, but a properly useful system remains as further work. The use of the propagation matrix modelling method with the catalogue data was demonstrated.

Chapter 4

Lenslet design

The main aim of the work reported by this thesis was to improve the design of meta-material lenslet arrays such as those described in Pisano et al.⁷⁸ in ways that might increase their performance or make them easier to manufacture. The improvements presented are widely applicable but were developed with two lenslet specifications in mind, one using a polypropylene dielectric and one using silicon, shown in Table 4.1.

Table 4.1. The specifications of the example lenses that were the focus of the lenslet design work reported in this chapter.

Dielectric	Polypropylene	Silicon
Diameter	6.3 mm	6.3 mm
Center frequency	200 GHz	150 GHz
Bandwidth	200 GHz	100 GHz
Focal length	2 mm	2 mm
Minimum layer spacing	10 μm	100 μm
Minimum feature size	10 μm	2 μm

These lenslets were chosen as proofs of concept and are typical of those employed in lenslet arrays intended for use in the focal plane of CMB instruments. The detection of B-mode polarisation, as introduced in section Chapter 1, requires very sensitive instrumentation and therefore components that impose the minimum of loss and distortion on the signal. As the device that collects the light onto the detectors, the lenslet array is important in this respect. The lenslets must collect light and focus it onto the detectors with as little chromatic aberration and radial distortion as possible.

To reduce the effects of thermal noise, CMB instruments operate at cryogenic temperatures, for which a lenslet using a silicon substrate is most appropriate. A polypropylene based lenslet design was also produced with the intention of using the in-house manufacturing facilities to make them. While polypropylene devices have been used at temperatures of a few Kelvin, thermal contraction problems

make silicon a better choice. It will be seen, however, that the significant difference in the refractive index of the two dielectrics has a major effect on the design.

The stacks of metal mesh grids that are used to implement the artificial dielectrics also act as low pass filters and therefore attenuate the signal above a cut-off frequency. Hence it is important to arrange for this cut-off frequency to be above the desired operating frequency band of the lens. A method of assessing this effect is discussed along with the associated limits on the lens design.

The manufacturing processes available imposed the minimum feature sizes listed in the table. The minimum feature size affects a number of design decisions and limits what can be achieved. Ways of overcoming these limits are also explored.

4.1 Simple path length lenslet design method

To design an operating metamaterial lenslet, the paths taken by light on its journey through the device must be considered. Considering rays starting at the focus and travelling through the lens, the structure must apply sufficient phase shift for them all to emerge from the lenslet in parallel. This also means, due to the reversibility of light, that the phase shift applied is enough to converge parallel light rays to the same focus. The simplest approach, that assumes all the ray bending occurs at the start of the metamaterial zone, is shown in Figure 4.1. Many authors, for example Nguyen et al.⁶³, Chen et al.⁵⁹ and Tao et al.¹¹⁸, used a method like this in their work. It is most appropriate for devices that are thin ($b < \lambda$) where the ray bending assumption is relatively accurate.

The figure also shows another feature of all the lenslets considered; the focus point is designed to be at the surface of the dielectric that carries the metamaterial grids. This allows an antenna to be constructed on this surface and eliminates one dielectric boundary the light must travel through. The dielectric boundary through which the parallel rays pass is still present however and must be accounted for.

The focal length, d , is 2 mm for these example lenses, leading to a relatively small f-number of 3.15. This is due to the sinuous antennas the design is intended for. These are small (around 1 mm in size) and have a wide main lobe which implies the lens must be positioned close to match. This does make the lens design a little more challenging.

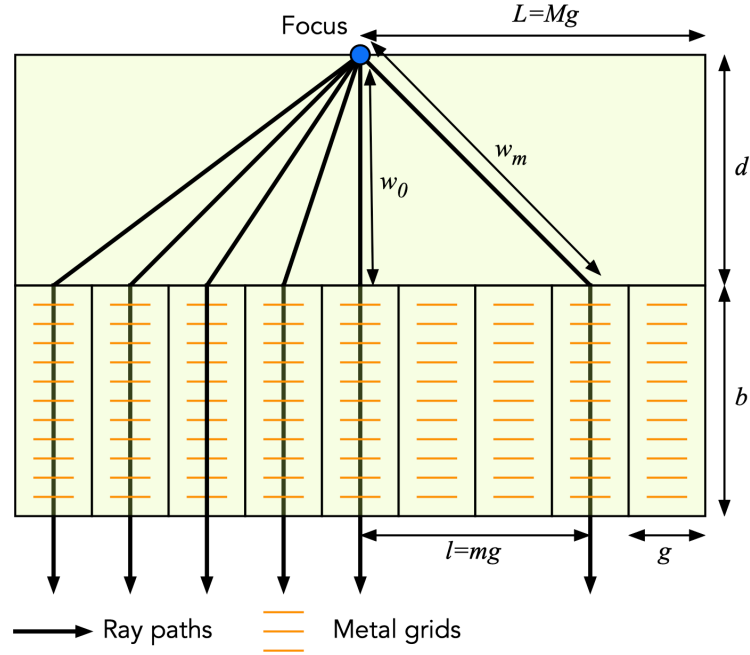


Figure 4.1. Simple path length design model. Light ray paths through the lenslet assume all the ray bending occurs at the start of the structure.

The phase of each ray, ϕ_m , with a wavelength in the dielectric, λ_d , as it reaches the top of the metamaterial column, m , is calculated by considering the path length, w_m . This is given by:

$$\phi_m = \frac{2\pi w_m}{\lambda_d}. \quad 4-1$$

Using simple geometry, this becomes:

$$\phi_m = \frac{2\pi\sqrt{d^2 + l^2}}{\lambda_d}. \quad 4-2$$

The phase shift that each metamaterial column must then add to its ray consists of the phase shift due to the column length of the dielectric, b , plus an extra phase shift (which the metamaterial grid will generate) to bring its ray into line with that of the outer column (the M th). This is given by:

$$\Delta\psi_m = \frac{2\pi b}{\lambda_d} + (\phi_M - \phi_m). \quad 4-3$$

Using equation 4-2 to substitute for ϕ_M and ϕ_m gives

$$\Delta\psi_m = \frac{2\pi b}{\lambda_d} + \left(\frac{2\pi\sqrt{d^2 + L^2}}{\lambda_d} - \frac{2\pi\sqrt{d^2 + l^2}}{\lambda_d} \right). \quad 4-4$$

Simplifying this becomes

$$\Delta\psi_m = \frac{2\pi(b + \sqrt{d^2 + L^2} - \sqrt{d^2 + l^2})}{\lambda_d}. \quad 4-5$$

The wavelength of the ray inside the metamaterial column (λ_e) is calculated using:

$$\Delta\psi_m = \frac{2\pi b}{\lambda_e}, \quad 4-6$$

which leads to

$$\frac{2\pi b}{\lambda_e} = \frac{2\pi(b + \sqrt{d^2 + L^2} - \sqrt{d^2 + l^2})}{\lambda_d}. \quad 4-7$$

Simplifying

$$\frac{\lambda_d}{\lambda_e} = \frac{\sqrt{d^2 + L^2} - \sqrt{d^2 + l^2}}{b} + 1, \quad 4-8$$

then using $\lambda = v/f$ this becomes

$$\frac{v_d}{v_e} = \frac{\sqrt{d^2 + L^2} - \sqrt{d^2 + l^2}}{b} + 1. \quad 4-9$$

The refractive index of a medium is given by $n = c/v$, the ratio of the velocity of light in vacuum and the velocity of light in the medium. Multiplying both sides by the refractive index of the dielectric:

$$\frac{v_d}{v_e} \frac{c}{v_d} = n_d \left(\frac{\sqrt{d^2 + L^2} - \sqrt{d^2 + l^2}}{b} + 1 \right) \quad 4-10$$

which is the desired effective refractive index of the column:

$$n_e = n_d \left(\frac{\sqrt{d^2 + L^2} - \sqrt{d^2 + l^2}}{b} + 1 \right). \quad 4-11$$

This can be used to calculate the maximum refractive index required (which will be in the centre column) by setting $l = 0$.

$$n_{e,max} = n_d \left(\frac{\sqrt{d^2 + L^2} - d}{b} + 1 \right). \quad 4-12$$

Equation 4-11 defines the required refractive indices for each column of the lens structure. These will be provided by artificial dielectrics consisting of layers of metal mesh embedded in the base dielectric (silicon or polypropylene) with appropriate unit cell and layer spacing. How these are selected will be investigated in section 4.2.1.

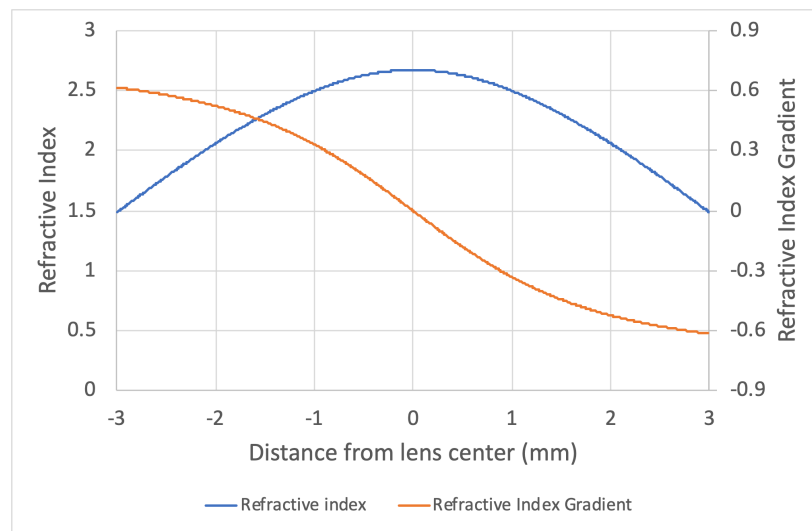


Figure 4.2. Variation of refractive index across a lens. This plot also shows how the refractive index gradient varies across the lens.

Figure 4.2 shows how the refractive index and refractive index gradient varies across the lens. The data for this plot was calculated from equation 4-11 using a column width of $10 \mu\text{m}$ to approximate a continuously changing refractive index. Although the refractive index at a particular point of the lens is important for determining the phase shift applied, it is the refractive index gradient that causes a wave to bend as different parts of the wavefront get different phase shifts.

4.1.1 Focal length compensation factor

This simple model of GRIN lenslet behaviour does have a number of shortcomings that lead to inaccurate results when the wavelength of the light passing through the structure is much shorter than the lenslet thickness. Lenslets designed with it

can show an amount of over-focussing, especially towards the edges, as the assumption that all the bending occurs at the lenslet boundary is violated. The reasons for this will be explored later in section 4.9, but they can successfully be accounted for using an empirically found compensation factor applied to the desired focal length.

A simple numerical factor applied to the desired focal length before the calculations for the column refractive indices will compensate for the mis-focussing of the simple model. A factor larger than one will move the focus away from the lens structure, smaller than one will move it towards. The actual value of compensation factor to use will be found by iteratively by running the HFSS model on designs generated using different values, homing in on the value that results in the desired far field pattern.

Depending on how much chromatic aberration is present in the lens structure, the compensation factor may also be frequency dependent. It should therefore be determined at the specified centre frequency of the design. The reduction of chromatic aberration itself is addressed by the choice of artificial dielectric, see section 4.2.1.

The values of compensation factor required to produce the desired focus can also be used as a measure of the success of a particular design model. A design model that requires a compensation factor of exactly one is the ideal, indicating the model accurately considers how light travels through the lens structure. Some modifications to the design model are described in section 4.9, but further work is necessary in this area.

4.2 A note on HFSS modelling

The commercial Ansys HFSS modelling package that was introduced in section 2.3 was used for all the modelling reported in this chapter. To enable this modelling to be undertaken on the desktop PC available to the author, methods of minimising the required computer resources were employed. These are described here.

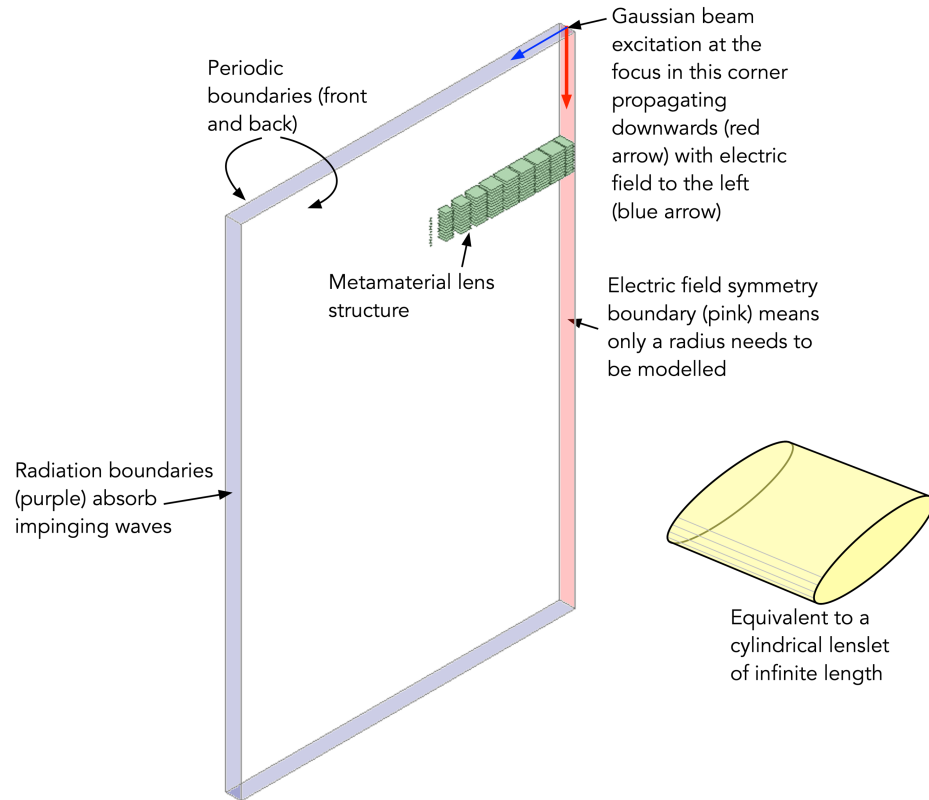


Figure 4.3. Initial HFSS modelling of metamaterial lenslet structures to minimise memory and execution time. The periodic boundaries make this an infinitely long cylindrical lenslet.

The modelling of lenslet designs using Ansys HFSS was split into two parts for this work. During the initial design and optimisation stages, a slice along the radius of the lenslet one metamaterial unit cell wide, was modelled (see Figure 4.3). Periodic boundary conditions on the front and back surfaces effectively make this a model of an infinitely long cylindrical lens as shown. The top, bottom, and left edges are assigned to be radiation boundaries, these (like the CPML perfectly matched layers of FDTD) absorb waves that reach them, simulating empty space extending outwards. Finally, the boundary on the right is marked as symmetrical. This causes the model to act as though a mirror image of the scene exists to the right of the boundary. Symmetrical boundaries must be marked electric or magnetic, depending on which field of the wave is normal to it, in this case electric. This approach minimises the size of the model, thus lowering the memory requirements and shortening the processing time, such that the models may be run on a standard desktop computer with just 32 gigabytes of RAM installed.

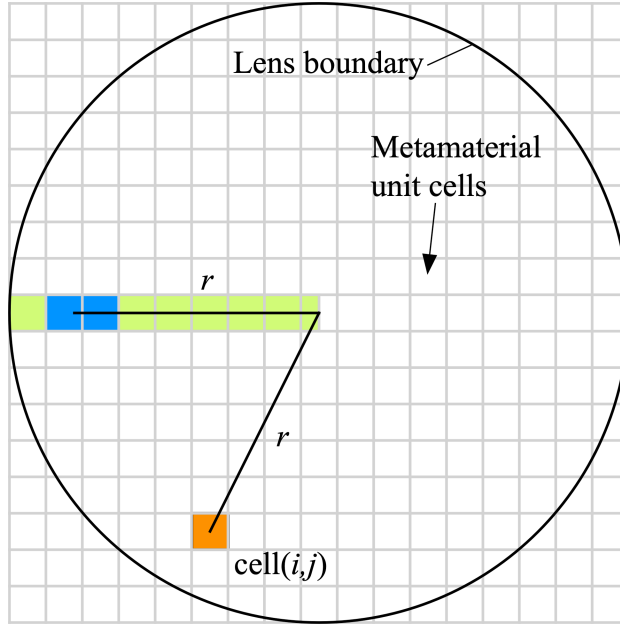


Figure 4.4. Extrapolating a lenslet radial stripe (in green) to a complete circle for a layer. This is a view of a layer looking from the top down, the green stripe corresponding to the metamaterial lens structure of Figure 4.3.

Once a satisfactory lenslet slice is found, the design along the radius is extrapolated to all the other cells that each lenslet layer covers as shown in Figure 4.4. This is a view of one of the layers in the metamaterial lens structure from above, the green cells corresponding to one of the green layers of Figure 4.3. The distance, r , from the centre of the lenslet to the centre of each target cell is calculated. The two adjacent cells at this radius on the diameter are then found and the target refractive index and (when required) incidence angle interpolated from them. A catalogue of capacitive patches and their refractive index (described later in section 4.6) was then used to find the patch ratio required for each cell. This is repeated for each layer to complete the lenslet. The full 3D lenslet can then be simulated in Ansys HFSS. The memory footprint of this simulation can be reduced by modelling just one quadrant of the lens using symmetry boundaries, one electric and one magnetic. Even this did not allow the model to run on the machine available to the author, leaving this step as further work.

4.2.1 Gaussian beams

The lenslet models were excited by placing a Gaussian beam at the intended focus point as shown in Figure 4.5. The beam waist, w_0 , was chosen such that the width as it encounters the lenslet structure, w_f , fills the lenslet.

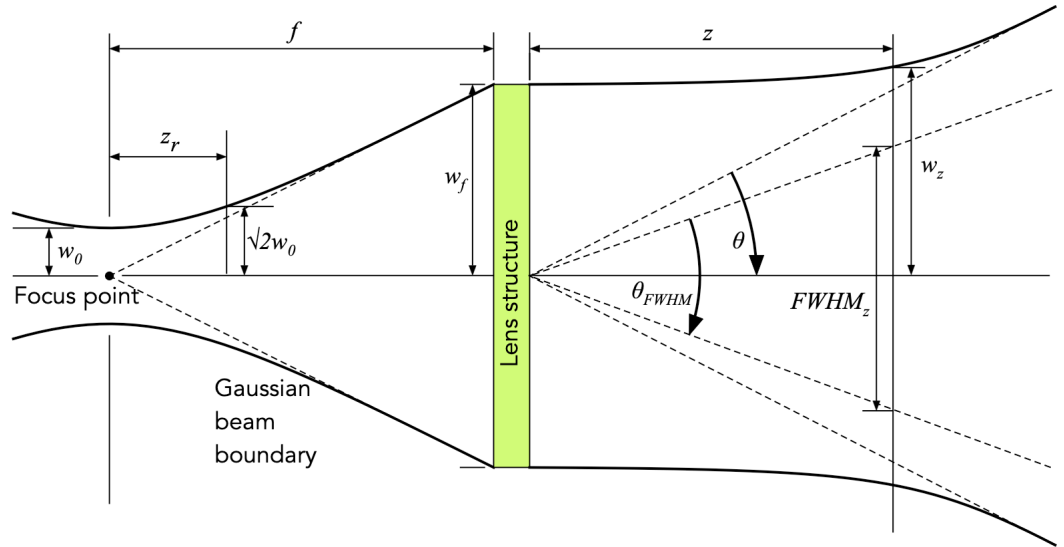


Figure 4.5. Gaussian beam at lenslet focal point.

The beam width, $w(z)$ of a Gaussian beam at a distance, z , is given by

$$w(z) = w_0 \sqrt{1 + \left(\frac{z}{z_r}\right)^2} \quad 4-13$$

where z_r , the Rayleigh range (the point at which the beam width is $\sqrt{2}w_0$), is given by (n is the refractive index of the medium and λ is the free space wavelength)

$$z_r = \frac{\pi w_0^2 n}{\lambda}. \quad 4-14$$

Using these equations, it can be shown that

$$w_0^2 = \frac{w(z)^2 \pm \sqrt{w(z)^4 - 4 \left(\frac{z\lambda}{\pi n}\right)^2}}{2} \quad 4-15$$

which allows the required beam waist to be calculated given the desired beam width at distance z . It should be noted that these standard Gaussian equations deal in a beam width expressed as a radius, the Ansys HFSS tool requires the beam waist diameter, $2w_0$.

When the lenslet is focussing correctly, the beam emerges from it as another Gaussian with a beam waist equal to the lenslet radius. The beam angle is given by

$$\theta = \frac{\lambda}{\pi n w_0}. \quad 4-16$$

Using the far field data that Ansys HFSS collects, the beam angle for the full width, half maximum (θ_{FWHM}) can be measured. This is related to the beam angle, θ , by

$$\theta_{FWHM} = \theta \sqrt{2 \ln 2}. \quad 4-17$$

The correct behaviour of a lenslet can therefore be assessed by comparing the expected full width, half maximum, beam angle with that measured from the modelling.

4.3 Artificial dielectrics

The use of closely spaced capacitive grids to produce an artificial dielectric with a designed refractive index was described by Zhang et al.³⁶ This technique can be used to provide cells with the effective refractive indices derived in the previous section for each column in a graded index lenslet. To allow the selection of the correct configuration of artificial dielectric for each column of the lenslet, a method of extracting the bulk parameters of a structure (the refractive index, electric permittivity, magnetic permeability etc.) from modelling results is required. This section describes three methods before choosing one for use in building a refractive index catalogue.

4.3.1 Measuring the phase velocity

The obvious method of finding the refractive index of any dielectric (artificial or otherwise) is to measure the phase velocity, v , of the wave passing through it and then calculate the refractive index directly from $n = c/v$. The phase velocity can be derived from a measurement of the phase shift through the structure. Consider a block of the dielectric, length L_m , to be measured in a modelling domain of size L_d , as shown in Figure 4.6.

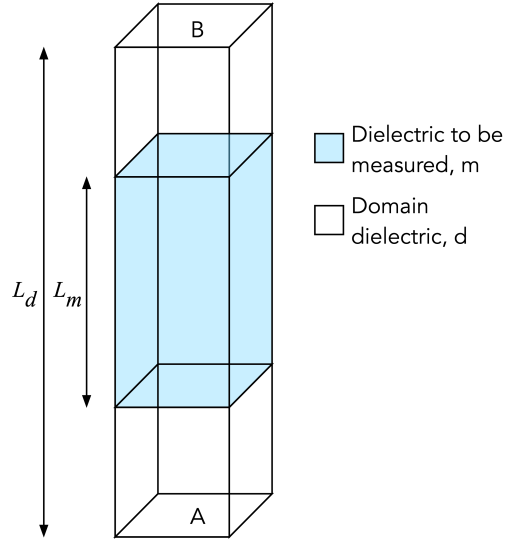


Figure 4.6. Model for measuring the phase velocity.

The phase shift of a wave entering face A of the domain and leaving face B depends on the wavelength of the wave in the dielectrics and the distance travelled in each:

$$\phi = 2\pi \frac{L_m}{\lambda_m} + 2\pi \frac{(L_d - L_m)}{\lambda_d}. \quad 4-18$$

If the dielectric being measured is now removed, the phase shift through the domain alone, which will be referred to as the reference, is just:

$$\phi_d = 2\pi \frac{L_d}{\lambda_d}. \quad 4-19$$

The phase shift due to the dielectric under test over and above the contribution from the domain is therefore the phase shift of the whole minus the phase shift of the reference:

$$\Delta\phi = \phi - \phi_d = 2\pi \frac{L_m}{\lambda_m} + 2\pi \frac{(L_d - L_m)}{\lambda_d} - 2\pi \frac{L_d}{\lambda_d}, \quad 4-20$$

which simplifies to

$$\Delta\phi = 2\pi \frac{L_m}{\lambda_m} - 2\pi \frac{L_m}{\lambda_d}. \quad 4-21$$

Using $\lambda = v/f$ and $v_d = c/n_d$ this becomes

$$\Delta\phi = 2\pi f \frac{L_m}{v_m} - 2\pi f \frac{L_m}{v_d}. \quad 4-22$$

Rearranging to get an equation for the refractive index of the dielectric under test, $n_m = c/v_m$:

$$n_m = \frac{c\Delta\phi}{2\pi f L_m} + n_d. \quad 4-23$$

If the modelling is performed in HFSS, the phase shift of the transmitted wave for both the whole model and the reference can be extracted from the argument of the complex S-parameter, S_{12} . The resulting phase shift angles must be ‘unwound’ to ascertain the correct branch. This can be achieved by inspecting the value as it changes with frequency, correcting for the wrap round between $\pm\pi$ appropriately.

This method of finding the refractive index has been used successfully with artificial dielectrics where the magnetic permeability is one. Due to the process of taking measurements of both the dielectric under test and a reference, the precise details of how the excitation ports couple to the model and the length of the modelling domain do not matter.

4.3.2 Matching with a test dielectric

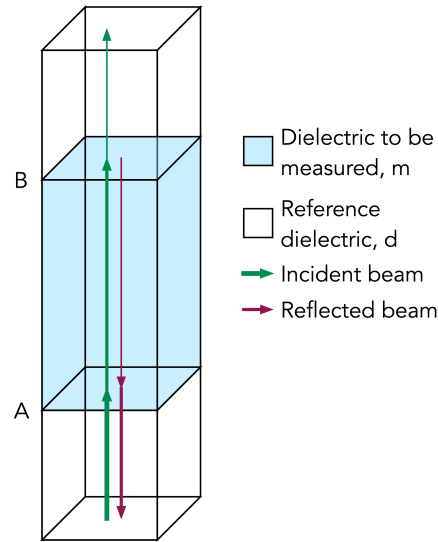


Figure 4.7. Matching with a test dielectric. The refractive index of the reference dielectric is varied until reflections from boundaries A and B are minimised.

A method of determining the refractive index of a dielectric that is reminiscent of bridge methods for the measurement of electronic components is described by Pisano et al⁴². A sample of the dielectric to be measured is placed between two

blocks of reference dielectric as shown in Figure 4.7. The refractive index of the reference dielectric is then varied, by changing the permittivity of the material in the modelling tool, until the reflections from the boundaries between the reference and the test dielectrics (marked A and B) are minimised. This happens when the reference dielectric refractive index is equal to that of the test dielectric.

This method is slower than the phase velocity measurement method. It requires the modelling tool to be run many times with different values of reference dielectric permittivity. It is another method that is immune to the precise details of how the excitation ports couple to the model and the length of the modelling domain.

4.3.3 Extraction from two port S-parameters

The extraction of the complex refractive index and impedance from the S-parameters that HFSS calculates has been described by a number of authors; Nicholson and Ross¹¹⁹, Chen et al.¹²⁰, Szabo et al.¹²¹ and Numan and Sharawi¹²². The derivation starts by writing down the equations for S_{11} and S_{21} , the reflection and transmission S-parameters respectively, for a wave incident on port 1 of a two port network, as shown in Figure 4.8.

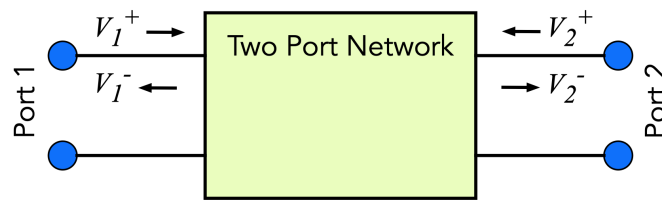


Figure 4.8. Signal flows in a two-port network.

These are defined (see Pozar¹²³ section 4.3 for example) to be:

$$S_{11} = \frac{V_1^-}{V_1^+} \quad S_{21} = \frac{V_2^-}{V_1^+} \quad 4-24$$

where V_1^+ is the wave incident into port 1, V_1^- is the wave reflected back out of port 1 and V_2^- is the wave transmitted out of port 2.

The method Nicholson and Ross describe is for measuring the parameters of a dielectric making up a coaxial cable, shown in Figure 4.9. The method is adapted here to waves passing through a dielectric in an HFSS model.

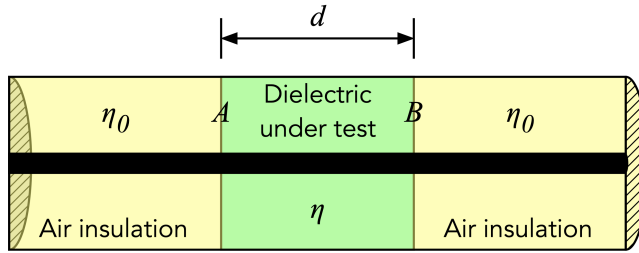


Figure 4.9. The test arrangement used by Nicholson and Ross to measure permittivity and permeability parameters.

Nicholson and Ross drew a signal flow graph to represent the behaviour of this two-port network, shown in Figure 4.10. The edges between the nodes of a signal flow graph represent the wave and are labelled with relative amplitudes. The reflection coefficient for the transition vacuum to dielectric is indicated by Γ . The reflection coefficient for the transition dielectric to vacuum is therefore $-\Gamma$.

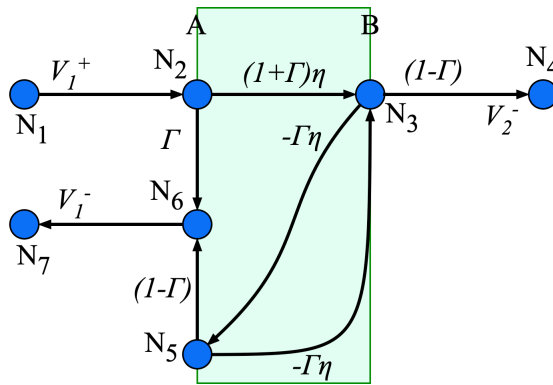


Figure 4.10. Signal flow graph for the Nicholson and Ross setup. The dielectric under test fills the pale blue zone with impedance, η . Notice that the transitions outside the test dielectric zone do not use the free space impedance.

The edge N_1 to N_2 represents the incident wave reaching the boundary A of the dielectric. The wave then splits into transmitted and reflected parts. The transmitted part travels through the dielectric to the boundary B (the edge N_2 to N_3). The reflected part (the edge N_2 to N_6) is combined with another reflected wave to form the reflected signal N_6 to N_7 . The transmitted signal (N_2 to N_3) splits into another pair of transmitted and reflected parts at boundary B. This transmitted part combines with the signal represented by N_5 to N_3 to form the wave that exits the dielectric (N_3 to N_4). The reflected part travels back through the dielectric to boundary A (N_3 to N_5) where it is split one last time into transmitted and reflected parts. This final transmitted part (N_5 to N_6) is combined with the original reflected part to form the wave reflected from the dielectric (N_6 to N_7). The final reflected

part passes back through the dielectric to boundary B (N_5 to N_3) where it forms part of the output wave (N_3 to N_4).

It can be seen that the impedance of the air insulated part of the test coaxial cable is not used. In the Nicholson and Ross experiment it is cancelled out by carefully selected cable lengths. In the HFSS model (Figure 4.11) there are vacuum zones between the ports and the test dielectric. These cannot be of zero size as it is necessary that the vacuum to dielectric boundaries exist. A modified signal flow graph that takes account of propagation through this zone, d_0 , assuming it is of the same length on both sides of the test dielectric, is shown in Figure 4.12.

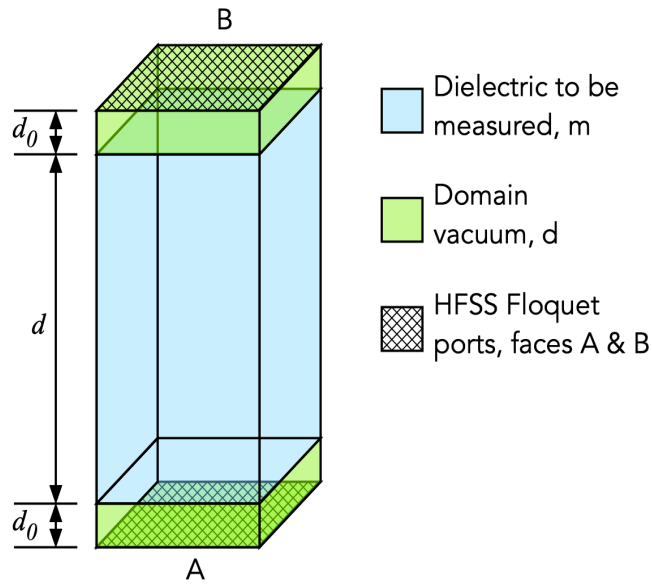


Figure 4.11. Measuring the refractive index using HFSS and S-parameters. The dielectric under test is sandwiched between two equal sized vacuum layers with the Floquet excitation ports (when using master slave boundaries) on the outer faces A and B.

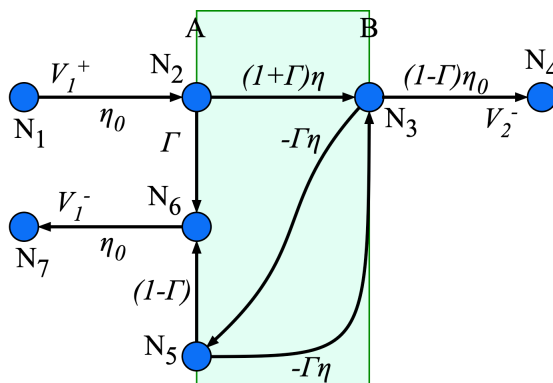


Figure 4.12. Signal flow graph with a vacuum zone on either side of the test dielectric.

The equations for the required S-parameters may now be written down from the signal flow graph using Mason's gain formula¹²⁴. The procedure for $S_{21} = V_2^-/V_1^+$ which corresponds to the gain from node 1 to node 4 is:

1. List all the forward paths through the network from N_1 to N_4 and write their gains down as the product of the gains of each segment. In this case there is just one: N_1 to N_2 to N_3 to N_4 and the gain is $G_1 = \eta_0(1 + \Gamma)\eta(1 - \Gamma)\eta_0$.
2. List all the loops in the network and write down their gains as the product of the gains of each segment. Again, this case has just a single loop: N_3 to N_5 to N_3 with gain $L_1 = (-\Gamma\eta)(-\Gamma\eta)$.
3. Compute the determinant of the network using this equation:

$$\Delta = 1 - \sum L_i + \sum L_i L_j - \sum L_i L_j L_k + \dots + (-1)^m \sum \dots + \dots$$

As there is only one loop, this is $\Delta = 1 - L_1$

4. Compute the cofactors of the determinant for each forward path. These are the determinants excluding the terms for the loops that the forward path touches. As there is only one forward path and it touches the only loop, this is $\Delta_1 = 1$.
5. Use the equation $G = \frac{y_{out}}{y_{in}} = \frac{\sum_{k=1}^N G_k \Delta_k}{\Delta}$ to write down the gain:

$$S_{21} = \frac{G_1 \Delta_1}{\Delta} = \frac{\eta_0(1 + \Gamma)\eta(1 - \Gamma)\eta_0}{1 - \Gamma^2 \eta^2} = \frac{\eta_0^2 \eta (1 - \Gamma^2)}{1 - \Gamma^2 \eta^2}. \quad 4-25$$

The method is then repeated for $S_{11} = V_1^-/V_1^+$, the gain from node 1 to node 7:

1. List all the forward paths through the network from N_1 to N_7 . This time there are two:

 N_1 to N_2 to N_3 to N_5 to N_6 to N_7 with $G_1 = \eta_0(1 + \Gamma)\eta(-\Gamma\eta)(1 - \Gamma)\eta_0$.

 N_1 to N_2 to N_6 to N_7 with $G_2 = \eta_0 \Gamma \eta_0$.
2. List all the loops in the network. The same as before: N_3 to N_5 to N_3 with gain $L_1 = (-\Gamma\eta)(-\Gamma\eta)$.
3. Compute the determinant of the network. As there is only one loop, this is $\Delta = 1 - L_1$

4. Compute the cofactors of the determinant for each forward path. There are two forward paths:

$\Delta_1 = 1$, this forward path touches the loop.

$\Delta_2 = 1 - L_1$, this forward path does not touch the loop, so this is just Δ .

5. Use the equation $G = \frac{y_{out}}{y_{in}} = \frac{\sum_{k=1}^N G_k \Delta_k}{\Delta}$ to write down the gain:

$$\begin{aligned} S_{11} &= \frac{G_1 \Delta_1 + G_2 \Delta_2}{\Delta} = \frac{\eta_0(1 + \Gamma)\eta(-\Gamma\eta)(1 - \Gamma)\eta_0 + \eta_0\Gamma\eta_0(1 - \eta^2\Gamma^2)}{1 - \Gamma^2\eta^2} \\ &= \frac{\eta_0^2\Gamma(1 - \eta^2)}{1 - \Gamma^2\eta^2}. \end{aligned} \quad 4-26$$

Equations 4-25 and 4-26 can then be solved for reflection coefficient, Γ , and impedance η . By analogy with Nicolson and Ross, take the sums and differences, defining V_S and V_D :

$$V_S = \frac{S_{21}}{\eta_0^2} + \frac{S_{11}}{\eta_0^2} = \frac{(1 - \Gamma^2)\eta}{1 - \Gamma^2\eta^2} + \frac{(1 - \eta^2)\Gamma}{1 - \Gamma^2\eta^2} \quad 4-27$$

$$V_D = \frac{S_{21}}{\eta_0^2} - \frac{S_{11}}{\eta_0^2} = \frac{(1 - \Gamma^2)\eta}{1 - \Gamma^2\eta^2} - \frac{(1 - \eta^2)\Gamma}{1 - \Gamma^2\eta^2}. \quad 4-28$$

Nicholson and Ross then state the result as:

$$\Gamma = X \pm \sqrt{X^2 - 1} \quad 4-29$$

$$\eta = \frac{V_S - \Gamma}{1 - V_S\Gamma} \quad 4-30$$

where $X = \frac{1 - V_S V_D}{V_S - V_D}$ and the square root to take in Equation 4-29 is the one that leads to $\Gamma \leq 1$. Deriving these is quite difficult, however it can be shown they are correct by first substituting for X and reorganising:

$$V_S\Gamma^2 - V_D\Gamma^2 + 2V_S V_D\Gamma - 2\Gamma + V_S - V_D = 0 \quad 4-31$$

$$\eta + \Gamma - V_S - V_D\Gamma\eta = 0 \quad 4-32$$

and then substituting for V_S and V_D :

$$\begin{aligned}
 & \left(\frac{(1-\Gamma^2)\eta}{1-\Gamma^2\eta^2} + \frac{(1-\eta^2)\Gamma}{1-\Gamma^2\eta^2} \right) \Gamma^2 - \left(\frac{(1-\Gamma^2)\eta}{1-\Gamma^2\eta^2} - \frac{(1-\eta^2)\Gamma}{1-\Gamma^2\eta^2} \right) \Gamma^2 \\
 & + 2 \left(\frac{(1-\Gamma^2)\eta}{1-\Gamma^2\eta^2} + \frac{(1-\eta^2)\Gamma}{1-\Gamma^2\eta^2} \right) \left(\frac{(1-\Gamma^2)\eta}{1-\Gamma^2\eta^2} - \frac{(1-\eta^2)\Gamma}{1-\Gamma^2\eta^2} \right) \Gamma \\
 & - 2\Gamma + \left(\frac{(1-\Gamma^2)\eta}{1-\Gamma^2\eta^2} + \frac{(1-\eta^2)\Gamma}{1-\Gamma^2\eta^2} \right) \\
 & - \left(\frac{(1-\Gamma^2)\eta}{1-\Gamma^2\eta^2} - \frac{(1-\eta^2)\Gamma}{1-\Gamma^2\eta^2} \right) = 0
 \end{aligned} \tag{4-33}$$

$$z + \Gamma - \left(\frac{(1-\Gamma^2)\eta}{1-\Gamma^2\eta^2} + \frac{(1-\eta^2)\Gamma}{1-\Gamma^2\eta^2} \right) - \left(\frac{(1-\Gamma^2)\eta}{1-\Gamma^2\eta^2} + \frac{(1-\eta^2)\Gamma}{1-\Gamma^2\eta^2} \right) \Gamma \eta = 0. \tag{4-34}$$

Expanding leads to all the terms cancelling out and showing that Equations 4-29 and 4-30 are correct.

In section 2.1.2 the relationship between the reflection coefficient at a boundary between two dielectrics and the impedance of the dielectrics was given. Using Equation 2-3 the reflection coefficient for the boundary A can be written as

$$\Gamma = \frac{\eta - \eta_0}{\eta + \eta_0}. \tag{4-35}$$

Using $\eta = \sqrt{\mu/\epsilon}$ and therefore $\eta = \sqrt{\mu_R\mu_0/\epsilon_R\epsilon_0} = \eta_0\sqrt{\mu_R/\epsilon_R}$ this becomes

$$\Gamma = \frac{\sqrt{\mu_R/\epsilon_R} - 1}{\sqrt{\mu_R/\epsilon_R} + 1} \tag{4-36}$$

which leads to

$$\frac{\mu_R}{\epsilon_R} = \left(\frac{1 + \Gamma}{\Gamma - 1} \right)^2 \tag{4-37}$$

The impedance of the dielectric can be written as

$$\eta = e^{-i\frac{\omega}{c}\sqrt{\mu_R\epsilon_R}d}, \tag{4-38}$$

a simple reorganisation leads to

$$\mu_R\epsilon_R = -\left(\frac{c}{\omega d} \ln \eta \right)^2. \tag{4-39}$$

Defining

$$c_1 = \frac{\mu_R}{\varepsilon_R} = \left(\frac{1 + \Gamma}{\Gamma - 1} \right)^2 \quad 4-40$$

$$c_2 = \mu_R \varepsilon_R = \left(\frac{ic}{\omega d} \ln \eta \right)^2 \quad 4-41$$

then dividing and multiplying these two equations leads to the relative electric permittivity and magnetic permeability

$$\varepsilon_R = \sqrt{\frac{c_2}{c_1}} \quad 4-42$$

$$\mu_R = \sqrt{c_1 c_2} . \quad 4-43$$

In order to calculate V_S and V_D from the S-parameters, the impedance of free space is required, which is given by

$$\eta_0 = e^{-i\frac{\omega}{c}d_0} . \quad 4-44$$

There is one remaining difficulty to overcome, in Equation 4-39 there is a natural logarithm of a complex number. The imaginary part of this function is multi-valued, and the correct branch must be deduced. Where this method is used in this work, the S-parameters are captured for an ascending range of frequencies. Since the imaginary part of the natural logarithm must be continuous with changing frequency, the step changes that occur at branch boundaries can be fixed by inspection during data processing by subtracting a suitable multiple of 2π .

4.3.4 The refractive index of a polypropylene block

To verify the accuracy of these three methods, the refractive index of a block of polypropylene 0.5 mm thick was measured. The results are shown in Figure 4.13.

The phase velocity measurement method showed an error in the refractive index of around 2% at the higher frequencies. At the lowest frequencies however, the error became quite large, rising to nearly 10%. The bridge method took the longest to find a value but returned very accurate results. Finally, the S-Parameter method found a value with an error less than 0.02% over the whole frequency range. This curve overlays the bridge method curve in the diagram.

All three methods produced results consistent with each other and with the modelled refractive index of 1.5 (which is also the accepted value for polypropylene, Flores-Mijangos and Beltrán-López, 2003¹²⁵ measured a value of 1.492 for the far infrared). The bridge method has the potential to be the most accurate, but at the expense of very long modelling times. The S-parameter method combines reasonable modelling times with accurate results and also has the advantage that it returns the complex permittivity and permeability rather than just the conventional refractive index. This is the method that was used for the remainder of this work and was implemented in the modelling tool described in Chapter 2.

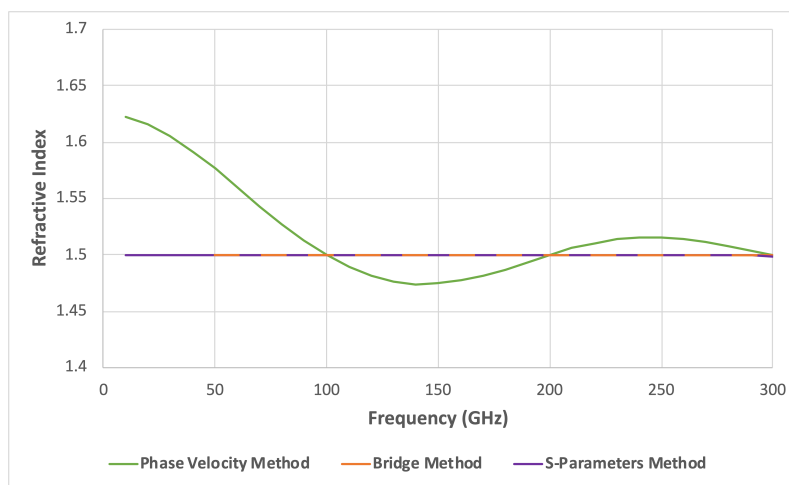


Figure 4.13. The refractive index using the three methods described of a model of a 0.5 mm polypropylene cube. The relative permittivity of the cube was modelled as 2.25 which corresponds to a refractive index of 1.5. The bridge and S-parameter methods results overlay each other, indicated by the orange and purple dashed.

4.3.5 Refractive index of the super-capacitive patch

The S-parameter method of refractive index extraction was used to measure the refractive index of the metamaterial mesh sequence from square patches to the super-capacitive patches of section 3.2.

The first investigation was of a multi-layer structure built from capacitive metamaterial meshes in a polypropylene dielectric. In addition to its properties as an artificial dielectric, such a structure also forms a low pass filter with a Chebyshev style response containing a fair amount of ripple in the passband. The cut-off frequency, of course, depends on the capacitance of the mesh. The lowest cut-off frequency being created by the mesh with the highest capacitance which for this

unit cell is the super-capacitance grid with a patch ratio of 206 and lies at just over 200 GHz.

The structure dimensions were a 160 mm unit cell with 25 mm layer spacing and 10 mm minimum feature size. The HFSS model layout is shown in Figure 4.14. As described in the procedure of section 4.3.3, a block of the artificial dielectric (ten layers of the mesh under test) is sandwiched between two vacuum layers. The top and bottom faces have Floquet ports to excite the model, while the sides were configured as periodic boundaries.

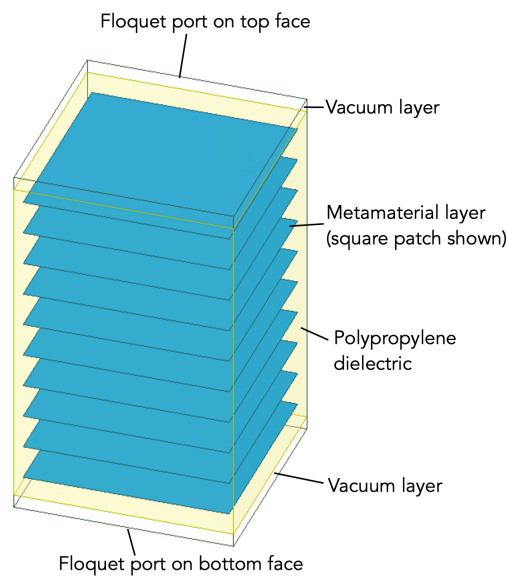


Figure 4.14. The HFSS model for the refractive index survey of the polypropylene embedded square patch to super-capacitive patch series.

The refractive index series is shown in Figure 4.15. The conventional square patches provide an effective refractive index of up to 4.6 at 200 GHz, rising only slightly with frequency. The super-capacitive patches increase the available effective refractive index quite significantly; the patch ratio 206.25 shape providing a value of 9.9 at 200 GHz. The downside is that the chromatic aberration indicated by the increasing refractive index with frequency is worse, and the low-pass filter cut-off limits the bandwidth.

A similar investigation was carried out for patches in a silicon dielectric with a layer spacing of 100 μm and a unit cell of 90 μm . The results of this are shown in Figure 4.16. The super-capacitive patches once again extend the available refractive indices beyond the range provided by the conventional square patch. At 200 GHz,

the 80 μm conventional square patch (patch ratio 89) gives a refractive index of 5.23.

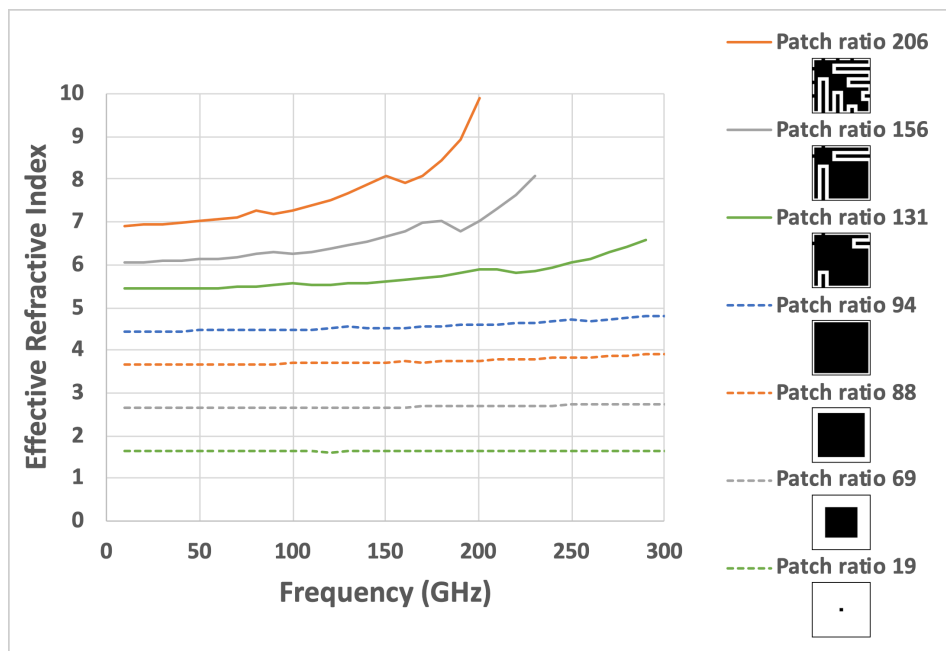


Figure 4.15. Polypropylene artificial dielectric series. Refractive indices for the sequence of metamaterial meshes from conventional square patches to supercapacitive patches for a 160 μm unit cell in a polypropylene dielectric with 25 μm layer spacing. The three solid curves stop short due to reaching the structure's cut-off frequency.

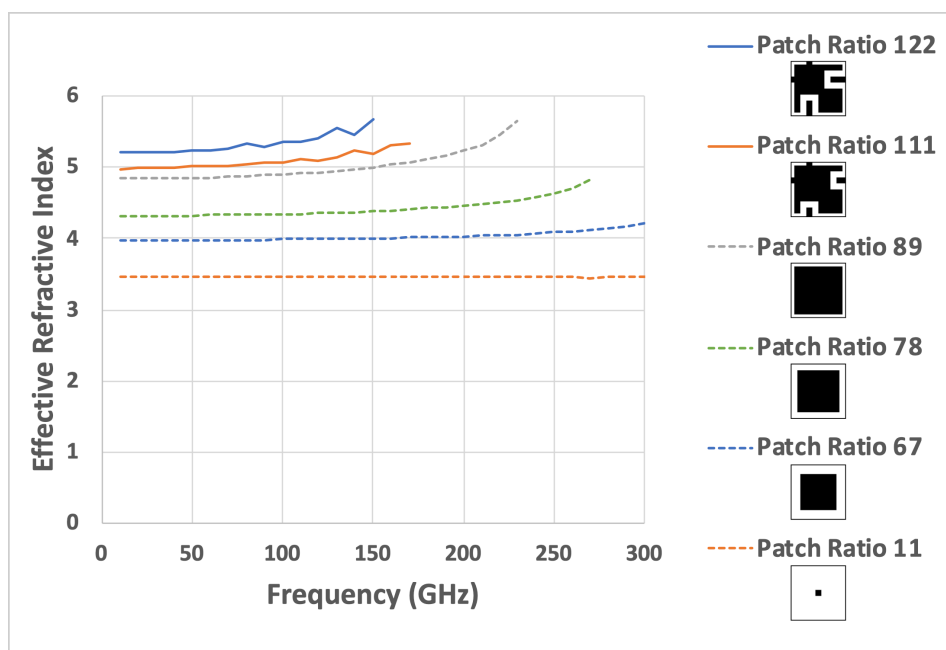


Figure 4.16. Silicon artificial dielectric series. Refractive indices for a sequence of patches in silicon with a 90 μm unit cell and 100 μm layer spacing. The lines that stop short indicate the structure's cut off frequency.

In both cases, the minimum refractive index is that provided by the substrate alone, with no embedded mesh. This is important to the discussion of anti-reflection layers in section 4.7.

4.3.6 Super-capacitive patches and lenslet designs

To demonstrate the effect of using super-capacitive patches in flat mesh lenslets a pair of small, simple, polypropylene examples were designed. The specification was for a 3 mm diameter lenslet with a focal length of 1 mm and an operating frequency of 200 GHz, chosen for ease of modelling rather than for any useful purpose. One design used only conventional square patches, the second used super-capacitive patches in its centre columns. Both were designed using the simple path length method of section 4.1. Since the aim was to demonstrate the equivalence of square and super-capacitive patch designs, these designs were not optimised for overall performance nor intended focal length, rather they were adjusted so that their electric field magnitude diagrams and far field plots matched closely. The conventional squares design required eleven layers while the super-capacitive patch design achieved very similar results with eight.

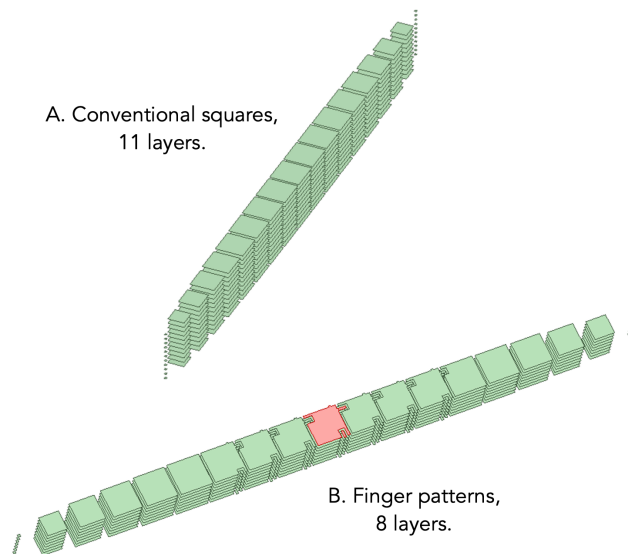


Figure 4.17. Example polypropylene lenslet designs using conventional square patches and super-capacitive patches. One super-capacitive patch has been highlighted.

The designs were modelled in Ansys HFSS (see Figure 4.17) as a slice across the diameter of the lenslet (the x direction) that was a single unit cell wide. Master/slave boundary conditions were applied on the y boundaries and a gaussian source was positioned at the focal point. As already discussed in section

4.2, the model is effectively of a cylindrical lenslet. The resulting electric field magnitude is shown in cross section in Figure 4.18.

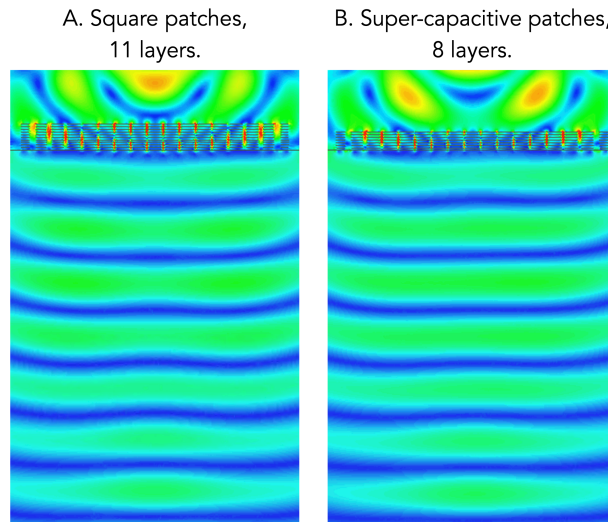


Figure 4.18. The electric field magnitude for the two lenslet designs in polypropylene with a gaussian source placed at the focus. They are aligned vertically to show the similarity of the wave fronts that have passed through the lens.

The far fields of the two lenslets were also captured using the far field feature of Ansys HFSS and are shown in Figure 4.19. The two curves are very similar; the eight-layer super-capacitive patch case has slightly more attenuation (measured as -0.16 dB at zero azimuth). The full width half maximum (FWHM) was 35.3° and 34.1° for square and super-capacitive patches respectively.

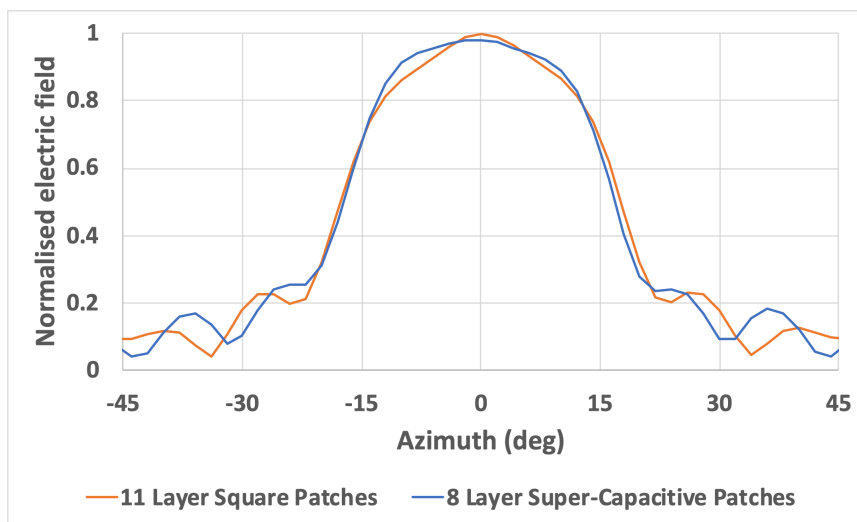


Figure 4.19. The far-fields of the two example lenses. The field was normalised to 1 at zero degrees azimuth for the eleven-layer conventional square patch lenslet.

In this example, the number of layers required was reduced from eleven to eight (27% fewer) with minimal effect on the performance of the lenslet (the shape of the far field curve may even have improved). This was also achieved by extending the available refractive range just a little beyond the conventional square, using only a single short finger of the super-capacitive patch. Section 4.4.2 will discuss the range of finger length it is possible to use for specific designs.

4.4 Choosing the column width

The basic concept of a GRIN lens assumes a continuous grading of the refractive index radially across the lens. The design method introduced in section 4.1 splits the lens into discrete columns of dielectric, which violates this assumption. In addition, the refractive index variation is to be generated in a column by changing metallic patch sizes within the metamaterial unit cell. This section investigates what effect discrete step changes to refractive index like this has on the behaviour of a lens and gives guidelines for choosing the width of the dielectric columns. In an implementation of such a device with artificial dielectrics using metamaterial meshes, the design columns must be an integer multiple of the mesh's unit cell, and there is no reason not to make the design column size the same as the unit cell. There are a few criteria that must be considered in this choice which will be covered here. The design specifications for the examples described here were given in Table 4.1.

4.4.1 Spatial resolution

The width of the columns controls the spatial resolution of the refractive index grading across the lenslet. Figure 4.20 shows the desired refractive index calculated by the method of section 4.1 for column widths of 50 μm and 500 μm over the diameter of a 6 mm GRIN lenslet. It can be seen that when the column size is large (the spatial resolution is low), the refractive index steps between adjacent columns also become large.

To investigate what effect this might have on the performance of a lenslet, GRIN lenslets using the two column widths were modelled in FDTD with a Gaussian source placed at the focus. Dielectric blocks with the desired refractive indices were used instead of metamaterial artificial dielectrics. This allowed the FDTD Yee cell to be quite large, thus reducing modelling time and memory requirements.

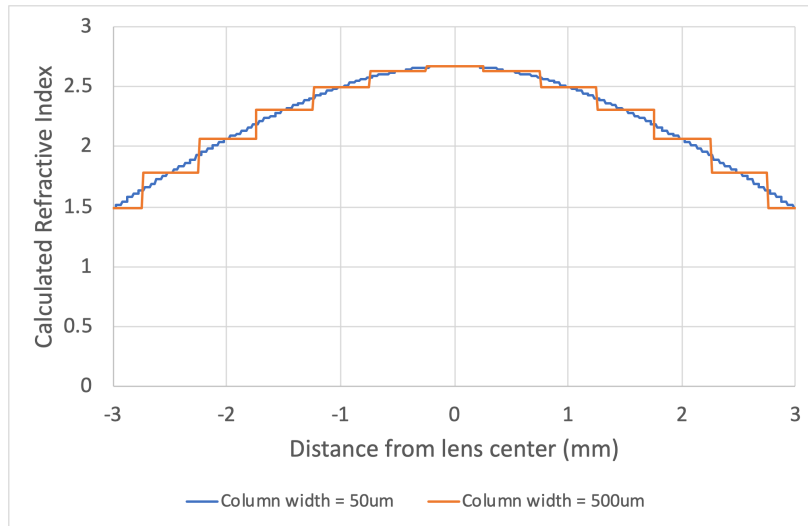


Figure 4.20. Calculated refractive index across the diameter of a 6mm GRIN lenslet for two column widths.

Figure 4.21 shows a cross-section of the resulting electric field magnitude for two frequencies passing through the two lenslets. At 100 GHz there is no noticeable difference between the two column widths (compare A and B in the diagram). At 400 GHz the story is different however (compare C and D); the outgoing Gaussian beam clearly has ripples imposed on it by the 500 μm column width.

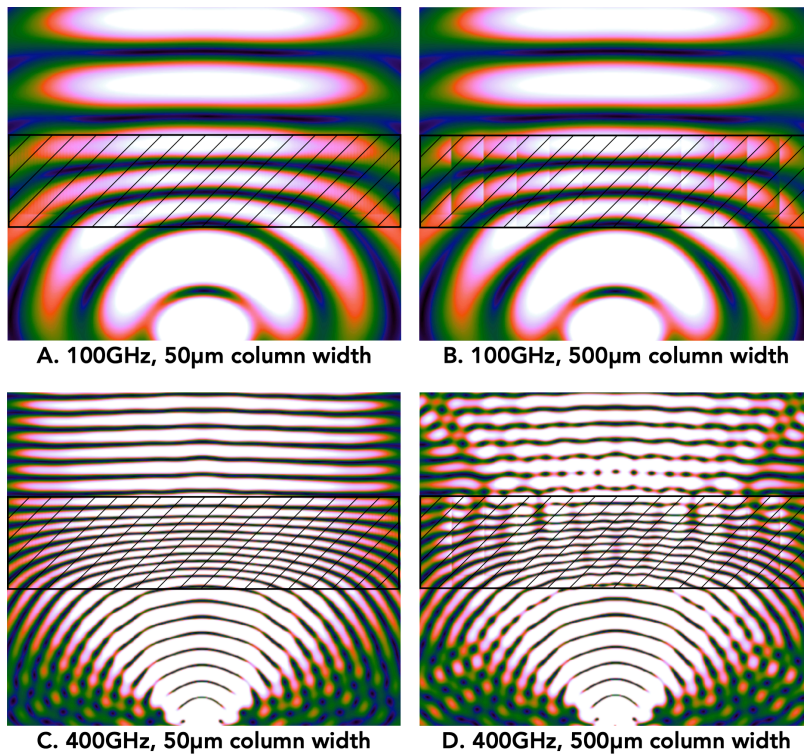


Figure 4.21. Effect of GRIN column width on lenslet behaviour. The cross-hatched area is the lenslet structure.

The effect of the column width on the behaviour of the lenslet was investigated further to quantify the deviation and establish guidelines. This study was carried out using the initial design of the polypropylene proof of concept lenslet. The effect is most pronounced at higher frequencies so the upper design frequency, 300 GHz, was concentrated on. The model again used dielectric blocks for the GRIN columns. The electric field magnitude at a cross section 2 mm above the lenslet was measured and normalised to its magnitude at the lenslet centre. Data were collected for column widths from 20 to 700 μm in 20 μm steps, selected plots are shown in Figure 4.22. These indicate that the column width starts to have an effect on performance from about 400 μm and gets progressively much worse as the column width increases further.

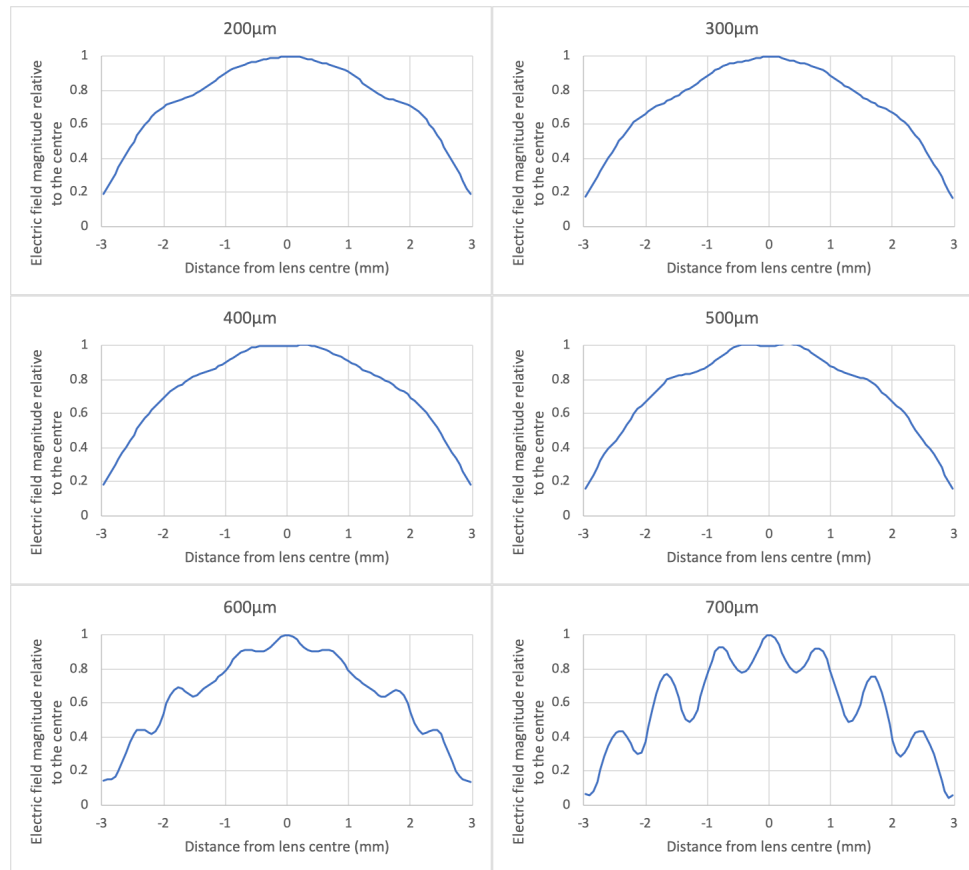


Figure 4.22. Effect of GRIN column width on the wavefront. The normalised electric field magnitude at a cross section 2 mm from the lenslet for selected GRIN column widths is shown.

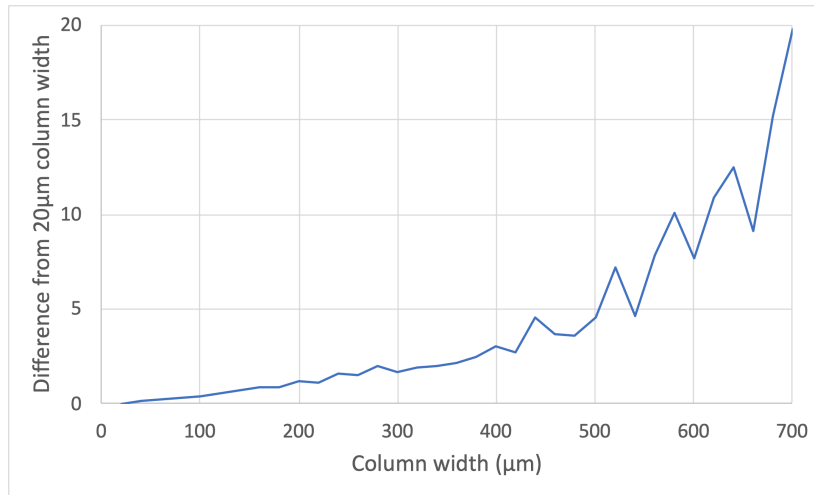


Figure 4.23. Deviation due to GRIN column width. Difference between the normalised electric field magnitude at a cross section 2 mm above the lenslet at various column widths and that at 20 μm .

The 20 μm data is taken to represent the ideal, (almost) continuously graded, case. Figure 4.23 shows how the response differs from this ideal as the column width varies. The difference is measured as the area between the two curves. This shows that the column width has an effect on the lenslet behaviour well before the ripples become visible to the naked eye at 400 μm .

The plot shows there is a steady change to the output shape from 20 μm up to 400 μm , then a faster change starts to become apparent. The general shape of the curve can be interpreted as the effect of more column widths progressively exceeding the wavelength of the light travelling through them as the column width grows. The central columns have the highest refractive index so will exceed their wavelength first, but they also have the smallest refractive index steps so will have least effect. Eventually, the outer columns exceed their wavelength, causing the biggest change due to their large refractive index steps.

There is clearly a constraint on the column width to avoid these distortions. In this polypropylene design, the outermost columns had a refractive index of 1.48 (just the polypropylene dielectric) while the inner columns were around 4.5 (roughly the maximum refractive index provided by conventional square patches in a metamaterial artificial dielectric). For the frequency 300 GHz, this corresponds to wavelengths of 670 μm in the edge columns and 220 μm in the centre columns. A useful guideline to avoid problems with spatial resolution is to keep the GRIN column width smaller than the wavelength of the specified centre frequency travelling in a dielectric with the refractive index required by the centre columns.

For the proof-of-concept lenslets being considered, a slightly higher central column refractive index of 5.2 was targeted for both polypropylene and silicon. To meet the guideline, this corresponds to upper limits on the GRIN column width of 190 μm for the polypropylene lenslet and 280 μm for the silicon (due to its lower required upper frequency limit).

4.4.2 Cut-off frequency

The artificial dielectrics described in section 4.2.1 that will be used to implement the GRIN columns, act as low pass filters whose cut-off frequency depends on the unit cell of the metamaterial and the size of the square patch. The column width must therefore be chosen such that the required maximum frequency lies below the cut-off. To inform this decision, a survey of the transmittance characteristics of ten layers of a range of unit cell sizes containing maximally sized square patches (unit cell size minus the minimum feature size) was made using modelling in HFSS for both polypropylene and silicon dielectrics.

Figure 4.24 shows the transmittance curve for the 250 μm polypropylene case. The filter effect has quite a soft roll off starting around 280 GHz and a lot of ripple in the passband. To make the presentation of many of these curves and the subsequent selection of a reasonable compromise easier, the mean of the minimum and maximum ripple will be drawn, as indicated in the figure.

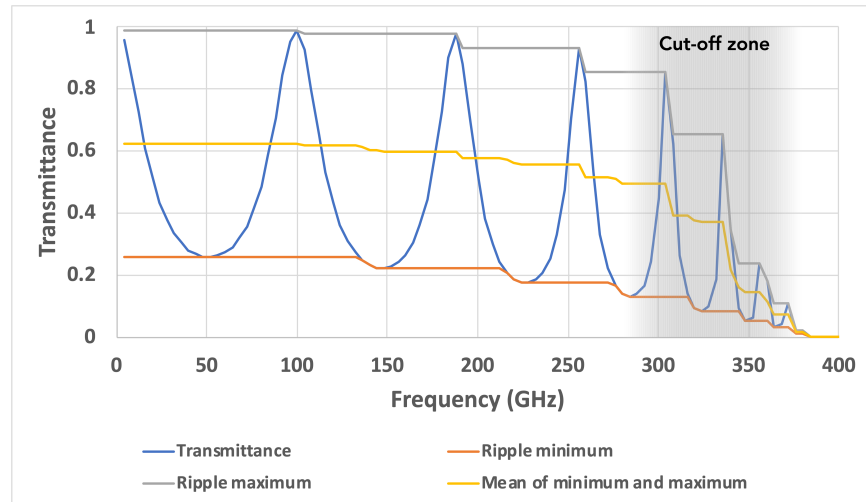


Figure 4.24. Transmittance of 10 layers of a 240 μm square patch with a 250 μm unit cell with a layer spacing of 25 μm in a polypropylene dielectric. The ripple minimum and maximum and their average are also shown.

Figure 4.25 shows the mean of the ripple for the range of unit cells modelled in polypropylene. The maximum design frequency of the polypropylene proof of

concept is 300 GHz. From this diagram it is clear that the unit cell should be no greater than 220 μm to avoid the low-pass filter roll off and that 190 μm or 160 μm would be better. This decision fits neatly with the spatial resolution guideline of section 4.4.1.

For the silicon proof-of-concept lenslet, much lower unit cell sizes (using a patch size of 10 μm less than the unit cell) are required to avoid the cut-off up to its upper design frequency of 200 GHz as shown in Figure 4.26. A unit cell size of 100 μm or less is indicated, 90 μm or even 80 μm being better which is maybe getting too small.

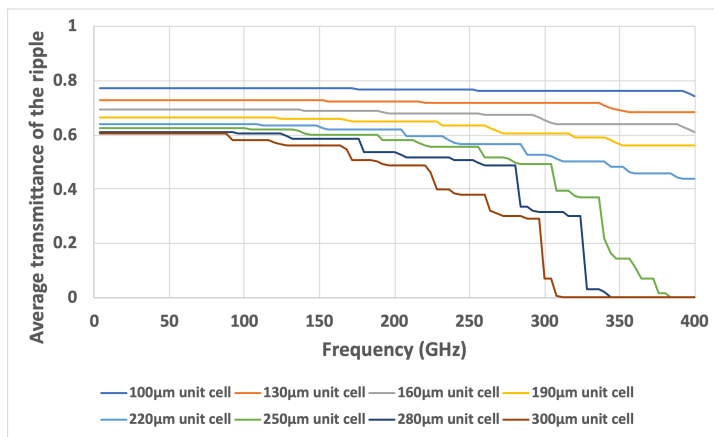


Figure 4.25. Polypropylene mean ripple transmittance. The average transmittance of the ripple for a range of unit cell sizes in polypropylene. Ten layers of a square patch 10 μm less than the unit cell with layer spacing of 25 μm were modelled for each case.

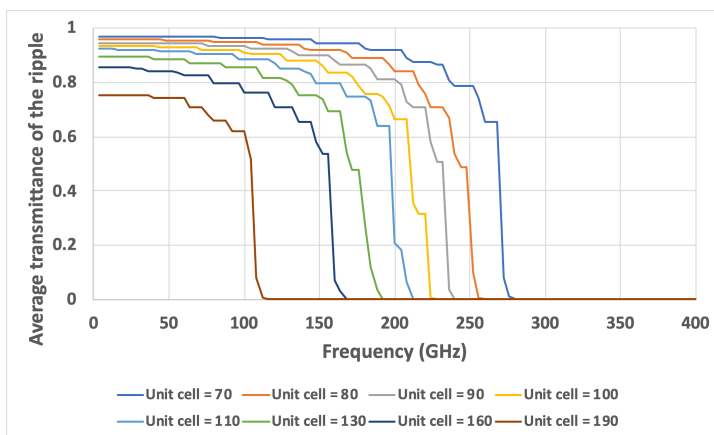


Figure 4.26. Silicon mean ripple transmittance. The average transmittance of the ripple for a range of unit cell sizes in silicon. Ten layers of a square patch 10 μm less than the unit cell with layer spacing of 100 μm were modelled for each case.

Smaller patch sizes can also be used to move the cut-off frequency away from the design frequency for a particular unit cell. Figure 4.27 shows the effect of varying the square patch size for a 160 μm unit cell in silicon. This plot is indicating that a 160 μm unit cell could be used if the patch ratio of the metamaterial mesh is limited to a maximum of 81, which corresponds to a square patch of size 140 μm .

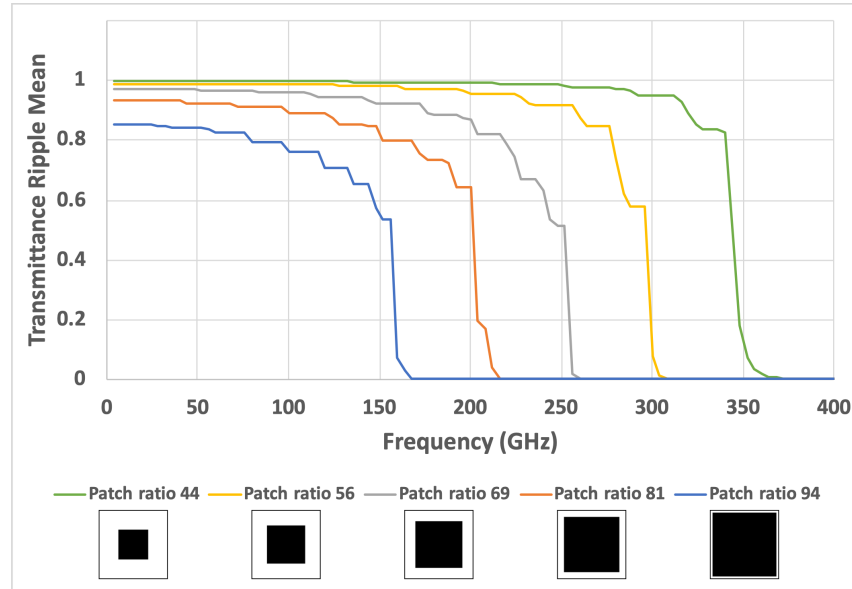


Figure 4.27. Silicon mean ripple transmittance and patch ratio. The average ripple transmittance for ten layers of various patch ratios for a 160 μm unit cell in a silicon dielectric.

Another approach to visualising the options is shown in Figure 4.28 as a heat map. The mean ripple transmittance at 200 GHz is given for a range of unit cells and patch ratios on a colour scale. This shows at a glance that the patch ratio for a 160 μm unit cell should be limited to 80 to avoid too much attenuation.

		Patch Ratio					
		40	50	60	70	80	90
Unit Cell	100 μm	1.0	1.0	1.0	1.0	0.9	0.7
	120 μm	1.0	1.0	1.0	0.9	0.8	0.5
	140 μm	1.0	1.0	1.0	0.9	0.6	0.0
	160 μm	1.0	1.0	0.9	0.8	0.6	0.0
	180 μm	1.0	1.0	0.9	0.7	0.1	0.0
	200 μm	1.0	1.0	0.9	0.5	0.0	0.0

Figure 4.28. Silicon mean ripple transmittance heat map. A view of the mean ripple transmittance (to 1 decimal place) for various patch ratios and unit cells at 200 GHz in a silicon dielectric.

4.4.3 Making the choice

The final choice of column width and thus the metamaterial unit cell for the proof-of-concept lenslets consists of a slightly iterative process considering the constraints discussed in sections 4.4.1 and 4.4.2. The spatial resolution constraint, taking into account the refractive indices of the intended artificial dielectrics (which themselves depend somewhat on the unit cell chosen), is guiding the choice to less than 190 μm for both the polypropylene and silicon designs. A unit cell of 160 μm was chosen to give good spatial resolution for both dielectrics.

The low-pass filter constraint is significant in different ways for the two lenslets. In the polypropylene design, it is less constraining than the spatial resolution at 220 μm . Therefore, with a 160 μm unit cell the available refractive index can be extended using the super-capacitive patches up to the equivalent of a 220 μm unit cell.

The situation is different for the silicon design, however. In this case the low-pass filter requirement is more constraining than the spatial resolution. With the 160 μm unit cell the maximum patch ratio that can be used is 80. There is no advantage in using super-capacitive patches to increase the maximum refractive index available with this choice.

4.5 Choosing the layer spacing.

The distance between the closely spaced layers is another important parameter that has not yet been addressed. The manufacturing constraints for the polypropylene and silicon lenslets are very different for this aspect. While layer spacings down to a few microns are available with polypropylene, a 100 μm minimum spacing is imposed on silicon due to that being the minimum thickness that can be successfully handled in the assembly process (thinner layers become too fragile to survive). The two cases are therefore considered separately. Table 4.1 lists the design specifications of the example polypropylene and silicon lenses considered.

4.5.1 Polypropylene

To inform the decision for the polypropylene dielectric, a survey of layer spacing for the chosen 160 μm unit cell was undertaken. Ten layers of a 150 μm square patch were modelled with layer spacings from 5 to 200 μm . Figure 4.29 shows the refractive index plotted against frequency for selected layer spacings while Figure 4.30 plots refractive index against layer spacing for selected frequencies.

The lower layer spacings lead to higher refractive indices. This is unsurprising as more of the capacitive metamaterial meshes are being used per unit thickness. The larger layer spacings bring down the cut-off frequency of the low-pass filter effect, guiding to a spacing less than 140 μm . To avoid chromatic aberration, a refractive index curve that is as flat as possible across the design band, 100 to 300 GHz, should be chosen. From Figure 4.30, the region above 100 μm shows increasing chromatic aberration as the 300 GHz curve deviates away from the others.

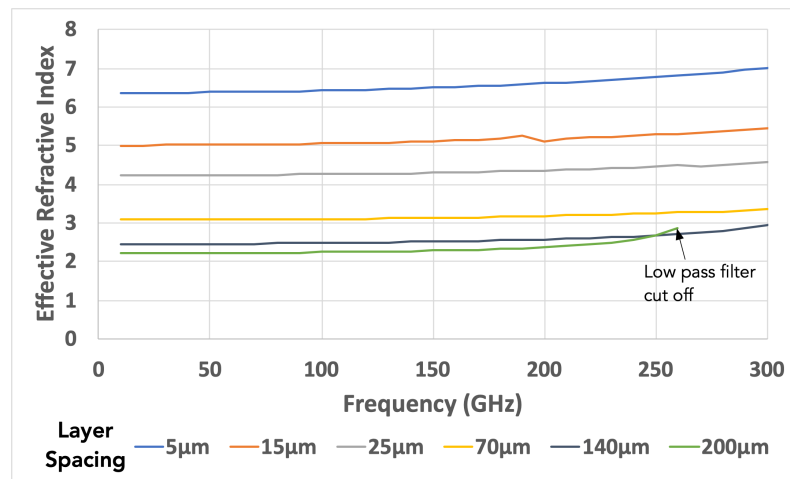


Figure 4.29. Polypropylene refractive index and layer spacing. Refractive index versus frequency for selected layer spacings of ten layers of 150 μm square patches with a 160 μm unit cell. At the higher layer spacings, the low-pass filter cut-off starts to impinge on the required frequency band.

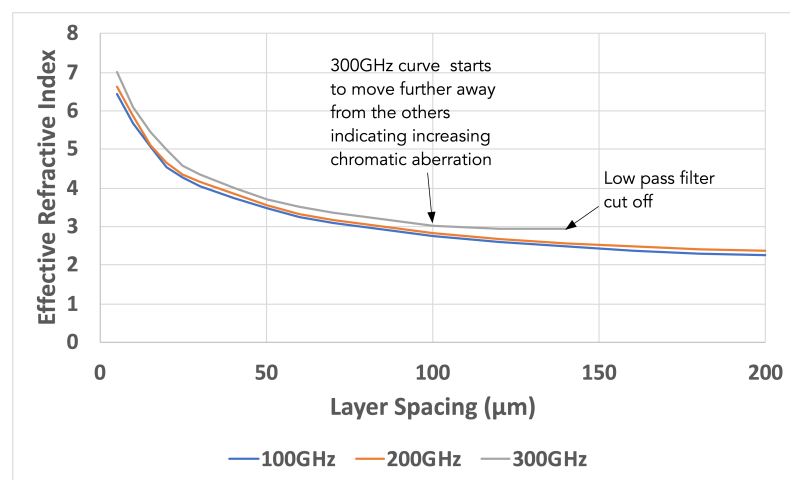


Figure 4.30. Polypropylene refractive index against layer spacing for 150 μm square patches with a 160 μm unit cell in polypropylene. Again, note the low-pass filter cut-off frequency at a layer spacing of 140 μm being important at 300 GHz.

To get a handle on how efficient the metamaterial meshes are, the graph of Figure 4.31 plots the phase shift the meshes are applying (over and above the phase shift due to the polypropylene dielectric) to the wave per layer against layer spacing. This shows that as the metamaterial meshes get closer together than the linear zone, they get less effective in terms of the amount of phase shift they each apply to the transmitted signal. To minimise the number of layers, therefore, a layer spacing from the linear zone should be selected. The desire for a thin lenslet structure and low chromatic aberration push the decision towards the smaller layer spacing end of the linear zone.

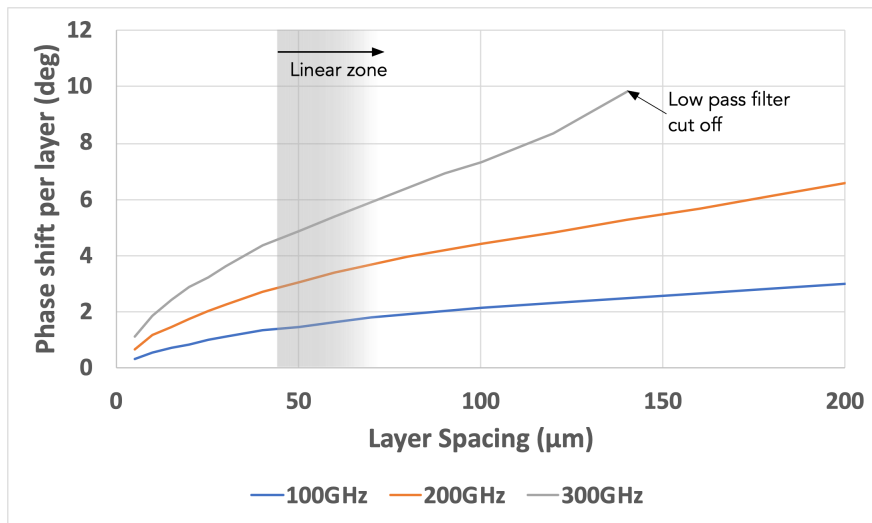


Figure 4.31. Polypropylene phase shift per metamaterial layer against layer spacing for the 150 μm square patches with a 160 μm unit cell in polypropylene. The efficiency of the layers falls off rapidly once the layer spacing is smaller than the linear zone.

One final consideration regarding the layer spacing is the fact that as the number of layers increases, attenuation through the device can increase. It was shown above that a layer spacing of 140 μm brings the cut-off frequency to 300 GHz with ten layers. The chosen layer spacing must therefore be sufficiently below this value for the attenuation at 300 GHz to be acceptable for the number of layers expected to be required for the polypropylene lenslet.

Figure 4.32 shows the average of the transmittance ripple, normalised to one at 10 GHz, for two spacings of fifteen layers. The 25 μm layer spacing causes very little attenuation across the whole of the design band. The 50 μm layer spacing, however, shows around 20% attenuation at the upper end, 300 GHz. The 50 μm layer spacing was chosen despite this to maximise the efficiency of the layers. Approaches to ameliorating the attenuation are explored in a section 4.7.

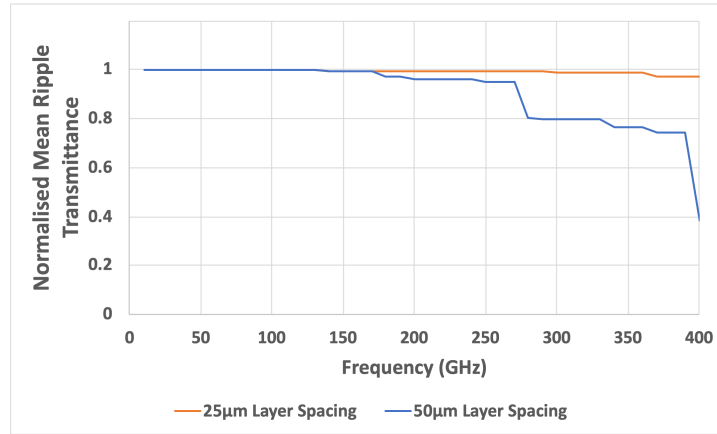


Figure 4.32. Polypropylene attenuation and layer spacing. Mean transmittance ripple, normalised at 10 GHz, for 15 layers of 150 μm square patches at a 160 μm unit cell in polypropylene. The larger layer spacing increases the attenuation over the higher frequencies of the design range (100 to 300 GHz). See Figure 4.24 for an explanation of the “mean ripple” concept.

4.5.2 Silicon

The decision-making process for the layer spacing of the polypropylene lenslet led to a preference for smaller values for this parameter. With silicon having a much higher refractive index than polypropylene, it would be expected that the same would be even more true in this case. However, the choice is effectively made by the limitations of the manufacturing processes to be used and is 100 μm . The effect of this constraint requires investigation.

Square patches of 120 μm and 130 μm (the upper limit already determined in section 4.4.3) in a 160 μm unit cell in silicon were modelled for twenty layers (the probable number of layers in the lenslet). Figure 4.33 shows the normalised mean transmittance ripple for these, indicating that the 130 μm upper limit imposes too much attenuation at the top of the design frequency band. The 120 μm square patch is acceptable although there is more attenuation than seen with the polypropylene case. Of course, the lower square patch size will lead to a lower maximum refractive index and thus more layers in the device. One consolation is that the 100 μm layer spacing will be efficient in terms of phase shift per metamaterial mesh and so should require slightly fewer layers than otherwise would be the case.

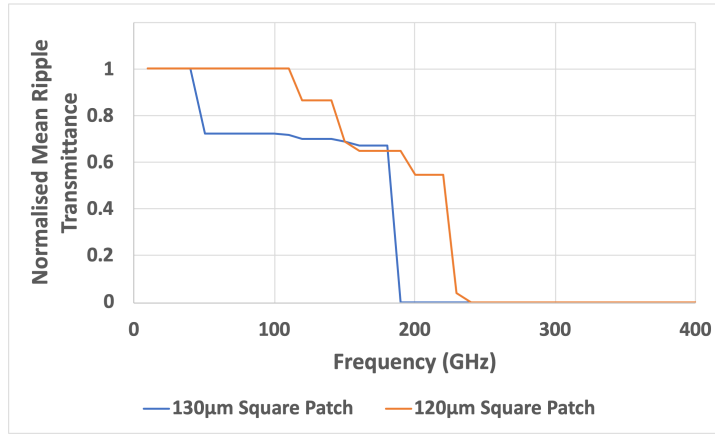


Figure 4.33. Silicon attenuation and patch size. Mean transmittance ripple, normalised at 10 GHz, for 20 layers of 130 μm and 120 μm square patches with 100 μm layer spacing at a 160 μm unit cell in silicon. The larger square size increases the attenuation at the upper end of the design frequency range (100 to 200 GHz). See Figure 4.24 for an explanation of the “mean ripple” concept.

4.6 Refractive index catalogues

With the unit cell and layer spacing parameters chosen, catalogues of the refractive indices of meshes with various patch ratios for the two dielectrics can be constructed. The modelling for these catalogues was all carried out with ten layers of mesh in Ansys HFSS. Only the density of the layers (i.e., the layer spacing) affects the refractive index in the body of the artificial dielectric, ten layers was chosen as it led to reasonable modelling times while still minimising any distortions to the results from the outer layers. This information will be used to choose the specific metamaterial meshes required for the artificial dielectric that implements the refractive index of each column of the lenslets. This task was performed using HFSS and the method described in section 4.3.3.

Figure 4.34 shows the catalogue for the polypropylene lenslet up to a patch ratio of 125 for the chosen unit cell and layer spacing. The extension of the refractive index range due to the super-capacitive patches can be clearly seen. At the higher patch ratios, the curves for the three frequencies shown (that cover the specified range of 100 to 300 GHz) begin to diverge, indicating a rise in chromatic aberration which will cause the focal points at different frequencies to diverge affecting the useful bandwidth of the device.

The refractive index catalogue for the silicon lenslet is shown in Figure 4.35. The maximum patch ratio was chosen as 75 (a 120 μm square patch in the 160 μm

unit cell) due to the attenuation rising drastically at the upper design frequency of 200 GHz, a limit that is indicated once more on this diagram.

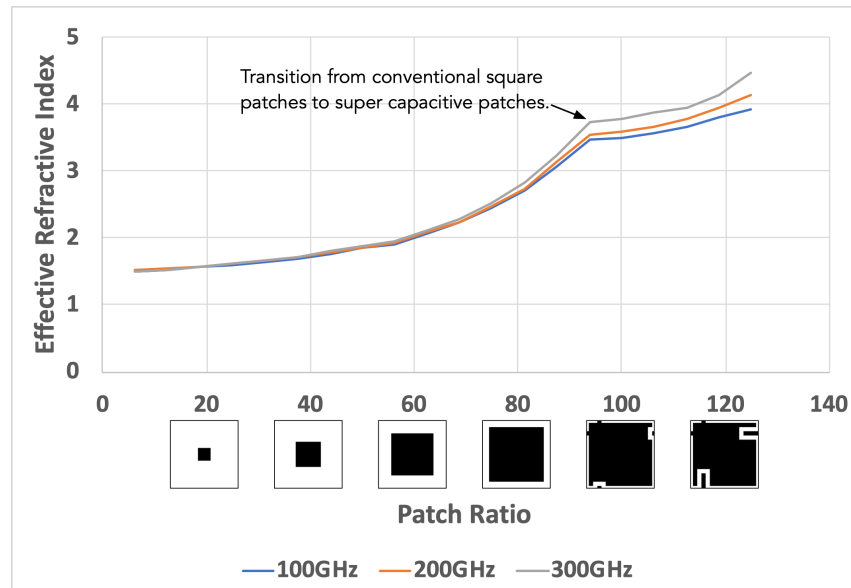


Figure 4.34. Polypropylene: refractive index against patch ratio for 160 μm unit cell metamaterial meshes spaced 50 μm apart.

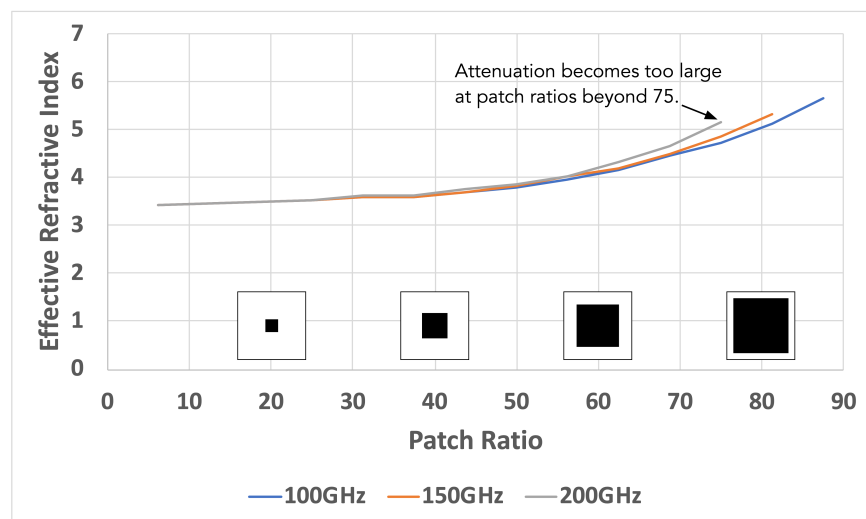


Figure 4.35. Silicon: refractive index against patch ratio for 160 μm unit cell metamaterial meshes spaced 100 μm apart. At 200 GHz, patch ratios beyond 75 impose too much attenuation (the low pass filter cut-off is reasonably sharp but more than 50% of the signal was used as a guide) to be useful.

4.7 Anti-reflection layers

In a GRIN lenslet, there is a transition between the carrier dielectric or the vacuum and the metamaterial part of the lenslet where the effective refractive index

changes. Some of the incident light will be reflected from these transitions. The well know principles of anti-reflection coatings (ARCs), first reported by Rayleigh¹²⁶, can be used to mitigate such reflections. Chen et al.⁵⁹ describe using metamaterial anti-reflection layers in this manner.

A layer of an intermediate dielectric with a refractive index that is the geometric mean of the two adjacent dielectrics and is one quarter wavelength thick will suppress the reflection for that frequency. This principle can be extended to multiple anti-reflection layers stacked together; these will be referred to as an anti-reflection “stages” and form one composite anti-reflection layer. More stages lead to less reflection, although returns diminish for each extra stage; one, two, three and four stage ARCs are shown in Figure 4.36. The equations for the refractive index of each stage are given in Table 4.2.

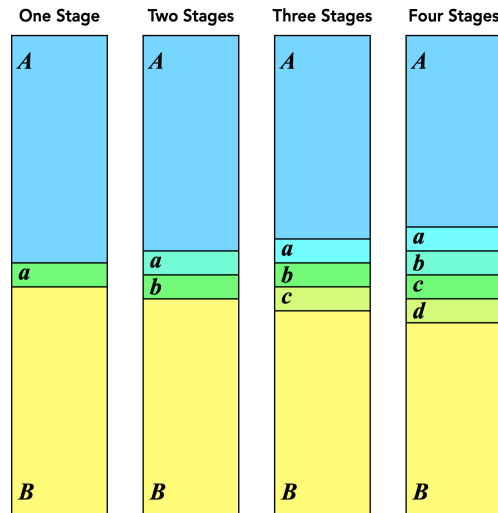


Figure 4.36. Anti-reflection stages with refractive indices a , b , c and d between two dielectrics with refractive indices A and B . One, two, three and four stage anti-reflection layers are shown.

Table 4.2. Anti-reflection layer formulae. The desired refractive index of stages, a , b , c , d ... in multi-stage anti-reflection coatings between two dielectrics with refractive indices A and B . The well-known formula for an anti-reflection stage (the geometric mean of the adjacent refractive indices) extended to two, three and four stages.

Stages	Refractive Index Formulae
One	$a = \sqrt{AB}$
Two	$a = \sqrt[3]{A^2B}$ $b = \sqrt[3]{AB^2}$
Three	$a = \sqrt[4]{A^3B}$ $b = \sqrt{AB}$ $c = \sqrt[4]{AB^3}$
Four	$a = \sqrt[5]{A^4B}$ $b = \sqrt[3]{A^2B}$ $c = \sqrt[3]{AB^2}$ $d = \sqrt[5]{AB^4}$

Zhang et al.¹²⁷ describe 500 stage and two-stage examples in the optical domain optimised using a genetic algorithm, referred to as graded index anti-reflection (GRIN AR) coatings. The two-stage design conforms to the above equations. They also mention the diminishing returns from further stages. When using artificial dielectrics implemented with metamaterial meshes in a lenslet, a large number of ARC stages is not useful; the size of such an ARC would swamp the size of the device. In the designs that follow, one, two or three ARC stages are considered.

The thickness of an anti-reflection stage implemented using a metal mesh based artificial dielectric is constrained to be an integral number of mesh layers. In the devices considered by the work reported here, the layer spacing is constant for all the mesh layers they contain, with the result that the thickness of anti-reflection stages can only take certain discrete sizes. This will tend to move the anti-reflection sweet spot away from the intended frequency, how far will be revealed by the modelling of the complete devices.

4.7.1 Possible structures

Consider the possible central columns of the two lenslets being designed here. Assuming the maximum refractive index available for polypropylene is approximately 4 and for silicon is 5, the columns will look like Figure 4.37 when using single stage ARCs. The main body does most of the work of the lenslet structure adding enough phase shift to allow rays passing through the edge columns to catch up. The ARC layer A matches the main body to the vacuum above the lenslet structure while ARC layer B matches it to the base dielectric that fills the space between the lenslet structure and the focus. The ARC layers themselves will, of course, also apply phase shift to the incident ray; as the ARC layers are different for each column this needs to be taken into account when calculating the desired thickness of the main body. The thicknesses of the ARC layers should be one quarter of the wavelength of the light passing through them at the centre frequency of the design (200 GHz for polypropylene and 150 GHz for silicon). This leads to sizes of 0.19 mm and 0.15 mm (ARC layers A and B respectively) for polypropylene and 0.22 mm and 0.12 mm for silicon.

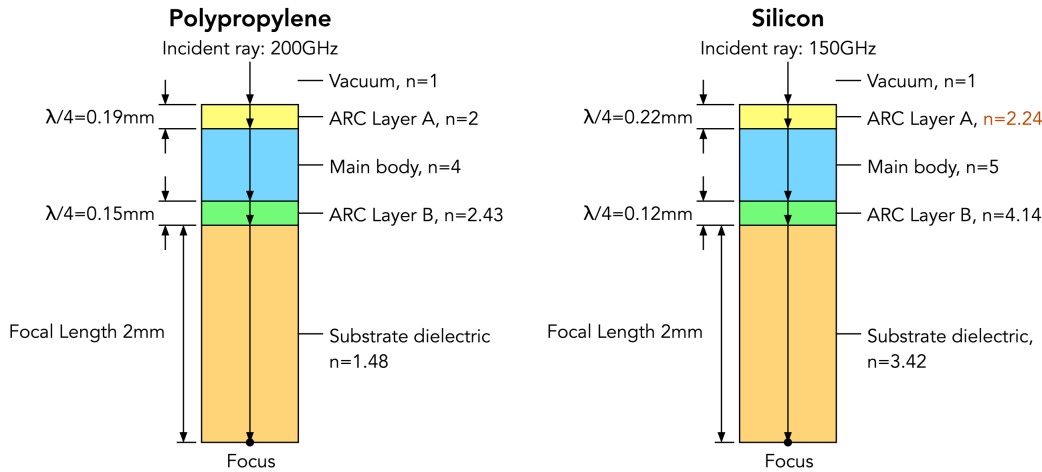


Figure 4.37. Lenslet structures with anti-reflection layers. Side view of the structure of a lenslet centre column for polypropylene (left) and silicon (right) showing main artificial dielectric and anti-reflection layers to match the main body to vacuum above and the base dielectric below. Notice that the silicon ARC layer A requires a refractive index that is not possible using capacitive metamaterial meshes; it requires a refractive index less than that of the silicon substrate itself.

Using this ARC scheme, the centre column is matched to its surroundings as part of the lenslet design process. This only works when the required refractive index of the ARC layers is greater than or equal to the refractive index of the base dielectric so that they can be made with capacitive metamaterial meshes. For the ARC layer that matches to the vacuum this can be a problem. In the silicon dielectric case in the diagram, ARC layer A requires a refractive index less than that of bulk silicon, therefore the match with vacuum cannot be made. This technique can be used with a polypropylene dielectric, although it does break down towards the edges of the lenslet when the main body refractive index falls below $n_{pp}^2 = 1.48^2 = 2.19$. The last few columns being unmatched does not affect performance too much, however.

With the silicon dielectric lenslet, a slightly different approach to matching with vacuum must be taken (Figure 4.38). This time the lenslet main body is matched to the bulk silicon both above and below with identical ARC layers. An additional ARC layer is then used to match the bulk silicon to vacuum at the top. Note that this extra ARC layer will have the same refractive index for all columns and therefore does not need to be taken into account during the main body calculations.

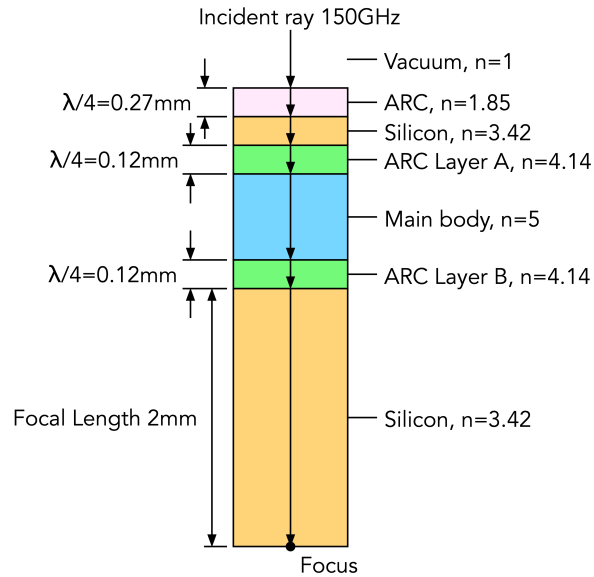


Figure 4.38. Silicon lenslet structure with anti-reflection layers. Side view of the structure of a lenslet centre column using a silicon dielectric. The lenslet main body is matched to silicon on both sides. Another ARC layer then matches silicon to vacuum above the main body.

4.7.2 The effects

To demonstrate the effect of ARC layers, possible centre columns for the polypropylene and silicon lenslets were modelled in HFSS. A block of artificial dielectric with the highest effective refractive index being contemplated, consisting of ten layers of metamaterial mesh, was surrounded by appropriate ARC layers as discussed. As it is only the effects of the ARC layers that are being studied by this modelling, the number of layers representing the main body of the lens column was unimportant and is not intended to be representative of the final lens structures.

Figure 4.39 shows HFSS models of the polypropylene centre column with and without anti-reflection layers. The main body consisted of ten layers of super-capacitive patches with a patch ratio of 118.75 in a unit cell of $160\text{ }\mu\text{m}$ with layer spacing of $50\text{ }\mu\text{m}$. Anti-reflection layer A, which matches the main body to vacuum, required a refractive index of 1.984 with thickness $189\text{ }\mu\text{m}$ and was implemented as four mesh layers of 58.7 patch ratio squares (total thickness $200\text{ }\mu\text{m}$). Anti-reflection layer B matching the main body to the bulk polypropylene (required refractive index of 2.414) was implemented as three mesh layers of patch ratio 73.64 squares (total thickness $150\text{ }\mu\text{m}$ compared with a required thickness of $155\text{ }\mu\text{m}$). These details are summarised in Table 4.3. The quantisation imposed by

the layer structure of the metamaterial meshes will more often than not require compromises to the anti-reflection layer thicknesses.

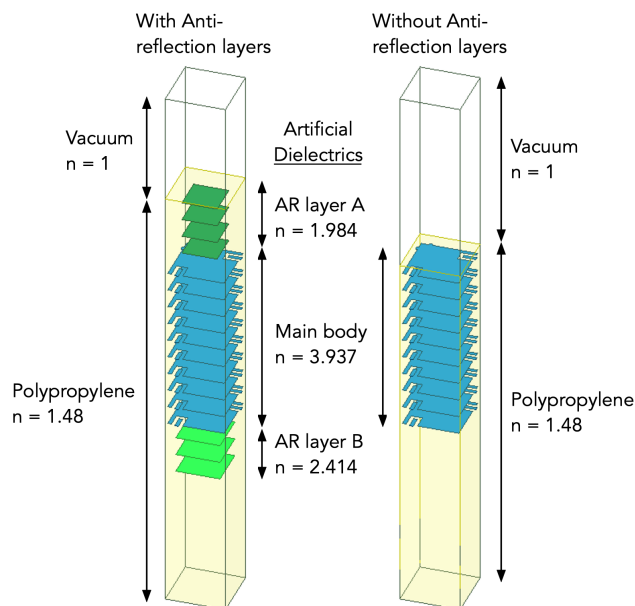


Figure 4.39. Possible centre columns of the polypropylene lenslet. The version on the left has the two anti-reflection layers, the version on the right does not.

Table 4.3. Polypropylene trial centre column structure details. The refractive indices and thicknesses of the layers of the trial centre column of the polypropylene lenslet.

	Refractive Index	Patch Ratio	Thickness ($\lambda/4$)	Number of Layers
Vacuum	1.0	-	-	-
AR Layer A	1.98	58.7	189 μm	4
Main Body	3.94	118.75	-	-
AR Layer B	2.41	73.6	155 μm	3
Polypropylene	1.48	-	-	-

The transmittances of these two column structures are shown in Figure 4.40. The anti-reflection layers reduce the attenuation significantly over most of the frequency band specified for the polypropylene lenslet. Incorporating them into the lenslet design will be important for its efficiency.

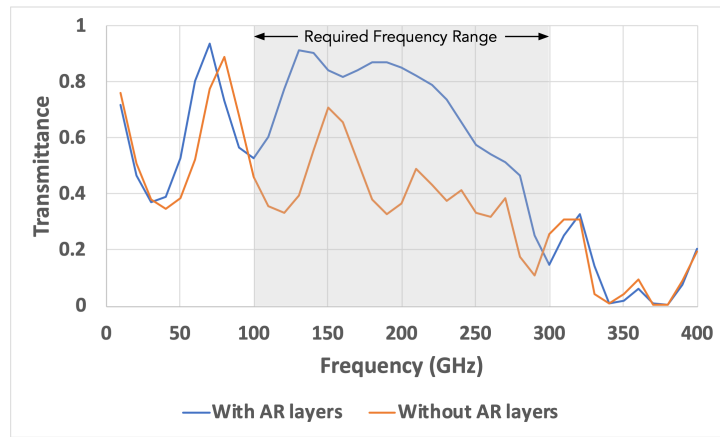


Figure 4.40. Polypropylene centre column attenuation. Transmittances of the centre column structure with and without the two anti-reflection layers for the polypropylene lenslet.

As already described, the anti-reflection layer on the top side of the silicon lenslet must follow a different structure; the main body is matched to the bulk silicon before that in turn is matched to the vacuum using a layer of suitable material. This could be silicon with drilled holes to reduce the refractive index appropriately (as assumed here) or a layer of quartz glass or similar material. The structures modelled in HFSS are shown in Figure 4.41 and the details are given in Table 4.4. Due to the larger metamaterial mesh layer spacing in the silicon lenslet, three stage anti-reflection layers could be used without the required total number of mesh layers becoming too large.

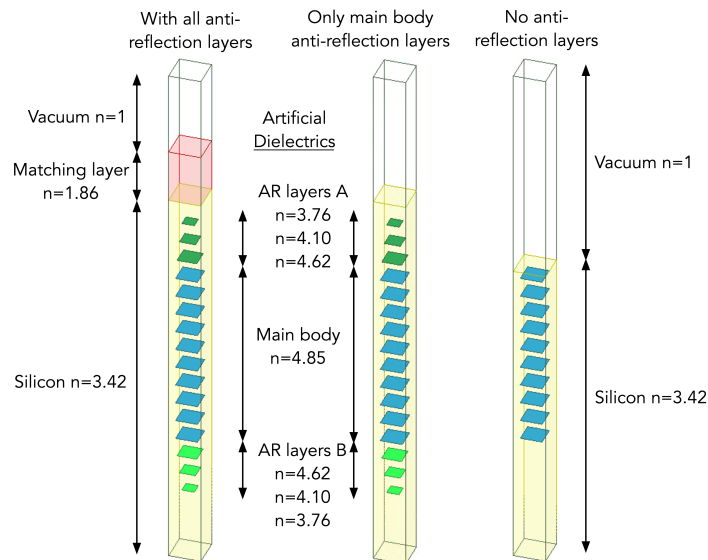


Figure 4.41. Possible centre columns of the silicon lenslet. The version on the left has three stage anti-reflection layers plus a vacuum matching layer, the version on the right has no anti-reflection layers.

Table 4.4. Silicon trial centre column structure details. The refractive indices and thicknesses of the layers of the trial centre column of the silicon lenslet.

	Refractive Index	Patch Ratio	Desired Thickness ($\lambda/4$)	Number of Layers
Vacuum	1.0	-	-	-
Matching Layer	1.84	-	272 μm	-
Silicon	3.42	-	100 μm	1
AR Layer A stage 1	3.76	38.86	133 μm	1
AR Layer A stage 2	4.10	50.23	122 μm	1
AR Layer A stage 3	4.62	61.01	108 μm	1
Main Body	4.86	68.05	-	-
AR Layer B stage 3	4.62	61.01	108 μm	1
AR Layer B stage 2	4.10	50.23	122 μm	1
AR Layer B stage 1	3.76	38.86	133 μm	1
Silicon	3.42	-	-	-

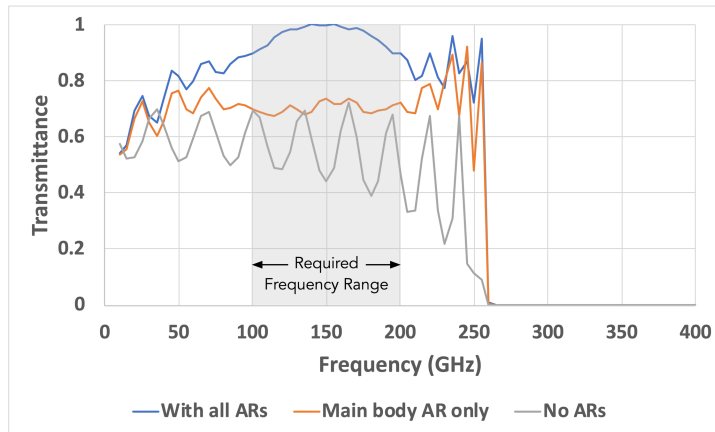


Figure 4.42. Silicon centre column attenuation. Transmittances of the centre column structure with and without anti-reflection layers for the silicon lenslet.

The transmittances of these two structures are shown in Figure 4.42. This shows that there is once again an advantage from utilising the anti-reflection layers. The attenuation in the desired frequency range is significantly reduced even more than seen earlier with the polypropylene lenslet. The effect of just the main body anti-reflection layers (i.e., no silicon to vacuum matching) is also included in the diagram. This indicates that the main body anti-reflection layers are responsible

for suppressing the ripples in the response while the silicon to vacuum matching suppresses a lot of reflection at that boundary leading to a transmittance of nearly one at the designed centre frequency.

4.8 Complete lenslet designs

Putting everything together allows the design of the model polypropylene and silicon lenslets to be settled on. A utility to automate the process was incorporated into the modelling tool described in Chapter 2. It first calculates the main body refractive indices required for each column and then adds the required anti-reflection layers, adjusting the main body refractive indices to account for the extra phase shift introduced. The catalogue of refractive index measurements allows selection of the patch ratio that implements the resulting refractive indices to meet the design specifications given in Table 4.1. The resulting designs were then modelled in Ansys HFSS. The process was repeated, varying the focal length compensation factor, until designs with the desired far field performance were achieved. The parameters of the design of the complete lenslets are summarised in Table 4.5.

Table 4.5. Lenslet design details.

Dielectric	Polypropylene	Polypropylene	Silicon
Patch Type	Square	Super-Capacitive	Square
Diameter	6.3 mm	6.3 mm	6.3mm
Center frequency	200 GHz	200 GHz	150 GHz
Bandwidth	200 GHz	200 GHz	100 GHz
Focal length (d in Figure 4.1)	2 mm	2 mm	2 mm
Layer spacing	50 μm	50 μm	100 μm
Number of layers	32	27	37
Lens thickness (b in Figure 4.1)	1.6 mm	1.35 mm	3.7 mm
Focal length compensation factor	1.0	1.0	1.25
Column width and metamaterial unit cell (g in Figure 4.1)	160 μm	160 μm	160 μm

4.8.1 Polypropylene

Two versions of the example polypropylene lenslet were created: the first using only conventional square patches, the second taking advantage of the extended refractive index range available from the super-capacitive patches of section 3.2.

The square patch design required 26 layers for the main body and 6 layers for the two single stage anti-reflection coatings on each side with a layer spacing of 50 μm for a total thickness of the lens structure of 1.60 mm. The focal length compensation factor (see section 4.1.1) used was 1.0, indicating that the design approximation that all ray bending takes place at the lens boundary is accurate for waves at 200 GHz in polypropylene because the lens thickness is not much greater than the wavelength.

Table 4.6. Square patch polypropylene lenslet, refractive indices. The refractive indices of the columns for the example polypropylene lenslet using square patches only. Column 1 is the centre, column 20 the outer edge. Darker blue indicates higher refractive index.

	Column Refractive Indices																			
	1	2	3	4	5	6	7	8	9	10	11	12	13	14	15	16	17	18	19	20
Layer	1	1.83	1.82	1.82	1.81	1.79	1.77	1.75	1.73	1.70	1.67	1.64	1.60	1.57	1.53	1.50	1.50	1.50	1.50	1.50
	2	1.83	1.82	1.82	1.81	1.79	1.77	1.75	1.73	1.70	1.67	1.64	1.60	1.57	1.53	1.50	1.50	1.50	1.50	1.50
	3	1.83	1.82	1.82	1.81	1.79	1.77	1.75	1.73	1.70	1.67	1.64	1.60	1.57	1.53	1.50	1.50	1.50	1.50	1.50
	4	3.34	3.33	3.30	3.26	3.21	3.15	3.07	2.99	2.89	2.79	2.69	2.57	2.46	2.33	2.21	2.07	1.93	1.79	1.65
	5	3.34	3.33	3.30	3.26	3.21	3.15	3.07	2.99	2.89	2.79	2.69	2.57	2.46	2.33	2.21	2.07	1.93	1.79	1.65
	6	3.34	3.33	3.30	3.26	3.21	3.15	3.07	2.99	2.89	2.79	2.69	2.57	2.46	2.33	2.21	2.07	1.93	1.79	1.65
	7	3.34	3.33	3.30	3.26	3.21	3.15	3.07	2.99	2.89	2.79	2.69	2.57	2.46	2.33	2.21	2.07	1.93	1.79	1.65
	8	3.34	3.33	3.30	3.26	3.21	3.15	3.07	2.99	2.89	2.79	2.69	2.57	2.46	2.33	2.21	2.07	1.93	1.79	1.65
	9	3.34	3.33	3.30	3.26	3.21	3.15	3.07	2.99	2.89	2.79	2.69	2.57	2.46	2.33	2.21	2.07	1.93	1.79	1.65
	10	3.34	3.33	3.30	3.26	3.21	3.15	3.07	2.99	2.89	2.79	2.69	2.57	2.46	2.33	2.21	2.07	1.93	1.79	1.65
	11	3.34	3.33	3.30	3.26	3.21	3.15	3.07	2.99	2.89	2.79	2.69	2.57	2.46	2.33	2.21	2.07	1.93	1.79	1.65
	12	3.34	3.33	3.30	3.26	3.21	3.15	3.07	2.99	2.89	2.79	2.69	2.57	2.46	2.33	2.21	2.07	1.93	1.79	1.65
	13	3.34	3.33	3.30	3.26	3.21	3.15	3.07	2.99	2.89	2.79	2.69	2.57	2.46	2.33	2.21	2.07	1.93	1.79	1.65
	14	3.34	3.33	3.30	3.26	3.21	3.15	3.07	2.99	2.89	2.79	2.69	2.57	2.46	2.33	2.21	2.07	1.93	1.79	1.65
	15	3.34	3.33	3.30	3.26	3.21	3.15	3.07	2.99	2.89	2.79	2.69	2.57	2.46	2.33	2.21	2.07	1.93	1.79	1.65
	16	3.34	3.33	3.30	3.26	3.21	3.15	3.07	2.99	2.89	2.79	2.69	2.57	2.46	2.33	2.21	2.07	1.93	1.79	1.65
	17	3.34	3.33	3.30	3.26	3.21	3.15	3.07	2.99	2.89	2.79	2.69	2.57	2.46	2.33	2.21	2.07	1.93	1.79	1.65
	18	3.34	3.33	3.30	3.26	3.21	3.15	3.07	2.99	2.89	2.79	2.69	2.57	2.46	2.33	2.21	2.07	1.93	1.79	1.65
	19	3.34	3.33	3.30	3.26	3.21	3.15	3.07	2.99	2.89	2.79	2.69	2.57	2.46	2.33	2.21	2.07	1.93	1.79	1.65
	20	3.34	3.33	3.30	3.26	3.21	3.15	3.07	2.99	2.89	2.79	2.69	2.57	2.46	2.33	2.21	2.07	1.93	1.79	1.65
	21	3.34	3.33	3.30	3.26	3.21	3.15	3.07	2.99	2.89	2.79	2.69	2.57	2.46	2.33	2.21	2.07	1.93	1.79	1.65
	22	3.34	3.33	3.30	3.26	3.21	3.15	3.07	2.99	2.89	2.79	2.69	2.57	2.46	2.33	2.21	2.07	1.93	1.79	1.65
	23	3.34	3.33	3.30	3.26	3.21	3.15	3.07	2.99	2.89	2.79	2.69	2.57	2.46	2.33	2.21	2.07	1.93	1.79	1.65
	24	3.34	3.33	3.30	3.26	3.21	3.15	3.07	2.99	2.89	2.79	2.69	2.57	2.46	2.33	2.21	2.07	1.93	1.79	1.65
	25	3.34	3.33	3.30	3.26	3.21	3.15	3.07	2.99	2.89	2.79	2.69	2.57	2.46	2.33	2.21	2.07	1.93	1.79	1.65
	26	3.34	3.33	3.30	3.26	3.21	3.15	3.07	2.99	2.89	2.79	2.69	2.57	2.46	2.33	2.21	2.07	1.93	1.79	1.65
	27	3.34	3.33	3.30	3.26	3.21	3.15	3.07	2.99	2.89	2.79	2.69	2.57	2.46	2.33	2.21	2.07	1.93	1.79	1.65
	28	3.34	3.33	3.30	3.26	3.21	3.15	3.07	2.99	2.89	2.79	2.69	2.57	2.46	2.33	2.21	2.07	1.93	1.79	1.65
	29	3.34	3.33	3.30	3.26	3.21	3.15	3.07	2.99	2.89	2.79	2.69	2.57	2.46	2.33	2.21	2.07	1.93	1.79	1.65
	30	2.24	2.23	2.23	2.21	2.19	2.17	2.15	2.12	2.08	2.05	2.01	1.97	1.92	1.87	1.82	1.76	1.70	1.64	1.57
	31	2.24	2.23	2.23	2.21	2.19	2.17	2.15	2.12	2.08	2.05	2.01	1.97	1.92	1.87	1.82	1.76	1.70	1.64	1.57
	32	2.24	2.23	2.23	2.21	2.19	2.17	2.15	2.12	2.08	2.05	2.01	1.97	1.92	1.87	1.82	1.76	1.70	1.64	1.57

The resulting patch sizes for the 160 μm unit cell are presented in Table 4.7 clearly showing the three groups of layers. The main body of the lenslet is layers 4-29. Layers 1-3 match the lenslet body to the vacuum, layers 30-32 match to polypropylene. Notice that the match to vacuum is not actually perfect as the patch ratio hits zero (at column 15) before reaching the edge of the lenslet. Column 20 is the 'reference' column whose delay all the other columns must compensate for.

Table 4.7. Square patch polypropylene lenslet, patch ratios. The patch ratios of the columns for the example polypropylene lenslet using square patches only. Column 1 is the centre, column 20 the outer edge. Darker red indicates higher patch ratio and thus higher refractive index.

	Column Patch Ratios																			
	1	2	3	4	5	6	7	8	9	10	11	12	13	14	15	16	17	18	19	20
Layer	1	45.9	45.7	45.3	44.6	43.8	42.7	41.5	40.1	36.9	33.3	29.4	25.1	20.6	9.8	0.0	0.0	0.0	0.0	0.0
	2	45.9	45.7	45.3	44.6	43.8	42.7	41.5	40.1	36.9	33.3	29.4	25.1	20.6	9.8	0.0	0.0	0.0	0.0	0.0
	3	45.9	45.7	45.3	44.6	43.8	42.7	41.5	40.1	36.9	33.3	29.4	25.1	20.6	9.8	0.0	0.0	0.0	0.0	0.0
	4	89.1	89.0	88.7	88.2	87.6	86.8	85.9	84.9	83.1	81.2	78.6	75.2	71.6	67.9	64.1	60.0	51.9	43.7	30.2
	5	89.1	89.0	88.7	88.2	87.6	86.8	85.9	84.9	83.1	81.2	78.6	75.2	71.6	67.9	64.1	60.0	51.9	43.7	30.2
	6	89.1	89.0	88.7	88.2	87.6	86.8	85.9	84.9	83.1	81.2	78.6	75.2	71.6	67.9	64.1	60.0	51.9	43.7	30.2
	7	89.1	89.0	88.7	88.2	87.6	86.8	85.9	84.9	83.1	81.2	78.6	75.2	71.6	67.9	64.1	60.0	51.9	43.7	30.2
	8	89.1	89.0	88.7	88.2	87.6	86.8	85.9	84.9	83.1	81.2	78.6	75.2	71.6	67.9	64.1	60.0	51.9	43.7	30.2
	9	89.1	89.0	88.7	88.2	87.6	86.8	85.9	84.9	83.1	81.2	78.6	75.2	71.6	67.9	64.1	60.0	51.9	43.7	30.2
	10	89.1	89.0	88.7	88.2	87.6	86.8	85.9	84.9	83.1	81.2	78.6	75.2	71.6	67.9	64.1	60.0	51.9	43.7	30.2
	11	89.1	89.0	88.7	88.2	87.6	86.8	85.9	84.9	83.1	81.2	78.6	75.2	71.6	67.9	64.1	60.0	51.9	43.7	30.2
	12	89.1	89.0	88.7	88.2	87.6	86.8	85.9	84.9	83.1	81.2	78.6	75.2	71.6	67.9	64.1	60.0	51.9	43.7	30.2
	13	89.1	89.0	88.7	88.2	87.6	86.8	85.9	84.9	83.1	81.2	78.6	75.2	71.6	67.9	64.1	60.0	51.9	43.7	30.2
	14	89.1	89.0	88.7	88.2	87.6	86.8	85.9	84.9	83.1	81.2	78.6	75.2	71.6	67.9	64.1	60.0	51.9	43.7	30.2
	15	89.1	89.0	88.7	88.2	87.6	86.8	85.9	84.9	83.1	81.2	78.6	75.2	71.6	67.9	64.1	60.0	51.9	43.7	30.2
	16	89.1	89.0	88.7	88.2	87.6	86.8	85.9	84.9	83.1	81.2	78.6	75.2	71.6	67.9	64.1	60.0	51.9	43.7	30.2
	17	89.1	89.0	88.7	88.2	87.6	86.8	85.9	84.9	83.1	81.2	78.6	75.2	71.6	67.9	64.1	60.0	51.9	43.7	30.2
	18	89.1	89.0	88.7	88.2	87.6	86.8	85.9	84.9	83.1	81.2	78.6	75.2	71.6	67.9	64.1	60.0	51.9	43.7	30.2
	19	89.1	89.0	88.7	88.2	87.6	86.8	85.9	84.9	83.1	81.2	78.6	75.2	71.6	67.9	64.1	60.0	51.9	43.7	30.2
	20	89.1	89.0	88.7	88.2	87.6	86.8	85.9	84.9	83.1	81.2	78.6	75.2	71.6	67.9	64.1	60.0	51.9	43.7	30.2
	21	89.1	89.0	88.7	88.2	87.6	86.8	85.9	84.9	83.1	81.2	78.6	75.2	71.6	67.9	64.1	60.0	51.9	43.7	30.2
	22	89.1	89.0	88.7	88.2	87.6	86.8	85.9	84.9	83.1	81.2	78.6	75.2	71.6	67.9	64.1	60.0	51.9	43.7	30.2
	23	89.1	89.0	88.7	88.2	87.6	86.8	85.9	84.9	83.1	81.2	78.6	75.2	71.6	67.9	64.1	60.0	51.9	43.7	30.2
	24	89.1	89.0	88.7	88.2	87.6	86.8	85.9	84.9	83.1	81.2	78.6	75.2	71.6	67.9	64.1	60.0	51.9	43.7	30.2
	25	89.1	89.0	88.7	88.2	87.6	86.8	85.9	84.9	83.1	81.2	78.6	75.2	71.6	67.9	64.1	60.0	51.9	43.7	30.2
	26	89.1	89.0	88.7	88.2	87.6	86.8	85.9	84.9	83.1	81.2	78.6	75.2	71.6	67.9	64.1	60.0	51.9	43.7	30.2
	27	89.1	89.0	88.7	88.2	87.6	86.8	85.9	84.9	83.1	81.2	78.6	75.2	71.6	67.9	64.1	60.0	51.9	43.7	30.2
	28	89.1	89.0	88.7	88.2	87.6	86.8	85.9	84.9	83.1	81.2	78.6	75.2	71.6	67.9	64.1	60.0	51.9	43.7	30.2
	29	89.1	89.0	88.7	88.2	87.6	86.8	85.9	84.9	83.1	81.2	78.6	75.2	71.6	67.9	64.1	60.0	51.9	43.7	30.2
	30	65.1	64.9	64.7	64.3	63.7	63.1	62.3	61.4	60.4	58.6	56.3	53.9	51.2	48.4	45.3	42.1	37.0	29.3	21.1
	31	65.1	64.9	64.7	64.3	63.7	63.1	62.3	61.4	60.4	58.6	56.3	53.9	51.2	48.4	45.3	42.1	37.0	29.3	21.1
	32	65.1	64.9	64.7	64.3	63.7	63.1	62.3	61.4	60.4	58.6	56.3	53.9	51.2	48.4	45.3	42.1	37.0	29.3	21.1

Figure 4.43 shows a cross section of the electric field magnitude at 200 GHz from the HFSS modelling of this design, overlaid with the lenslet structure. The model was excited by a Gaussian beam located at the focus with a waist appropriate for the frequency such that the transmitted beam filled much of the lens diameter. For the electric field magnitudes and the far fields over the whole frequency range see Figure 4.44. There are signs of over focussing on the upper end of the frequency range (300 GHz) and under focussing on the lower end (100 GHz), but overall, the qualitative performance looks good. The full width, half maxima of the far field at various frequencies is given in Table 4.8 (along with the beam waist of the excitation Gaussian).

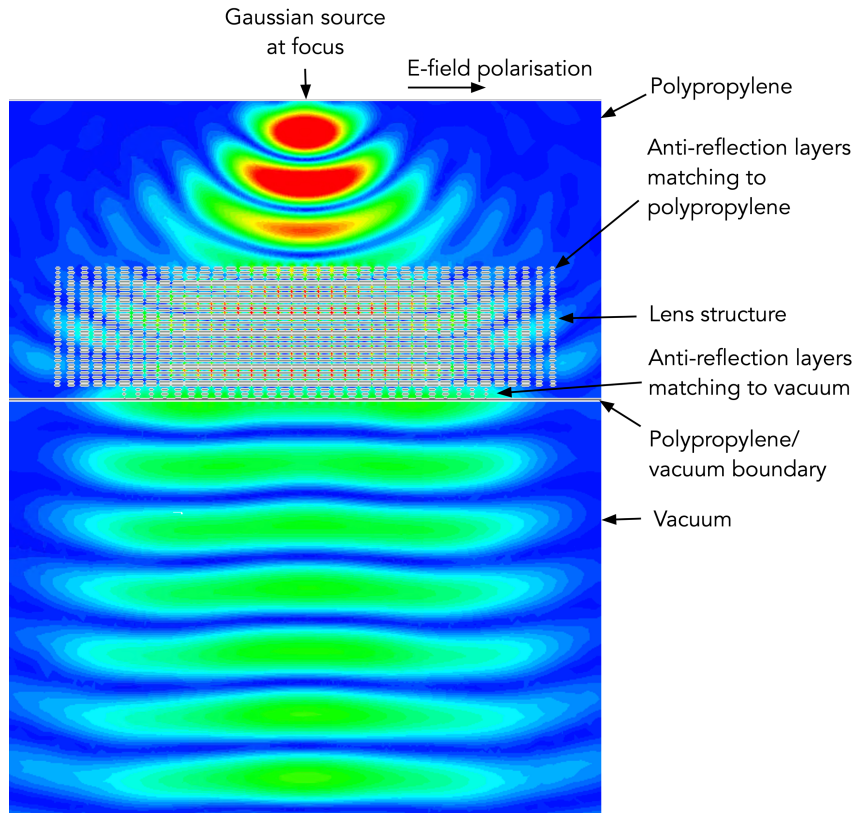


Figure 4.43. Polypropylene lenslet, square patches, E field. The electric field magnitude of the example polypropylene lenslet using artificial dielectrics made with square patches at 200 GHz.

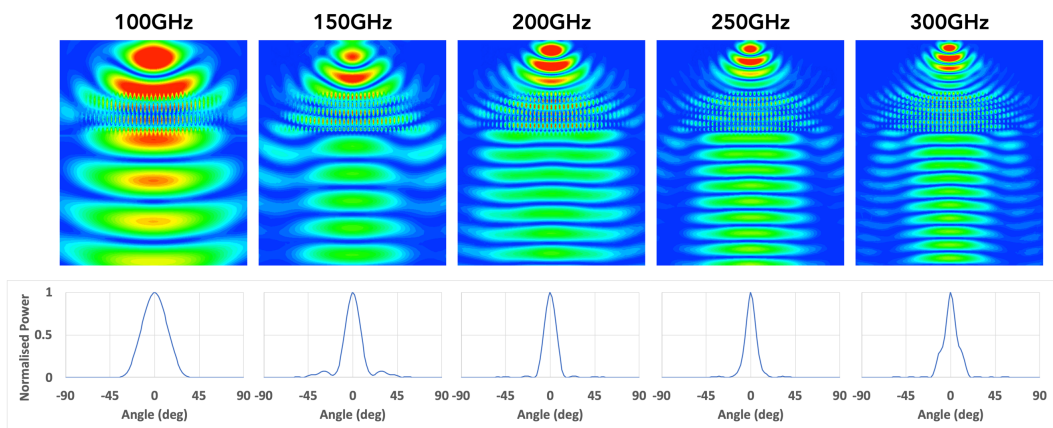


Figure 4.44. Polypropylene lenslet, square patches, far field. Electric field magnitude and far field plots (power normalised to 1 at an angle of zero degrees) for the polypropylene lenslet using square patches. There's evidence of a over focussing at 300 GHz.

Table 4.8. FWHM for the square patch polypropylene design. The FWHM beam angle measured from the modelling matches the calculated value for 200 GHz (not surprising, this is the frequency the lens was optimised for). The measured value deviates from the calculated for the other frequencies, especially 300 GHz.

Frequency	Excitation beam waist radius, w_0	Measured far field FWHM beam angle	Calculate FWHM beam angle
100 GHz	0.435 mm	16.2°	13.0°
150 GHz	0.288 mm	9.3°	8.6°
200 GHz	0.215 mm	6.5°	6.5°
250 GHz	0.172 mm	7.5°	5.2°
300 GHz	0.144 mm	10.3°	4.3°

Using super-capacitive patches allows the example polypropylene lenslet to be implemented using fewer layers. The version presented in Figure 4.45 has 27 layers and utilises patch ratios up to 118 with a single centred finger and a 15 μm minimum feature size. The refractive indices for each layer and column are listed in Table 4.10 and the patch ratios are in Table 4.11.

Figure 4.46 shows the performance of the super-capacitive patches over the whole frequency range. The predicted reduction in bandwidth is quite apparent, at 300 GHz, the side lobes are becoming prominent. The far field plots also show the equivalent data obtained from square patches using the same normalisation, showing how closely the characteristics match except for the outer frequencies of the design range (100 and 300 GHz).

Table 4.9. FWHM for the super-capacitive patch polypropylene design. The FWHM beam angle measured from the modelling is a good match for the calculated value at 200 GHz. The measured value deviates from the calculated for the other frequencies, especially 300 GHz. The values for the square patch example are also included in this table for comparison purposes.

Frequency	Excitation beam waist radius, w_0	Measured far field FWHM beam angle	Calculated FWHM beam angle	Measured FWHM for square patches
100 GHz	0.435 mm	16.2°	13.0°	16.2°
150 GHz	0.288 mm	8.0°	8.6°	9.3°
200 GHz	0.215 mm	6.3°	6.5°	6.5°
250 GHz	0.172 mm	7.7°	5.2°	7.5°
300 GHz	0.144 mm	11.4°	4.3°	10.3°

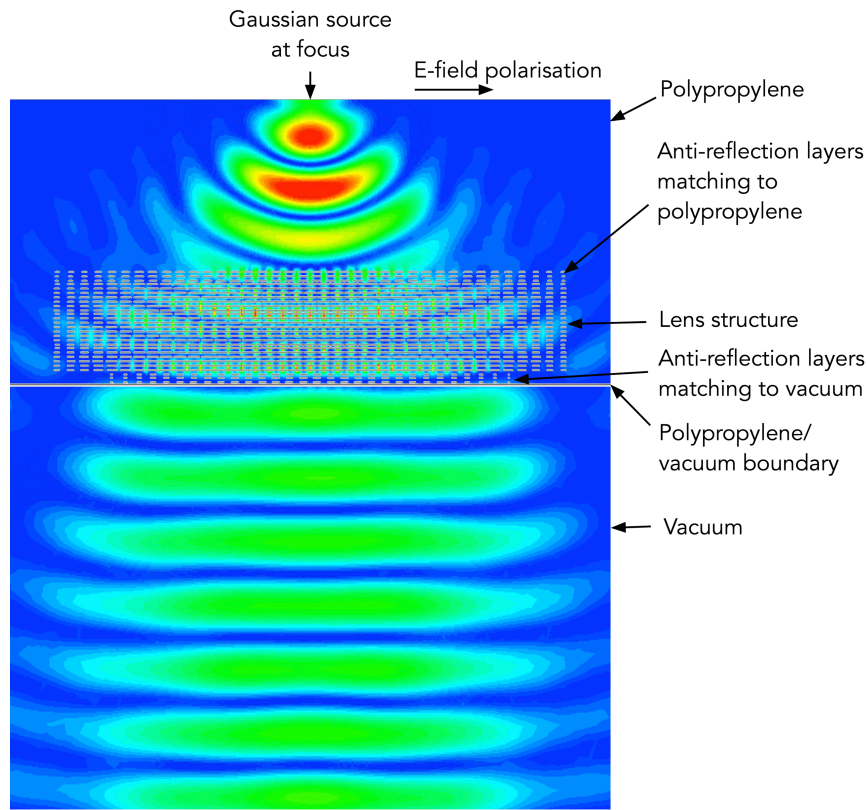


Figure 4.45. Polypropylene lenslet, super-capacitive, E field. The electric field magnitude at 200 GHz of the example polypropylene lenslet using artificial dielectrics made with super-capacitive patches.

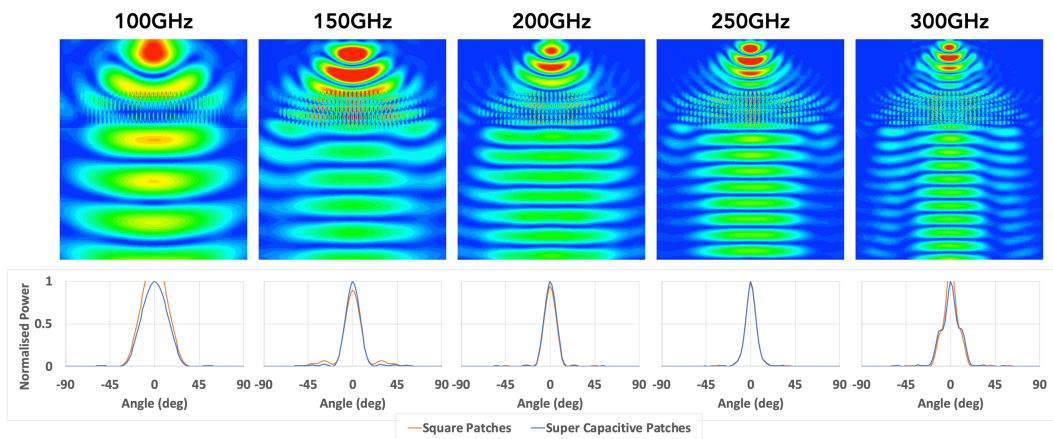


Figure 4.46. Polypropylene lenslet, super-capacitive, far field. Electric field magnitude and far field plots (power normalised to 1 at an angle of zero degrees) for the polypropylene lenslet using super-capacitive patches. The far field for the square patch version is also plotted (in orange), normalised to the same value. The performance of the super-capacitive patches is quite poor at 300 GHz, as expected.

Table 4.10. Super-capacitive patch polypropylene lenslet, refractive indices. The refractive indices of the columns for the example polypropylene lenslet using super-capacitive patches. Column 1 is the centre, column 20 the outer edge. Darker blue indicates higher refractive index.

	Column Refractive Indices																			
	1	2	3	4	5	6	7	8	9	10	11	12	13	14	15	16	17	18	19	20
Layer	1	1.96	1.96	1.95	1.93	1.92	1.89	1.87	1.84	1.81	1.77	1.73	1.69	1.64	1.59	1.54	1.50	1.50	1.50	1.50
	2	1.96	1.96	1.95	1.93	1.92	1.89	1.87	1.84	1.81	1.77	1.73	1.69	1.64	1.59	1.54	1.50	1.50	1.50	1.50
	3	1.96	1.96	1.95	1.93	1.92	1.89	1.87	1.84	1.81	1.77	1.73	1.69	1.64	1.59	1.54	1.50	1.50	1.50	1.50
	4	3.85	3.83	3.79	3.74	3.67	3.59	3.49	3.38	3.26	3.13	2.99	2.85	2.70	2.54	2.38	2.22	2.04	1.86	1.68
	5	3.85	3.83	3.79	3.74	3.67	3.59	3.49	3.38	3.26	3.13	2.99	2.85	2.70	2.54	2.38	2.22	2.04	1.86	1.68
	6	3.85	3.83	3.79	3.74	3.67	3.59	3.49	3.38	3.26	3.13	2.99	2.85	2.70	2.54	2.38	2.22	2.04	1.86	1.68
	7	3.85	3.83	3.79	3.74	3.67	3.59	3.49	3.38	3.26	3.13	2.99	2.85	2.70	2.54	2.38	2.22	2.04	1.86	1.68
	8	3.85	3.83	3.79	3.74	3.67	3.59	3.49	3.38	3.26	3.13	2.99	2.85	2.70	2.54	2.38	2.22	2.04	1.86	1.68
	9	3.85	3.83	3.79	3.74	3.67	3.59	3.49	3.38	3.26	3.13	2.99	2.85	2.70	2.54	2.38	2.22	2.04	1.86	1.68
	10	3.85	3.83	3.79	3.74	3.67	3.59	3.49	3.38	3.26	3.13	2.99	2.85	2.70	2.54	2.38	2.22	2.04	1.86	1.68
	11	3.85	3.83	3.79	3.74	3.67	3.59	3.49	3.38	3.26	3.13	2.99	2.85	2.70	2.54	2.38	2.22	2.04	1.86	1.68
	12	3.85	3.83	3.79	3.74	3.67	3.59	3.49	3.38	3.26	3.13	2.99	2.85	2.70	2.54	2.38	2.22	2.04	1.86	1.68
	13	3.85	3.83	3.79	3.74	3.67	3.59	3.49	3.38	3.26	3.13	2.99	2.85	2.70	2.54	2.38	2.22	2.04	1.86	1.68
	14	3.85	3.83	3.79	3.74	3.67	3.59	3.49	3.38	3.26	3.13	2.99	2.85	2.70	2.54	2.38	2.22	2.04	1.86	1.68
	15	3.85	3.83	3.79	3.74	3.67	3.59	3.49	3.38	3.26	3.13	2.99	2.85	2.70	2.54	2.38	2.22	2.04	1.86	1.68
	16	3.85	3.83	3.79	3.74	3.67	3.59	3.49	3.38	3.26	3.13	2.99	2.85	2.70	2.54	2.38	2.22	2.04	1.86	1.68
	17	3.85	3.83	3.79	3.74	3.67	3.59	3.49	3.38	3.26	3.13	2.99	2.85	2.70	2.54	2.38	2.22	2.04	1.86	1.68
	18	3.85	3.83	3.79	3.74	3.67	3.59	3.49	3.38	3.26	3.13	2.99	2.85	2.70	2.54	2.38	2.22	2.04	1.86	1.68
	19	3.85	3.83	3.79	3.74	3.67	3.59	3.49	3.38	3.26	3.13	2.99	2.85	2.70	2.54	2.38	2.22	2.04	1.86	1.68
	20	3.85	3.83	3.79	3.74	3.67	3.59	3.49	3.38	3.26	3.13	2.99	2.85	2.70	2.54	2.38	2.22	2.04	1.86	1.68
	21	3.85	3.83	3.79	3.74	3.67	3.59	3.49	3.38	3.26	3.13	2.99	2.85	2.70	2.54	2.38	2.22	2.04	1.86	1.68
	22	3.85	3.83	3.79	3.74	3.67	3.59	3.49	3.38	3.26	3.13	2.99	2.85	2.70	2.54	2.38	2.22	2.04	1.86	1.68
	23	3.85	3.83	3.79	3.74	3.67	3.59	3.49	3.38	3.26	3.13	2.99	2.85	2.70	2.54	2.38	2.22	2.04	1.86	1.68
	24	3.85	3.83	3.79	3.74	3.67	3.59	3.49	3.38	3.26	3.13	2.99	2.85	2.70	2.54	2.38	2.22	2.04	1.86	1.68
	25	2.40	2.40	2.39	2.37	2.35	2.32	2.29	2.25	2.21	2.17	2.12	2.07	2.01	1.95	1.89	1.82	1.75	1.67	1.59
	26	2.40	2.40	2.39	2.37	2.35	2.32	2.29	2.25	2.21	2.17	2.12	2.07	2.01	1.95	1.89	1.82	1.75	1.67	1.59
	27	2.40	2.40	2.39	2.37	2.35	2.32	2.29	2.25	2.21	2.17	2.12	2.07	2.01	1.95	1.89	1.82	1.75	1.67	1.59

Table 4.11. Example polypropylene lenslet, super-capacitive patches. The patch ratios of the columns for the example polypropylene lenslet using super-capacitive patches. Column 1 is the centre, column 20 the outer edge. Darker red indicates higher patch ratio and thus higher refractive index.

	Column Patch Ratios																			
	1	2	3	4	5	6	7	8	9	10	11	12	13	14	15	16	17	18	19	20
Layer	1	53.7	53.4	52.9	52.1	51.0	49.7	48.2	46.5	44.6	42.5	40.2	35.3	29.8	23.9	14.4	0.0	0.0	0.0	0.0
	2	53.7	53.4	52.9	52.1	51.0	49.7	48.2	46.5	44.6	42.5	40.2	35.3	29.8	23.9	14.4	0.0	0.0	0.0	0.0
	3	53.7	53.4	52.9	52.1	51.0	49.7	48.2	46.5	44.6	42.5	40.2	35.3	29.8	23.9	14.4	0.0	0.0	0.0	0.0
	4	118.1	117.3	115.7	113.4	93.3	92.2	91.0	89.6	88.2	86.6	85.0	82.2	78.9	74.2	69.4	64.4	58.3	48.0	34.7
	5	118.1	117.3	115.7	113.4	93.3	92.2	91.0	89.6	88.2	86.6	85.0	82.2	78.9	74.2	69.4	64.4	58.3	48.0	34.7
	6	118.1	117.3	115.7	113.4	93.3	92.2	91.0	89.6	88.2	86.6	85.0	82.2	78.9	74.2	69.4	64.4	58.3	48.0	34.7
	7	118.1	117.3	115.7	113.4	93.3	92.2	91.0	89.6	88.2	86.6	85.0	82.2	78.9	74.2	69.4	64.4	58.3	48.0	34.7
	8	118.1	117.3	115.7	113.4	93.3	92.2	91.0	89.6	88.2	86.6	85.0	82.2	78.9	74.2	69.4	64.4	58.3	48.0	34.7
	9	118.1	117.3	115.7	113.4	93.3	92.2	91.0	89.6	88.2	86.6	85.0	82.2	78.9	74.2	69.4	64.4	58.3	48.0	34.7
	10	118.1	117.3	115.7	113.4	93.3	92.2	91.0	89.6	88.2	86.6	85.0	82.2	78.9	74.2	69.4	64.4	58.3	48.0	34.7
	11	118.1	117.3	115.7	113.4	93.3	92.2	91.0	89.6	88.2	86.6	85.0	82.2	78.9	74.2	69.4	64.4	58.3	48.0	34.7
	12	118.1	117.3	115.7	113.4	93.3	92.2	91.0	89.6	88.2	86.6	85.0	82.2	78.9	74.2	69.4	64.4	58.3	48.0	34.7
	13	118.1	117.3	115.7	113.4	93.3	92.2	91.0	89.6	88.2	86.6	85.0	82.2	78.9	74.2	69.4	64.4	58.3	48.0	34.7
	14	118.1	117.3	115.7	113.4	93.3	92.2	91.0	89.6	88.2	86.6	85.0	82.2	78.9	74.2	69.4	64.4	58.3	48.0	34.7
	15	118.1	117.3	115.7	113.4	93.3	92.2	91.0	89.6	88.2	86.6	85.0	82.2	78.9	74.2	69.4	64.4	58.3	48.0	34.7
	16	118.1	117.3	115.7	113.4	93.3	92.2	91.0	89.6	88.2	86.6	85.0	82.2	78.9	74.2	69.4	64.4	58.3	48.0	34.7
	17	118.1	117.3	115.7	113.4	93.3	92.2	91.0	89.6	88.2	86.6	85.0	82.2	78.9	74.2	69.4	64.4	58.3	48.0	34.7
	18	118.1	117.3	115.7	113.4	93.3	92.2	91.0	89.6	88.2	86.6	85.0	82.2	78.9	74.2	69.4	64.4	58.3	48.0	34.7
	19	118.1	117.3	115.7	113.4	93.3	92.2	91.0	89.6	88.2	86.6	85.0	82.2	78.9	74.2	69.4	64.4	58.3	48.0	34.7
	20	118.1	117.3	115.7	113.4	93.3	92.2	91.0	89.6	88.2	86.6	85.0	82.2	78.9	74.2	69.4	64.4	58.3	48.0	34.7
	21	118.1	117.3	115.7	113.4	93.3	92.2	91.0	89.6	88.2	86.6	85.0	82.2	78.9	74.2	69.4	64.4	58.3	48.0	34.7
	22	118.1	117.3	115.7	113.4	93.3	92.2	91.0	89.6	88.2	86.6	85.0	82.2	78.9	74.2	69.4	64.4	58.3	48.0	34.7
	23	118.1	117.3	115.7	113.4	93.3	92.2	91.0	89.6	88.2	86.6	85.0	82.2	78.9	74.2	69.4	64.4	58.3	48.0	34.7
	24	118.1	117.3	115.7	113.4	93.3	92.2	91.0	89.6	88.2	86.6	85.0	82.2	78.9	74.2	69.4	64.4	58.3	48.0	34.7
	25	70.0	69.8	69.5	69.0	68.3	67.5	66.5	65.5	64.2	62.9	61.5	59.8	56.6	53.2	49.5	45.6	41.4	33.3	23.2
	26	70.0	69.8	69.5	69.0	68.3	67.5	66.5	65.5	64.2	62.9	61.5	59.8	56.6	53.2	49.5	45.6	41.4	33.3	23.2
	27	70.0	69.8	69.5	69.0	68.3	67.5	66.5	65.5	64.2	62.9	61.5	59.8	56.6	53.2	49.5	45.6	41.4	33.3	23.2

4.8.2 Silicon

The example silicon lenslet was designed with 37 mesh layers in total consisting of 31 mesh layers for the main body and three-stage anti-reflection layers (A and B) on each side. The patch ratios used are shown in Table 4.12, the maximum was 70.1 (the centre columns of layer 1) in line with the decisions made earlier. The corresponding refractive indices are shown in Table 4.13. The design required a focal length compensation factor of 1.25.

Figure 4.47 shows the resulting electric field magnitude of a cross-section of the model. The waist of the excitation gaussian beam was chosen so that the output beam filled the lens. The wavelength changes as the light propagates across the transitions between the silicon dielectric, the matching layer and the vacuum are apparent.

Figure 4.48 shows the electric field magnitude and the normalised far field for the whole frequency range. These indicate that the lenslet behaves well from 100 to 175 GHz. The beam below the lenslet (in the vacuum) is parallel at the designed centre frequency of 150 GHz, under focussed at lower frequencies and over focussed at higher frequencies, as expected from earlier work on the refractive index of artificial dielectrics. At 200 GHz the side lobes are becoming particularly prominent.

Table 4.14 presents the beam waists used for the gaussian excitation beam for each frequency, along with the measured and calculated FWHM beam angles. These show that the lens is performing reasonably at the centre frequency, but further optimisation may be possible.

Table 4.12. Example silicon lenslet, square patches. Patch ratios for the cells of the 37 layer silicon lenslet using a 160 μm unit cell. Column 1 is the centre, 20 is the outer edge. Darker red indicates higher patch ratio and thus higher refractive index.

		Column Patch Ratios																			
		1	2	3	4	5	6	7	8	9	10	11	12	13	14	15	16	17	18	19	20
Layer	1	40.3	40.2	40.1	39.8	39.1	38.2	37.2	36.0	34.7	33.2	31.6	29.8	27.9	25.9	23.8	21.5	18.2	13.2	7.9	0.0
	2	51.8	51.6	51.4	51.0	50.4	49.7	49.0	48.1	47.0	45.9	44.7	43.4	42.0	40.5	36.9	32.2	27.2	22.1	13.5	0.0
	3	62.4	62.3	62.0	61.7	61.2	60.6	59.7	58.3	56.6	54.8	52.9	50.8	48.5	46.2	43.7	41.1	35.6	27.7	19.1	0.0
	4	70.1	69.9	69.6	69.0	68.3	67.4	66.4	65.2	63.9	62.4	60.9	58.6	55.5	52.2	48.7	45.2	41.5	33.4	22.4	0.0
	5	70.1	69.9	69.6	69.0	68.3	67.4	66.4	65.2	63.9	62.4	60.9	58.6	55.5	52.2	48.7	45.2	41.5	33.4	22.4	0.0
	6	70.1	69.9	69.6	69.0	68.3	67.4	66.4	65.2	63.9	62.4	60.9	58.6	55.5	52.2	48.7	45.2	41.5	33.4	22.4	0.0
	7	70.1	69.9	69.6	69.0	68.3	67.4	66.4	65.2	63.9	62.4	60.9	58.6	55.5	52.2	48.7	45.2	41.5	33.4	22.4	0.0
	8	70.1	69.9	69.6	69.0	68.3	67.4	66.4	65.2	63.9	62.4	60.9	58.6	55.5	52.2	48.7	45.2	41.5	33.4	22.4	0.0
	9	70.1	69.9	69.6	69.0	68.3	67.4	66.4	65.2	63.9	62.4	60.9	58.6	55.5	52.2	48.7	45.2	41.5	33.4	22.4	0.0
	10	70.1	69.9	69.6	69.0	68.3	67.4	66.4	65.2	63.9	62.4	60.9	58.6	55.5	52.2	48.7	45.2	41.5	33.4	22.4	0.0
	11	70.1	69.9	69.6	69.0	68.3	67.4	66.4	65.2	63.9	62.4	60.9	58.6	55.5	52.2	48.7	45.2	41.5	33.4	22.4	0.0
	12	70.1	69.9	69.6	69.0	68.3	67.4	66.4	65.2	63.9	62.4	60.9	58.6	55.5	52.2	48.7	45.2	41.5	33.4	22.4	0.0
	13	70.1	69.9	69.6	69.0	68.3	67.4	66.4	65.2	63.9	62.4	60.9	58.6	55.5	52.2	48.7	45.2	41.5	33.4	22.4	0.0
	14	70.1	69.9	69.6	69.0	68.3	67.4	66.4	65.2	63.9	62.4	60.9	58.6	55.5	52.2	48.7	45.2	41.5	33.4	22.4	0.0
	15	70.1	69.9	69.6	69.0	68.3	67.4	66.4	65.2	63.9	62.4	60.9	58.6	55.5	52.2	48.7	45.2	41.5	33.4	22.4	0.0
	16	70.1	69.9	69.6	69.0	68.3	67.4	66.4	65.2	63.9	62.4	60.9	58.6	55.5	52.2	48.7	45.2	41.5	33.4	22.4	0.0
	17	70.1	69.9	69.6	69.0	68.3	67.4	66.4	65.2	63.9	62.4	60.9	58.6	55.5	52.2	48.7	45.2	41.5	33.4	22.4	0.0
	18	70.1	69.9	69.6	69.0	68.3	67.4	66.4	65.2	63.9	62.4	60.9	58.6	55.5	52.2	48.7	45.2	41.5	33.4	22.4	0.0
	19	70.1	69.9	69.6	69.0	68.3	67.4	66.4	65.2	63.9	62.4	60.9	58.6	55.5	52.2	48.7	45.2	41.5	33.4	22.4	0.0
	20	70.1	69.9	69.6	69.0	68.3	67.4	66.4	65.2	63.9	62.4	60.9	58.6	55.5	52.2	48.7	45.2	41.5	33.4	22.4	0.0
	21	70.1	69.9	69.6	69.0	68.3	67.4	66.4	65.2	63.9	62.4	60.9	58.6	55.5	52.2	48.7	45.2	41.5	33.4	22.4	0.0
	22	70.1	69.9	69.6	69.0	68.3	67.4	66.4	65.2	63.9	62.4	60.9	58.6	55.5	52.2	48.7	45.2	41.5	33.4	22.4	0.0
	23	70.1	69.9	69.6	69.0	68.3	67.4	66.4	65.2	63.9	62.4	60.9	58.6	55.5	52.2	48.7	45.2	41.5	33.4	22.4	0.0
	24	70.1	69.9	69.6	69.0	68.3	67.4	66.4	65.2	63.9	62.4	60.9	58.6	55.5	52.2	48.7	45.2	41.5	33.4	22.4	0.0
	25	70.1	69.9	69.6	69.0	68.3	67.4	66.4	65.2	63.9	62.4	60.9	58.6	55.5	52.2	48.7	45.2	41.5	33.4	22.4	0.0
	26	70.1	69.9	69.6	69.0	68.3	67.4	66.4	65.2	63.9	62.4	60.9	58.6	55.5	52.2	48.7	45.2	41.5	33.4	22.4	0.0
	27	70.1	69.9	69.6	69.0	68.3	67.4	66.4	65.2	63.9	62.4	60.9	58.6	55.5	52.2	48.7	45.2	41.5	33.4	22.4	0.0
	28	70.1	69.9	69.6	69.0	68.3	67.4	66.4	65.2	63.9	62.4	60.9	58.6	55.5	52.2	48.7	45.2	41.5	33.4	22.4	0.0
	29	70.1	69.9	69.6	69.0	68.3	67.4	66.4	65.2	63.9	62.4	60.9	58.6	55.5	52.2	48.7	45.2	41.5	33.4	22.4	0.0
	30	70.1	69.9	69.6	69.0	68.3	67.4	66.4	65.2	63.9	62.4	60.9	58.6	55.5	52.2	48.7	45.2	41.5	33.4	22.4	0.0
	31	70.1	69.9	69.6	69.0	68.3	67.4	66.4	65.2	63.9	62.4	60.9	58.6	55.5	52.2	48.7	45.2	41.5	33.4	22.4	0.0
	32	70.1	69.9	69.6	69.0	68.3	67.4	66.4	65.2	63.9	62.4	60.9	58.6	55.5	52.2	48.7	45.2	41.5	33.4	22.4	0.0
	33	70.1	69.9	69.6	69.0	68.3	67.4	66.4	65.2	63.9	62.4	60.9	58.6	55.5	52.2	48.7	45.2	41.5	33.4	22.4	0.0
	34	70.1	69.9	69.6	69.0	68.3	67.4	66.4	65.2	63.9	62.4	60.9	58.6	55.5	52.2	48.7	45.2	41.5	33.4	22.4	0.0
	35	62.4	62.3	62.0	61.7	61.2	60.6	59.7	58.3	56.6	54.8	52.9	50.8	48.5	46.2	43.7	41.1	35.6	27.7	19.1	0.0
	36	51.8	51.6	51.4	51.0	50.4	49.7	49.0	48.1	47.0	45.9	44.7	43.4	42.0	40.5	36.9	32.2	27.2	22.1	13.5	0.0
	37	40.3	40.2	40.1	39.8	39.1	38.2	37.2	36.0	34.7	33.2	31.6	29.8	27.9	25.9	23.8	21.5	18.2	13.2	7.9	0.0

Table 4.13. Example silicon lenslet, square patches, refractive indices. Refractive indices for the cells of the 37 layer silicon lenslet using a 160 μm unit cell. Column 1 is the centre, 20 is the outer edge. Darker blue indicates higher refractive index.

	Column Refractive Indices																				
	1	2	3	4	5	6	7	8	9	10	11	12	13	14	15	16	17	18	19	20	
Layer	1	3.78	3.78	3.78	3.77	3.76	3.75	3.74	3.73	3.71	3.70	3.68	3.66	3.64	3.61	3.59	3.56	3.54	3.51	3.48	3.45
	2	4.14	4.14	4.13	4.12	4.10	4.08	4.06	4.03	3.99	3.96	3.92	3.88	3.83	3.79	3.74	3.68	3.63	3.57	3.51	3.45
	3	4.54	4.54	4.52	4.50	4.47	4.44	4.40	4.35	4.30	4.24	4.18	4.11	4.04	3.97	3.89	3.81	3.72	3.63	3.54	3.45
	4	4.98	4.97	4.95	4.92	4.88	4.83	4.77	4.70	4.62	4.54	4.45	4.36	4.26	4.16	4.05	3.93	3.82	3.70	3.58	3.45
	5	4.98	4.97	4.95	4.92	4.88	4.83	4.77	4.70	4.62	4.54	4.45	4.36	4.26	4.16	4.05	3.93	3.82	3.70	3.58	3.45
	6	4.98	4.97	4.95	4.92	4.88	4.83	4.77	4.70	4.62	4.54	4.45	4.36	4.26	4.16	4.05	3.93	3.82	3.70	3.58	3.45
	7	4.98	4.97	4.95	4.92	4.88	4.83	4.77	4.70	4.62	4.54	4.45	4.36	4.26	4.16	4.05	3.93	3.82	3.70	3.58	3.45
	8	4.98	4.97	4.95	4.92	4.88	4.83	4.77	4.70	4.62	4.54	4.45	4.36	4.26	4.16	4.05	3.93	3.82	3.70	3.58	3.45
	9	4.98	4.97	4.95	4.92	4.88	4.83	4.77	4.70	4.62	4.54	4.45	4.36	4.26	4.16	4.05	3.93	3.82	3.70	3.58	3.45
	10	4.98	4.97	4.95	4.92	4.88	4.83	4.77	4.70	4.62	4.54	4.45	4.36	4.26	4.16	4.05	3.93	3.82	3.70	3.58	3.45
	11	4.98	4.97	4.95	4.92	4.88	4.83	4.77	4.70	4.62	4.54	4.45	4.36	4.26	4.16	4.05	3.93	3.82	3.70	3.58	3.45
	12	4.98	4.97	4.95	4.92	4.88	4.83	4.77	4.70	4.62	4.54	4.45	4.36	4.26	4.16	4.05	3.93	3.82	3.70	3.58	3.45
	13	4.98	4.97	4.95	4.92	4.88	4.83	4.77	4.70	4.62	4.54	4.45	4.36	4.26	4.16	4.05	3.93	3.82	3.70	3.58	3.45
	14	4.98	4.97	4.95	4.92	4.88	4.83	4.77	4.70	4.62	4.54	4.45	4.36	4.26	4.16	4.05	3.93	3.82	3.70	3.58	3.45
	15	4.98	4.97	4.95	4.92	4.88	4.83	4.77	4.70	4.62	4.54	4.45	4.36	4.26	4.16	4.05	3.93	3.82	3.70	3.58	3.45
	16	4.98	4.97	4.95	4.92	4.88	4.83	4.77	4.70	4.62	4.54	4.45	4.36	4.26	4.16	4.05	3.93	3.82	3.70	3.58	3.45
	17	4.98	4.97	4.95	4.92	4.88	4.83	4.77	4.70	4.62	4.54	4.45	4.36	4.26	4.16	4.05	3.93	3.82	3.70	3.58	3.45
	18	4.98	4.97	4.95	4.92	4.88	4.83	4.77	4.70	4.62	4.54	4.45	4.36	4.26	4.16	4.05	3.93	3.82	3.70	3.58	3.45
	19	4.98	4.97	4.95	4.92	4.88	4.83	4.77	4.70	4.62	4.54	4.45	4.36	4.26	4.16	4.05	3.93	3.82	3.70	3.58	3.45
	20	4.98	4.97	4.95	4.92	4.88	4.83	4.77	4.70	4.62	4.54	4.45	4.36	4.26	4.16	4.05	3.93	3.82	3.70	3.58	3.45
	21	4.98	4.97	4.95	4.92	4.88	4.83	4.77	4.70	4.62	4.54	4.45	4.36	4.26	4.16	4.05	3.93	3.82	3.70	3.58	3.45
22	4.98	4.97	4.95	4.92	4.88	4.83	4.77	4.70	4.62	4.54	4.45	4.36	4.26	4.16	4.05	3.93	3.82	3.70	3.58	3.45	
23	4.98	4.97	4.95	4.92	4.88	4.83	4.77	4.70	4.62	4.54	4.45	4.36	4.26	4.16	4.05	3.93	3.82	3.70	3.58	3.45	
24	4.98	4.97	4.95	4.92	4.88	4.83	4.77	4.70	4.62	4.54	4.45	4.36	4.26	4.16	4.05	3.93	3.82	3.70	3.58	3.45	
25	4.98	4.97	4.95	4.92	4.88	4.83	4.77	4.70	4.62	4.54	4.45	4.36	4.26	4.16	4.05	3.93	3.82	3.70	3.58	3.45	
26	4.98	4.97	4.95	4.92	4.88	4.83	4.77	4.70	4.62	4.54	4.45	4.36	4.26	4.16	4.05	3.93	3.82	3.70	3.58	3.45	
27	4.98	4.97	4.95	4.92	4.88	4.83	4.77	4.70	4.62	4.54	4.45	4.36	4.26	4.16	4.05	3.93	3.82	3.70	3.58	3.45	
28	4.98	4.97	4.95	4.92	4.88	4.83	4.77	4.70	4.62	4.54	4.45	4.36	4.26	4.16	4.05	3.93	3.82	3.70	3.58	3.45	
29	4.98	4.97	4.95	4.92	4.88	4.83	4.77	4.70	4.62	4.54	4.45	4.36	4.26	4.16	4.05	3.93	3.82	3.70	3.58	3.45	
30	4.98	4.97	4.95	4.92	4.88	4.83	4.77	4.70	4.62	4.54	4.45	4.36	4.26	4.16	4.05	3.93	3.82	3.70	3.58	3.45	
31	4.98	4.97	4.95	4.92	4.88	4.83	4.77	4.70	4.62	4.54	4.45	4.36	4.26	4.16	4.05	3.93	3.82	3.70	3.58	3.45	
32	4.98	4.97	4.95	4.92	4.88	4.83	4.77	4.70	4.62	4.54	4.45	4.36	4.26	4.16	4.05	3.93	3.82	3.70	3.58	3.45	
33	4.98	4.97	4.95	4.92	4.88	4.83	4.77	4.70	4.62	4.54	4.45	4.36	4.26	4.16	4.05	3.93	3.82	3.70	3.58	3.45	
34	4.98	4.97	4.95	4.92	4.88	4.83	4.77	4.70	4.62	4.54	4.45	4.36	4.26	4.16	4.05	3.93	3.82	3.70	3.58	3.45	
35	4.54	4.54	4.52	4.50	4.47	4.44	4.40	4.35	4.30	4.24	4.18	4.11	4.04	3.97	3.89	3.81	3.72	3.63	3.54	3.45	
36	4.14	4.14	4.13	4.12	4.10	4.08	4.06	4.03	3.99	3.96	3.92	3.88	3.83	3.79	3.74	3.68	3.63	3.57	3.51	3.45	
37	3.78	3.78	3.78	3.77	3.76	3.75	3.74	3.73	3.71	3.70	3.68	3.66	3.64	3.61	3.59	3.56	3.54	3.51	3.48	3.45	

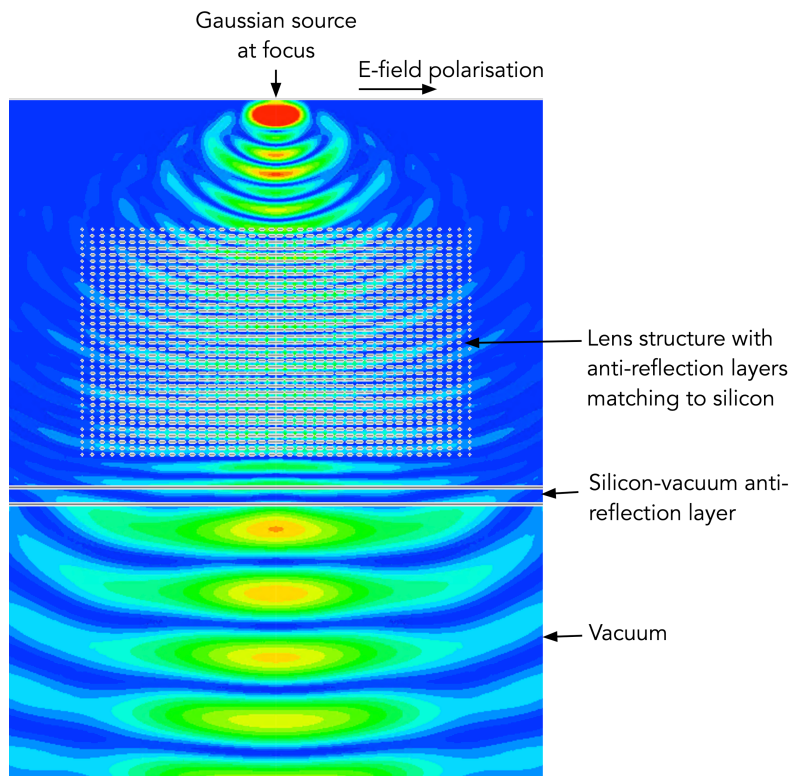


Figure 4.47. Silicon lenslet, square patches, E field. The electric field magnitude of the example silicon lenslet consisting of 37 layers at 150 GHz. Indications of the position of the metallic mesh grid and other features are overlaid.

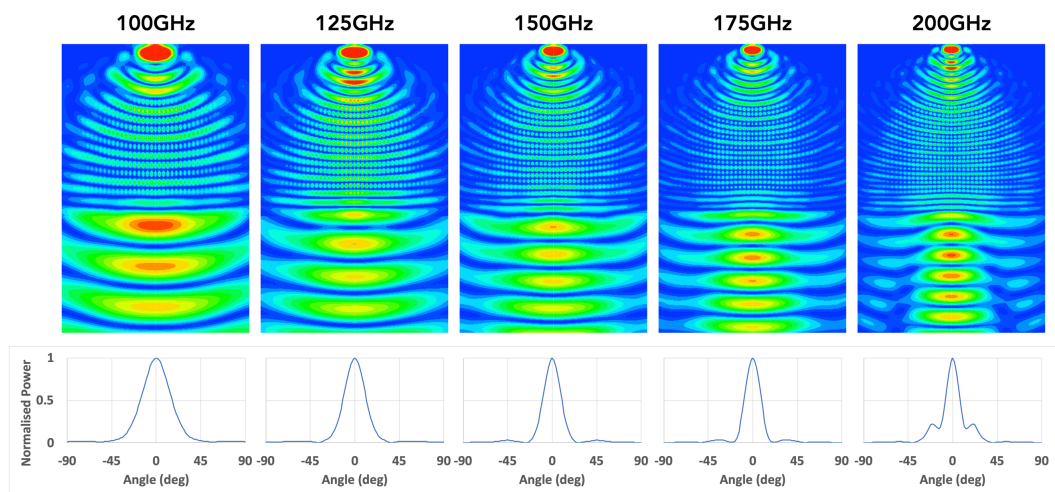


Figure 4.48. Silicon lenslet, square patches, far field. Electric field magnitude and far field plots for the initial silicon lenslet modelling without the transition to vacuum. The behaviour of the lenslet deteriorates beyond 175 GHz.

Table 4.14. Full width, half maximum for the square patch silicon design. The FWHM beam angle measured from the modelling is a fair match for the calculated value at 150 GHz. The measured value deviates from the calculated for the other frequencies.

Frequency	Excitation beam waist radius, w_0	Measured far field FWHM beam angle	Calculated FWHM beam angle
100 GHz	0.46 mm	17.4°	13.5°
125 GHz	0.37 mm	13.1°	10.8°
150 GHz	0.30 mm	9.3°	9.0°
175 GHz	0.26 mm	10.9°	7.7°
200 GHz	0.23 mm	11.6°	6.7°

4.9 Improving the simple path length model

Section 4.1 introduced a simple path length model of GRIN lenslet behaviour but noted it had a number of shortcomings that were accounted for by a focal length compensation factor. In this section, shortcomings are identified, and possible solutions proposed.

4.9.1 Bending at the lenslet structure boundary

The assumption that all the bending of light rays incident on the structure occurs at the boundary to the structure is incorrect for GRIN lenslets. Rather, the rays bend slowly as they pass through the refractive index grading. This means that rays on the edges of the lenslet can pass through columns nearer the centre (where the refractive index is higher) than their assigned column, accumulating more phase shift than was intended. This effect is more pronounced the thicker the lenslet is.

To demonstrate this issue, a simple adaptation of the computer graphics ray tracing algorithm first proposed by Appel¹²⁸ and improved to include refraction (and other optical effects) by Whitted¹²⁹ was used. Rays were traced from the focus, through the lenslet structure, out to infinity; only the path of the ray was considered important, unlike in the computer graphics application where intensity is also taken account.

A ray bends in a GRIN structure due to the transverse refractive index gradient it encounters. To model this, the refractive index is sampled on both sides of the ray and bending is applied in response to the difference between the two.

The algorithm consists of tracking the ray in a stepwise manner as shown in Figure 4.49. Each step consists of a location and a unit vector indicating the current direction of the ray. The location of the next step, $m + 1$, is calculated by advancing a distance, Δr , in the direction of the unit vector from step m . The refractive index is sampled at two locations, n_1 and n_2 , a distance Δs each side of the ray halfway between these steps. The distance δr was then calculated from the difference in phase shifts of the path from a_1 to b_1 and from a_2 to b_2 . This in turn allows the angle, θ , through which to rotate the unit vector to be calculated from:

$$\theta = \tan^{-1} \left[\frac{(n_2 - n_1) \Delta r}{n_2 2\Delta s} \right]. \quad 4-45$$

The two parameters, Δr and Δs , should be chosen to be small enough to accurately trace the path.

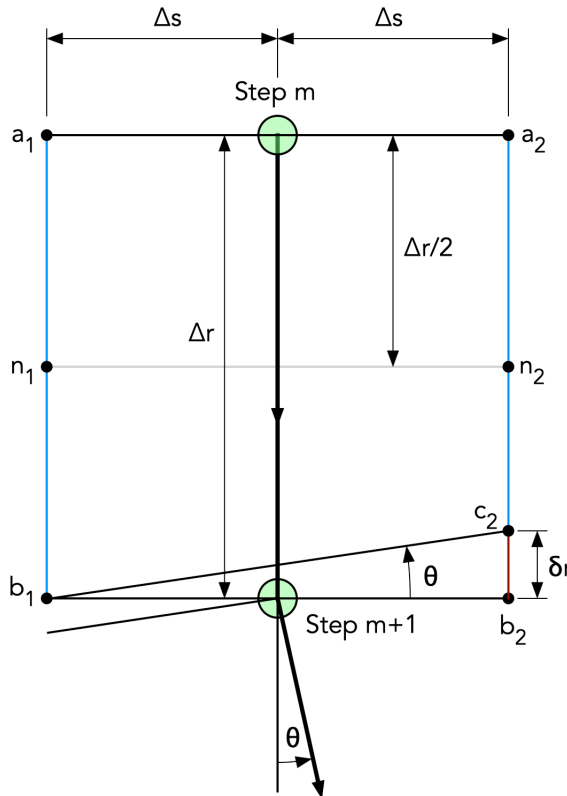


Figure 4.49. Ray tracing concept. A single step in the ray tracing algorithm used to investigate the passage of waves through a GRIN lenslet structure.

The results of using this algorithm with the lenslet structures described earlier reveal the extent to which the rays deviate from the simple model. Figure 4.50 shows rays traced through the polypropylene design described in section 4.8.1. It is apparent that while the centre of the lenslet is a little under focussed, the edges

are still very over focussed. The rays at the edges clearly pass through many of the GRIN columns on their journey rather than the single column the simple model assumes. These rays encounter far more phase shift and see a steeper refractive index grading than intended, causing the over-focussing that the compensation factor adjusts for. In addition, each column boundary crossing has the potential to reflect some of the energy, adversely affecting the gain of the device.

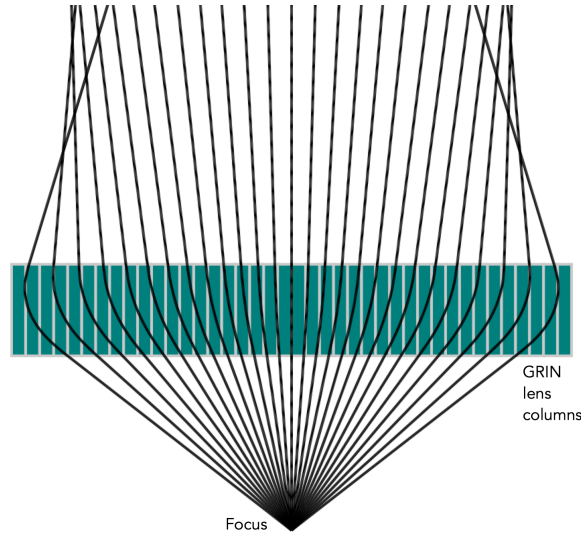


Figure 4.50. Polypropylene lenslet ray tracing. Rays passing through an example polypropylene lenslet designed using the simple path length model. Notice how most rays pass through multiple columns, especially towards the edges of the lenslet.

4.9.2 Metamaterial artificial dielectrics incidence angle

Another fault is associated with the measured refractive index of the artificial dielectrics. Typically, they are modelled with normally incident waves with the assumption that the effective refractive index does not vary with incident angle. This is, however, not true for artificial dielectrics constructed using metallic patch meshes. As the angle of incidence increases, the apparent spacing of the mesh layers increases and the effective unit cell decreases due to geometry. Both these effects will tend to reduce the effective refractive index.

The effect of incidence angle on the effective refractive index of these artificial dielectrics was investigated using HFSS. Figure 4.51 shows the model setup used. The method used to derive the refractive index from the S-parameters, described in section 4.3.3, relies on waves normally incident onto the test dielectric. The meta-material mesh layers must therefore be arranged at an angle in the artificial dielectric. This does complicate the master/slave boundaries along the x axis as there will be a discontinuity in the mesh layer. HFSS does allow an

angle offset to be applied to the slave, but that also will cause a problem; effectively a step in the z sides of the artificial dielectric block making it difficult to determine d_0 . Instead, the layout in the figure was used, modelling six columns of the mesh to minimise the effect the boundary discontinuity has on the results (it was found with a quick survey that six columns was sufficient for this purpose).

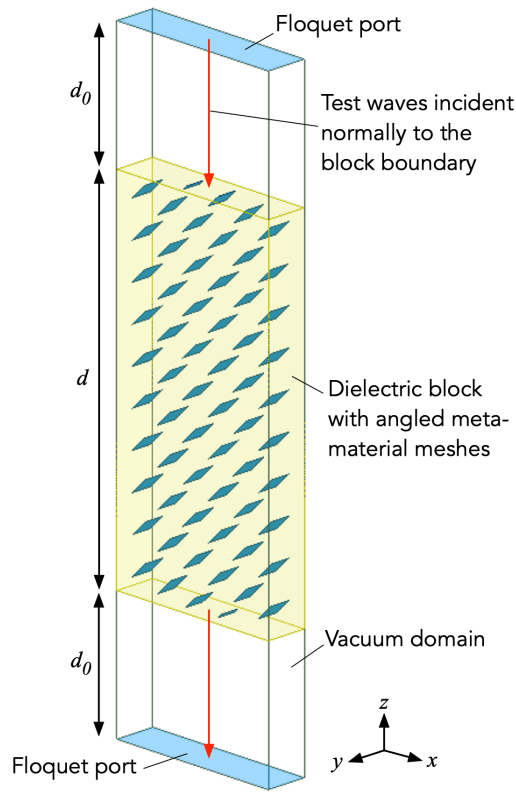


Figure 4.51. Angle of incidence modelling. Modelling arrangement for the HFSS investigation into the effect of incidence angle on the refractive index of artificial dielectrics constructed from meta-material meshes.

This model was used to measure the effective refractive indices of blocks of artificial dielectrics with meta-material mesh layers at angles from 0 to 60° to the z boundary of the block for various sizes of capacitive patch. Figure 4.52 shows selected results for silicon based artificial dielectrics using a meta-material mesh with a unit cell of 160 μm and a layer spacing of 100 μm at a frequency of 150 GHz. At the larger patch sizes, there is some evidence of a slight increase in refractive index up to an incidence angle of around 20°. Thereafter, the refractive index falls away roughly linearly to the maximum angle studied. This effect can be used to minimise the amount of modelling and data collection required to build the incidence angle compensation tables.

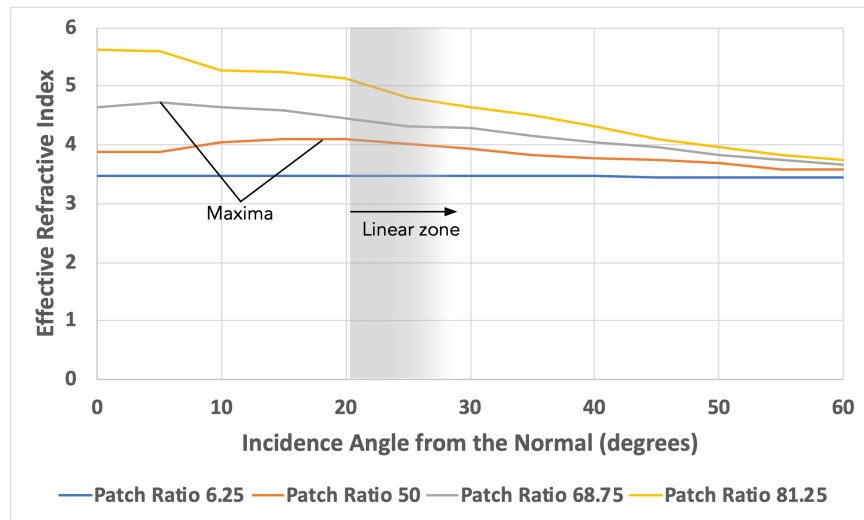


Figure 4.52. Effect of incidence angle on refractive index. Effective refractive index of a silicon based artificial dielectric against incidence angle at 150 GHz for selected meta-material patch sizes. The refractive index at zero incidence angle was the value used in the simple design model.

The simple design method assumes the rays always encounter the artificial dielectric with normal incidence. This is not true for a large majority of the lens structure, as can be seen from the right-hand (straight column) side of Figure 4.53. The only places it is true are at the top layer and the centre column. Everywhere else, the rays meet the artificial dielectric cell at a non-normal angle. Towards the edge of the lenslet, this will cause rays to encounter a lower refractive index than they should, leading to under-focussing. This is a smaller effect than the over-focussing described in section 4.9.1 as the design still requires a compensation factor that reduces focussing.

4.9.3 Following the rays

An improvement on the simple design that follows the paths of the rays through the device would allow the column boundary crossing and non-normal incidence issues to be addressed. Figure 4.53 shows the proposed concept. Inside the lenslet structure, the GRIN columns are arranged to follow the path of the ray. This requires the column width (and therefore the unit cell of a metamaterial implementation) to vary along the ray, being smallest at the lenslet edge nearest the focus. The ray encounters two bending mechanisms; firstly, Snell's law applies at the boundary nearest the focus, secondly, the effect of the graded index causes the ray to follow a curved path through the structure.

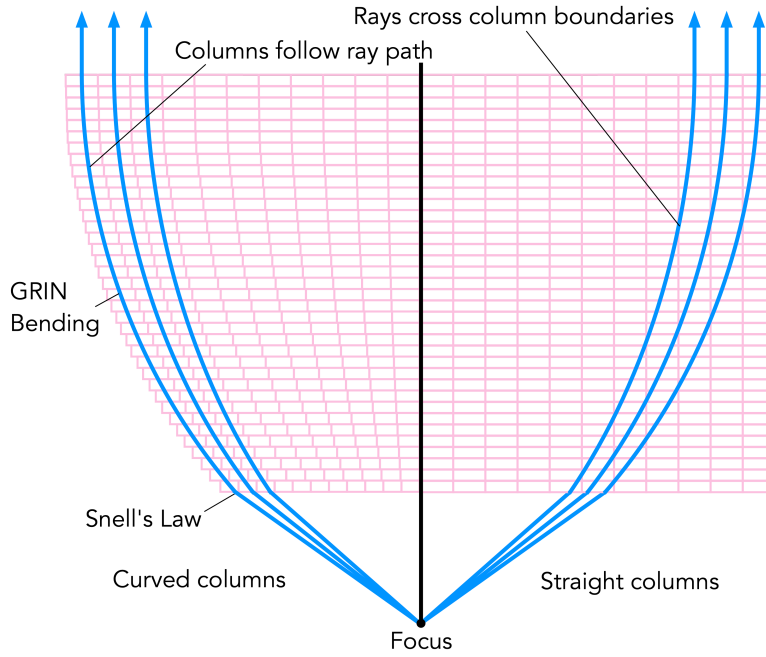


Figure 4.53. Curved column concept. A lenslet structure in which the GRIN columns follow the ray paths is shown on the left compared to the original straight column design on the right.

To design a lenslet using this recipe, the column width, refractive index, ray path length and angle of incidence must be calculated for each cell in the GRIN array. This can be achieved using some simple geometry. To start with, an equation for the curved part of the ray path is determined. Figure 4.54 shows the path of a ray assuming it follows an arc of a circle inside the structure. The ray starts at the focus, point C, which will also be the coordinate origin in this derivation. It travels to point A where it encounters the edge of the lenslet structure, column $m \in \{1..M\}$, at angle θ_m to the normal given by:

$$\theta_m = \tan^{-1} \left(\frac{l_m}{d} \right). \quad 4-46$$

The ray is refracted at the boundary according to Snell's law and therefore enters the lenslet structure at the angle θ'_m where n_d is the refractive index of the dielectric between the focus and the lenslet and n_m is the main refractive index of this column:

$$\theta'_m = \sin^{-1} \left(\frac{n_d}{n_m} \sin \theta_m \right). \quad 4-47$$

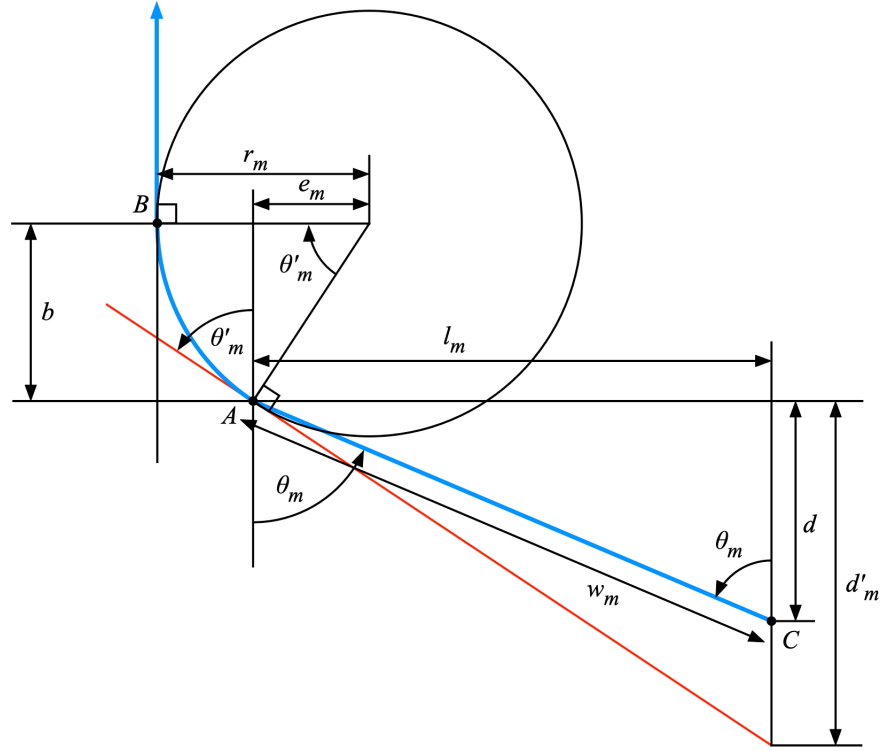


Figure 4.54. Curved column geometry. The path of a ray (in blue) from the focus (point C) passing through a lenslet structure (points A to B).

Simple geometry then leads to equations for the radius of the circle, r_m :

$$r_m = \frac{b}{\sin \theta'_m} \quad 4-48$$

and the distance e_m :

$$e_m = r_m \cos \theta'_m . \quad 4-49$$

Using the focus, point C, as the coordinate system origin, the equation of the circle is therefore:

$$(x - e_m + l_m)^2 + (y - d - b)^2 = r_m^2 . \quad 4-50$$

The distance of the centre of a column from the centre of the lenslet, l_m , depends on whether there are an even or odd number of columns in the lenslet and is given by:

$$l_m = \begin{cases} mg - \frac{g}{2} & \text{even } m \\ mg - g & \text{odd } m \end{cases} . \quad 4-51$$

To calculate the column width of each cell, consider rays that pass through the structure on the two edges of a column, as shown in Figure 4.55. The y coordinate of each layer, $n \in (1..N)$, where the layer spacing is s , is given by:

$$y_n = d + ns - \frac{s}{2}. \quad 4-52$$

For each layer, the x coordinates of points A and B can be determined using Equation 4-50.

$$x_{mnA} = e_{mA} + \frac{g}{2} - l_m + \sqrt{r_{mA}^2 - (y_n - d - b)^2} \quad 4-53$$

$$x_{mnB} = e_{mB} - \frac{g}{2} - l + \sqrt{r_{mB}^2 - (y_n - d - b)^2} \quad 4-54$$

where g is the nominal column width at the boundary of the lenslet structure nearest the focus. The column width of the cell in column m on layer n is therefore:

$$g_{mn} = x_{mnA} - x_{mnB}. \quad 4-55$$

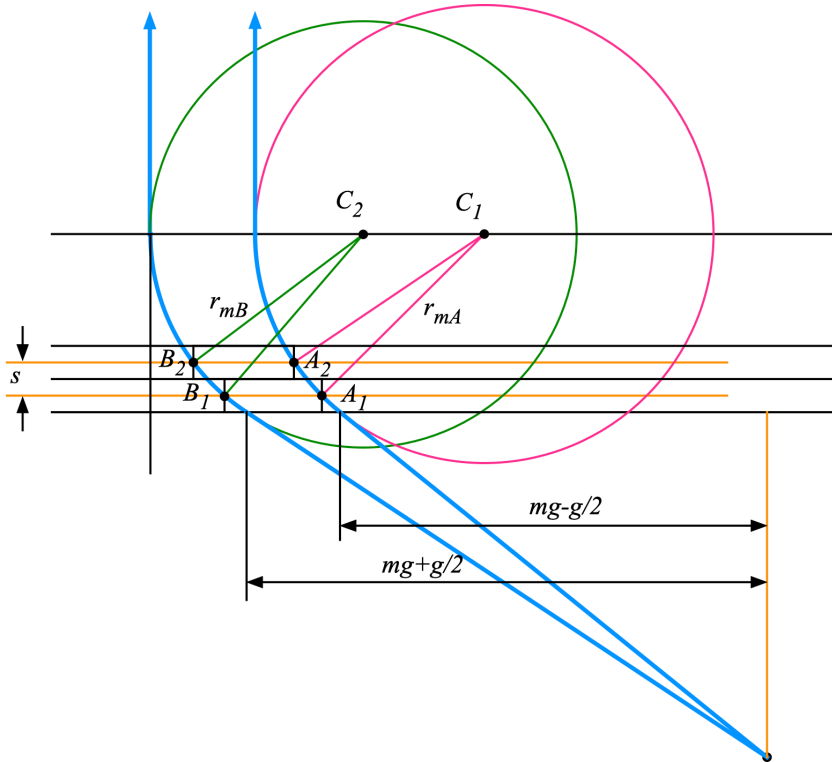


Figure 4.55. Curved column unit cell geometry. The cell width in each layer is determined by the geometry of the pair of rays passing along the edges of a column.

The incidence angle the ray makes at each cell and the length of the path it follows inside the cell must also be calculated. Figure 4.56 shows a close up of the geometry of the ray passing through a cell.

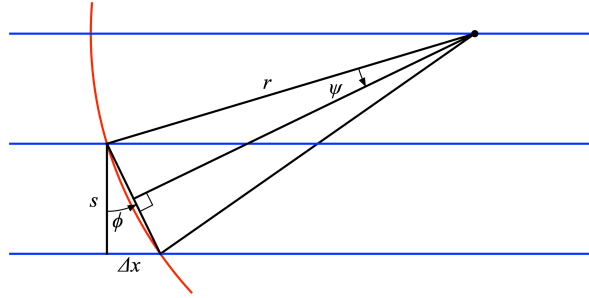


Figure 4.56. Curved column geometry, ray close up. Close up of a ray passing through a cell.

Again, using simple geometry, the incidence angle is given by:

$$\theta_{m,n} = \tan^{-1} \frac{\Delta x_{m,n}}{s} \quad 4-56$$

where

$$\Delta x_{m,n} = x_{m,n+1} - x_{m,n} . \quad 4-57$$

The two x coordinates can be found using the equation of the circle given by Equation 4-50:

$$x_{m,n} = e_m - l_m + \sqrt{r_m^2 - (y_n - d - b)^2} \quad 4-58$$

$$x_{m,n+1} = e_m - l + \sqrt{r_m^2 - (y_{n+1} - d - b)^2} \quad 4-59$$

where

$$y_n = d + (n - 1)s \quad 4-60$$

$$y_{n+1} = d + ns . \quad 4-61$$

The length of the arc inside the cell is given by:

$$p_{mn} = 2r_m \psi_m \quad 4-62$$

where

$$\psi_m = \sin^{-1} \frac{\sqrt{s^2 + \Delta x_{mn}^2}}{2r_m}. \quad 4-63$$

The argument then proceeds in a similar fashion to the simple design model. The phase shift due to the path length from the focus to the start of a curved column, where n_d is the refractive index of the dielectric that fills this space, is given by:

$$\phi_{Am} = \frac{2\pi f n_d \sqrt{d^2 + l_m^2}}{c}. \quad 4-64$$

The phase shift induced by a curved column is the sum of all the phase shifts induced by the cells in that column. It is expressed this way as the refractive index of all the cells in the column will not be the same, those that form the anti-reflection layers will be different. It is given by:

$$\phi_{Bm} = \sum_{n=0}^{N-1} \frac{2\pi f p_{m,n} n_{m,n}}{c}. \quad 4-65$$

To bring the wavefronts into line, the phase shift the curved columns induce must compensate for the varying path lengths from the focus to the start of the column. The ray passing through the outer column, $m = M$, takes the longest path, so its curved column is assigned the minimum refractive index, n_d , throughout. The other columns must then have this phase shift:

$$\phi_{Bm} = \phi_{BM} + \phi_{AM} - \phi_{Am}. \quad 4-66$$

Substituting and simplifying:

$$\sum_{n=0}^{N-1} p_{m,n} n_{m,n} = n_d \left(\sum_{n=0}^{N-1} p_{M,n} + \sqrt{d^2 + l_M^2} - \sqrt{d^2 + l_m^2} \right). \quad 4-67$$

At this point all the necessary math is known but it is noted that the algorithm must be recursive; the main column refractive indices are calculated using the column path lengths which themselves depend on the main column refractive indices. In addition, the anti-reflection layer refractive indices depend on the main column refractive indices which in turn depend on the anti-reflection layer refractive indices. The algorithm therefore starts by setting the main column refractive indices, n_m , all to n_d , effectively ignoring the effect of Snell's law at the beginning,

making it possible to calculate the equations of the ray arcs. In addition, no anti-reflection layers are allowed for, making all the cells in a column have the same (main) refractive index, n_m , which allows Equation 4-67 to be simplified to:

$$n_m = \frac{n_d \left(p_M + f\sqrt{d^2 + l_M^2} - f\sqrt{d^2 + l_m^2} \right)}{p_m}. \quad 4-68$$

This information then allows the width, incidence angle and path length to be calculated for each cell. The outer few layers' refractive indices are then reduced to implement the anti-reflection layers. There will now be an error between the phase shift the columns are now inducing and that required, which allows a modification to the main column refractive index to be calculated. The algorithm then loops, recalculating the column width, incidence angle and path length etc. After a number of loops, the parameters for all the column cells will be known to a reasonable accuracy.

The final stage is to assign metamaterial patch sizes to each column cell. The column width, refractive index and incidence angle are all taken into account. This step requires a reasonably extensive catalogue of the refractive indices achieved by artificial dielectrics using various unit cells and patch sizes modelled with waves at a range of incidence angles. HFSS was used to build the catalogues, Table 4.15 details the contents of the catalogue for the example silicon lenslet that will be described next. Linear interpolation was used to choose the patch ratio for each column cell so as to provide the required refractive index.

Table 4.15. Refractive index catalogue contents. The contents of the catalogue created using HFSS for the curved column design process for the example lenslet in a silicon dielectric. The effective permittivity and permeability were extracted from the S-parameters for each combination of these parameters.

Parameter	Range
Unit cell	120 to 200 mm in steps of 20 mm
Patch ratios	5, 20, 40, 60, 80, 85, 90
Incidence angle	0°, 5°, 10°, 20°, 40°, 60°
Frequency	10 to 400 GHz in steps of 10 GHz.

A design with curved columns for the silicon example lenslet was prepared without anti-reflection layers. The unit cell sizes of each column for each layer calculated using the geometry described above are shown in Table 4.16, notice how each

column of each layer can have a different size. The resulting electric field magnitude is shown in Figure 4.57.

Table 4.16. Curved column widths. The unit cell sizes (in μm) of the columns for the initial curved column design of the example silicon lenslet. Darker green indicates larger unit cell.

		Unit Cell Size (μm) for each Column																
		1	2	3	4	5	6	7	8	9	10	11	12	13	14	15	16	17
Layer	1	124	124	124	124	124	124	124	124	124	124	124	124	124	124	125	125	126
	2	129	129	129	129	129	128	128	128	128	128	128	128	128	129	129	130	131
	3	133	133	133	133	133	132	132	132	132	132	132	132	132	132	133	134	135
	4	137	137	137	137	136	136	136	136	136	136	136	136	136	136	137	138	140
	5	141	141	141	140	140	140	140	139	139	139	139	139	139	139	140	141	143
	6	144	144	144	144	144	143	143	143	142	142	142	142	142	143	143	145	147
	7	148	148	148	148	147	147	147	146	146	145	145	145	145	146	146	148	150
	8	152	151	151	151	151	150	150	149	149	148	148	148	148	148	149	150	153
	9	155	155	155	154	154	153	153	152	152	151	151	151	151	151	152	153	155
	10	158	158	158	157	157	156	156	155	154	154	153	153	153	153	154	155	158
	11	161	161	161	160	160	159	159	158	157	156	156	155	155	156	156	158	160
	12	164	164	164	163	163	162	161	160	160	159	158	158	158	158	158	160	162
	13	167	167	166	166	165	165	164	163	162	161	160	160	160	160	160	162	164
	14	169	169	169	168	168	167	166	165	164	163	163	162	162	162	162	163	166
	15	172	172	171	171	170	169	168	167	166	165	164	164	163	163	164	165	167
	16	174	174	174	173	172	171	170	169	168	167	166	166	165	165	165	167	169
	17	177	176	176	175	175	174	172	171	170	169	168	167	167	166	167	168	170
	18	179	179	178	177	177	175	174	173	172	171	170	169	168	168	168	169	172
	19	181	180	180	179	178	177	176	175	173	172	171	170	169	169	169	170	173
	20	182	182	182	181	180	179	178	176	175	174	172	171	171	170	171	171	174
	21	184	184	184	183	182	181	179	178	176	175	174	173	172	171	172	172	175
	22	186	186	185	184	183	182	181	179	178	176	175	174	173	172	172	173	176
	23	187	187	186	186	185	183	182	180	179	177	176	175	174	173	173	174	176
	24	188	188	188	187	186	184	183	181	180	178	177	176	175	174	174	175	177
	25	190	189	189	188	187	185	184	182	181	179	178	176	175	175	175	176	178
	26	191	190	190	189	188	186	185	183	181	180	178	177	176	175	175	176	178
	27	191	191	191	190	189	187	186	184	182	180	179	178	177	176	176	177	179
	28	192	192	191	191	189	188	186	184	183	181	179	178	177	176	176	177	179
	29	193	193	192	191	190	188	187	185	183	181	180	178	177	177	177	177	179
	30	193	193	193	192	190	189	187	185	184	182	180	179	178	177	177	178	180
	31	194	193	193	192	191	189	187	186	184	182	180	179	178	177	177	178	180
	32	194	194	193	192	191	189	188	186	184	182	181	179	178	177	177	178	180
	33	194	194	193	192	191	189	188	186	184	182	181	179	178	177	177	178	180

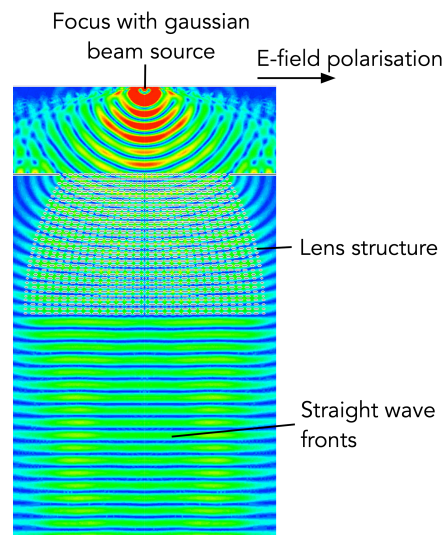


Figure 4.57. Curved column demonstration E field. A design for the silicon example lenslet using curved columns with focal length compensation factor of 1.0. There are no anti-reflection layers and no interface to vacuum in this example which was measured at the centre frequency of the specification, 150 GHz.

The most encouraging feature of this design is that a focal length compensation factor of 1.0 (in other words, no compensation factor) leads to wavefronts that are remarkably straight. This indicates that the design model accurately takes into account how the waves propagate through the lenslet structure. In addition, the mask blocks the light that would otherwise miss the lenslet structure and reveals that little energy emerges from the sides of the structure.

4.9.4 Following the rays in three dimensions

The procedure outlined in section 4.9.3 is useful for generating effectively a strip along the diameter of a lenslet, suitable for modelling in HFSS using the low memory footprint method described in section 4.2. However, due to the varying unit cell size along the diameter, it is not possible to extend the design to a full quadrant using the method of section 4.2; the fully variable unit cell design is not practical for the construction of a circular lenslet using meshes consisting of square patches.

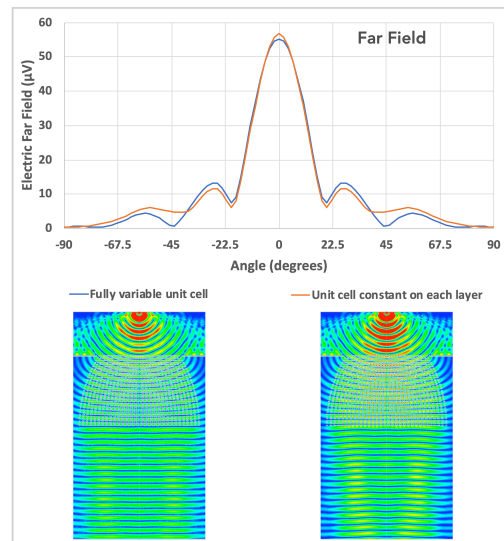


Figure 4.58. Constant column size with curved columns. Comparison of the behaviour of the same lenslet design using curved columns with fully variable unit cell size and layer constant unit cell size including the far field performance, at 150 GHz.

To overcome this issue, the unit cell can be kept constant on each layer (it will still be different from layer to layer to maintain the curved column structure). The calculated unit cell size was replaced with the average unit cell size throughout each layer. This allows each layer to consist of a mesh of patches on a uniform unit cell. Examining the unit cell along the diameter of each layer (as shown in Table 4.16), it can be seen that the variation is not insignificant, so the effects of this approximation must be understood. Figure 4.58 shows the effect by

comparing the same silicon lenslet design using fully variable and layer constant unit cell sizes.

The approximation is shown to make a small difference. The wavefronts are not quite as straight with constant unit cells and there is a hint of a slight over focussing. The far field plot indicates that there is a little more power in the central beam and the side lobe pattern is different. The reflection characteristics are also different, evidenced by the apparent change in intensity of the incident beam. The waves do still follow the form of the curved lenslet structure though and leakage sideways looks the same. On the whole, the penalty for requiring a constant unit cell size on each layer is acceptable.

4.9.5 The full silicon lenslet

To implement the full example silicon lenslet using curved columns, the anti-reflection layers must be added along with the transition to a vacuum. This leads to the return of the focal length compensation factor as the presence of cells in the structure with the refractive indices required for the anti-reflection layers is not fully accounted for by the design model. These cells have a lower refractive index, so the design model overestimates the bending contributed by them, this results in the design requiring a focal length compensation factor of less than 1 (0.85 in this example). Figure 4.59 presents the electric field magnitude at 150 GHz of the resulting lenslet overlaid with the lenslet structure. Table 4.19 details the unit cell size for each layer and the patch ratio for each cell and Table 4.20 shows the refractive indices. It is implemented in 35 layers, a reduction of 2 layers from the straight column design of section 4.8.2. The design parameters are shown in Table 4.17 compared with the original straight column design.

Table 4.17. Curved column Silicon lenslet design details compared with the straight column version from section 4.8.2.

Columns	Straight	Curved
Patch Type	Square	Square
Diameter	6.3mm	6.3 mm
Center frequency	150 GHz	150 GHz
Bandwidth	100 GHz	100 GHz
Focal length (d in Figure 4.1)	2 mm	2 mm
Layer spacing	100 μm	100 μm
Number of layers	37	35
Lens thickness (b in Figure 4.1)	3.7 mm	3.5 mm
Focal length compensation factor	1.25	0.85

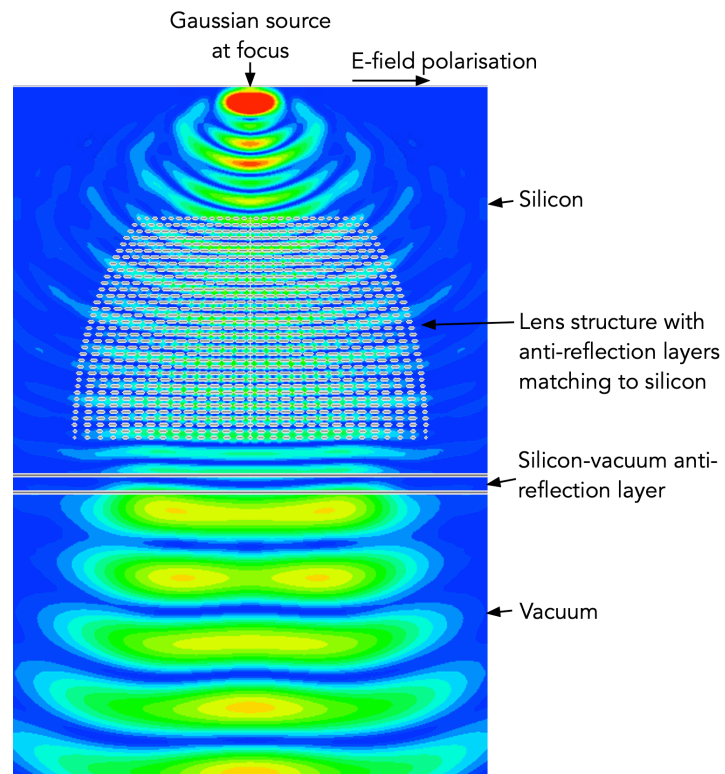


Figure 4.59. Curved column silicon lenslet, E field magnitude. Example silicon lenslet implemented using curved columns at 150 GHz. The lenslet structure and other features are overlaid for reference.

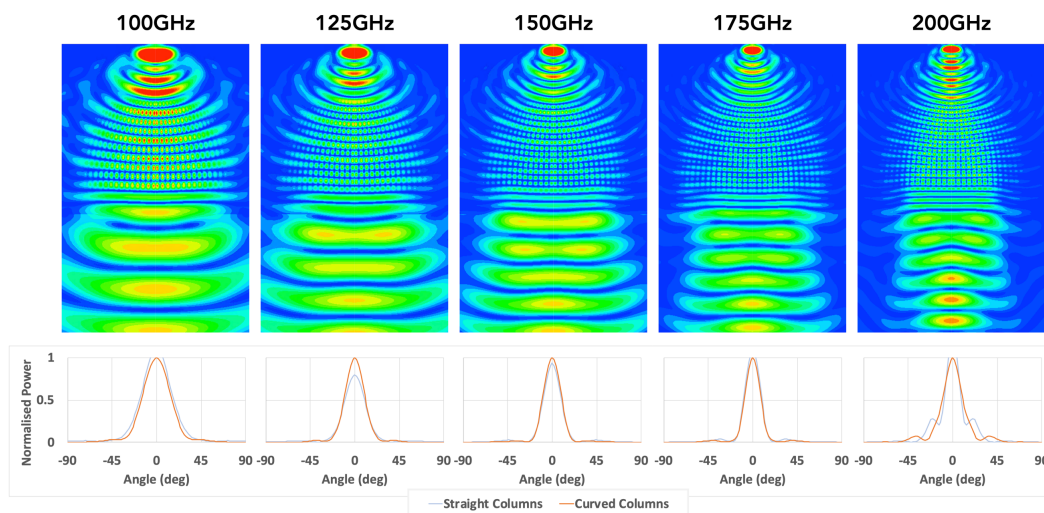


Figure 4.60. Curved column lenslet, far field. Electric field magnitude and far field plots for the curved column silicon lenslet design. The far field plots also show the straight column far fields normalised to the same scale.

Figure 4.60 shows the far field and electric field magnitudes for the design at a number of frequencies over the design band. Rather like the straight column version of section 4.8.2, there's under focussing apparent at 100 GHz and over focussing at 200 GHz, although maybe not as much. The far field plots are normalised so that 1 corresponds to the power through the curved lenslet on its axis, the straight column far fields included as a reference are normalised to the same value. This shows that at the centre frequency, the curved column implementation transmits more power. Table 4.18 shows the measured and calculated FWHM angles for the output beam in the far field, which indicates that the curved column design conforms over a wider frequency range.

Table 4.18. Full width, half maximum for the curved column silicon design. The FWHM beam angle measured from the modelling compared with the angle expected. The measured values for the straight column version of section 4.8.2 are included for comparison.

Frequency	Excitation beam waist radius, w_0	Measured far field FWHM beam angle	Calculated FWHM beam angle	Straight columns FWHM beam angle
100 GHz	0.46 mm	15.6°	13.5°	17.4°
125 GHz	0.37 mm	11.2°	10.8°	13.1°
150 GHz	0.30 mm	9.4°	9.0°	9.3°
175 GHz	0.26 mm	7.9°	7.7°	10.9°
200 GHz	0.23 mm	13.6°	6.7°	11.6°

Table 4.19. Curved column patch ratios. Unit cell sizes and patch ratios for the cells of the 35 layer silicon lenslet implemented using square columns and constant unit cell per layer. Column 1 is the centre of the lenslet, 16 is the outer edge. Darker red indicates larger patch ratio.

		Unit Cell μm	Column Patch Ratios															
			1	2	3	4	5	6	7	8	9	10	11	12	13	14	15	16
Layer	1	125	42.0	42.0	41.8	41.6	41.6	41.8	42.0	42.5	42.8	42.6	41.3	38.4	33.4	25.4	16.8	0.0
	2	130	59.9	59.9	59.8	59.4	58.6	57.3	55.5	53.5	53.2	53.1	52.6	51.3	47.8	42.2	27.1	0.0
	3	134	67.4	67.5	67.5	67.2	66.8	66.3	65.3	63.8	62.9	62.4	60.7	58.5	55.6	49.4	38.4	0.0
	4	139	74.5	74.8	74.8	74.5	74.0	73.8	73.0	71.6	70.0	69.1	68.0	65.4	60.8	54.9	43.0	0.0
	5	143	73.1	73.6	73.8	73.4	72.7	72.5	71.8	70.4	68.6	67.7	66.5	63.9	59.4	53.6	42.3	0.0
	6	146	71.5	72.3	72.6	72.2	71.4	71.2	70.4	69.2	67.4	66.1	64.7	62.2	58.0	52.3	41.7	0.0
	7	150	70.0	70.9	71.5	71.1	70.3	69.8	69.1	68.0	66.2	64.5	63.1	60.5	56.6	51.1	41.0	0.0
	8	154	68.6	69.7	70.4	70.0	69.2	68.5	67.9	66.7	65.1	63.0	61.4	58.9	55.2	49.9	40.2	0.0
	9	157	67.2	68.4	69.3	69.0	68.1	67.3	66.6	65.5	63.9	61.8	59.8	57.3	53.8	48.9	39.5	0.0
	10	160	66.0	67.3	68.3	68.1	67.1	66.1	65.4	64.4	62.8	60.7	58.3	55.7	52.5	47.8	38.7	0.0
	11	163	65.8	66.8	67.6	67.6	66.7	65.6	64.9	63.8	62.2	60.0	57.2	54.6	51.4	47.0	37.9	0.0
	12	166	65.5	66.4	67.1	67.0	66.3	65.2	64.4	63.2	61.6	59.3	56.5	53.5	50.5	46.2	37.1	0.0
	13	169	65.3	66.1	66.5	66.5	65.9	64.9	63.9	62.8	61.1	58.7	55.9	52.5	49.5	45.5	36.3	0.0
	14	171	65.1	65.7	66.0	66.0	65.4	64.6	63.5	62.3	60.6	58.2	55.3	52.0	48.5	44.8	35.5	0.0
	15	174	64.9	65.4	65.6	65.5	65.0	64.2	63.1	62.0	60.2	57.7	54.8	51.5	47.8	44.1	34.7	0.0
	16	176	64.7	65.1	65.2	65.0	64.6	63.8	62.8	61.6	59.9	57.3	54.4	51.1	47.4	43.4	33.9	0.0
	17	178	64.6	64.8	64.8	64.6	64.1	63.4	62.5	61.3	59.6	57.0	54.0	50.7	47.1	43.1	33.1	0.0
	18	180	64.4	64.6	64.5	64.2	63.7	63.1	62.2	61.1	59.3	56.7	53.7	50.4	46.8	42.8	32.3	0.0
	19	182	64.2	64.4	64.4	64.1	63.5	62.9	62.0	60.9	59.2	56.5	53.6	50.2	46.6	42.6	31.4	0.0
	20	184	64.0	64.2	64.2	63.9	63.4	62.8	61.9	60.7	59.1	56.4	53.4	50.1	46.4	42.4	30.6	0.0
	21	185	63.8	64.1	64.0	63.8	63.3	62.7	61.8	60.6	58.9	56.2	53.2	49.9	46.2	42.2	29.7	0.0
	22	187	63.7	63.9	63.9	63.7	63.2	62.6	61.6	60.5	58.7	56.0	53.0	49.7	46.0	41.9	28.9	0.0
	23	188	63.5	63.7	63.7	63.5	63.1	62.5	61.6	60.4	58.5	55.8	52.8	49.4	45.8	41.7	28.1	0.0
	24	190	63.4	63.6	63.6	63.4	62.9	62.3	61.5	60.3	58.4	55.7	52.6	49.2	45.5	41.5	27.3	0.0
	25	191	63.2	63.4	63.4	63.2	62.8	62.2	61.4	60.2	58.3	55.5	52.4	49.0	45.3	41.2	26.5	0.0
	26	192	63.1	63.3	63.3	63.1	62.6	62.0	61.2	60.2	58.2	55.4	52.3	48.9	45.1	41.0	25.8	0.0
	27	193	63.0	63.2	63.1	62.9	62.4	61.8	61.0	60.0	58.1	55.3	52.2	48.7	45.0	40.9	25.2	0.0
	28	193	62.9	63.1	63.0	62.7	62.3	61.6	60.7	59.7	58.0	55.2	52.1	48.6	44.9	40.8	24.9	0.0
	29	194	62.9	63.0	62.9	62.6	62.1	61.3	60.4	59.3	57.6	55.0	52.0	48.5	44.8	40.7	24.5	0.0
	30	195	62.8	62.9	62.7	62.4	61.9	61.1	60.1	58.9	57.1	54.6	51.6	48.3	44.6	40.5	24.1	0.0
	31	195	62.7	62.8	62.6	62.2	61.7	60.8	59.8	58.5	56.6	54.1	51.3	48.1	44.5	40.5	23.8	0.0
	32	196	62.7	62.7	62.5	62.1	61.5	60.6	59.4	58.0	56.2	53.7	50.9	47.8	44.4	40.5	24.1	0.0
	33	196	55.3	55.4	55.2	54.8	54.1	53.3	52.2	50.9	49.3	47.6	45.6	43.5	41.0	37.2	19.0	0.0
	34	196	47.4	47.3	47.2	46.9	46.4	45.8	45.1	44.3	43.3	42.2	41.0	38.4	31.1	23.0	13.9	0.0
	35	196	39.9	39.8	39.6	38.7	37.5	36.0	34.2	32.2	29.8	27.1	24.2	21.0	17.3	13.3	8.7	0.0

Table 4.20. Curved column, refractive indices. Refractive indices for the cells of the 35 layer silicon lenslet with curved columns. Darker blue indicates higher refractive index.

		Column Refractive Indices															
		1	2	3	4	5	6	7	8	9	10	11	12	13	14	15	16
Layer	1	3.74	3.73	3.73	3.72	3.71	3.70	3.69	3.67	3.65	3.63	3.61	3.58	3.56	3.53	3.49	3.45
	2	4.05	4.04	4.03	4.02	4.00	3.98	3.94	3.91	3.87	3.83	3.78	3.73	3.67	3.60	3.53	3.45
	3	4.38	4.38	4.36	4.34	4.31	4.27	4.22	4.16	4.10	4.03	3.95	3.87	3.78	3.68	3.57	3.45
	4	4.75	4.74	4.72	4.68	4.64	4.58	4.51	4.43	4.34	4.24	4.14	4.02	3.90	3.76	3.62	3.45
	5	4.75	4.74	4.72	4.68	4.64	4.58	4.51	4.43	4.34	4.24	4.14	4.02	3.90	3.76	3.62	3.45
	6	4.75	4.74	4.72	4.68	4.64	4.58	4.51	4.43	4.34	4.24	4.14	4.02	3.90	3.76	3.62	3.45
	7	4.75	4.74	4.72	4.68	4.64	4.58	4.51	4.43	4.34	4.24	4.14	4.02	3.90	3.76	3.62	3.45
	8	4.75	4.74	4.72	4.68	4.64	4.58	4.51	4.43	4.34	4.24	4.14	4.02	3.90	3.76	3.62	3.45
	9	4.75	4.74	4.72	4.68	4.64	4.58	4.51	4.43	4.34	4.24	4.14	4.02	3.90	3.76	3.62	3.45
	10	4.75	4.74	4.72	4.68	4.64	4.58	4.51	4.43	4.34	4.24	4.14	4.02	3.90	3.76	3.62	3.45
	11	4.75	4.74	4.72	4.68	4.64	4.58	4.51	4.43	4.34	4.24	4.14	4.02	3.90	3.76	3.62	3.45
	12	4.75	4.74	4.72	4.68	4.64	4.58	4.51	4.43	4.34	4.24	4.14	4.02	3.90	3.76	3.62	3.45
	13	4.75	4.74	4.72	4.68	4.64	4.58	4.51	4.43	4.34	4.24	4.14	4.02	3.90	3.76	3.62	3.45
	14	4.75	4.74	4.72	4.68	4.64	4.58	4.51	4.43	4.34	4.24	4.14	4.02	3.90	3.76	3.62	3.45
	15	4.75	4.74	4.72	4.68	4.64	4.58	4.51	4.43	4.34	4.24	4.14	4.02	3.90	3.76	3.62	3.45
	16	4.75	4.74	4.72	4.68	4.64	4.58	4.51	4.43	4.34	4.24	4.14	4.02	3.90	3.76	3.62	3.45
	17	4.75	4.74	4.72	4.68	4.64	4.58	4.51	4.43	4.34	4.24	4.14	4.02	3.90	3.76	3.62	3.45
	18	4.75	4.74	4.72	4.68	4.64	4.58	4.51	4.43	4.34	4.24	4.14	4.02	3.90	3.76	3.62	3.45
	19	4.75	4.74	4.72	4.68	4.64	4.58	4.51	4.43	4.34	4.24	4.14	4.02	3.90	3.76	3.62	3.45
	20	4.75	4.74	4.72	4.68	4.64	4.58	4.51	4.43	4.34	4.24	4.14	4.02	3.90	3.76	3.62	3.45
	21	4.75	4.74	4.72	4.68	4.64	4.58	4.51	4.43	4.34	4.24	4.14	4.02	3.90	3.76	3.62	3.45
	22	4.75	4.74	4.72	4.68	4.64	4.58	4.51	4.43	4.34	4.24	4.14	4.02	3.90	3.76	3.62	3.45
	23	4.75	4.74	4.72	4.68	4.64	4.58	4.51	4.43	4.34	4.24	4.14	4.02	3.90	3.76	3.62	3.45
	24	4.75	4.74	4.72	4.68	4.64	4.58	4.51	4.43	4.34	4.24	4.14	4.02	3.90	3.76	3.62	3.45
	25	4.75	4.74	4.72	4.68	4.64	4.58	4.51	4.43	4.34	4.24	4.14	4.02	3.90	3.76	3.62	3.45
	26	4.75	4.74	4.72	4.68	4.64	4.58	4.51	4.43	4.34	4.24	4.14	4.02	3.90	3.76	3.62	3.45
	27	4.75	4.74	4.72	4.68	4.64	4.58	4.51	4.43	4.34	4.24	4.14	4.02	3.90	3.76	3.62	3.45
	28	4.75	4.74	4.72	4.68	4.64	4.58	4.51	4.43	4.34	4.24	4.14	4.02	3.90	3.76	3.62	3.45
	29	4.75	4.74	4.72	4.68	4.64	4.58	4.51	4.43	4.34	4.24	4.14	4.02	3.90	3.76	3.62	3.45
	30	4.75	4.74	4.72	4.68	4.64	4.58	4.51	4.43	4.34	4.24	4.14	4.02	3.90	3.76	3.62	3.45
	31	4.75	4.74	4.72	4.68	4.64	4.58	4.51	4.43	4.34	4.24	4.14	4.02	3.90	3.76	3.62	3.45
	32	4.75	4.74	4.72	4.68	4.64	4.58	4.51	4.43	4.34	4.24	4.14	4.02	3.90	3.76	3.62	3.45
	33	4.38	4.38	4.36	4.34	4.31	4.27	4.22	4.16	4.10	4.03	3.95	3.87	3.78	3.68	3.57	3.45
	34	4.05	4.04	4.03	4.02	4.00	3.98	3.94	3.91	3.87	3.83	3.78	3.73	3.67	3.60	3.53	3.45
37	3.74	3.73	3.73	3.72	3.71	3.70	3.69	3.67	3.65	3.63	3.61	3.58	3.56	3.53	3.49	3.45	

4.9.6 Final thoughts on 3D

The method of extending radial slices that have been modelled into full 3D spherical lenslets outlined in section 4.2 may not lead to an optimal implementation of a curved column lenslet due to the metamaterial columns off the main axis no longer following the same curves as the light rays. One way of solving this would be to use metamaterial cells on each layer that are curved segments as shown in Figure 4.61. A further advantage of this layout is that the compromise described in section 4.9.4 would no longer be required. There is a lot more investigation of the properties of patches in these cells to be done before a layout such as this is practical, most of which will necessarily be further work.

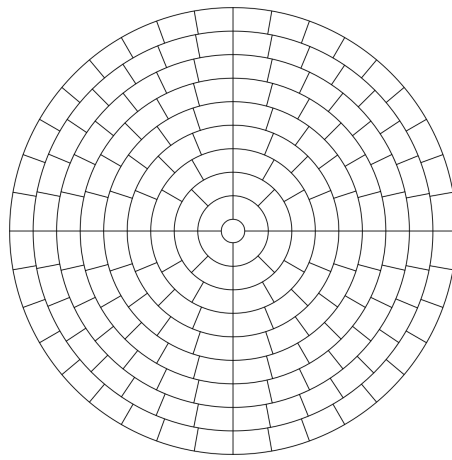


Figure 4.61. Possible layer layout for a curved column lenslet.

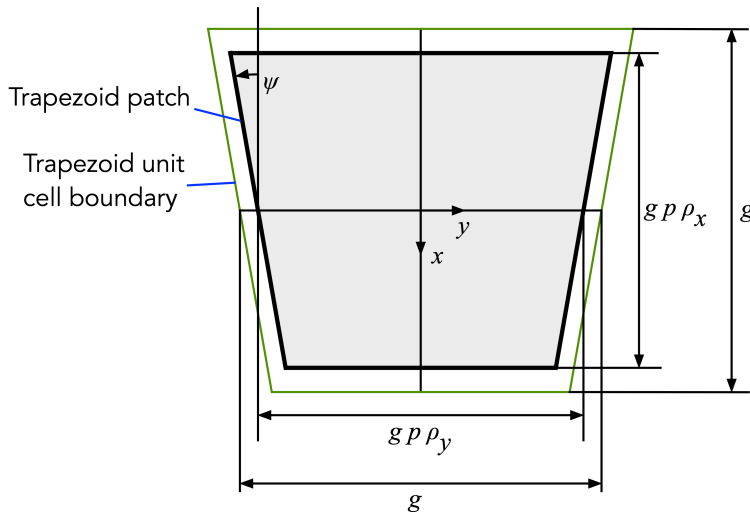


Figure 4.62. A trapezoid patch in a trapezoid unit cell.

As a first step, a trapezoid patch and cell was modelled. A trapezoid can be regarded as an approximation for many of the cells in the segmented layout, especially in the outer rows. The dimensions are shown in Figure 4.62.

Immediately apparent is the fact that this shape can be birefringent. The unit cell, g , defines the height and the central width of the cell. The patch ratio, p , was again used to represent the overall size of the patch along with two compensation factors, ρ_x and ρ_y which combined with g specify the height and central width of the patch. The idea is that ρ_x and ρ_y are chosen such that the refractive index of the patch is the same for both the x and y polarisations for a given p .

To establish if suitable values of ρ_x and ρ_y exist, at least for an example trapezoid, the patch was modelled in HFSS and the refractive index for both polarisations measured using the S-parameter method. An arrangement of six patches in alternating directions, as shown in Figure 4.63, was used to allow master-slave boundaries to be used. In addition, this layout can also be used to investigate the behaviour at non-normal angles of incidence, as described in section 4.9.2.

Figure 4.64 shows the refractive index of a trapezoid patch (patch ratio 60, unit cell $150\ \mu\text{m}$) for both polarisations compared with the equivalent square patch in the same unit cell. The compensation factors, ρ_x and ρ_y , have been chosen to bring the trapezoid's curves close to the square's curve. The correspondence is particularly good around 150 GHz, only dropping off beyond 200 GHz.

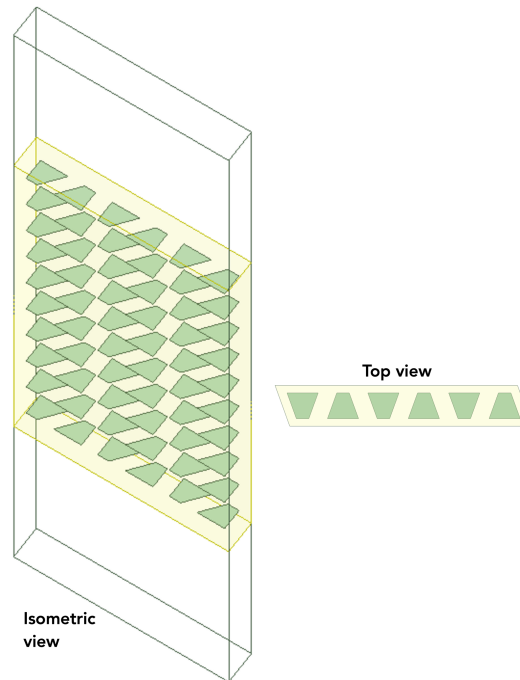


Figure 4.63. HFSS model of trapezoid patches.

This taste of the behaviour of a trapezoid patch is just the beginning if the curved segment concept is to be achieved. A lot of further work is necessary to analyse the behaviour of all the different patches required, including at non-normal incidences, and to determine the ρ_x and ρ_y in every case. In addition, especially towards the centres of the layers, how accurate the trapezoid approximation of the curved segments is, needs to be investigated.

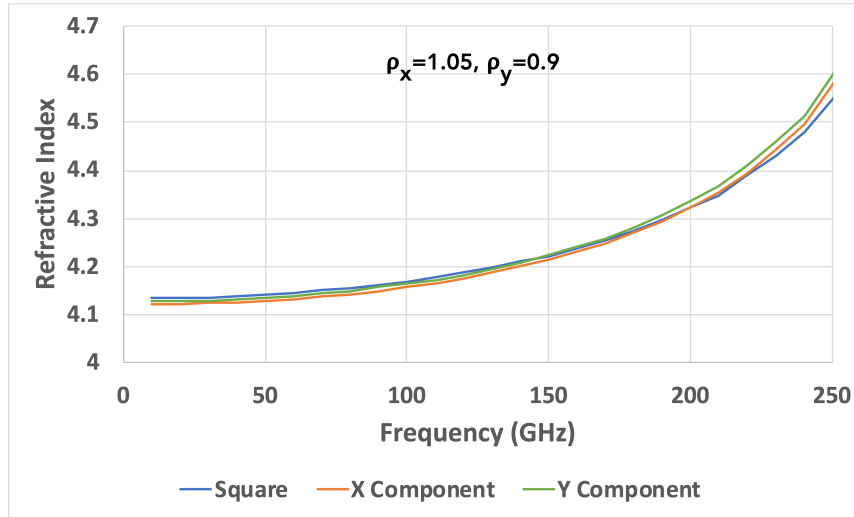


Figure 4.64. Refractive index of a trapezoid patch with a patch ratio of 60 in a 160 μm unit cell compared with the equivalent square patch.

4.10 Conclusions

The feasibility of designing reasonable metamaterial mesh lenslet structures using the simple design model was demonstrated despite its shortcomings; a compensation factor being introduced to allow for them. The steps required to make sensible decisions regarding such parameters as the metamaterial unit cell and layer spacing were explored in detail. The use of internal anti-reflection layers to match the lenslet structure to the carrier dielectric (in addition to matching the dielectric to the surrounding vacuum) was shown to make a significant difference to the performance.

The applicability of artificial dielectrics using the super-capacitive patch was investigated and for the polypropylene lenslet design found to be useful, allowing the saving of five layers over a square patch design. Lenslets were designed for the targeted polypropylene specification with and without super-capacitive patches. The design with such patches required 27 layers including anti-reflection layers, while without them 32 layers were necessary. The far field performance between the two designs matched well except at the highest frequency studied,

where the effect of the shifted low pass filter roll-off with super-capacitive patches became apparent. A saving (in this case) of 15% of the layers may be useful if the reduced bandwidth is not an issue for the application. The basic behaviour of the super-capacitive patch lenslet was modelled over the design bandwidth, but the effect of any resonances outside this range remains as further work, as do any differences in loss, transmission and reflection caused by real world metallic patches replacing the perfect electrical conductors in the model.

It was also shown that super-capacitive patches were not suitable for use with the example silicon lenslet specification. This was due to the low pass filter cut-off frequency lying in the required frequency band. The silicon example design was therefore implemented using only conventional square patches and consisted of 37 layers including six anti-reflection layers. This compares with the lenslet reported by Pisano et al⁶⁵ that contained 34 layers but didn't deploy anti-reflection layers. Although the specifications were not strictly comparable, it indicates that this implementation of the simple design method is producing results consistent with existing work.

The shortcomings of the simple design model were investigated and an alternative using curved columns that followed the rays through the lenslet structure was proposed. This has the potential to eliminate the need for a focal length compensation factor, although this first cut at the algorithm overestimates the ray bending achieved which may be due to the anti-reflection layers not being properly accounted for.

Further work is required to assess (and optimise if necessary) the losses of the proposed lenslet designs over their bandwidths when modelled with copper rather than perfect electric conductor patches and to estimate their gains. A much larger future project is to construct them to verify that they perform in the way the modelling indicates. In addition, the curved column design model requires extending to account for the internal anti-reflection layers.

The extension of the cylindrical models of the curved column structures to a fully three-dimensional circular lenslet also remains as an issue that has not been finalised. The approximation proposed in section 4.2 requires further investigation and may not be completely appropriate for the curved column case. The trapezoidal proposal of section 4.9.6 may be better. Further modelling and device construction will be required to determine this.

The possibility of using the genetic algorithm described in section 2.4 for optimising lenslet designs was explored and appropriate fitness functions were investigated. Such an approach may be especially applicable to the curved column lenslets. However, this approach remains as further work due to the large amounts of modelling necessary which would require more cluster computer time than was available to the author.

Chapter 5 Summary

The work presented in this thesis started by investigating the behaviour of well-known metamaterial structures used in the implementation of millimetre wave optical filter devices before progressing to their use in lenslets and lenslet arrays. The two subjects are connected due to the fact that longitudinal columns through a lenslet structure can be regarded as low pass filters.

Chapter 1 introduced the subjects and provided a context for the work.

Chapter 2 discussed modelling techniques and described the modelling software written by the author that was used in later chapters.

Chapter 3 presented work done by the author investigating alternative metamaterial patch shapes to the conventional square. The use of a genetic algorithm to search for shapes that improved the performance of low-pass filters from the set of patterns available from $N \times N$ pixel patches (extending the work of Ge and Esselle³⁰) produced incremental results. There was an indication that rounding the corners of the square patches had a beneficial effect in the case of the Chebyshev response, but other than that, the conclusion was that the square patch is as good as it gets. This bears out the experience of the Filters Team at Cardiff University who have found that keeping the square patch corners as sharp as possible improves the cut-off of their Butterworth style filters.

However, the constraints applied to the patterns in the $N \times N$ pixel patch set may have been too tight. The requirement for four-fold symmetry of the patterns was a severe limiting factor; although it forced all patterns in the set to be non-birefringent it did not produce the set of all non-birefringent patterns. The restrictions on the value of N to keep the search space a practical size also limited pattern complexity, for example it made patterns that were even remotely fractal difficult to represent.

The concept of 'improvements' to the desired low pass filter device were also hard to specify. The work concentrated on the obvious aspects, ripple in the pass band, steepness of the cut-off and number of layers. But there may be other aspects of the filter response that could be improved that were not anticipated by the fitness functions used to assess the results of the genetic algorithm. This demonstrates

that in some ways, the genetic algorithm does require some knowledge of the result in order to be successful.

An alternative to the scatter-gun approach of the genetic algorithm is to deliberately design a pattern with a specific aim, without being restricted to a particular set of shapes. This approach was followed by considering how the capacitance of a capacitive patch is created and then modifying the shape to increase it. This led the author to propose a shape with fingers that grow into adjacent patches, increasing the inter-patch capacitance by increasing the length of the parallel edges (termed the super-capacitive patch). The result was certainly not four-fold symmetric (though not birefringent) and the value of N required for its representation by an $N \times N$ pixelated pattern would have been at the upper end of those considered suitable for the genetic algorithm. Masks of this super-capacitive patch are under preparation for the manufacture of devices to allow the verification of the basic modelling. The super-capacitive patch is a rather complex shape and how minor manufacturing errors affect its performance could be important and should be investigated, both through further modelling and experimental work.

It was shown that super-capacitive patches do extend the sequence of admittance characteristics in ways that are useful and novel, both in filters and in artificial dielectrics. A filter with a wider stopband was demonstrated in section 3.2.3. Further work is required to completely suppress the signal in the stopband and to improve roll off as well as to construct one and verify the modelling. The application of the patch to artificial dielectrics was also investigated and the possibility of higher achievable refractive indices was shown in section 4.3.5

Chapter 4 then starts by detailing the development process behind metamaterial GRIN lenses using a simple design model. The various decisions that must be made in a GRIN lens design to settle on the unit cell size, layer spacing, and number of layers were considered from the viewpoint of two example lens specifications, one in polypropylene, one in silicon. It was shown that as a result, the super-capacitive patch was only appropriate for use with the polypropylene example lens. With the silicon lens, the cut-off frequency of artificial dielectrics with the high refractive index created by them impinged on the specified frequency range.

The desired refractive index for each layer of each column of the lens structure was then calculated. To be able to convert these refractive indices into the appropriate metamaterial patch sizes that implement them, an artificial dielectric

catalogue was required. A method of measuring the permittivity and permeability parameters of artificial dielectrics was chosen from three found in the literature. A procedure using the S-parameters of a block of the dielectric under test measured by HFSS was developed and used to create the catalogue. This, along with linear interpolation, was then used to specify the patch ratios required.

It was then shown that to achieve good results from the designed lenses it was necessary to use a focal length compensation factor to overcome shortcomings of the design model that led to the focussing effect to be under-estimated when the lens thickness becomes greater than the wavelength of the light travelling through it. However, with suitable compensation factors, good solutions were obtained for both the polypropylene and silicon example specifications. In the polypropylene case, solutions with and without super-capacitive patches were obtained, the use of the latter leading to fewer layers being required against a slight bandwidth trade off. Further work is required to construct these designs and verify the modelling, especially the effects of the super-capacitive patches on the polypropylene version.

The need for the focal length compensation factor was an indication of problems with the simple design methodology. These shortcomings were explored, and two major issues identified; the path of rays through the structure was not properly represented and the incidence angle of light on the metamaterial artificial dielectrics was being ignored. Changes made to address these led the author to propose a method of designing lenses using curved columns. This resulted in columns that followed the path the light took through the structure and also allowed the incidence angle to be calculated for each layer of each column.

To account for the incidence angle of rays on the artificial dielectrics, the refractive index catalogue was extended to include the angle. This required the method of measuring the S-parameters using HFSS to be changed to cover non-normally incident radiation. Section 4.9.2 describes the approach taken by the author to achieve this.

Lenses produced using this initial implementation of the curved column method were much less in need of a compensation factor. The internal anti-reflection layers were not properly accounted for which may be the source of the remaining modelling error. The modelling showed that little light emerged from the sides of the lens structure and that slightly fewer layers were necessary.

Further modelling work is required to develop the curved column approach before an example can be constructed and tested. The underlying geometry should be extended to cover the anti-reflection layers and the method of implementing rotational symmetry to produce a circular lenslet improved. Once satisfactory three-dimensional performance has been achieved, masks can be made, and an example constructed and tested.

The possibility of using segment-like patches (approximated by trapezoids) was briefly looked at. The otherwise birefringent nature of these patches was corrected through careful patch spacing. This approach is also worth taking further as it has the potential to increase the efficiency of devices utilising it, especially in the step to the full circular lenslet.

The work described in this thesis, especially that in Chapter 4, was badly affected by the Covid-19 pandemic. The construction and testing of examples was severely delayed, converting the project into modelling and theory only. The novel metamaterial lenslet devices proposed, however, have applications in CMB instrument focal planes where their possible efficiency and manufacturability improvements would be of use.

Bibliography

- (1) Samtleben, D.; Staggs, S.; Winstein, B. The Cosmic Microwave Background for Pedestrians: A Review for Particle and Nuclear Physicists. *Annu. Rev. Nucl. Part. Sci.* **2007**, *57* (1), 245–283.
<https://doi.org/10.1146/annurev.nucl.54.070103.181232>.
- (2) Sirtori, C. Bridge for the Terahertz Gap. *Nature* **2002**, *417* (6885), 132–133.
<https://doi.org/10.1038/417132b>.
- (3) Nyquist, H. Thermal Agitation of Electric Charge in Conductors. *Phys. Rev.* **1928**, *32* (1), 110–113. <https://doi.org/10.1103/PhysRev.32.110>.
- (4) Seljak, U. Measuring Polarization In Cosmic Microwave Background. *Astrophys. J.* **1997**, *482* (1), 6–16. <https://doi.org/10.1086/304123>.
- (5) Seljak, U.; Zaldarriaga, M. Signature of Gravity Waves in the Polarization of the Microwave Background. *Phys. Rev. Lett.* **1997**, *78* (11), 2054–2057.
<https://doi.org/10.1103/PhysRevLett.78.2054>.
- (6) Ishino, H. LiteBIRD. *Int. J. Mod. Phys. Conf. Ser.* **2016**, *43*, 1660192.
<https://doi.org/10.1142/S2010194516601927>.
- (7) Ade, P. A. R.; Pisano, G.; Tucker, C.; Weaver, S. O. A Review of Metal Mesh Filters. In *Millimeter and Submillimeter Detectors and Instrumentation for Astronomy III*; Zmuidzinas, J., Holland, W. S., Withington, S., Duncan, W. D., Eds.; SPIE: Bellingham, WA, 2006.
- (8) Lamarre, J. M.; Puget, J. L.; Bouchet, F.; Ade, P. A. R.; Benoit, A.; Bernard, J. P.; Bock, J. J.; de Bernardis, P.; Charra, J.; Couchot, F.; Delabrouille, J.; Efstathiou, G.; Giard, M.; Guyot, G.; Lange, A. E.; Maffei, B.; Murphy, A.; Pajot, F.; Piat, M.; Ristorcelli, I.; Santos, D.; Sudiwala, R. V.; Sygnet, J. F.; Torre, J. P.; Yurchenko, V.; Yvon, D. The Planck High Frequency Instrument, a Third Generation CMB Experiment, and a Full Sky Submillimeter Survey. *New Astron. Rev.* **2003**, *47* (11–12), 1017–1024.
<https://doi.org/10.1016/j.newar.2003.09.006>.
- (9) Kosowsky, A. The Atacama Cosmology Telescope. *New Astron. Rev.* **2003**, *47* (11), 939–943. <https://doi.org/10.1016/j.newar.2003.09.003>.
- (10) Audley, M. D.; Holland, W. S.; Duncan, W. D.; Atkinson, D.; Cliffe, M.; Ellis, M.; Gao, X.; Gostick, D. C.; Hodson, T.; Kelly, D.; MacIntosh, M. J.;

- McGregor, H.; Peacocke, T.; Robson, I.; Smith, I.; Irwin, K. D.; Hilton, G. C.; Ullom, J. N.; Walton, A.; Dunare, C.; Parkes, W.; Ade, P. A. R.; Bintley, D.; Gannaway, F.; Griffin, M.; Pisano, G.; Sudiwala, R. V.; Walker, I.; Woodcraft, A.; Fich, M.; Halpern, M.; Mitchell, G.; Naylor, D.; Bastien, P. SCUBA-2: A Large-Format TES Array for Submillimetre Astronomy. *Nucl. Instrum. Methods Phys. Res. Sect. Accel. Spectrometers Detect. Assoc. Equip.* **2004**, 520 (1), 479–482. <https://doi.org/10.1016/j.nima.2003.11.378>.
- (11) Griffin, M.; Abergel, A.; Ade, P.; André, P.; Baluteau, J.-P.; Bock, J.; Franceschini, A.; Gear, W.; Glenn, J.; Griffin, D.; King, K.; Lellouch, E.; Naylor, D.; Olofsson, G.; Perez-Fournon, I.; Rowan-Robinson, M.; Saraceno, P.; Sawyer, E.; Smith, A.; Swinyard, B.; Vigroux, L.; Wright, G. Herschel-SPIRE: Design, Performance, and Scientific Capabilities. In *Space Telescopes and Instrumentation I: Optical, Infrared, and Millimeter*; International Society for Optics and Photonics, 2006; Vol. 6265, p 62650A. <https://doi.org/10.1117/12.670783>.
- (12) Poglitsch, A.; Waelkens, C.; Bauer, O. H.; Cepa, J.; Feuchtgruber, H.; Henning, T.; Hoof, C. van; Kerschbaum, F.; Lemke, D.; Renotte, E.; Rodriguez, L.; Saraceno, P.; Vandenbussche, B. The Photodetector Array Camera and Spectrometer (PACS) for the Herschel Space Observatory. In *Space Telescopes and Instrumentation I: Optical, Infrared, and Millimeter*; International Society for Optics and Photonics, 2006; Vol. 6265, p 62650B. <https://doi.org/10.1117/12.670654>.
- (13) Munk, B. A. *Frequency Selective Surfaces: Theory and Design*; John Wiley & Sons, Inc.: Hoboken, NJ, USA, 2000. <https://doi.org/10.1002/0471723770>.
- (14) Schurig, D.; Mock, J. J.; Justice, B. J.; Cummer, S. A.; Pendry, J. B.; Starr, A. F.; Smith, D. R. Metamaterial Electromagnetic Cloak at Microwave Frequencies. *Science* **2006**, 314 (5801), 977–980. <https://doi.org/10.1126/science.1133628>.
- (15) Ergin, T.; Stenger, N.; Brenner, P.; Pendry, J. B.; Wegener, M. Three-Dimensional Invisibility Cloak at Optical Wavelengths. *Science* **2010**, 328 (5976), 337–339.
- (16) Ulrich, R. Far-Infrared Properties of Metallic Mesh and Its Complementary Structure. *Infrared Phys.* 7 (1), 37–50.

- (17) Ade, P.A.R. Astronomical and Atmospheric Studies at Far-Infrared Wavelengths, London University, London, 1973.
- (18) Timusk, T.; Richards, P. L. Near Millimeter Wave Bandpass Filters. *Appl. Opt.* **1981**, 20 (8), 1355–1360. <https://doi.org/10.1364/AO.20.001355>.
- (19) Pisano, G.; Tucker, C.; Ade, P. A. R.; Moseley, P.; Ng, M. W. Metal Mesh Based Metamaterials for Millimetre Wave and THz Astronomy Applications. In *2015 8th UK, Europe, China Millimeter Waves and THz Technology Workshop (UCMMT)*; 2015; pp 1–4. <https://doi.org/10.1109/UCMMT.2015.7460631>.
- (20) Sushko, O.; Pigeon, M.; Kreouzis, T.; Parini, C.; Donnan, R.; Dubrovka, R. Low-Cost Inkjet-Printed FSS Band-Pass Filters for 100 and 300 GHz. In *2016 10th European Conference on Antennas and Propagation (EuCAP)*; 2016; pp 1–3. <https://doi.org/10.1109/EuCAP.2016.7481780>.
- (21) Sun, J.; Hu, F. Three-Dimensional Printing Technologies for Terahertz Applications: A Review. *Int. J. RF Microw. Comput.-Aided Eng.* **2020**, 30 (1), e21983. <https://doi.org/10.1002/mmce.21983>.
- (22) Kundu, A.; Das, S.; Maity, S.; Gupta, B.; Lahiri, S. K.; Saha, H. A Tunable Band-Stop Filter Using a Metamaterial Structure and MEMS Bridges on a Silicon Substrate. *J. Micromechanics Microengineering* **2012**, 22 (4), 045004. <https://doi.org/10.1088/0960-1317/22/4/045004>.
- (23) Tucker, C. E.; Ade, P. A. R. Thermal Filtering for Large Aperture Cryogenic Detector Arrays. In *Millimeter and Submillimeter Detectors and Instrumentation for Astronomy III*; International Society for Optics and Photonics, 2006; Vol. 6275, p 62750T. <https://doi.org/10.1117/12.673159>.
- (24) Moallem, M.; Sarabandi, K. A Single-Layer Metamaterial-Based Polarizer and Bandpass Frequency Selective Surface with an Adjacent Transmission Zero. In *2011 IEEE International Symposium on Antennas and Propagation (APSURSI)*; 2011; pp 2649–2652. <https://doi.org/10.1109/APS.2011.5997069>.
- (25) Wang, Y.; Yang, B.; Tian, Y.; Donnan, R. S.; Lancaster, M. J. Micromachined Thick Mesh Filters for Millimeter-Wave and Terahertz Applications. *IEEE Trans. Terahertz Sci. Technol.* **2014**, 4 (2), 247–253. <https://doi.org/10.1109/TTHZ.2013.2296564>.
- (26) Melo, A. M.; Gobbi, A. L.; Piazzetta, M. H. O.; da Silva, A. M. P. A. Cross-Shaped Terahertz Metal Mesh Filters: Historical Review and Results

- <https://www.hindawi.com/journals/aot/2012/530512/> (accessed 2020 -07 -14). <https://doi.org/10.1155/2012/530512>.
- (27) Monacelli, B.; Pryor, J. B.; Munk, B. A.; Kotter, D.; Boreman, G. D. Infrared Frequency Selective Surface Based on Circuit-Analog Square Loop Design. *IEEE Trans. Antennas Propag.* **2005**, 53 (2), 745–752. <https://doi.org/10.1109/TAP.2004.841290>.
- (28) Navarro-Cía, M.; Kuznetsov, S. A.; Aznabet, M.; Beruete, M.; Falcone, F.; Ayza, M. S. Route for Bulk Millimeter Wave and Terahertz Metamaterial Design. *IEEE J. Quantum Electron.* **2011**, 47 (3), 375–385. <https://doi.org/10.1109/JQE.2010.2090512>.
- (29) Wu, T. K. Novel Metamaterial Absorber with Fractal Elements. In *2015 IEEE International Symposium on Antennas and Propagation USNC/URSI National Radio Science Meeting*; 2015; pp 244–245. <https://doi.org/10.1109/APS.2015.7304508>.
- (30) Ge, Y.; Esselle, K. P. GA/FDTD Technique for the Design and Optimisation of Periodic Metamaterials. *Antennas Propag. IET Microw.* **2007**, 1 (1), 158–164. <https://doi.org/10.1049/iet-map:20050313>.
- (31) Sui, S.; Ma, H.; Wang, J.; Pang, Y.; Qu, S. Topology Optimization Design of a Lightweight Ultra-Broadband Wide-Angle Resistance Frequency Selective Surface Absorber. *J. Phys. Appl. Phys.* **2015**, 48 (21), 215101. <https://doi.org/10.1088/0022-3727/48/21/215101>.
- (32) Sui, S.; Ma, H.; Wang, J.; Pang, Y.; Zhang, J.; Qu, S. Two-Dimensional QR-Coded Metamaterial Absorber. *Appl. Phys. A* **2016**, 122 (1), 28. <https://doi.org/10.1007/s00339-015-9545-x>.
- (33) Ranjan, P.; Choubey, A.; Mahto, S. K.; Sinha, R. A Six-Band Ultra-Thin Polarization-Insensitive Pixelated Metamaterial Absorber Using a Novel Binary Wind Driven Optimization Algorithm. *J. Electromagn. Waves Appl.* **2018**, 32 (18), 2367–2385. <https://doi.org/10.1080/09205071.2018.1510344>.
- (34) Ranjan, P.; Mahto, S. K.; Choubey, A. BWDO Algorithm and Its Application in Antenna Array and Pixelated Metasurface Synthesis. *Antennas Propag. IET Microw.* **2019**, 13 (9), 1263–1270. <https://doi.org/10.1049/iet-map.2018.5051>.
- (35) Kock, W. E. Metallic Delay Lenses. *Bell Syst. Tech. J.* **1948**, 27 (1), 58–82. <https://doi.org/10.1002/j.1538-7305.1948.tb01331.x>.

- (36) Zhang, J.; Ade, P. a. R.; Mauskopf, P.; Moncelsi, L.; Savini, G.; Whitehouse, N. New Artificial Dielectric Metamaterial and Its Application as a Terahertz Antireflection Coating. *Appl. Opt.* **2009**, *48* (35), 6635–6642. <https://doi.org/10.1364/AO.48.006635>.
- (37) Bernard, J.-Ph.; Ade, P.; André, Y.; Aumont, J.; Bautista, L.; Bray, N.; Bernardis, P. de; Boulade, O.; Bousquet, F.; Bouzit, M.; Buttice, V.; Caillat, A.; Charra, M.; Chaigneau, M.; Crane, B.; Crussaire, J.-P.; Douchin, F.; Doumayrou, E.; Dubois, J.-P.; Engel, C.; Etcheto, P.; Gélot, P.; Griffin, M.; Foenard, G.; Grabarnik, S.; Hargrave, P.; Hughes, A.; Laureijs, R.; Lepennec, Y.; Leriche, B.; Longval, Y.; Maestre, S.; Maffei, B.; Martignac, J.; Marty, C.; Marty, W.; Masi, S.; Mirc, F.; Misawa, R.; Montel, J.; Montier, L.; Mot, B.; Narbonne, J.; Nicot, J.-M.; Pajot, F.; Parot, G.; Pérot, E.; Pimentao, J.; Pisano, G.; Ponthieu, N.; Ristorcelli, I.; Rodriguez, L.; Roudil, G.; Salatino, M.; Savini, G.; Simonella, O.; Saccoccio, M.; Tapie, P.; Tauber, J.; Torre, J.-P.; Tucker, C. PILOT: A Balloon-Borne Experiment to Measure the Polarized FIR Emission of Dust Grains in the Interstellar Medium. *Exp. Astron.* **2016**, *42* (2), 199–227. <https://doi.org/10.1007/s10686-016-9506-1>.
- (38) Fissel, L. M.; Ade, P. A. R.; Angilè, F. E.; Benton, S. J.; Chapin, E. L.; Devlin, M. J.; Gandilo, N. N.; Gundersen, J. O.; Hargrave, P. C.; Hughes, D. H.; Klein, J.; Korotkov, A. L.; Marsden, G.; Matthews, T. G.; Moncelsi, L.; Mroczkowski, T. K.; Netterfield, C. B.; Novak, G.; Olmi, L.; Pascale, E.; Savini, G.; Scott, D.; Shariff, J. A.; Soler, J. D.; Thomas, N. E.; Truch, M. D. P.; Tucker, C. E.; Tucker, G. S.; Ward-Thompson, D.; Wiebe, D. V. The Balloon-Borne Large-Aperture Submillimeter Telescope for Polarimetry: BLAST-Pol. In *Millimeter, Submillimeter, and Far-Infrared Detectors and Instrumentation for Astronomy V*; International Society for Optics and Photonics, 2010; Vol. 7741, p 77410E. <https://doi.org/10.1117/12.857601>.
- (39) Zhang, J.; Ade, P. A. R.; Mauskopf, P.; Savini, G.; Moncelsi, L.; Whitehouse, N. Polypropylene Embedded Metal Mesh Broadband Achromatic Half-Wave Plate for Millimeter Wavelengths. *Appl. Opt.* **2011**, *50* (21), 3750–3757. <https://doi.org/10.1364/AO.50.003750>.
- (40) Syed, W. H.; Neto, A. Front-to-Back Ratio Enhancement of Planar Printed Antennas by Means of Artificial Dielectric Layers. *IEEE Trans. Antennas Propag.* **2013**, *61* (11), 5408–5416. <https://doi.org/10.1109/TAP.2013.2275915>.

- (41) Pisano, G.; Ade, P. A. R.; Tucker, C. Experimental Realization of an Achromatic Magnetic Mirror Based on Metamaterials. *Appl. Opt.* **2016**, *55* (18), 4814–4819. <https://doi.org/10.1364/AO.55.004814>.
- (42) Pisano, G.; Maffei, B.; Ade, P. A. R.; Bernardis, P. de; Maagt, P. de; Ellison, B.; Henry, M.; Ng, M. W.; Schott, B.; Tucker, C. Multi-Octave Metamaterial Reflective Half-Wave Plate for Millimeter and Sub-Millimeter Wave Applications. *Appl. Opt.* **2016**, *55* (36), 10255–10262. <https://doi.org/10.1364/AO.55.010255>.
- (43) Cavallo, D.; Syed, W. H.; Neto, A. Closed-Form Analysis of Artificial Dielectric Layers—Part I: Properties of a Single Layer Under Plane-Wave Incidence. *IEEE Trans. Antennas Propag.* **2014**, *62* (12), 6256–6264. <https://doi.org/10.1109/TAP.2014.2365233>.
- (44) Cavallo, D.; Syed, W. H.; Neto, A. Closed-Form Analysis of Artificial Dielectric Layers—Part II: Extension to Multiple Layers and Arbitrary Illumination. *IEEE Trans. Antennas Propag.* **2014**, *62* (12), 6265–6273. <https://doi.org/10.1109/TAP.2014.2365236>.
- (45) Maxwell, J. C. *Camb. Dublin Math J* **1854**, *8* (188).
- (46) Luneburg, R. K. *Mathematical Theory of Optics*; Brown U. Press: Providence RI, 1944.
- (47) Robinson, J. G. P. Spherical Microwave Lens. US2849713A, August 26, 1958.
- (48) Sinclair, W. J. Graded Index Lens Structure Suitable for Optical Fiber Termination. US5172271A, December 15, 1992.
- (49) Xin, H.; Liang, M. 3-D-Printed Microwave and THz Devices Using Polymer Jetting Techniques. *Proc. IEEE* **2017**, *105* (4), 737–755. <https://doi.org/10.1109/JPROC.2016.2621118>.
- (50) Kundtz, N.; Smith, D. R. Extreme-Angle Broadband Metamaterial Lens. *Nat. Mater.* **2010**, *9* (2), 129–132. <https://doi.org/10.1038/nmat2610>.
- (51) Chen, H.; Chan, C. T.; Sheng, P. Transformation Optics and Metamaterials. *Nat. Mater.* **2010**, *9* (5), 387–396. <https://doi.org/10.1038/nmat2743>.
- (52) Pendry, J. B.; Schurig, D.; Smith, D. R. Controlling Electromagnetic Fields. *Science* **2006**, *312* (5781), 1780–1782. <https://doi.org/10.1126/science.1125907>.

- (53) Leonhardt, U. Optical Conformal Mapping. *Science* **2006**, 312 (5781), 1777–1780. <https://doi.org/10.1126/science.1126493>.
- (54) Hunt, J. D. Metamaterials for Computational Imaging. PhD, Duke University, 2013.
- (55) Luque-González, J. M.; Halir, R.; Wangüemert-Pérez, J. G.; de-Oliva-Rubio, J.; Schmid, J. H.; Cheben, P.; Molina-Fernández, Í.; Ortega-Moñux, A. An Ultracompact GRIN-Lens-Based Spot Size Converter Using Subwavelength Grating Metamaterials. *Laser Photonics Rev.* **2019**, 13 (11), 1900172. <https://doi.org/10.1002/lpor.201900172>.
- (56) Mishra, B. P.; Sahu, S.; Parashar, S. K. S.; Pathak, S. K. A Compact Wideband and High Gain GRIN Metamaterial Lens Antenna System Suitable for C, X, Ku Band Application. *Optik* **2018**, 165, 266–274. <https://doi.org/10.1016/j.ijleo.2018.03.092>.
- (57) Kitayama, D.; Yaita, M.; Song, H.-J. Laminated Metamaterial Flat Lens at Millimeter-Wave Frequencies. *Opt. Express* **2015**, 23 (18), 23348–23356. <https://doi.org/10.1364/OE.23.023348>.
- (58) Baghel, A. K.; Kulkarni, S. S.; Nayak, S. K. Far-Field Wireless Power Transfer Using GRIN Lens Metamaterial at GHz Frequency. *IEEE Microw. Wirel. Compon. Lett.* **2019**, 29 (6), 424–426. <https://doi.org/10.1109/LMWC.2019.2912056>.
- (59) Chen, X.; Feng Ma, H.; Ying Zou, X.; Xiang Jiang, W.; Jun Cui, T. Three-Dimensional Broadband and High-Directivity Lens Antenna Made of Metamaterials. *J. Appl. Phys.* **2011**, 110 (4), 044904. <https://doi.org/10.1063/1.3622596>.
- (60) Defrance, F.; Jung-Kubiak, C.; Rahiminejad, S.; Macioce, T.; Sayers, J.; Connors, J.; Radford, S. J. E.; Chattopadhyay, G.; Golwala, S. R. Flat Low-Loss Silicon Gradient Index Lens for Millimeter and Submillimeter Wavelengths. *J. Low Temp. Phys.* **2020**, 199 (1), 376–383. <https://doi.org/10.1007/s10909-019-02255-x>.
- (61) He, Y.; Eleftheriades, G. V. A Highly-Efficient Flat Graded-Index Dielectric Lens for Millimeter-Wave Application. In *2017 IEEE International Symposium on Antennas and Propagation USNC/URSI National Radio Science Meeting*; 2017; pp 2655–2656. <https://doi.org/10.1109/APUSNCURSINRSM.2017.8073370>.

- (62) He, Y.; Eleftheriades, G. V. Matched, Low-Loss, and Wideband Graded-Index Flat Lenses for Millimeter-Wave Applications. *IEEE Trans. Antennas Propag.* **2018**, 66 (3), 1114–1123. <https://doi.org/10.1109/TAP.2018.2790173>.
- (63) Nguyen, V. N.; Yonak, S. H.; Smith, D. R. Millimeter-Wave Artificial Dielectric Gradient Index Lenses. In *2009 3rd European Conference on Antennas and Propagation*; 2009; pp 1886–1890.
- (64) Savini, G.; Ade, P. A. R.; Zhang, J. A New Artificial Material Approach for Flat THz Frequency Lenses. *Opt. Express* **2012**, 20 (23), 25766–25773. <https://doi.org/10.1364/OE.20.025766>.
- (65) Pisano, G.; Austermann, J.; Beall, J.; Halverson, N.; Hubmayr, J.; Jaehnig, G.; McKenney, C. M.; Raymond, B.; Suzuki, A. Development of Flat Silicon-Based Mesh Lens Arrays for Millimeter and Sub-Millimeter Wave Astronomy. *J. Low Temp. Phys.* **2020**, 199 (3), 923–934. <https://doi.org/10.1007/s10909-019-02327-y>.
- (66) Sukumlyn, T. W. Lens Structure. US2216965A, October 8, 1940.
- (67) Yamamoto, T.; Mishina, Y.; Oda, M. Graded Index Lens Array. US4852982A, August 1, 1989.
- (68) Schnitzer, M. J. Graded-Index Lens Microscopes. US6643071B2, November 4, 2003.
- (69) Lier, E. Antenna Array with Metamaterial Lens. US8164531B2, April 24, 2012.
- (70) Schulwitz, L.; Mortazawi, A. A Compact Millimeter-Wave Horn Antenna Array Fabricated through Layer-by-Layer Stereolithography. In *2008 IEEE Antennas and Propagation Society International Symposium*; 2008; pp 1–4. <https://doi.org/10.1109/APS.2008.4619409>.
- (71) Li, Y.; Ge, L.; Wang, J.; Da, S.; Cao, D.; Wang, J.; Liu, Y. 3-D Printed High-Gain Wideband Waveguide Fed Horn Antenna Arrays for Millimeter-Wave Applications. *IEEE Trans. Antennas Propag.* **2019**, 67 (5), 2868–2877. <https://doi.org/10.1109/TAP.2019.2899008>.
- (72) Nibarger, J. P.; Beall, J. A.; Becker, D.; Britton, J.; Cho, H.-M.; Fox, A.; Hilton, G. C.; Hubmayr, J.; Li, D.; McMahon, J.; Niemack, M. D.; Irwin, K. D.; Van Lanen, J.; Yoon, K. W. An 84 Pixel All-Silicon Corrugated Feedhorn for CMB Measurements. *J. Low Temp. Phys.* **2012**, 167 (3), 522–527. <https://doi.org/10.1007/s10909-011-0428-z>.

- (73) Chattopadhyay, G.; Chao-Lin Kuo; Day, P.; Bock, J. J.; Zmuidzinas, J.; Lange, A. E. Planar Antenna Arrays for CMB Polarization Detection. In *2007 Joint 32nd International Conference on Infrared and Millimeter Waves and the 15th International Conference on Terahertz Electronics*; 2007; pp 184–185. <https://doi.org/10.1109/ICIMW.2007.4516451>.
- (74) Huo, Y.; Taylor, G. W.; Bansal, R. Planar Log-Periodic Antennas on Extended Hemispherical Silicon Lenses for Millimeter/Submillimeter Wave Detection Applications. *Int. J. Infrared Millim. Waves* **2002**, 23 (6), 819–839. <https://doi.org/10.1023/A:1015738932198>.
- (75) Nitta, T.; Naruse, M.; Sekimoto, Y.; Mitsui, K.; Okada, N.; Karatsu, K.; Sekine, M.; Matsuo, H.; Noguchi, T.; Uzawa, Y.; Seta, M.; Nakai, N. Beam Pattern Measurements of Millimeter-Wave Kinetic Inductance Detector Camera With Direct Machined Silicon Lens Array. *IEEE Trans. Terahertz Sci. Technol.* **2013**, 3 (1), 56–62. <https://doi.org/10.1109/TTHZ.2012.2235123>.
- (76) Suzuki, A.; Arnold, K.; Edwards, J.; Engargiola, G.; Holzapfel, W.; Keating, B.; Lee, A. T.; Meng, X. F.; Myers, M. J.; O'Brient, R.; Quealy, E.; Rebeiz, G.; Richards, P. L.; Rosen, D.; Siritanasak, P. Multi-Chroic Dual-Polarization Bolometric Detectors for Studies of the Cosmic Microwave Background. *J. Low Temp. Phys.* **2014**, 176 (5), 650–656. <https://doi.org/10.1007/s10909-013-1049-5>.
- (77) Suzuki, A.; Ade, P.; Akiba, Y.; Aleman, C.; Arnold, K.; Baccigalupi, C.; Barch, B.; Barron, D.; Bender, A.; Boettger, D.; Borrill, J.; Chapman, S.; Chinone, Y.; Cukierman, A.; Dobbs, M.; Ducout, A.; Dunner, R.; Elleflot, T.; Errard, J.; Fabbian, G.; Feeney, S.; Feng, C.; Fujino, T.; Fuller, G.; Gilbert, A.; Goeckner-Wald, N.; Groh, J.; Haan, T. D.; Hall, G.; Halverson, N.; Hamada, T.; Hasegawa, M.; Hattori, K.; Hazumi, M.; Hill, C.; Holzapfel, W.; Hori, Y.; Howe, L.; Inoue, Y.; Irie, F.; Jaehnig, G.; Jaffe, A.; Jeong, O.; Katayama, N.; Kaufman, J.; Kazemzadeh, K.; Keating, B.; Kermish, Z.; Keskitalo, R.; Kisner, T.; Kusaka, A.; Jeune, M. L.; Lee, A.; Leon, D.; Linder, E.; Lowry, L.; Matsuda, F.; Matsumura, T.; Miller, N.; Mizukami, K.; Montgomery, J.; Navaroli, M.; Nishino, H.; Peloton, J.; Poletti, D.; Puglisi, G.; Rebeiz, G.; Raum, C.; Reichardt, C.; Richards, P.; Ross, C.; Rotermund, K.; Segawa, Y.; Sherwin, B.; Shirley, I.; Siritanasak, P.; Stebor, N.; Stompor, R.; Suzuki, J.; Tajima, O.; Takada, S.; Takakura, S.; Takatori, S.; Tikhomirov, A.; Tomaru, T.; Westbrook, B.; Whitehorn, N.; Yamashita, T.; Zahn, A.; Zahn, O. The Polarbear-2 and

- the Simons Array Experiments. *J. Low Temp. Phys.* **2016**, 184 (3), 805–810. <https://doi.org/10.1007/s10909-015-1425-4>.
- (78) Pisano, G.; Maffei, B.; Robinson, M.; Deo, P.; van der Vorst, M.; Trappe, N.; Tucker, C. Planar Mesh-Lens Arrays for Millimeter and Sub-Mm Wave Focal Planes. In *2016 41st International Conference on Infrared, Millimeter, and Terahertz waves (IRMMW-THz)*; 2016; pp 1–2. <https://doi.org/10.1109/IRMMW-THz.2016.7758897>.
- (79) Trappe, N.; Bucher, M.; Bernardis, P. de; Delabrouille, J.; Deo, P.; Petris, M. D.; Doherty, S.; Ghribi, A.; Gradziel, M.; Kuzmin, L.; Maffei, B.; Masi, S.; Murphy, J. A.; Noviello, F.; O’Sullivan, C.; Pagano, L.; Piacentini, F.; Piat, M.; Pisano, G.; Robinson, M.; Stompor, R.; Tartari, A.; Traini, A.; Vorst, M. van der; Verhoeve, P.; Zhu, C. Next Generation Sub-Millimetre Wave Focal Plane Array Coupling Concepts: An ESA TRP Project to Develop Multichroic Focal Plane Pixels for Future CMB Polarisation Experiments. In *Millimeter, Submillimeter, and Far-Infrared Detectors and Instrumentation for Astronomy IX*; International Society for Optics and Photonics, 2018; Vol. 10708, p 107082H. <https://doi.org/10.1117/12.2313480>.
- (80) Orfanidis, S. Electromagnetic Waves and Antennas <http://www.ece.rutgers.edu/~orfanidi/ewa/> (accessed 2017 -11 -07).
- (81) Yee, K. Numerical Solution of Initial Boundary Value Problems Involving Maxwell’s Equations in Isotropic Media. *IEEE Trans. Antennas Propag.* **1966**, 14 (3), 302–307. <https://doi.org/10.1109/TAP.1966.1138693>.
- (82) Taflove, A.; Hagness, S. C. *Computational Electrodynamics: The Finite-Difference Time-Domain Method*; Artech House, 2005.
- (83) Schneider, J. B. Understanding the Finite-Difference Time-Domain Method www.eecs.wsu.edu/~schneidj/ufdttd (accessed 2020 -03 -23).
- (84) ANSYS HFSS: High Frequency Electromagnetic Field Simulation Software <https://www.ansys.com/en-gb/products/electronics/ansys-hfss> (accessed 2019 -12 -08).
- (85) Holland, J. *Adaptation in Natural and Artificial Systems: An Introductory Analysis with Applications to Biology, Control, and Artificial Intelligence*; MIT Press, 1992.
- (86) Eiben, A. E.; Smith, J. E. *Introduction to Evolutionary Computing*; Springer, 1998.

- (87) Krishnakumar, K. Micro-Genetic Algorithms For Stationary And Non-Stationary Function Optimization. In *Intelligent Control and Adaptive Systems*; International Society for Optics and Photonics, 1990; Vol. 1196, pp 289–297. <https://doi.org/10.1117/12.969927>.
- (88) CST Studio Suite 3D EM simulation and analysis software <https://www.3ds.com/products-services/simulia/products/cst-studio-suite/> (accessed 2020 -10 -11).
- (89) Huray, P. G. *Maxwell's Equations*; Wiley-IEEE Press, 2011.
- (90) Lee, S.-W.; Zarrillo, G.; Law, C.-L. Simple Formulas for Transmission Through Periodic Metal Grids or Plates http://www.ittc.ku.edu/~callen/Hi-Z_surfaces/Lee1982TAPpp904-909.pdf (accessed 2018 -02 -19).
- (91) Arnaud, J. A.; Pelow, F. A. Resonant-Grid Quasi-Optical Diplexers. *Bell Syst. Tech. J.* **1975**, 54 (2), 263–283. <https://doi.org/10.1002/j.1538-7305.1975.tb02838.x>.
- (92) Anderson, I. On the Theory of Self-Resonant Grids. *Bell Syst. Tech. J.* **1975**, 54 (10), 1725–1731. <https://doi.org/10.1002/j.1538-7305.1975.tb03551.x>.
- (93) Chen, C.-C. Transmission of Microwave Through Perforated Flat Plates of Finite Thickness. *IEEE Trans. Microw. Theory Tech.* **1973**, 21 (1), 1–6. <https://doi.org/10.1109/TMTT.1973.1127906>.
- (94) Potter, M.; Bérenger, J.-P. A Review of the Total Field/Scattered Field Technique for the FDTD Method. *E-Fermat.org*.
- (95) Chew, W. C.; Weedon, W. H. A 3-D Perfectly Matched Medium from Modified Maxwells Equations with Stretched Coordinates. *IEEE Microw. Guid. Wave Lett* **1994**, 7, 599–604.
- (96) Roden, J. A.; Gedney, S. D. Convolution PML (CPML): An Efficient FDTD Implementation of the CFS–PML for Arbitrary Media. *Microw. Opt. Technol. Lett.* **2000**, 27 (5), 334–339. [https://doi.org/10.1002/1098-2760\(20001205\)27:5<334::AID-MOP14>3.0.CO;2-A](https://doi.org/10.1002/1098-2760(20001205)27:5<334::AID-MOP14>3.0.CO;2-A).
- (97) Maloney, J. G.; Smith, G. S. The Efficient Modeling of Thin Material Sheets in the Finite-Difference Time-Domain (FDTD) Method. *IEEE Trans. Antennas Propag.* **1992**, 40 (3), 323–330. <https://doi.org/10.1109/8.135475>.

- (98) Bhavikatti, S. S. *Finite Element Analysis*; New Age International P Ltd, Publishers: New Delhi, 2005.
- (99) Floquet theory - Encyclopedia of Mathematics
https://encyclopediaofmath.org/index.php?title=Floquet_theory (accessed 2021 -04 -24).
- (100) Goldberg, D. E. *Genetic Algorithms in Search, Optimization and Machine Learning*; Addison-Wesley: Reading, Mass., 1988.
- (101) Haupt, R. L.; Werner, D. H. *Genetic Algorithms in Electromagnetics*; John Wiley & Sons: Hoboken, NJ, USA, 2007.
- (102) Winder, S. *Analog and Digital Filter Design*; Elsevier, 2002.
<https://doi.org/10.1016/B978-0-7506-7547-5.X5000-3>.
- (103) Butterworth, S. On the Theory of Filter Amplifiers. *Wirel. Eng.* **1930**, 7, 536–541.
- (104) Weinberg, L.; Slepian, P. Takahasi's Results on Tchebycheff and Butterworth Ladder Networks. *IRE Trans. Circuit Theory* **1960**, 7 (2), 88–101. <https://doi.org/10.1109/TCT.1960.1086643>.
- (105) The Gnome Project. The GTK Project - A free and open-source cross-platform widget toolkit <https://www.gtk.org/> (accessed 2020 -10 -03).
- (106) Booch, G.; Jacobson, I.; Rumbaugh, J. *The Unified Modeling Language User Guide*, 2nd ed.; Addison-Wesley object technology series; Addison-Wesley: Upper Saddle River, NJ, 2005.
- (107) Pilone, D. *UML 2.0 Pocket Reference*, First edition.; O'Reilly: Sebastopol, CA ; Farnham, Beijing ; Farnham, 2006.
- (108) Quinlan, D.; Wells, J. B.; Kamareddine, F. BNF-Style Notation as It Is Actually Used. In *Intelligent Computer Mathematics*; Kaliszyk, C., Brady, E., Kohlhase, A., Sacerdoti Coen, C., Eds.; Lecture Notes in Computer Science; Springer International Publishing: Cham, 2019; pp 187–204.
https://doi.org/10.1007/978-3-030-23250-4_13.
- (109) Lee, S.-W.; Zarrillo, G.; Law, C.-L. Simple Formulas for Transmission through Periodic Metal Grids or Plates. *IEEE Trans. Antennas Propag.* **1982**, 30 (5), 904–909. <https://doi.org/10.1109/TAP.1982.1142923>.
- (110) Ulrich, R. Far-Infrared Properties of Metallic Mesh and Its Complementary Structure. *Infrared Phys.* **1967**, 7 (1), 37–55.
[https://doi.org/10.1016/0020-0891\(67\)90028-0](https://doi.org/10.1016/0020-0891(67)90028-0).

- (111) Thompson, J. A.; Pisano, G. Use of Evolutionary Computing Algorithms in the Design of Millimetre-Wave Metamaterial Devices. In *Millimeter, Submillimeter, and Far-Infrared Detectors and Instrumentation for Astronomy IX*; International Society for Optics and Photonics, 2018; Vol. 10708, p 107083H. <https://doi.org/10.1117/12.2312441>.
- (112) Thompson, J. A.; Pisano, G.; Tucker, C. Mesh Low-Pass Filters for Millimeter-Wave Applications: Is the Square Capacitive Shape Optimal? *J. Astron. Telesc. Instrum. Syst.* **2020**, 6 (3), 036003. <https://doi.org/10.1117/1.JATIS.6.3.036003>.
- (113) Ge, Y.; Esselle, K. P. Design of Single-Band and Dual-Band AMC Surfaces by Combining a Micro-Genetic Algorithm with the Spectral FDTD Method. In *2006 IEEE Antennas and Propagation Society International Symposium*; 2006; pp 3853–3856. <https://doi.org/10.1109/APS.2006.1711464>.
- (114) Thompson, J.; Pisano, G.; Tucker, C. Super-Capacitive Patches and Their Use in Low Pass Filters and Artificial Dielectrics. *Opt. Eng.* **2021**, *Accepted for publication*.
- (115) Harvey, J. E.; Pfisterer, R. N. Understanding Diffraction Grating Behavior: Including Conical Diffraction and Rayleigh Anomalies from Transmission Gratings. *Opt. Eng.* **2019**, 58 (8), 087105. <https://doi.org/10.1117/1.OE.58.8.087105>.
- (116) Fowler, J. W.; Niemack, M. D.; Dicker, S. R.; Aboobaker, A. M.; Ade, P. a. R.; Battistelli, E. S.; Devlin, M. J.; Fisher, R. P.; Halpern, M.; Hargrave, P. C.; Hincks, A. D.; Kaul, M.; Klein, J.; Lau, J. M.; Limon, M.; Marriage, T. A.; Mauskopf, P. D.; Page, L.; Staggs, S. T.; Swetz, D. S.; Switzer, E. R.; Thornton, R. J.; Tucker, C. E. Optical Design of the Atacama Cosmology Telescope and the Millimeter Bolometric Array Camera. *Appl. Opt.* **2007**, 46 (17), 3444–3454. <https://doi.org/10.1364/AO.46.003444>.
- (117) Swetz, D. S.; Ade, P. A. R.; Amiri, M.; Appel, J. W.; Battistelli, E. S.; Burger, B.; Chervenak, J.; Devlin, M. J.; Dicker, S. R.; Doriese, W. B.; Dünner, R.; Essinger-Hileman, T.; Fisher, R. P.; Fowler, J. W.; Halpern, M.; Hasselfield, M.; Hilton, G. C.; Hincks, A. D.; Irwin, K. D.; Jarosik, N.; Kaul, M.; Klein, J.; Lau, J. M.; Limon, M.; Marriage, T. A.; Marsden, D.; Martocci, K.; Mauskopf, P.; Moseley, H.; Netterfield, C. B.; Niemack, M. D.; Nolta, M. R.; Page, L. A.; Parker, L.; Staggs, S. T.; Stryzak, O.; Switzer, E. R.; Thornton, R.; Tucker, C.; Wollack, E.; Zhao, Y. Overview

- of the Atacama Cosology Telescope: Receiver, Instrumentation and Telescope Systems. *Astrophys. J. Suppl. Ser.* **2011**, 194 (2), 41.
<https://doi.org/10.1088/0067-0049/194/2/41>.
- (118) Tao, Z.; Jiang, W. X.; Ma, H. F.; Cui, T. J. High-Gain and High-Efficiency GRIN Metamaterial Lens Antenna With Uniform Amplitude and Phase Distributions on Aperture. *IEEE Trans. Antennas Propag.* **2018**, 66 (1), 16–22. <https://doi.org/10.1109/TAP.2017.2767639>.
- (119) Nicolson, A. M.; Ross, G. F. Measurement of the Intrinsic Properties of Materials by Time-Domain Techniques. *IEEE Trans. Instrum. Meas.* **1970**, 19 (4), 377–382. <https://doi.org/10.1109/TIM.1970.4313932>.
- (120) Chen, X.; Grzegorzczak, T. M.; Wu, B.-I.; Pacheco, J.; Kong, J. A. Robust Method to Retrieve the Constitutive Effective Parameters of Metamaterials. *Phys. Rev. E* **2004**, 70 (1), 016608.
<https://doi.org/10.1103/PhysRevE.70.016608>.
- (121) Szabó, Z.; Park, G.-H.; Hedge, R.; Li, E.-P. A Unique Extraction of Metamaterial Parameters Based on Kramers–Kronig Relationship. *IEEE Trans. Microw. Theory Tech.* **2010**, 58 (10), 2646–2653.
<https://doi.org/10.1109/TMTT.2010.2065310>.
- (122) Numan, A. B.; Sharawi, M. S. Extraction of Material Parameters for Metamaterials Using a Full-Wave Simulator [Education Column]. *IEEE Antennas Propag. Mag.* **2013**, 55 (5), 202–211.
<https://doi.org/10.1109/MAP.2013.6735515>.
- (123) Pozar, D. M. *Microwave Engineering*, 4th ed.; Wiley: Hoboken, N.J., 2012.
- (124) Mason, S. J. Feedback Theory-Further Properties of Signal Flow Graphs. *Proc. IRE* **1956**, 44 (7), 920–926.
<https://doi.org/10.1109/JRPROC.1956.275147>.
- (125) Flores-Mijangos, J.; Beltrán-López, V. Far-Infrared Laser Measurement of the Refractive Index of Polypropylene. *Appl. Opt.* **2003**, 42 (3), 592–596.
<https://doi.org/10.1364/AO.42.000592>.
- (126) Rayleigh, Lord. On Reflection of Vibrations at the Confines of Two Media between Which the Transition Is Gradual. *Proc. Lond. Math. Soc.* **1879**, s1-11 (1), 51–56. <https://doi.org/10.1112/plms/s1-11.1.51>.
- (127) Zhang, J.-C.; Xiong, L.-M.; Fang, M.; He, H.-B. Wide-Angle and Broadband Graded-Refractive-Index Antireflection Coatings. *Chin. Phys. B* **2013**, 22 (4), 044201. <https://doi.org/10.1088/1674-1056/22/4/044201>.

- (128) Appel, A. Some Techniques for Shading Machine Renderings of Solids. In *Proceedings of the April 30--May 2, 1968, spring joint computer conference*; AFIPS '68 (Spring); Association for Computing Machinery: Atlantic City, New Jersey, 1968; pp 37–45.
<https://doi.org/10.1145/1468075.1468082>.
- (129) Whitted, T. An Improved Illumination Model for Shaded Display. *SIGGRAPH Comput Graph* **1979**, 13 (2), 14.
<https://doi.org/10.1145/965103.807419>.
- (130) Berenger, J.-P. A Perfectly Matched Layer for the Absorption of Electromagnetic Waves. *J. Comput. Phys.* **1994**, 114 (2), 185–200.
<https://doi.org/10.1006/jcph.1994.1159>.

Appendix A

Propagation matrix derivation

The propagation matrix modelling method derived here is expanded from Orfandis⁸⁰ chapters 2 and 5. The main aim of this appendix is to document all the mathematical steps (avoiding such terms as ‘obviously’) in enough detail that even this writer can follow them. This allowed the implementation of the method in the software created as part of the project reported by this thesis to proceed with confidence and should provide sufficient reference to allow future development.

A.1 One dimensional plane waves

Consider uniform plane waves propagating in a lossless medium in the z direction; the electric and magnetic field components only depend on time and the z position. Starting from the time harmonic version of Maxwell’s curl equations (section 7.10 of Huray⁸⁹ for example):

$$\nabla \times \mathbf{E} = -i\mu\omega\mathbf{H} \quad \text{A-1}$$

$$\nabla \times \mathbf{H} = i\varepsilon\omega\mathbf{E} \quad \text{A-2}$$

The electric and magnetic fields have no dependency on x and y, so $\frac{\partial}{\partial x} = 0$ and $\frac{\partial}{\partial y} = 0$. The curl of a vector that depends only on z, $\mathbf{F}(z)$, expands as follows:

$$\nabla \times \mathbf{F}(z) = \left(0 - \frac{\partial F_y}{\partial z}\right)\mathbf{i} + \left(\frac{\partial F_x}{\partial z} - 0\right)\mathbf{j} + (0 - 0)\mathbf{k} \quad \text{A-3}$$

If the cross product of the z axis unit vector with the partial differential of this vector with respect to z is expanded, the result is also:

$$\mathbf{k} \times \frac{\partial \mathbf{F}(z)}{\partial z} = \left(0 - \frac{\partial F_y}{\partial z}\right)\mathbf{i} + \left(\frac{\partial F_x}{\partial z} - 0\right)\mathbf{j} + (0 - 0)\mathbf{k} \quad \text{A-4}$$

This relationship can therefore be written:

$$\nabla \times \mathbf{F}(z) = \mathbf{k} \times \frac{\partial \mathbf{F}(z)}{\partial z} \quad \text{A-5}$$

Using this, Maxwell’s time harmonic curl equations can be written as:

$$\mathbf{k} \times \frac{\partial \mathbf{E}(z)}{\partial z} = -i\mu\omega \mathbf{H}(z) \quad \text{A-6}$$

$$\mathbf{k} \times \frac{\partial \mathbf{H}(z)}{\partial z} = i\varepsilon\omega \mathbf{E}(z) \quad \text{A-7}$$

Taking the cross product of equation A-6 with \mathbf{k} leads to

$$\left(\mathbf{k} \times \frac{\partial \mathbf{E}(z)}{\partial z} \right) \times \mathbf{k} = -i\mu\omega \mathbf{H}(z) \times \mathbf{k} \quad \text{A-8}$$

Then using the vector triple product identity $(a \times b) \times c = (c \cdot a)b - (c \cdot b)a$ this can be expanded to

$$(\mathbf{k} \cdot \mathbf{k}) \frac{\partial \mathbf{E}(z)}{\partial z} - \left(\frac{\partial \mathbf{E}(z)}{\partial z} \cdot \mathbf{k} \right) \mathbf{k} = -i\mu\omega \mathbf{H}(z) \times \mathbf{k} \quad \text{A-9}$$

Then using $\mathbf{k} \cdot \mathbf{k} = 1$ and $\frac{\partial \mathbf{E}}{\partial z} \cdot \mathbf{k} = \frac{\partial E_z}{\partial z} = 0$:

$$\frac{\partial \mathbf{E}(z)}{\partial z} = -i\mu\omega \mathbf{H}(z) \times \mathbf{k} \quad \text{A-10}$$

Using the anti-commutativity of the vector cross product on equation A-7 gives:

$$\frac{\partial \mathbf{H}(z)}{\partial z} \times \mathbf{k} = -i\varepsilon\omega \mathbf{E}(z) \quad \text{A-11}$$

Using the characteristic impedance, $\eta = \sqrt{\mu/\varepsilon}$, and $c = 1/\sqrt{\mu\varepsilon}$, the substitutions $\varepsilon = 1/\eta c$ and $\mu = \eta/c$ can be used to form this pair of coupled equations:

$$\frac{\partial \mathbf{E}(z)}{\partial z} = -\frac{1}{c} \eta i\omega \mathbf{H}(z) \times \mathbf{k} \quad \text{A-12}$$

$$\frac{\partial}{\partial z} (\eta \mathbf{H}(z) \times \mathbf{k}) = -\frac{1}{c} i\omega \mathbf{E}(z) \quad \text{A-13}$$

Next, the define the forward and backward electric fields as:

$$\mathbf{E}_+(z) = \frac{1}{2} (\mathbf{E}(z) + \eta \mathbf{H}(z) \times \mathbf{k}) \quad \text{A-14}$$

$$\mathbf{E}_-(z) = \frac{1}{2} (\mathbf{E}(z) - \eta \mathbf{H}(z) \times \mathbf{k}) \quad \text{A-15}$$

Adding and subtracting these equations and using $\mathbf{k} \cdot \mathbf{k} = 1$ and $\mathbf{k} \cdot \mathbf{H}(z) = 0$ (due to there being no z component) leads to:

$$\mathbf{E}(z) = \mathbf{E}_+(z) + \mathbf{E}_-(z) \quad \text{A-16}$$

$$\mathbf{H}(z) = \frac{1}{\eta} \mathbf{k} \times (\mathbf{E}_+(z) - \mathbf{E}_-(z)) \quad \text{A-17}$$

Substituting into equations A-12 and A-13:

$$\frac{\partial \mathbf{E}_+(z)}{\partial z} + \frac{\partial \mathbf{E}_-(z)}{\partial z} = -\frac{1}{c} \left(i\omega \mathbf{k} \times (\mathbf{E}_+(z) - \mathbf{E}_-(z)) \right) \times \mathbf{k} \quad \text{A-18}$$

$$\frac{\partial}{\partial z} \left(\left(\mathbf{k} \times (\mathbf{E}_+(z) - \mathbf{E}_-(z)) \right) \times \mathbf{k} \right) = -\frac{1}{c} i\omega \mathbf{E}_+(z) - \frac{1}{c} i\omega \mathbf{E}_-(z) \quad \text{A-19}$$

Using the vector triple product identity $(a \times b) \times c = (c \cdot a)b - (c \cdot b)a$ along with $\mathbf{k} \cdot \mathbf{k} = 1$ and $\mathbf{k} \cdot \mathbf{F} = 0$ this becomes

$$\frac{\partial \mathbf{E}_+(z)}{\partial z} + \frac{\partial \mathbf{E}_-(z)}{\partial z} = -\frac{1}{c} i\omega \mathbf{E}_+(z) + \frac{1}{c} i\omega \mathbf{E}_-(z) \quad \text{A-20}$$

$$\frac{\partial \mathbf{E}_+(z)}{\partial z} - \frac{\partial \mathbf{E}_-(z)}{\partial z} = -\frac{1}{c} i\omega \mathbf{E}_+(z) - \frac{1}{c} i\omega \mathbf{E}_-(z) \quad \text{A-21}$$

Adding and subtracting to decouple them:

$$\frac{\partial \mathbf{E}_+(z)}{\partial z} = -\frac{i\omega}{c} \mathbf{E}_+(z) \quad \text{A-22}$$

$$\frac{\partial \mathbf{E}_-(z)}{\partial z} = \frac{i\omega}{c} \mathbf{E}_-(z) \quad \text{A-23}$$

Using the angular wave number $k = \omega/c = \omega\sqrt{\mu\epsilon}$:

$$\frac{\partial \mathbf{E}_+(z)}{\partial z} = -ik \mathbf{E}_+(z) \quad \text{A-24}$$

$$\frac{\partial \mathbf{E}_-(z)}{\partial z} = ik \mathbf{E}_-(z) \quad \text{A-25}$$

These have solutions:

$$\mathbf{E}_+(z) = \mathbf{E}_{0+} e^{-ikz} \quad \text{A-26}$$

$$\mathbf{E}_-(z) = \mathbf{E}_{0-} e^{ikz} \quad \text{A-27}$$

Substituting back into equations A-16 and A-17 leads to a general solution:

$$\mathbf{E}(z) = \mathbf{E}_{0+}e^{-ikz} + \mathbf{E}_{0-}e^{ikz} \quad \text{A-28}$$

$$\mathbf{H}(z) = \frac{1}{\eta} \mathbf{k} \times (\mathbf{E}_{0+}e^{-ikz} - \mathbf{E}_{0-}e^{ikz}) \quad \text{A-29}$$

For a plane wave linearly polarised in the x direction the following can be used:

$$\mathbf{E}(z) = \mathbf{i}E_x(z) = \mathbf{i}E(z) \quad \text{A-30}$$

$$\mathbf{H}(z) = \mathbf{j}H_y(z) = \mathbf{j}H(z) \quad \text{A-31}$$

And the general solution becomes

$$\mathbf{i}E(z) = \mathbf{i}E_{0+}e^{-ikz} + \mathbf{i}E_{0-}e^{ikz} \quad \text{A-32}$$

$$\mathbf{j}H(z) = \frac{1}{\eta} \mathbf{k} \times \mathbf{i}(E_{0+}e^{-ikz} - E_{0-}e^{ikz}) \quad \text{A-33}$$

Simplifying and using equations A-16 and A-17 leads back to:

$$E(z) = E_+(z) + E_-(z) \quad \text{A-34}$$

$$H(z) = \frac{1}{\eta} (E_+(z) - E_-(z)) \quad \text{A-35}$$

Which can be expressed in matrix form:

$$\begin{bmatrix} E \\ H \end{bmatrix} = \begin{bmatrix} 1 & 1 \\ \eta^{-1} & -\eta^{-1} \end{bmatrix} \begin{bmatrix} E_+ \\ E_- \end{bmatrix} \quad \text{A-36}$$

Adding and subtracting to invert these equations:

$$E_+(z) = \frac{1}{2} (E(z) + \eta H(z)) \quad \text{A-37}$$

$$E_-(z) = \frac{1}{2} (E(z) - \eta H(z)) \quad \text{A-38}$$

Which can also be written in matrix form

$$\begin{bmatrix} E_+ \\ E_- \end{bmatrix} = \frac{1}{2} \begin{bmatrix} 1 & \eta \\ 1 & -\eta \end{bmatrix} \begin{bmatrix} E \\ H \end{bmatrix} \quad \text{A-39}$$

A.2 The propagation matrix

Orfanadis then derives a matrix that represents the behaviour of a wave travelling in a dielectric. Considering a wave propagating along the z axis as shown in Figure 2.1. For the two positions, z_1 and z_2 , from equation A-26 the forward fields can be written as:

$$E_{2+} = E_{0+}e^{-ikz_2} \quad \text{A-40}$$

$$E_{1+} = E_{0+}e^{-ikz_1} = E_{2+}e^{ikl} \quad \text{A-41}$$

And from equation A-27 the backward fields as:

$$E_{2-} = E_{0-}e^{ikz_2} \quad \text{A-42}$$

$$E_{1-} = E_{0-}e^{ikz_1} = E_{2-}e^{-ikl} \quad \text{A-43}$$

therefore, E_{1+} and E_{1-} can be written in terms of E_{2+} and E_{2-} in matrix form:

$$\begin{bmatrix} E_{1+} \\ E_{1-} \end{bmatrix} = \begin{bmatrix} e^{ikl} & 0 \\ 0 & e^{-ikl} \end{bmatrix} \begin{bmatrix} E_{2+} \\ E_{2-} \end{bmatrix} \quad \text{A-44}$$

Using equation A-36:

$$\begin{bmatrix} E_1 \\ H_1 \end{bmatrix} = \begin{bmatrix} 1 & 1 \\ \eta^{-1} & -\eta^{-1} \end{bmatrix} \begin{bmatrix} E_{1+} \\ E_{1-} \end{bmatrix} = \begin{bmatrix} 1 & 1 \\ \eta^{-1} & -\eta^{-1} \end{bmatrix} \begin{bmatrix} e^{ikl} & 0 \\ 0 & e^{-ikl} \end{bmatrix} \begin{bmatrix} E_{2+} \\ E_{2-} \end{bmatrix} \quad \text{A-45}$$

Then using equation A-39 to completely remove the forward and backward fields:

$$\begin{bmatrix} E_1 \\ H_1 \end{bmatrix} = \frac{1}{2} \begin{bmatrix} 1 & 1 \\ \eta^{-1} & -\eta^{-1} \end{bmatrix} \begin{bmatrix} e^{ikl} & 0 \\ 0 & e^{-ikl} \end{bmatrix} \begin{bmatrix} 1 & \eta \\ 1 & -\eta \end{bmatrix} \begin{bmatrix} E_2 \\ H_2 \end{bmatrix} \quad \text{A-46}$$

Multiplying out the matrices:

$$\begin{bmatrix} E_1 \\ H_1 \end{bmatrix} = \frac{1}{2} \begin{bmatrix} e^{ikl} + e^{-ikl} & \eta(e^{ikl} - e^{-ikl}) \\ \eta^{-1}(e^{ikl} - e^{-ikl}) & e^{ikl} + e^{-ikl} \end{bmatrix} \begin{bmatrix} E_2 \\ H_2 \end{bmatrix} \quad \text{A-47}$$

Using Euler's formula, the propagation matrix equation can be written as:

$$\begin{bmatrix} E_1 \\ H_1 \end{bmatrix} = \begin{bmatrix} \cos kl & \eta i \sin kl \\ \eta^{-1} i \sin kl & \cos kl \end{bmatrix} \begin{bmatrix} E_2 \\ H_2 \end{bmatrix} \quad \text{A-48}$$

A.3 The matching matrix for two dielectrics

To investigate the behaviour of a wave at a boundary between two dielectrics with characteristic impedances η and η' , Orfanidis considers a plane wave propagating in the z direction as shown in Figure 2.2. The electric and magnetic fields are required to be continuous over the boundary, so:

$$E = E' \quad \text{A-49}$$

$$H = H' \quad \text{A-50}$$

Using the forward and backward fields of equations A-34 and A-35 these become

$$E_+ + E_- = E'_+ + E'_- \quad \text{A-51}$$

$$\frac{1}{\eta}(E_+ - E_-) = \frac{1}{\eta'}(E'_+ - E'_-) \quad \text{A-52}$$

After a trivial reorganisation:

$$E_+ + E_- = E'_+ + E'_- \quad \text{A-53}$$

$$E_+ - E_- = \frac{\eta}{\eta'}E'_+ - \frac{\eta}{\eta'}E'_- \quad \text{A-54}$$

Then adding and subtracting them:

$$2E_+ = \left(\frac{\eta}{\eta'} + 1\right)E'_+ + \left(1 - \frac{\eta}{\eta'}\right)E'_- \quad \text{A-55}$$

$$2E_- = \left(1 - \frac{\eta}{\eta'}\right)E'_+ + \left(1 + \frac{\eta}{\eta'}\right)E'_- \quad \text{A-56}$$

And rearranging:

$$E_+ = \frac{\eta + \eta'}{2\eta'} \left[E'_+ + \left(\frac{\eta' - \eta}{\eta + \eta'} \right) E'_- \right] \quad \text{A-57}$$

$$E_- = \frac{\eta + \eta'}{2\eta'} \left[\left(\frac{\eta' - \eta}{\eta + \eta'} \right) E'_+ + E'_- \right] \quad \text{A-58}$$

Defining the reflection and transmission coefficients as

$$\Gamma = \frac{\eta' - \eta}{\eta + \eta'} \quad \text{A-59}$$

$$\tau = \frac{2\eta'}{\eta + \eta'} \quad \text{A-60}$$

Allows them to be written as

$$E_+ = \frac{1}{\tau} [E'_+ + \Gamma E'_-] \quad \text{A-61}$$

$$E_- = \frac{1}{\tau} [\Gamma E'_+ + E'_-] \quad \text{A-62}$$

Which can be written in matrix form:

$$\begin{bmatrix} E_+ \\ E_- \end{bmatrix} = \frac{1}{\tau} \begin{bmatrix} 1 & \Gamma \\ \Gamma & 1 \end{bmatrix} \begin{bmatrix} E'_+ \\ E'_- \end{bmatrix} \quad \text{A-63}$$

A.4 Matching matrices for capacitive and inductive grids

To extend Orfanidis' treatment to metallic meshes, consider the negligibly thin grid embedded in a dielectric as shown in Figure 2.4. Using the transmission and reflection coefficients, the following relationships can be written:

$$E'_+ = TE_+ + RE'_- \quad \text{A-64}$$

$$E_- = RE_+ + TE'_- \quad \text{A-65}$$

Rearranging

$$E_+ = \frac{1}{T} E'_+ - \frac{R}{T} E'_- \quad \text{A-66}$$

$$E_- = RE_+ + TE'_- \quad \text{A-67}$$

Substituting the first into the second and using $R = T - 1$:

$$E_+ = \frac{1}{T} E'_+ - \frac{T-1}{T} E'_- \quad \text{A-68}$$

$$E_- = (T-1) \left(\frac{1}{T} E'_+ - \frac{T-1}{T} E'_- \right) + TE'_- \quad \text{A-69}$$

Rearranging again:

$$E_+ = \frac{E'_+}{T} + \frac{(1-T)E'_-}{T} \quad \text{A-70}$$

$$E_- = \frac{(T-1)E'_+}{T} + \frac{(2T-1)E'_-}{T} \quad \text{A-71}$$

Substituting $T = \frac{1}{1+Y}$, rearranging and writing in matrix form:

$$\begin{bmatrix} E_+ \\ E_- \end{bmatrix} = \begin{bmatrix} 1+Y & Y \\ -Y & 1-Y \end{bmatrix} \begin{bmatrix} E'_+ \\ E'_- \end{bmatrix} \quad \text{A-72}$$

Appendix B

Derivation of FDTD stepping equations

The derivation of the equations for the FDTD method detailed here is expanded mainly from Taflove and Hagness⁸². Like Appendix A, the aim is to produce an easy-to-follow derivation without any obscure large steps as reference documentation for the implementation of FDTD in the software developed during the project. In this author's experience, a complete understanding of the origin of equations to be expressed in software greatly aids the development and maintenance of the code.

B.1 Derivation of the basic FDTD equations

Starting from Maxwell's curl equations (Faraday's law and Ampere's law) expressed in terms of the \mathbf{E} and \mathbf{H} fields. In addition, the existence of magnetic monopoles is assumed and a term for the magnetic current density, \mathbf{M} , is included, with a magnetic conductivity constant, σ^* , in symmetry with the electric conductivity constant.

$$\nabla \times \mathbf{E} = -\mu \frac{\partial \mathbf{H}}{\partial t} - (\mathbf{M} + \sigma^* \mathbf{H}) \quad \text{B-1}$$

$$\nabla \times \mathbf{H} = \varepsilon \frac{\partial \mathbf{E}}{\partial t} + (\mathbf{J} + \sigma \mathbf{E}) \quad \text{B-2}$$

These equations can be rearranged into these forms

$$\nabla \times \mathbf{E} = -\mu \frac{\partial \mathbf{H}}{\partial t} - (\mathbf{M} + \sigma^* \mathbf{H}) \quad \text{B-3}$$

$$\nabla \times \mathbf{H} = \varepsilon \frac{\partial \mathbf{E}}{\partial t} + (\mathbf{J} + \sigma \mathbf{E}) \quad \text{B-4}$$

Expanding the curls into Cartesian coordinates leads to

$$\begin{aligned}
 \frac{\partial H_x}{\partial t} &= -\frac{1}{\mu} \left(\frac{\partial E_z}{\partial y} - \frac{\partial E_y}{\partial z} + M_x + \sigma^* H_x \right) \\
 \frac{\partial H_y}{\partial t} &= -\frac{1}{\mu} \left(\frac{\partial E_x}{\partial z} - \frac{\partial E_z}{\partial x} + M_y + \sigma^* H_y \right) \\
 \frac{\partial H_z}{\partial t} &= -\frac{1}{\mu} \left(\frac{\partial E_y}{\partial x} - \frac{\partial E_x}{\partial y} + M_z + \sigma^* H_z \right)
 \end{aligned} \tag{B-5}$$

$$\begin{aligned}
 \frac{\partial E_x}{\partial t} &= \frac{1}{\varepsilon} \left(\frac{\partial H_z}{\partial y} - \frac{\partial H_y}{\partial z} - J_x - \sigma E_x \right) \\
 \frac{\partial E_y}{\partial t} &= \frac{1}{\varepsilon} \left(\frac{\partial H_x}{\partial z} - \frac{\partial H_z}{\partial x} - J_y - \sigma E_y \right) \\
 \frac{\partial E_z}{\partial t} &= \frac{1}{\varepsilon} \left(\frac{\partial H_y}{\partial x} - \frac{\partial H_x}{\partial y} - J_z - \sigma E_z \right)
 \end{aligned} \tag{B-6}$$

A bar notation is introduced to indicate the position of a field component on the grid and its time step. For example, the $E_x|_{i,j+\frac{1}{2},k+\frac{1}{2}}^{n+\frac{1}{2}}$ notation means the E_x component at time step $n + \frac{1}{2}$ and spatial position $i, j + \frac{1}{2}, k + \frac{1}{2}$. For quantities that are time invariant, the time step superscript will be absent, an example of this is $\varepsilon|_{i,j+\frac{1}{2},k+\frac{1}{2}}$, the value of electric permittivity at the spatial position $i, j + \frac{1}{2}, k + \frac{1}{2}$. Note that the indices used here are not identical to those used by Taflov and Hagness but are equivalent; it was felt that these values better reveal the symmetry of the system. The electric field x component equation then becomes:

$$\begin{aligned}
 &\frac{E_x|_{i,j+\frac{1}{2},k+\frac{1}{2}}^{n+\frac{1}{2}} - E_x|_{i,j+\frac{1}{2},k+\frac{1}{2}}^{n-\frac{1}{2}}}{\Delta t} \\
 &= \frac{1}{\varepsilon|_{i,j+\frac{1}{2},k+\frac{1}{2}}} \left(\frac{H_z|_{i,j+1,k+\frac{1}{2}}^n - H_z|_{i,j,k+\frac{1}{2}}^n}{\Delta y} \right. \\
 &\quad - \frac{H_y|_{i,j+\frac{1}{2},k+1}^n - H_y|_{i,j+\frac{1}{2},k}^n}{\Delta z} - J_x|_{i,j+\frac{1}{2},k+\frac{1}{2}}^n \\
 &\quad \left. - \sigma|_{i,j+\frac{1}{2},k+\frac{1}{2}} E_x|_{i,j+\frac{1}{2},k+\frac{1}{2}}^n \right)
 \end{aligned} \tag{B-7}$$

The right-hand side contains only values calculated at time step n . This includes the displacement current which depends on the electric field, but the electric field is only evaluated at time steps $n \pm \frac{1}{2}$. The value at time step n can be approximated by the average of the electric field calculated at the adjacent half steps, i.e.

$$E_x|_{i,j+\frac{1}{2},k+\frac{1}{2}}^n = \frac{E_x|_{i,j+\frac{1}{2},k+\frac{1}{2}}^{n+\frac{1}{2}} + E_x|_{i,j+\frac{1}{2},k+\frac{1}{2}}^{n-\frac{1}{2}}}{2} \quad \text{B-8}$$

Substituting this into equation B-7 leads to

$$\begin{aligned} & \frac{E_x|_{i,j+\frac{1}{2},k+\frac{1}{2}}^{n+\frac{1}{2}} - E_x|_{i,j+\frac{1}{2},k+\frac{1}{2}}^{n-\frac{1}{2}}}{\Delta t} \\ &= \frac{1}{\varepsilon|_{i,j+\frac{1}{2},k+\frac{1}{2}}} \left(\frac{H_z|_{i,j+1,k+\frac{1}{2}}^n - H_z|_{i,j,k+\frac{1}{2}}^n}{\Delta y} \right. \\ & \quad - \frac{H_y|_{i,j+\frac{1}{2},k+1}^n - H_y|_{i,j+\frac{1}{2},k}^n}{\Delta z} - J_x|_{i,j+\frac{1}{2},k+\frac{1}{2}}^n \\ & \quad \left. - \sigma|_{i,j+\frac{1}{2},k+\frac{1}{2}} \left(\frac{E_x|_{i,j+\frac{1}{2},k+\frac{1}{2}}^{n+\frac{1}{2}} + E_x|_{i,j+\frac{1}{2},k+\frac{1}{2}}^{n-\frac{1}{2}}}{2} \right) \right) \end{aligned} \quad \text{B-9}$$

Rearranging to get an equation for the next half step of the electric field x component leads to:

$$\begin{aligned} E_x|_{i,j+\frac{1}{2},k+\frac{1}{2}}^{n+\frac{1}{2}} &= \frac{\frac{\Delta t}{\varepsilon|_{i,j+\frac{1}{2},k+\frac{1}{2}}}}{\left(1 + \frac{\sigma|_{i,j+\frac{1}{2},k+\frac{1}{2}}\Delta t}{2\varepsilon|_{i,j+\frac{1}{2},k+\frac{1}{2}}} \right)} \left(\frac{H_z|_{i,j+1,k+\frac{1}{2}}^n - H_z|_{i,j,k+\frac{1}{2}}^n}{\Delta y} \right. \\ & \quad \left. - \frac{H_y|_{i,j+\frac{1}{2},k+1}^n - H_y|_{i,j+\frac{1}{2},k}^n}{\Delta z} - J_x|_{i,j+\frac{1}{2},k+\frac{1}{2}}^n \right) \\ & \quad + E_x|_{i,j+\frac{1}{2},k+\frac{1}{2}}^{n-\frac{1}{2}} \frac{\left(1 - \frac{\sigma|_{i,j+\frac{1}{2},k+\frac{1}{2}}\Delta t}{2\varepsilon|_{i,j+\frac{1}{2},k+\frac{1}{2}}} \right)}{\left(1 + \frac{\sigma|_{i,j+\frac{1}{2},k+\frac{1}{2}}\Delta t}{2\varepsilon|_{i,j+\frac{1}{2},k+\frac{1}{2}}} \right)} \end{aligned} \quad \text{B-10}$$

Using the same procedure for the other components of the electric field leads to two further update equations. For the y component:

$$\begin{aligned}
 E_y|_{i+\frac{1}{2},j,k+\frac{1}{2}}^{n+\frac{1}{2}} &= \frac{\frac{\Delta t}{\varepsilon|_{i+\frac{1}{2},j,k+\frac{1}{2}}}}{\left(1 + \frac{\sigma|_{i+\frac{1}{2},j,k+\frac{1}{2}}\Delta t}{2\varepsilon|_{i+\frac{1}{2},j,k+\frac{1}{2}}}\right)} \left(\frac{H_x|_{i+\frac{1}{2},j,k+1}^n - H_x|_{i+\frac{1}{2},j,k}^n}{\Delta z} \right. \\
 &\quad \left. - \frac{H_z|_{i+1,j,k+\frac{1}{2}}^n - H_z|_{i,j,k+\frac{1}{2}}^n}{\Delta x} - J_y|_{i+\frac{1}{2},j,k+\frac{1}{2}}^n \right) \\
 &\quad + E_y|_{i+\frac{1}{2},j,k+\frac{1}{2}}^{n-\frac{1}{2}} \frac{\left(1 - \frac{\sigma|_{i+\frac{1}{2},j,k+\frac{1}{2}}\Delta t}{2\varepsilon|_{i+\frac{1}{2},j,k+\frac{1}{2}}}\right)}{\left(1 + \frac{\sigma|_{i+\frac{1}{2},j,k+\frac{1}{2}}\Delta t}{2\varepsilon|_{i+\frac{1}{2},j,k+\frac{1}{2}}}\right)}
 \end{aligned} \tag{B-11}$$

And the Z component:

$$\begin{aligned}
 E_z|_{i+\frac{1}{2},j+\frac{1}{2},k}^{n+\frac{1}{2}} &= \frac{\frac{\Delta t}{\varepsilon|_{i+\frac{1}{2},j+\frac{1}{2},k}}}{\left(1 + \frac{\sigma|_{i+\frac{1}{2},j+\frac{1}{2},k}\Delta t}{2\varepsilon|_{i+\frac{1}{2},j+\frac{1}{2},k}}\right)} \left(\frac{H_y|_{i+1,j+\frac{1}{2},k}^n - H_y|_{i,j+\frac{1}{2},k}^n}{\Delta x} \right. \\
 &\quad \left. - \frac{H_x|_{i+\frac{1}{2},j+1,k}^n - H_x|_{i+\frac{1}{2},j,k}^n}{\Delta y} - J_z|_{i+\frac{1}{2},j+\frac{1}{2},k}^n \right) \\
 &\quad + E_z|_{i+\frac{1}{2},j+\frac{1}{2},k}^{n-\frac{1}{2}} \frac{\left(1 - \frac{\sigma|_{i+\frac{1}{2},j+\frac{1}{2},k}\Delta t}{2\varepsilon|_{i+\frac{1}{2},j+\frac{1}{2},k}}\right)}{\left(1 + \frac{\sigma|_{i+\frac{1}{2},j+\frac{1}{2},k}\Delta t}{2\varepsilon|_{i+\frac{1}{2},j+\frac{1}{2},k}}\right)}
 \end{aligned} \tag{B-12}$$

Using the same arguments for the magnetic fields, again starting with the x component:

$$\begin{aligned}
 &\frac{H_x|_{i+\frac{1}{2},j,k}^{n+1} - H_x|_{i+\frac{1}{2},j,k}^n}{\Delta t} \\
 &= -\frac{1}{\mu|_{i+\frac{1}{2},j,k}} \left(\frac{E_z|_{i+\frac{1}{2},j+\frac{1}{2},k}^{n+\frac{1}{2}} - E_z|_{i+\frac{1}{2},j-\frac{1}{2},k}^{n+\frac{1}{2}}}{\Delta y} \right. \\
 &\quad \left. - \frac{E_y|_{i+\frac{1}{2},j-\frac{1}{2},k}^{n+\frac{1}{2}} - E_y|_{i+\frac{1}{2},j+\frac{1}{2},k}^{n+\frac{1}{2}}}{\Delta z} - M_x|_{i+\frac{1}{2},j,k}^n \right. \\
 &\quad \left. + \sigma^*|_{i+\frac{1}{2},j,k} H_x|_{i+\frac{1}{2},j,k}^{n+\frac{1}{2}} \right)
 \end{aligned} \tag{B-13}$$

The right-hand side contains only values calculated at time step $n + \frac{1}{2}$. This includes the magnetic displacement current which depends on the magnetic field, but the magnetic field is only evaluated at time step n . Using the average of the magnetic field of the two adjacent half steps:

$$H_x|_{i+\frac{1}{2},j,k}^{n+\frac{1}{2}} = \frac{H_x|_{i+\frac{1}{2},j,k}^{n+1} + H_x|_{i+\frac{1}{2},j,k}^n}{2} \quad \text{B-14}$$

Substituting this into equation B-13 leads to

$$\begin{aligned} & \frac{H_x|_{i+\frac{1}{2},j,k}^{n+1} - H_x|_{i+\frac{1}{2},j,k}^n}{\Delta t} \\ &= -\frac{1}{\mu|_{i+\frac{1}{2},j,k}} \left(\frac{E_z|_{i+\frac{1}{2},j+\frac{1}{2},k}^{n+\frac{1}{2}} - E_z|_{i+\frac{1}{2},j-\frac{1}{2},k}^{n+\frac{1}{2}}}{\Delta y} \right. \\ & \quad \left. - \frac{E_y|_{i+\frac{1}{2},j-\frac{1}{2},k}^{n+\frac{1}{2}} - E_y|_{i+\frac{1}{2},j+\frac{1}{2},k}^{n+\frac{1}{2}}}{\Delta z} + M_x|_{i+\frac{1}{2},j,k}^n \right. \\ & \quad \left. + \sigma^*|_{i+\frac{1}{2},j,k} \left(\frac{H_x|_{i+\frac{1}{2},j,k}^{n+1} + H_x|_{i+\frac{1}{2},j,k}^n}{2} \right) \right) \end{aligned} \quad \text{B-15}$$

Rearranging to get an equation for the next step:

$$\begin{aligned} H_x|_{i+\frac{1}{2},j,k}^{n+1} &= \frac{\frac{\Delta t}{\mu|_{i+\frac{1}{2},j,k}}}{\left(1 + \frac{\sigma^*|_{i+\frac{1}{2},j,k} \Delta t}{2\mu|_{i+\frac{1}{2},j,k}}\right)} \left(-\frac{E_z|_{i+\frac{1}{2},j+\frac{1}{2},k}^{n+\frac{1}{2}} - E_z|_{i+\frac{1}{2},j-\frac{1}{2},k}^{n+\frac{1}{2}}}{\Delta y} \right. \\ & \quad \left. + \frac{E_y|_{i+\frac{1}{2},j,k+\frac{1}{2}}^{n+\frac{1}{2}} - E_y|_{i+\frac{1}{2},j,k-\frac{1}{2}}^{n+\frac{1}{2}}}{\Delta z} - M_x|_{i+\frac{1}{2},j,k}^n \right) \\ & \quad + H_x|_{i+\frac{1}{2},j,k}^n \frac{\left(1 - \frac{\sigma^*|_{i+\frac{1}{2},j,k} \Delta t}{2\mu|_{i+\frac{1}{2},j,k}}\right)}{\left(1 + \frac{\sigma^*|_{i+\frac{1}{2},j,k} \Delta t}{2\mu|_{i+\frac{1}{2},j,k}}\right)} \end{aligned} \quad \text{B-16}$$

And then similarly for the other magnetic field components, for y:

$$\begin{aligned}
 H_y|_{i,j+\frac{1}{2},k}^{n+1} = & \frac{\frac{\Delta t}{\mu|_{i,j+\frac{1}{2},k}}}{\left(1 + \frac{\sigma^*|_{i,j+\frac{1}{2},k}\Delta t}{2\mu|_{i,j+\frac{1}{2},k}}\right)} \left(-\frac{E_x|_{i,j+\frac{1}{2},k+\frac{1}{2}}^{n+\frac{1}{2}} - E_x|_{i,j+\frac{1}{2},k-\frac{1}{2}}^{n+\frac{1}{2}}}{\Delta z} \right. \\
 & + \frac{E_z|_{i+\frac{1}{2},j+\frac{1}{2},k}^{n+\frac{1}{2}} - E_z|_{i-\frac{1}{2},j+\frac{1}{2},k}^{n+\frac{1}{2}}}{\Delta x} - M_y|_{i,j+\frac{1}{2},k}^{n+\frac{1}{2}} \Bigg) \\
 & + H_y|_{i,j+\frac{1}{2},k}^n \frac{\left(1 - \frac{\sigma^*|_{i,j+\frac{1}{2},k}\Delta t}{2\mu|_{i,j+\frac{1}{2},k}}\right)}{\left(1 + \frac{\sigma^*|_{i,j+\frac{1}{2},k}\Delta t}{2\mu|_{i,j+\frac{1}{2},k}}\right)}
 \end{aligned} \tag{B-17}$$

And finally, the z component:

$$\begin{aligned}
 H_z|_{i,j,k+\frac{1}{2}}^{n+1} = & \frac{\frac{\Delta t}{\mu|_{i,j,k+\frac{1}{2}}}}{\left(1 + \frac{\sigma^*|_{i,j,k+\frac{1}{2}}\Delta t}{2\mu|_{i,j,k+\frac{1}{2}}}\right)} \left(-\frac{E_y|_{i+\frac{1}{2},j,k+\frac{1}{2}}^{n+\frac{1}{2}} - E_y|_{i-\frac{1}{2},j,k+\frac{1}{2}}^{n+\frac{1}{2}}}{\Delta x} \right. \\
 & + \frac{E_x|_{i,j+\frac{1}{2},k+\frac{1}{2}}^{n+\frac{1}{2}} - E_x|_{i,j-\frac{1}{2},k+\frac{1}{2}}^{n+\frac{1}{2}}}{\Delta y} - M_z|_{i,j,k+\frac{1}{2}}^{n+\frac{1}{2}} \Bigg) \\
 & + H_z|_{i,j,k+\frac{1}{2}}^n \frac{\left(1 - \frac{\sigma^*|_{i,j,k+\frac{1}{2}}\Delta t}{2\mu|_{i,j,k+\frac{1}{2}}}\right)}{\left(1 + \frac{\sigma^*|_{i,j,k+\frac{1}{2}}\Delta t}{2\mu|_{i,j,k+\frac{1}{2}}}\right)}
 \end{aligned} \tag{B-18}$$

The Yee grid will be filled from a small number of materials, each cell containing a single material that defines the constants ε, μ, σ and σ^* which are not time dependent. The following can therefore be pre-calculated for each material:

$$c_{ae} = \frac{\frac{\Delta t}{\varepsilon}}{\left(1 + \frac{\sigma\Delta t}{2\varepsilon}\right)} \quad c_{be} = \frac{\left(1 - \frac{\sigma\Delta t}{2\varepsilon}\right)}{\left(1 + \frac{\sigma\Delta t}{2\varepsilon}\right)} \tag{B-19}$$

$$c_{ah} = \frac{\frac{\Delta t}{\mu}}{\left(1 + \frac{\sigma^*\Delta t}{2\mu}\right)} \quad c_{bh} = \frac{\left(1 - \frac{\sigma^*\Delta t}{2\mu}\right)}{\left(1 + \frac{\sigma^*\Delta t}{2\mu}\right)} \tag{B-20}$$

Substituting these into equations B-10, B-11 and B-12 gives this set of electric field update equations:

$$\begin{aligned}
 E_x|_{i,j+\frac{1}{2},k+\frac{1}{2}}^{n+\frac{1}{2}} = & C_{ae}|_{i,j+\frac{1}{2},k+\frac{1}{2}} \left(\frac{H_z|_{i,j+1,k+\frac{1}{2}}^n - H_z|_{i,j,k+\frac{1}{2}}^n}{\Delta y} \right. \\
 & \left. - \frac{H_y|_{i,j+\frac{1}{2},k+1}^n - H_y|_{i,j+\frac{1}{2},k}^n}{\Delta z} - J_x|_{i,j+\frac{1}{2},k+\frac{1}{2}}^n \right) \\
 & + E_x|_{i,j+\frac{1}{2},k+\frac{1}{2}}^{n-\frac{1}{2}} C_{be}|_{i,j+\frac{1}{2},k+\frac{1}{2}}
 \end{aligned} \tag{B-21}$$

$$\begin{aligned}
 E_y|_{i+\frac{1}{2},j,k+\frac{1}{2}}^{n+\frac{1}{2}} = & C_{ae}|_{i+\frac{1}{2},j,k+\frac{1}{2}} \left(\frac{H_x|_{i+\frac{1}{2},j,k+1}^n - H_x|_{i+\frac{1}{2},j,k}^n}{\Delta z} \right. \\
 & \left. - \frac{H_z|_{i+1,j,k+\frac{1}{2}}^n - H_z|_{i,j,k+\frac{1}{2}}^n}{\Delta x} - J_y|_{i+\frac{1}{2},j,k+\frac{1}{2}}^n \right) \\
 & + E_y|_{i+\frac{1}{2},j,k+\frac{1}{2}}^{n-\frac{1}{2}} C_{be}|_{i+\frac{1}{2},j,k+\frac{1}{2}}
 \end{aligned} \tag{B-22}$$

$$\begin{aligned}
 E_z|_{i+\frac{1}{2},j+\frac{1}{2},k}^{n+\frac{1}{2}} = & C_{ae}|_{i+\frac{1}{2},j+\frac{1}{2},k} \left(\frac{H_y|_{i+1,j+\frac{1}{2},k}^n - H_y|_{i,j+\frac{1}{2},k}^n}{\Delta x} \right. \\
 & \left. - \frac{H_x|_{i+\frac{1}{2},j+1,k}^n - H_x|_{i+\frac{1}{2},j,k}^n}{\Delta y} - J_z|_{i+\frac{1}{2},j+\frac{1}{2},k}^n \right) \\
 & + E_z|_{i+\frac{1}{2},j+\frac{1}{2},k}^{n-\frac{1}{2}} C_{be}|_{i+\frac{1}{2},j+\frac{1}{2},k}
 \end{aligned} \tag{B-23}$$

Substituting into equations B-16, B-17 and B-18 gives as set of magnetic field update equations:

$$\begin{aligned}
 H_x|_{i+\frac{1}{2},j,k}^{n+1} = & C_{ah}|_{i+\frac{1}{2},j,k} \left(- \frac{E_z|_{i+\frac{1}{2},j+\frac{1}{2},k}^{n+\frac{1}{2}} - E_z|_{i+\frac{1}{2},j-\frac{1}{2},k}^{n+\frac{1}{2}}}{\Delta y} \right. \\
 & \left. + \frac{E_y|_{i+\frac{1}{2},j,k+\frac{1}{2}}^{n+\frac{1}{2}} - E_y|_{i+\frac{1}{2},j,k-\frac{1}{2}}^{n+\frac{1}{2}}}{\Delta z} - M_x|_{i+\frac{1}{2},j,k}^{n+\frac{1}{2}} \right) \\
 & + H_x|_{i+\frac{1}{2},j,k}^n C_{bh}|_{i+\frac{1}{2},j,k}
 \end{aligned} \tag{B-24}$$

$$\begin{aligned}
 H_y|_{i,j+\frac{1}{2},k}^{n+1} = & C_{ah}|_{i,j+\frac{1}{2},k} \left(-\frac{E_x|_{i,j+\frac{1}{2},k+\frac{1}{2}}^{n+\frac{1}{2}} - E_x|_{i,j+\frac{1}{2},k-\frac{1}{2}}^{n+\frac{1}{2}}}{\Delta z} \right. \\
 & \left. + \frac{E_z|_{i+\frac{1}{2},j+\frac{1}{2},k}^{n+\frac{1}{2}} - E_z|_{i-\frac{1}{2},j+\frac{1}{2},k}^{n+\frac{1}{2}}}{\Delta x} - M_y|_{i,j+\frac{1}{2},k}^{n+\frac{1}{2}} \right) \\
 & + H_y|_{i,j+\frac{1}{2},k}^n C_{bh}|_{i,j+\frac{1}{2},k}
 \end{aligned} \tag{B-25}$$

$$\begin{aligned}
 H_z|_{i,j,k+\frac{1}{2}}^{n+1} = & C_{ah}|_{i,j,k+\frac{1}{2}} \left(-\frac{E_y|_{i+\frac{1}{2},j,k+\frac{1}{2}}^{n+\frac{1}{2}} - E_y|_{i-\frac{1}{2},j,k+\frac{1}{2}}^{n+\frac{1}{2}}}{\Delta x} \right. \\
 & \left. + \frac{E_x|_{i,j+\frac{1}{2},k+\frac{1}{2}}^{n+\frac{1}{2}} - E_x|_{i,j-\frac{1}{2},k+\frac{1}{2}}^{n+\frac{1}{2}}}{\Delta y} - M_z|_{i,j,k+\frac{1}{2}}^{n+\frac{1}{2}} \right) \\
 & + H_z|_{i,j,k+\frac{1}{2}}^n C_{bh}|_{i,j,k+\frac{1}{2}}
 \end{aligned} \tag{B-26}$$

B.2 Incident plane waves

Deriving the update equations for the one-dimensional auxiliary grid Maxwell's curl equations are once again the starting point, but this time with no magnetic or electric currents and always in vacuum. The conductivity terms are left in in so that the absorbing layer at the end of the auxiliary grid can be implemented.

$$\frac{\partial \mathbf{E}}{\partial t} = \frac{1}{\epsilon_0} \nabla \times \mathbf{H} - \frac{1}{\epsilon_0} \sigma \mathbf{E} \tag{B-27}$$

$$\frac{\partial \mathbf{H}}{\partial t} = -\frac{1}{\mu_0} \nabla \times \mathbf{E} - \frac{1}{\mu_0} \sigma^* \mathbf{H} \tag{B-28}$$

The z axis is aligned with the direction of propagation of the incident wave and the x axis with the electric field polarization. This implies that for the electric field, the z and y components are always zero and for the magnetic field, the z and x components are always zero. Expanding the curls and dropping the zero components, the equations become:

$$\frac{\partial E_x}{\partial t} = -\frac{1}{\epsilon_0} \frac{\partial H_y}{\partial z} - \frac{1}{\epsilon_0} \sigma E_x \tag{B-29}$$

$$\frac{\partial H_y}{\partial t} = -\frac{1}{\mu_0} \frac{\partial E_x}{\partial z} - \frac{1}{\mu_0} \sigma^* H_y \quad \text{B-30}$$

Then using finite differences on the one-dimensional Yee grid, where E_x is on the whole-numbered grid points and H_y is offset by half a grid point.

$$\frac{E_x|_i^{n+\frac{1}{2}} - E_x|_i^{n-\frac{1}{2}}}{\Delta t} = -\frac{1}{\varepsilon_0} \frac{H_y|_{i+\frac{1}{2}}^n - H_y|_{i-\frac{1}{2}}^n}{\Delta z} - \frac{1}{\varepsilon_0} \sigma|_i E_x|_i^n \quad \text{B-31}$$

$$\frac{H_y|_{i+\frac{1}{2}}^{n+1} - H_y|_{i+\frac{1}{2}}^n}{\Delta t} = -\frac{1}{\mu_0} \frac{E_x|_{i+1}^{n+\frac{1}{2}} - E_x|_i^{n+\frac{1}{2}}}{\Delta z} - \frac{1}{\mu_0} \sigma^*|_i H_y|_{i+\frac{1}{2}}^{n+\frac{1}{2}} \quad \text{B-32}$$

As in the three-dimensional case, the average of successive time points approximates the off-step time terms:

$$\frac{E_x|_i^{n+\frac{1}{2}} - E_x|_i^{n-\frac{1}{2}}}{\Delta t} = -\frac{1}{\varepsilon_0} \frac{H_y|_{i+\frac{1}{2}}^n - H_y|_{i-\frac{1}{2}}^n}{\Delta z} - \frac{\sigma|_i}{2\varepsilon_0} (E_x|_i^{n+\frac{1}{2}} + E_x|_i^{n-\frac{1}{2}}) \quad \text{B-33}$$

$$\frac{H_y|_{i+\frac{1}{2}}^{n+1} - H_y|_{i+\frac{1}{2}}^n}{\Delta t} = -\frac{1}{\mu_0} \frac{E_x|_{i+1}^{n+\frac{1}{2}} - E_x|_i^{n+\frac{1}{2}}}{\Delta z} - \frac{\sigma^*|_i}{2\mu_0} (H_y|_{i+\frac{1}{2}}^{n+1} + H_y|_{i+\frac{1}{2}}^n) \quad \text{B-34}$$

Rearranging leads to these update equations:

$$E_x|_i^{n+\frac{1}{2}} = E_x|_i^{n-\frac{1}{2}} \frac{\left(1 - \frac{\sigma|_i \Delta t}{2\varepsilon_0}\right)}{\left(1 + \frac{\sigma|_i \Delta t}{2\varepsilon_0}\right)} - \frac{\frac{\Delta t}{\varepsilon_0}}{\left(1 + \frac{\sigma|_i \Delta t}{2\varepsilon_0}\right)} \left(\frac{H_y|_{i,j+\frac{1}{2},k+1}^n - H_y|_{i,j+\frac{1}{2},k}^n}{\Delta z} \right) \quad \text{B-35}$$

$$H_y|_{i+\frac{1}{2}}^{n+1} = H_y|_{i+\frac{1}{2}}^n \frac{\left(1 - \frac{\sigma^*|_{i+\frac{1}{2}} \Delta t}{2\mu_0}\right)}{\left(1 + \frac{\sigma^*|_{i+\frac{1}{2}} \Delta t}{2\mu_0}\right)} - \frac{\frac{\Delta t}{\mu_0}}{\left(1 + \frac{\sigma^*|_{i+\frac{1}{2}} \Delta t}{2\mu_0}\right)} \left(\frac{E_x|_{i+1}^{n+\frac{1}{2}} - E_x|_i^{n+\frac{1}{2}}}{\Delta z} \right) \quad \text{B-36}$$

To use the incident wave, it must be projected onto the surface between the scattered field zone and the total field zone. For each cell on this surface, the distance, d , from the corner at which the plane wave first encounters the surface to the cell is required. For ease of implementation and use, the incident wave is restricted to the y-z plane. Figure 2.1 shows a plane wave encountering the bottom left corner first.

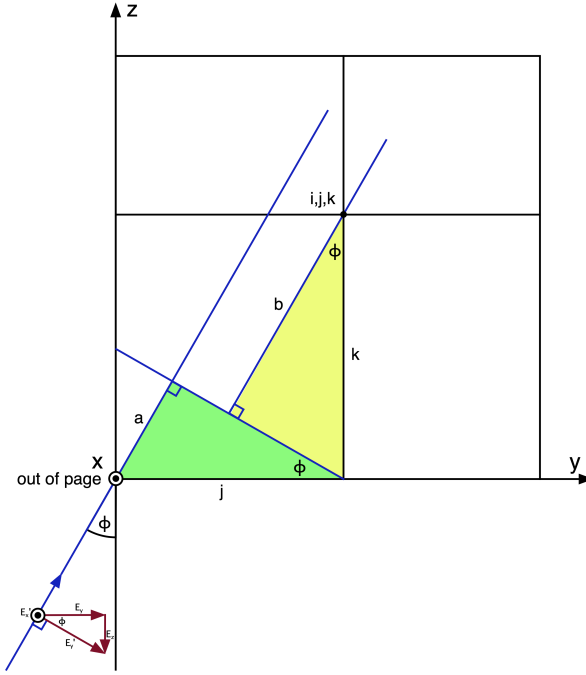


Figure B.1. FDTD plane wave geometry. An incoming plane wave encountering a corner of the surface between the total and scattered field zones at azimuth angle ϕ .

If the first corner encountered is C , then the distance from the corner to the point projected onto the wave is:

$$d = a + b = (j - C_y) \sin \phi + (k - C_z) \cos \phi \quad \text{B-37}$$

Once the distance is calculated, the electric and magnetic field strengths at this position can be linearly interpolated from the auxiliary grid (represented by $E(d)$ and $H(d)$) and the desired polarisation ψ applied. The desired electric and magnetic field components are then

$$\begin{aligned} E'_x &= E_x(d) \cos \psi \\ E'_y &= E_y(d) \sin \psi \cos \phi \\ E'_z &= -E_z(d) \sin \psi \sin \phi \end{aligned} \quad \text{B-38}$$

$$\begin{aligned} H'_y &= -H_x(d) \sin \psi \\ H'_x &= H_y(d) \cos \psi \cos \phi \\ H'_z &= -H_z(d) \cos \psi \sin \phi \end{aligned} \quad \text{B-39}$$

As the calculation passes over the boundary between the two zones, corrections need to be made where the difference in a component straddles the boundary. First, the total field zone is defined to be:

$$\begin{aligned} i_0 &\leq i_z \leq i_1 \\ j_0 &\leq j_z \leq j_1 \\ k_0 &\leq k_z \leq k_1 \end{aligned} \quad \text{B-40}$$

Then at each of the six boundary faces, the E and H field equations are inspected, looking for components where a difference crosses the boundary. These cases can be corrected by adding or subtracting the incident field component depending on whether the target point is inside or outside the zone. This process leads to the following corrections.

The $i = i_0 - 1$ face, $j = j_0 \dots j_1$, $k = k_0 \dots k_1$

$$E_z|_{i+\frac{1}{2},j+\frac{1}{2},k}^{n+\frac{1}{2}} = \left\{ E_z|_{i+\frac{1}{2},j+\frac{1}{2},k}^{n+\frac{1}{2}} \right\}_{orig} - \frac{\Delta t}{\epsilon_0 \Delta y} H_{y,inc}|_{i+1,j+\frac{1}{2},k}^n \quad \text{B-41}$$

$$E_y|_{i+\frac{1}{2},j,k+\frac{1}{2}}^{n+\frac{1}{2}} = \left\{ E_y|_{i+\frac{1}{2},j,k+\frac{1}{2}}^{n+\frac{1}{2}} \right\}_{orig} + \frac{\Delta t}{\epsilon_0 \Delta y} H_{z,inc}|_{i+1,j,k+\frac{1}{2}}^n \quad \text{B-42}$$

The $i = i_0$ face, $j = j_0 \dots j_1$, $k = k_0 \dots k_1$

$$H_y|_{i,j+\frac{1}{2},k}^{n+1} = \left\{ H_y|_{i,j+\frac{1}{2},k}^{n+1} \right\}_{orig} - \frac{\Delta t}{\mu_0 \Delta y} E_{z,inc}|_{i-\frac{1}{2},j+\frac{1}{2},k}^{n+\frac{1}{2}} \quad \text{B-43}$$

$$H_z|_{i,j,k+\frac{1}{2}}^{n+1} = \left\{ H_z|_{i,j,k+\frac{1}{2}}^{n+1} \right\}_{orig} + \frac{\Delta t}{\mu_0 \Delta y} E_{y,inc}|_{i-\frac{1}{2},j,k+\frac{1}{2}}^{n+\frac{1}{2}} \quad \text{B-44}$$

The $i = i_1$ face, $j = j_0 \dots j_1$, $k = k_0 \dots k_1$

$$E_z|_{i+\frac{1}{2},j+\frac{1}{2},k}^{n+\frac{1}{2}} = \left\{ E_z|_{i+\frac{1}{2},j+\frac{1}{2},k}^{n+\frac{1}{2}} \right\}_{orig} + \frac{\Delta t}{\epsilon_0 \Delta y} H_{y,inc}|_{i+1,j+\frac{1}{2},k}^n \quad \text{B-45}$$

$$E_y|_{i+\frac{1}{2},j,k+\frac{1}{2}}^{n+\frac{1}{2}} = \left\{ E_y|_{i+\frac{1}{2},j,k+\frac{1}{2}}^{n+\frac{1}{2}} \right\}_{orig} - \frac{\Delta t}{\epsilon_0 \Delta y} H_{z,inc}|_{i+1,j,k+\frac{1}{2}}^n \quad \text{B-46}$$

The $i = i_1 + 1$ face, $j = j_0 \dots j_1$, $k = k_0 \dots k_1$

$$H_y|_{i,j+\frac{1}{2},k}^{n+1} = \left\{ H_y|_{i,j+\frac{1}{2},k}^{n+1} \right\}_{orig} + \frac{\Delta t}{\mu_0 \Delta y} E_{z,inc}|_{i-\frac{1}{2},j+\frac{1}{2},k}^{n+\frac{1}{2}} \quad \text{B-47}$$

$$H_z|_{i,j,k+\frac{1}{2}}^{n+1} = \left\{ H_z|_{i,j,k+\frac{1}{2}}^{n+1} \right\}_{orig} - \frac{\Delta t}{\mu_0 \Delta y} E_{y,inc}|_{i-\frac{1}{2},j,k+\frac{1}{2}}^{n+\frac{1}{2}} \quad \text{B-48}$$

The $j = j_0 - 1$ face, $i = i_0 \dots i_1$, $k = k_0 \dots k_1$

$$E_x|_{i,j+\frac{1}{2},k+\frac{1}{2}}^{n+\frac{1}{2}} = \left\{ E_x|_{i,j+\frac{1}{2},k+\frac{1}{2}}^{n+\frac{1}{2}} \right\}_{orig} - \frac{\Delta t}{\varepsilon_0 \Delta x} H_{z,inc}|_{i,j+1,k+\frac{1}{2}}^n \quad \text{B-49}$$

$$E_z|_{i+\frac{1}{2},j+\frac{1}{2},k}^{n+\frac{1}{2}} = \left\{ E_z|_{i+\frac{1}{2},j+\frac{1}{2},k}^{n+\frac{1}{2}} \right\}_{orig} + \frac{\Delta t}{\varepsilon_0 \Delta x} H_{x,inc}|_{i+\frac{1}{2},j+1,k}^n \quad \text{B-50}$$

The $j = j_0$ face, $i = i_0 \dots i_1$, $k = k_0 \dots k_1$

$$H_z|_{i,j,k+\frac{1}{2}}^{n+1} = \left\{ H_z|_{i,j,k+\frac{1}{2}}^{n+1} \right\}_{orig} - \frac{\Delta t}{\mu_0 \Delta x} E_{x,inc}|_{i,j-\frac{1}{2},k+\frac{1}{2}}^{n+\frac{1}{2}} \quad \text{B-51}$$

$$H_x|_{i+\frac{1}{2},j,k}^{n+1} = \left\{ H_x|_{i+\frac{1}{2},j,k}^{n+1} \right\}_{orig} + \frac{\Delta t}{\mu_0 \Delta x} E_{z,inc}|_{i+\frac{1}{2},j-\frac{1}{2},k}^{n+\frac{1}{2}} \quad \text{B-52}$$

The $j = j_1$ face, $i = i_0 \dots i_1$, $k = k_0 \dots k_1$

$$E_x|_{i,j+\frac{1}{2},k+\frac{1}{2}}^{n+\frac{1}{2}} = \left\{ E_x|_{i,j+\frac{1}{2},k+\frac{1}{2}}^{n+\frac{1}{2}} \right\}_{orig} - \frac{\Delta t}{\varepsilon_0 \Delta x} H_{z,inc}|_{i,j+1,k+\frac{1}{2}}^n \quad \text{B-53}$$

$$E_z|_{i+\frac{1}{2},j+\frac{1}{2},k}^{n+\frac{1}{2}} = \left\{ E_z|_{i+\frac{1}{2},j+\frac{1}{2},k}^{n+\frac{1}{2}} \right\}_{orig} + \frac{\Delta t}{\varepsilon_0 \Delta x} H_{x,inc}|_{i+\frac{1}{2},j+1,k}^n \quad \text{B-54}$$

The $j = j_1 + 1$ face, $i = i_0 \dots i_1$, $k = k_0 \dots k_1$

$$H_z|_{i,j,k+\frac{1}{2}}^{n+1} = \left\{ H_z|_{i,j,k+\frac{1}{2}}^{n+1} \right\}_{orig} + \frac{\Delta t}{\mu_0 \Delta x} E_{x,inc}|_{i,j-\frac{1}{2},k+\frac{1}{2}}^{n+\frac{1}{2}} \quad \text{B-55}$$

$$H_x|_{i+\frac{1}{2},j,k}^{n+1} = \left\{ H_x|_{i+\frac{1}{2},j,k}^{n+1} \right\}_{orig} - \frac{\Delta t}{\mu_0 \Delta x} E_{z,inc}|_{i+\frac{1}{2},j-\frac{1}{2},k}^{n+\frac{1}{2}} \quad \text{B-56}$$

The $k = k_0 - 1$ face, $i = i_0 \dots i_1$, $j = j_0 \dots j_1$

$$E_x|_{i,j+\frac{1}{2},k+\frac{1}{2}}^{n+\frac{1}{2}} = \left\{ E_x|_{i,j+\frac{1}{2},k+\frac{1}{2}}^{n+\frac{1}{2}} \right\}_{orig} + \frac{\Delta t}{\varepsilon_0 \Delta z} H_{y,inc}|_{i,j+\frac{1}{2},k+1}^n \quad \text{B-57}$$

$$E_y|_{i+\frac{1}{2},j,k+\frac{1}{2}}^{n+\frac{1}{2}} = \left\{ E_y|_{i+\frac{1}{2},j,k+\frac{1}{2}}^{n+\frac{1}{2}} \right\}_{orig} - \frac{\Delta t}{\varepsilon_0 \Delta z} H_{x,inc}|_{i+\frac{1}{2},j,k+1}^n \quad \text{B-58}$$

The $k = k_0$ face, $i = i_0 \dots i_1$, $j = j_0 \dots j_1$

$$H_y|_{i,j+\frac{1}{2},k}^{n+1} = \left\{ H_y|_{i,j+\frac{1}{2},k}^{n+1} \right\}_{orig} + \frac{\Delta t}{\mu_0 \Delta z} E_{x,inc}|_{i,j+\frac{1}{2},k-\frac{1}{2}}^{n+\frac{1}{2}} \quad \text{B-59}$$

$$H_x|_{i+\frac{1}{2},j,k}^{n+1} = \left\{ H_x|_{i+\frac{1}{2},j,k}^{n+1} \right\}_{orig} - \frac{\Delta t}{\mu_0 \Delta Z} E_{y,inc}|_{i+\frac{1}{2},j,k-\frac{1}{2}}^{n+\frac{1}{2}} \quad \text{B-60}$$

The $k = k_1$ face, $i = i_0 \dots i_1$, $j = j_0 \dots j_1$

$$E_x|_{i,j+\frac{1}{2},k+\frac{1}{2}}^{n+\frac{1}{2}} = \left\{ E_x|_{i,j+\frac{1}{2},k+\frac{1}{2}}^{n+\frac{1}{2}} \right\}_{orig} - \frac{\Delta t}{\varepsilon_0 \Delta Z} H_{y,inc}|_{i,j+\frac{1}{2},k+1}^n \quad \text{B-61}$$

$$E_y|_{i+\frac{1}{2},j,k+\frac{1}{2}}^{n+\frac{1}{2}} = \left\{ E_y|_{i+\frac{1}{2},j,k+\frac{1}{2}}^{n+\frac{1}{2}} \right\}_{orig} + \frac{\Delta t}{\varepsilon_0 \Delta Z} H_{x,inc}|_{i+\frac{1}{2},j,k+1}^n \quad \text{B-62}$$

The $k = k_1 + 1$ face, $i = i_0 \dots i_1$, $j = j_0 \dots j_1$

$$H_y|_{i,j+\frac{1}{2},k}^{n+1} = \left\{ H_y|_{i,j+\frac{1}{2},k}^{n+1} \right\}_{orig} - \frac{\Delta t}{\mu_0 \Delta Z} E_{x,inc}|_{i,j+\frac{1}{2},k-\frac{1}{2}}^{n+\frac{1}{2}} \quad \text{B-63}$$

$$H_x|_{i+\frac{1}{2},j,k}^{n+1} = \left\{ H_x|_{i+\frac{1}{2},j,k}^{n+1} \right\}_{orig} + \frac{\Delta t}{\mu_0 \Delta Z} E_{y,inc}|_{i+\frac{1}{2},j,k-\frac{1}{2}}^{n+\frac{1}{2}} \quad \text{B-64}$$

To make this scheme work, the magnetic field auxiliary grid must be read one step in advance of the electric field auxiliary grid. This is to take account of an implementation detail of the main grid; an electric field boundary cell is calculated from the difference between the adjacent magnetic field cells, one inside the boundary one outside. The problem is that the magnetic cell that needs correction is inside the boundary, while the electric cell is outside; the auxiliary cells required are displaced from each other. To compensate for this, the magnetic auxiliary grid is advanced by one step, otherwise the scattered field zone is not properly corrected for the electric field.

B.3 1D plane wave incident on a lossy region

To emulate a model surrounded by an infinite space, waves that encounter the boundary of the domain must be absorbed. This is true for both the main three-dimensional grid and the one-dimensional auxiliary grid used by the total field/scattered field method of injecting a plane wave. Taflov and Hagness address this by first reviewing the physics of a wave encountering a lossy material, this section expands on that treatment. In addition to being an introduction, this also has direct applicability to the one-dimensional auxiliary grid of section 0.

Shown in Figure 2.7 is a scenario where the region of space $x < 0$ is lossless and the region $x \geq 0$ has electric conductivity σ and magnetic conductivity σ^* . Starting from the time harmonic versions of Maxwell's equations:

$$\nabla \times \mathbf{E} = -i\omega\mu\mathbf{H} - \sigma^*\mathbf{H} \quad \text{B-65}$$

$$\nabla \times \mathbf{H} = i\omega\varepsilon\mathbf{E} + \sigma\mathbf{E} \quad \text{B-66}$$

Which can be rearranged to:

$$\nabla \times \mathbf{E} = -i\omega\left(\mu - \frac{i\sigma^*}{\omega}\right)\mathbf{H} \quad \text{B-67}$$

$$\nabla \times \mathbf{H} = i\omega\left(\varepsilon - \frac{i\sigma}{\omega}\right)\mathbf{E} \quad \text{B-68}$$

Defining the complex permittivity and permeability respectively to be

$$\bar{\mu} = \mu - \frac{i\sigma^*}{\omega} \quad \bar{\varepsilon} = \varepsilon - \frac{i\sigma}{\omega} \quad \text{B-69}$$

The equations can then be written as

$$\nabla \times \mathbf{E} = -i\omega\bar{\mu}\mathbf{H} \quad \text{B-70}$$

$$\nabla \times \mathbf{H} = i\omega\bar{\varepsilon}\mathbf{E} \quad \text{B-71}$$

In the one-dimensional case, with the wave polarized in the z direction, the electric field will be given by (γ is the propagation constant)

$$\mathbf{E} = \hat{\mathbf{z}}e^{-\gamma x} \quad \text{B-72}$$

Then the magnetic field is

$$\mathbf{H} = -\frac{1}{i\omega\bar{\mu}}\nabla \times \hat{\mathbf{z}}e^{-\gamma x} \quad \text{B-73}$$

Expanding the curl leads to

$$\mathbf{H} = -\hat{\mathbf{y}}\frac{\gamma}{i\omega\bar{\mu}}e^{-\gamma x} \quad \text{B-74}$$

This allows the calculation of the characteristic impedance from the ratio of the electric and magnetic field components:

$$\eta = -\frac{e^{-\gamma x}}{-\frac{\gamma}{i\omega\bar{\mu}}e^{-\gamma x}} = \frac{i\omega\bar{\mu}}{\gamma} \quad \text{B-75}$$

Using the other curl equation of B-70 and substituting the magnetic field of equation B-74 and the electric field of equation B-72.

$$-\nabla \times \hat{\mathbf{y}} \frac{\gamma}{i\omega\bar{\mu}} e^{-\gamma x} = i\omega\bar{\varepsilon}\hat{\mathbf{z}}e^{-\gamma x} \quad \text{B-76}$$

Again, expanding the curl:

$$\hat{\mathbf{z}} \frac{\gamma^2}{i\omega\bar{\mu}} e^{-\gamma x} = i\omega\bar{\varepsilon}\hat{\mathbf{z}}e^{-\gamma x} \quad \text{B-77}$$

Simplifying and solving for γ :

$$\gamma = i\omega\sqrt{\bar{\mu}\bar{\varepsilon}} \quad \text{B-78}$$

The propagation constant γ is also often written as

$$\gamma = \alpha + i\beta \quad \text{B-79}$$

Where α represents the attenuation and β the angular wave number $k = \omega/c = \omega\sqrt{\bar{\mu}\bar{\varepsilon}}$.

Substituting equation B-78 into equation B-75 for the characteristic impedance:

$$\eta = \frac{i\omega\bar{\mu}}{i\omega\sqrt{\bar{\mu}\bar{\varepsilon}}} \quad \text{B-80}$$

Which leads to this equation for the characteristic impedance:

$$\eta = \sqrt{\frac{\bar{\mu}}{\bar{\varepsilon}}} \quad \text{B-81}$$

Returning to the scenario of Figure 2.7, the electric and magnetic components of the incident field can be written as (the subscript 1 indicating the properties of the lossless zone so $\beta_1 = \omega\sqrt{\mu_1\varepsilon_1}$):

$$E_z = e^{-j\beta_1 x} \quad \text{B-82}$$

$$H_y = -\frac{1}{\eta_1} e^{-j\beta_1 x} \quad \text{B-83}$$

Introducing the reflection coefficient, Γ , allows equations for the reflected electric and magnetic components to be written:

$$E_z^r = \Gamma e^{j\beta_1 x} \quad \text{B-84}$$

$$H_y^r = \frac{\Gamma}{\eta_1} e^{j\beta_1 x} \quad \text{B-85}$$

Similarly, with the introduction of the transmission coefficient, τ , equations for the transmitted components can be written (the subscript 2 indicating the properties of the lossy zone):

$$E_z^t = \tau e^{-j\beta_2 x} \quad \text{B-86}$$

$$H_y^t = -\frac{\tau}{\eta_2} e^{-j\beta_2 x} \quad \text{B-87}$$

At $x = 0$, the boundary between the two zones, the sum of the incident and reflected waves must equal the transmitted wave. This requirement for the electric field leads to:

$$1 + \Gamma = \tau \quad \text{B-88}$$

And for the magnetic fields to:

$$1 - \Gamma = \frac{\eta_1}{\eta_2} \tau \quad \text{B-89}$$

Substituting τ from equation B-88 and rearranging gives:

$$\Gamma = \frac{\eta_2 - \eta_1}{\eta_2 + \eta_1} \quad \text{B-90}$$

For the lossy region to match the lossless region no reflection can occur at the boundary and $\Gamma = 0$. It follows therefore that $\eta_1 = \eta_2$. Using equation B-81 for the characteristic impedance and expanding the complex permittivities and permeabilities (equation B-69) this can be expressed as:

$$\sqrt{\frac{\mu_1 \left(1 - \frac{i\sigma_1^*}{\omega\mu_1}\right)}{\varepsilon_1 \left(1 - \frac{i\sigma_1}{\omega\varepsilon_1}\right)}} = \sqrt{\frac{\mu_2 \left(1 - \frac{i\sigma_2^*}{\omega\mu_2}\right)}{\varepsilon_2 \left(1 - \frac{i\sigma_2}{\omega\varepsilon_2}\right)}} \quad \text{B-91}$$

Then, rearranging and making $\mu_1/\varepsilon_1 = \mu_2/\varepsilon_2$, which is easily done by making $\mu_1 = \mu_2 = \mu$ and $\varepsilon_1 = \varepsilon_2 = \varepsilon$ another matching requirement can be found ($\sigma_1^* = 0$ and $\sigma_1 = 0$ for the lossless zone):

$$\frac{\sigma_2^*}{\mu} = \frac{\sigma_2}{\varepsilon} \quad \text{B-92}$$

The auxiliary grid used for the scattered field/total field method of injecting a plane wave into the main FDTD grid can make use of this result directly.

B.4 Berenger's split coordinate perfectly matched layer

The lossy region described in B.3 only works correctly for waves at normal incidence to it, other waves are reflected back into the model. To counter this, Berenger¹³⁰ proposed a split coordinate approach to produce a perfect matched layer (PML). This section is an expansion of the treatment from Taflove and Hagness.

Assume each field component is split into two parts (each part corresponds to the contribution from the differential of the other field components from the curl expansion).

$$\begin{aligned} E_x &= E_{xy} + E_{xz} & E_y &= E_{yx} + E_{yz} & E_z &= E_{zx} + E_{zy} \\ H_x &= H_{xy} + H_{xz} & H_y &= H_{yx} + H_{yz} & H_z &= H_{zx} + H_{zy} \end{aligned} \quad \text{B-93}$$

For example, from the electric field x component of ampere's law:

$$\left(\varepsilon \frac{\partial}{\partial t} + \sigma \right) E_x = \frac{\partial}{\partial y} H_z - \frac{\partial}{\partial z} H_y \quad \text{B-94}$$

Substituting the split fields

$$\left(\varepsilon \frac{\partial}{\partial t} + \sigma \right) (E_{xy} + E_{xz}) = \frac{\partial}{\partial y} (H_{zx} + H_{zy}) - \frac{\partial}{\partial z} (H_{yx} + H_{yz}) \quad \text{B-95}$$

And separating into two equations, allowing the use of different values of conductivity for the two parts:

$$\left(\varepsilon \frac{\partial}{\partial t} + \sigma_y \right) E_{xy} = \frac{\partial}{\partial y} (H_{zx} + H_{zy}) \quad \text{B-96}$$

$$\left(\varepsilon \frac{\partial}{\partial t} + \sigma_z \right) E_{xz} = - \frac{\partial}{\partial z} (H_{yx} + H_{yz}) \quad \text{B-97}$$

Repeating for the other electric components:

$$\left(\varepsilon \frac{\partial}{\partial t} + \sigma_z \right) E_{yz} = \frac{\partial}{\partial z} (H_{xy} + H_{xz}) \quad \text{B-98}$$

$$\left(\varepsilon \frac{\partial}{\partial t} + \sigma_x\right) E_{yx} = -\frac{\partial}{\partial x} (H_{zx} + H_{zy}) \quad \text{B-99}$$

$$\left(\varepsilon \frac{\partial}{\partial t} + \sigma_x\right) E_{zx} = \frac{\partial}{\partial x} (H_{yx} + H_{yz}) \quad \text{B-100}$$

$$\left(\varepsilon \frac{\partial}{\partial t} + \sigma_y\right) E_{zy} = -\frac{\partial}{\partial y} (H_{xy} + H_{xz}) \quad \text{B-101}$$

and for the magnetic field components

$$\left(\mu \frac{\partial}{\partial t} + \sigma_y^*\right) H_{xy} = -\frac{\partial}{\partial y} (E_{zx} + E_{zy}) \quad \text{B-102}$$

$$\left(\mu \frac{\partial}{\partial t} + \sigma_z^*\right) H_{xz} = \frac{\partial}{\partial z} (E_{yx} + E_{yz}) \quad \text{B-103}$$

$$\left(\mu \frac{\partial}{\partial t} + \sigma_z^*\right) H_{yz} = -\frac{\partial}{\partial z} (E_{xy} + E_{xz}) \quad \text{B-104}$$

$$\left(\mu \frac{\partial}{\partial t} + \sigma_x^*\right) H_{yx} = \frac{\partial}{\partial x} (E_{zx} + E_{zy}) \quad \text{B-105}$$

$$\left(\mu \frac{\partial}{\partial t} + \sigma_x^*\right) H_{zx} = -\frac{\partial}{\partial x} (E_{yx} + E_{yz}) \quad \text{B-106}$$

$$\left(\mu \frac{\partial}{\partial t} + \sigma_y^*\right) H_{zy} = \frac{\partial}{\partial y} (E_{xy} + E_{xz}) \quad \text{B-107}$$

Normally incident waves for each part can be matched separately, using the same matching condition as section 0 ($w = x, y, z$):

$$\sigma_w^* = \frac{\sigma_w \mu_0}{\varepsilon_0} \quad \text{B-108}$$

Each boundary zone has a set of three (σ_w, σ_w^*) pairs which are non-zero only for the normal to w direction.

An FDTD implementation of these equations will need to store each part of the split field for each component of E and H . The FDTD update equations in the boundary therefore become, for the electric field:

$$\begin{aligned} E_{xy}|_{i,j+\frac{1}{2},k+\frac{1}{2}}^{n+\frac{1}{2}} = & C_{aey}|_{i,j+\frac{1}{2},k+\frac{1}{2}} \frac{\left(H_{zx}|_{i,j+1,k+\frac{1}{2}}^n + H_{zy}|_{i,j+1,k+\frac{1}{2}}^n\right) - \left(H_{zx}|_{i,j,k+\frac{1}{2}}^n + H_{zy}|_{i,j,k+\frac{1}{2}}^n\right)}{\Delta y} \\ & + E_{xy}|_{i,j+\frac{1}{2},k+\frac{1}{2}}^{n-\frac{1}{2}} C_{bey}|_{i,j+\frac{1}{2},k+\frac{1}{2}} \end{aligned} \quad \text{B-109}$$

$$E_{xz}|_{i,j+\frac{1}{2},k+\frac{1}{2}}^{n+\frac{1}{2}} = -C_{aez}|_{i,j+\frac{1}{2},k+\frac{1}{2}} \frac{\left(H_{yz}|_{i,j+\frac{1}{2},k+1}^n + H_{yx}|_{i,j+\frac{1}{2},k+1}^n\right) - \left(H_{yz}|_{i,j+\frac{1}{2},k}^n + H_{yx}|_{i,j+\frac{1}{2},k}^n\right)}{\Delta z} + E_{xz}|_{i,j+\frac{1}{2},k+\frac{1}{2}}^{n-\frac{1}{2}} C_{bez}|_{i,j+\frac{1}{2},k+\frac{1}{2}} \quad \text{B-110}$$

$$E_{yz}|_{i+\frac{1}{2},j,k+\frac{1}{2}}^{n+\frac{1}{2}} = C_{aez}|_{i+\frac{1}{2},j,k+\frac{1}{2}} \frac{\left(H_{xy}|_{i+\frac{1}{2},j,k+1}^n + H_{xz}|_{i+\frac{1}{2},j,k+1}^n\right) - \left(H_{xy}|_{i+\frac{1}{2},j,k}^n + H_{xz}|_{i+\frac{1}{2},j,k}^n\right)}{\Delta z} + E_{yz}|_{i+\frac{1}{2},j,k+\frac{1}{2}}^{n-\frac{1}{2}} C_{bez}|_{i+\frac{1}{2},j,k+\frac{1}{2}} \quad \text{B-111}$$

$$E_{yx}|_{i+\frac{1}{2},j,k+\frac{1}{2}}^{n+\frac{1}{2}} = -C_{aex}|_{i+\frac{1}{2},j,k+\frac{1}{2}} \frac{\left(H_{zx}|_{i+1,j,k+\frac{1}{2}}^n + H_{zy}|_{i+1,j,k+\frac{1}{2}}^n\right) - \left(H_{zx}|_{i,j,k+\frac{1}{2}}^n + H_{zy}|_{i,j,k+\frac{1}{2}}^n\right)}{\Delta x} + E_{yx}|_{i+\frac{1}{2},j,k+\frac{1}{2}}^{n-\frac{1}{2}} C_{bex}|_{i+\frac{1}{2},j,k+\frac{1}{2}} \quad \text{B-112}$$

$$E_{zx}|_{i+\frac{1}{2},j+\frac{1}{2},k}^{n+\frac{1}{2}} = C_{aex}|_{i+\frac{1}{2},j+\frac{1}{2},k} \frac{\left(H_{yz}|_{i+1,j+\frac{1}{2},k}^n + H_{yx}|_{i+1,j+\frac{1}{2},k}^n\right) - \left(H_{yz}|_{i,j+\frac{1}{2},k}^n + H_{yx}|_{i,j+\frac{1}{2},k}^n\right)}{\Delta x} + E_{zx}|_{i+\frac{1}{2},j+\frac{1}{2},k}^{n-\frac{1}{2}} C_{bex}|_{i+\frac{1}{2},j+\frac{1}{2},k} \quad \text{B-113}$$

$$E_{zy}|_{i+\frac{1}{2},j+\frac{1}{2},k}^{n+\frac{1}{2}} = -C_{aey}|_{i+\frac{1}{2},j+\frac{1}{2},k} \frac{\left(H_{xy}|_{i+\frac{1}{2},j+1,k}^n + H_{xz}|_{i+\frac{1}{2},j+1,k}^n\right) - \left(H_{xy}|_{i+\frac{1}{2},j,k}^n + H_{xz}|_{i+\frac{1}{2},j,k}^n\right)}{\Delta y} + E_{zy}|_{i+\frac{1}{2},j+\frac{1}{2},k}^{n-\frac{1}{2}} C_{bey}|_{i+\frac{1}{2},j+\frac{1}{2},k} \quad \text{B-114}$$

Where:

$$C_{aew} = \frac{\frac{\Delta t}{\varepsilon}}{\left(1 + \frac{\sigma_w \Delta t}{2\varepsilon}\right)} \quad C_{bew} = \frac{\left(1 - \frac{\sigma_w \Delta t}{2\varepsilon}\right)}{\left(1 + \frac{\sigma_w \Delta t}{2\varepsilon}\right)} \quad w = x, y, z \quad \text{B-115}$$

And for the magnetic field:

$$H_{xy}|_{i+\frac{1}{2},j,k}^{n+1} = -C_{ahy}|_{i+\frac{1}{2},j,k} \frac{\left(E_{zx}|_{i+\frac{1}{2},j+\frac{1}{2},k}^{n+\frac{1}{2}} + E_{zy}|_{i+\frac{1}{2},j+\frac{1}{2},k}^{n+\frac{1}{2}}\right) - \left(E_{zx}|_{i+\frac{1}{2},j-\frac{1}{2},k}^{n+\frac{1}{2}} + E_{zy}|_{i+\frac{1}{2},j-\frac{1}{2},k}^{n+\frac{1}{2}}\right)}{\Delta y} + H_{xy}|_{i+\frac{1}{2},j,k}^n C_{bhy}|_{i+\frac{1}{2},j,k} \quad \text{B-116}$$

$$H_{xz}|_{i+\frac{1}{2},j,k}^{n+1} = +C_{ahz}|_{i+\frac{1}{2},j,k} \frac{\left(E_{yz}|_{i+\frac{1}{2},j,k+\frac{1}{2}}^{n+\frac{1}{2}} + E_{yx}|_{i+\frac{1}{2},j,k+\frac{1}{2}}^{n+\frac{1}{2}}\right) - \left(E_{yz}|_{i+\frac{1}{2},j,k-\frac{1}{2}}^{n+\frac{1}{2}} + E_{yx}|_{i+\frac{1}{2},j,k-\frac{1}{2}}^{n+\frac{1}{2}}\right)}{\Delta z} + H_{xz}|_{i+\frac{1}{2},j,k}^n C_{bhz}|_{i+\frac{1}{2},j,k} \quad \text{B-117}$$

$$H_{yz}|_{i,j+\frac{1}{2},k}^{n+1} = -C_{ahz}|_{i,j+\frac{1}{2},k} \frac{\left(E_{xy}|_{i,j+\frac{1}{2},k+\frac{1}{2}}^{n+\frac{1}{2}} + E_{xz}|_{i,j+\frac{1}{2},k+\frac{1}{2}}^{n+\frac{1}{2}}\right) - \left(E_{xy}|_{i,j+\frac{1}{2},k-\frac{1}{2}}^{n+\frac{1}{2}} + E_{xz}|_{i,j+\frac{1}{2},k-\frac{1}{2}}^{n+\frac{1}{2}}\right)}{\Delta z} + H_{yz}|_{i,j+\frac{1}{2},k}^n C_{bhz}|_{i,j+\frac{1}{2},k} \quad \text{B-118}$$

$$H_{yx}|_{i,j+\frac{1}{2},k}^{n+1} = +C_{ahx}|_{i,j+\frac{1}{2},k} \frac{\left(E_{zx}|_{i+\frac{1}{2},j+\frac{1}{2},k}^{n+\frac{1}{2}} + E_{zy}|_{i+\frac{1}{2},j+\frac{1}{2},k}^{n+\frac{1}{2}}\right) - \left(E_{zx}|_{i-\frac{1}{2},j+\frac{1}{2},k}^{n+\frac{1}{2}} + E_{zy}|_{i-\frac{1}{2},j+\frac{1}{2},k}^{n+\frac{1}{2}}\right)}{\Delta x} + H_{yx}|_{i,j+\frac{1}{2},k}^n C_{bhx}|_{i,j+\frac{1}{2},k} \quad \text{B-119}$$

$$H_{zx}|_{i,j,k+\frac{1}{2}}^{n+1} = -C_{ahx}|_{i,j,k+\frac{1}{2}} \frac{\left(E_{yz}|_{i+\frac{1}{2},j,k+\frac{1}{2}}^{n+\frac{1}{2}} + E_{yx}|_{i+\frac{1}{2},j,k+\frac{1}{2}}^{n+\frac{1}{2}}\right) - \left(E_{yz}|_{i-\frac{1}{2},j,k+\frac{1}{2}}^{n+\frac{1}{2}} + E_{yx}|_{i-\frac{1}{2},j,k+\frac{1}{2}}^{n+\frac{1}{2}}\right)}{\Delta x} + H_{zx}|_{i,j,k+\frac{1}{2}}^n C_{bhx}|_{i,j,k+\frac{1}{2}} \quad \text{B-120}$$

$$H_{zy}|_{i,j,k+\frac{1}{2}}^{n+1} = +C_{ahy}|_{i,j,k+\frac{1}{2}} \frac{\left(E_{xy}|_{i,j+\frac{1}{2},k+\frac{1}{2}}^{n+\frac{1}{2}} + E_{xz}|_{i,j+\frac{1}{2},k+\frac{1}{2}}^{n+\frac{1}{2}}\right) - \left(E_{xy}|_{i,j-\frac{1}{2},k+\frac{1}{2}}^{n+\frac{1}{2}} + E_{xz}|_{i,j-\frac{1}{2},k+\frac{1}{2}}^{n+\frac{1}{2}}\right)}{\Delta y} + H_{zy}|_{i,j,k+\frac{1}{2}}^n C_{bhy}|_{i,j,k+\frac{1}{2}} \quad \text{B-121}$$

Where:

$$C_{ahw} = \frac{\frac{\Delta t}{\mu}}{\left(1 + \frac{\sigma_w^* \Delta t}{2\mu}\right)} \quad C_{bhw} = \frac{\left(1 - \frac{\sigma_w^* \Delta t}{2\mu}\right)}{\left(1 + \frac{\sigma_w^* \Delta t}{2\mu}\right)} \quad w = x, y, z \quad \text{B-122}$$

B.5 The convolutional perfectly matched layer

An efficient implementation of a stretched field algorithm (see Chew and Weedon⁹⁵) referred to as the Convolutional PML (CPML) was described by Roden and Gedney⁹⁶. Using this method, the CPML electric field update equations in the boundary layers become (from Taflove and Hagness, the new terms in red)

$$E_x|_{i,j+\frac{1}{2},k+\frac{1}{2}}^{n+1} = C_{aex}|_{i,j+\frac{1}{2},k+\frac{1}{2}} \left(\frac{H_z|_{i,j+1,k+\frac{1}{2}}^n - H_z|_{i,j,k+\frac{1}{2}}^n}{\kappa_y|_{j+\frac{1}{2}} \Delta y} - \frac{H_y|_{i,j+\frac{1}{2},k+1}^n - H_y|_{i,j+\frac{1}{2},k}^n}{\kappa_z|_{k+\frac{1}{2}} \Delta z} - J_x|_{i,j+\frac{1}{2},k+\frac{1}{2}}^n + \Psi_{Ex,y}|_{i,j+\frac{1}{2},k+\frac{1}{2}}^n - \Psi_{Ex,z}|_{i,j+\frac{1}{2},k+\frac{1}{2}}^n \right) + E_x|_{i,j+\frac{1}{2},k+\frac{1}{2}}^{n-\frac{1}{2}} C_{bex}|_{i,j+\frac{1}{2},k+\frac{1}{2}} \quad \text{B-123}$$

$$\begin{aligned}
 E_y|_{i+\frac{1}{2},j,k+\frac{1}{2}}^{n+\frac{1}{2}} = & C_{aey}|_{i+\frac{1}{2},j,k+\frac{1}{2}} \left(\frac{H_x|_{i+\frac{1}{2},j,k+1}^n - H_x|_{i+\frac{1}{2},j,k}^n}{\kappa_z|_{k+\frac{1}{2}}\Delta z} \right. \\
 & - \frac{H_z|_{i+1,j,k+\frac{1}{2}}^n - H_z|_{i,j,k+\frac{1}{2}}^n}{\kappa_x|_{i+\frac{1}{2}}\Delta x} - J_y|_{i+\frac{1}{2},j,k+\frac{1}{2}}^n + \Psi_{E_{y,z}}|_{i+\frac{1}{2},j,k+\frac{1}{2}}^n \\
 & \left. - \Psi_{E_{y,x}}|_{i+\frac{1}{2},j,k+\frac{1}{2}}^n \right) + E_y|_{i+\frac{1}{2},j,k+\frac{1}{2}}^{n-\frac{1}{2}} C_{bey}|_{i+\frac{1}{2},j,k+\frac{1}{2}}
 \end{aligned} \tag{B-124}$$

$$\begin{aligned}
 E_z|_{i+\frac{1}{2},j+\frac{1}{2},k}^{n+\frac{1}{2}} = & C_{aez}|_{i+\frac{1}{2},j+\frac{1}{2},k} \left(\frac{H_y|_{i+1,j+\frac{1}{2},k}^n - H_y|_{i,j+\frac{1}{2},k}^n}{\kappa_x|_{i+\frac{1}{2}}\Delta x} \right. \\
 & - \frac{H_x|_{i+\frac{1}{2},j+1,k}^n - H_x|_{i+\frac{1}{2},j,k}^n}{\kappa_y|_{j+\frac{1}{2}}\Delta y} - J_z|_{i+\frac{1}{2},j+\frac{1}{2},k}^n + \Psi_{E_{z,x}}|_{i+\frac{1}{2},j+\frac{1}{2},k}^n \\
 & \left. - \Psi_{E_{z,y}}|_{i+\frac{1}{2},j+\frac{1}{2},k}^n \right) + E_z|_{i+\frac{1}{2},j+\frac{1}{2},k}^{n-\frac{1}{2}} C_{bez}|_{i+\frac{1}{2},j+\frac{1}{2},k}
 \end{aligned} \tag{B-125}$$

where

$$C_{aew} = \frac{\frac{\Delta t}{\varepsilon}}{\left(1 + \frac{\sigma_w \Delta t}{2\varepsilon}\right)} \quad C_{bew} = \frac{\left(1 - \frac{\sigma_w \Delta t}{2\varepsilon}\right)}{\left(1 + \frac{\sigma_w \Delta t}{2\varepsilon}\right)} \quad w = x, y, z. \tag{B-126}$$

The magnetic equations become:

$$\begin{aligned}
 H_x|_{i+\frac{1}{2},j,k}^{n+1} = & C_{ah}|_{i+\frac{1}{2},j,k} \left(- \frac{E_z|_{i+\frac{1}{2},j+\frac{1}{2},k}^{n+\frac{1}{2}} - E_z|_{i+\frac{1}{2},j-\frac{1}{2},k}^{n+\frac{1}{2}}}{\kappa_y|_j\Delta y} \right. \\
 & + \frac{E_y|_{i+\frac{1}{2},j,k+\frac{1}{2}}^{n+\frac{1}{2}} - E_y|_{i+\frac{1}{2},j,k-\frac{1}{2}}^{n+\frac{1}{2}}}{\kappa_z|_k\Delta z} - M_x|_{i+\frac{1}{2},j,k}^{n+\frac{1}{2}} + \Psi_{H_{x,z}}|_{i+\frac{1}{2},j,k}^{n+\frac{1}{2}} \\
 & \left. - \Psi_{H_{x,y}}|_{i+\frac{1}{2},j,k}^{n+\frac{1}{2}} \right) + H_x|_{i+\frac{1}{2},j,k}^n C_{bh}|_{i+\frac{1}{2},j,k}
 \end{aligned} \tag{B-127}$$

$$\begin{aligned}
 H_y|_{i,j+\frac{1}{2},k}^{n+1} = & C_{ah}|_{i,j+\frac{1}{2},k} \left(-\frac{E_x|_{i,j+\frac{1}{2},k+\frac{1}{2}}^{n+\frac{1}{2}} - E_x|_{i,j+\frac{1}{2},k-\frac{1}{2}}^{n+\frac{1}{2}}}{\kappa_z|_k \Delta z} \right. \\
 & + \frac{E_z|_{i+\frac{1}{2},j+\frac{1}{2},k}^{n+\frac{1}{2}} - E_z|_{i-\frac{1}{2},j+\frac{1}{2},k}^{n+\frac{1}{2}}}{\kappa_x|_i \Delta x} - M_y|_{i,j+\frac{1}{2},k}^{n+\frac{1}{2}} + \Psi_{H_{y,x}}|_{i,j+\frac{1}{2},k}^{n+\frac{1}{2}} \\
 & \left. - \Psi_{H_{y,z}}|_{i,j+\frac{1}{2},k}^{n+\frac{1}{2}} \right) + H_y|_{i,j+\frac{1}{2},k}^n C_{bh}|_{i,j+\frac{1}{2},k}
 \end{aligned} \tag{B-128}$$

$$\begin{aligned}
 H_z|_{i,j,k+\frac{1}{2}}^{n+1} = & C_{ah}|_{i,j,k+\frac{1}{2}} \left(-\frac{E_y|_{i+\frac{1}{2},j,k+\frac{1}{2}}^{n+\frac{1}{2}} - E_y|_{i-\frac{1}{2},j,k+\frac{1}{2}}^{n+\frac{1}{2}}}{\kappa_x|_i \Delta x} \right. \\
 & + \frac{E_x|_{i,j+\frac{1}{2},k+\frac{1}{2}}^{n+\frac{1}{2}} - E_x|_{i,j-\frac{1}{2},k+\frac{1}{2}}^{n+\frac{1}{2}}}{\kappa_y|_j \Delta y} - M_z|_{i,j,k+\frac{1}{2}}^{n+\frac{1}{2}} + \Psi_{H_{z,y}}|_{i,j,k+\frac{1}{2}}^{n+\frac{1}{2}} \\
 & \left. - \Psi_{H_{z,x}}|_{i,j,k+\frac{1}{2}}^{n+\frac{1}{2}} \right) + H_z|_{i,j,k+\frac{1}{2}}^n C_{bh}|_{i,j,k+\frac{1}{2}}
 \end{aligned} \tag{B-129}$$

where

$$C_{ahw} = \frac{\frac{\Delta t}{\mu}}{\left(1 + \frac{\sigma_w^* \Delta t}{2\mu}\right)} \quad C_{bhw} = \frac{\left(1 - \frac{\sigma_w^* \Delta t}{2\mu}\right)}{\left(1 + \frac{\sigma_w^* \Delta t}{2\mu}\right)} \quad w = x, y, z. \tag{B-130}$$

Inside the PML, due to the matching condition $\sigma_w^* = \frac{\sigma_w \mu}{\varepsilon}$, this leads to

$$C_{ahw} = \frac{\frac{\Delta t}{\mu}}{\left(1 + \frac{\sigma_w \Delta t}{2\varepsilon}\right)} \quad C_{bhw} = \frac{\left(1 - \frac{\sigma_w \Delta t}{2\varepsilon}\right)}{\left(1 + \frac{\sigma_w \Delta t}{2\varepsilon}\right)} \quad w = x, y, z. \tag{B-131}$$

The discrete unknowns, Ψ , are updated as follows:

$$\Psi_{E_{x,y}}|_{i,j+\frac{1}{2},k+\frac{1}{2}}^n = b_y|_{j+\frac{1}{2}} \Psi_{E_{x,y}}|_{i,j+\frac{1}{2},k+\frac{1}{2}}^{n-1} + c_y|_{j+\frac{1}{2}} \left(\frac{H_z|_{i,j+1,k+\frac{1}{2}}^n - H_z|_{i,j,k+\frac{1}{2}}^n}{\Delta y} \right) \tag{B-132}$$

$$\Psi_{E_{x,z}}|_{i,j+\frac{1}{2},k+\frac{1}{2}}^n = b_z|_{k+\frac{1}{2}} \Psi_{E_{x,z}}|_{i,j+\frac{1}{2},k+\frac{1}{2}}^{n-1} + c_z|_{k+\frac{1}{2}} \left(\frac{H_y|_{i,j+\frac{1}{2},k+1}^n - H_y|_{i,j+\frac{1}{2},k}^n}{\Delta z} \right) \tag{B-133}$$

$$\Psi_{E_{y,z}} \Big|_{i+\frac{1}{2},j,k+\frac{1}{2}}^n = b_z \Big|_{k+\frac{1}{2}} \Psi_{E_{y,z}} \Big|_{i+\frac{1}{2},j,k+\frac{1}{2}}^{n-1} + c_z \Big|_{k+\frac{1}{2}} \left(\frac{H_x \Big|_{i+\frac{1}{2},j,k+\frac{1}{2}}^n - H_x \Big|_{i+\frac{1}{2},j,k}^n}{\Delta z} \right) \quad \text{B-134}$$

$$\Psi_{E_{y,x}} \Big|_{i+\frac{1}{2},j,k+\frac{1}{2}}^n = b_x \Big|_{i+\frac{1}{2}} \Psi_{E_{y,x}} \Big|_{i+\frac{1}{2},j,k+\frac{1}{2}}^{n-1} + c_x \Big|_{i+\frac{1}{2}} \left(\frac{H_z \Big|_{i+\frac{1}{2},j,k+\frac{1}{2}}^n - H_z \Big|_{i,j,k+\frac{1}{2}}^n}{\Delta x} \right) \quad \text{B-135}$$

$$\Psi_{E_{z,x}} \Big|_{i+\frac{1}{2},j+\frac{1}{2},k}^n = b_x \Big|_{i+\frac{1}{2}} \Psi_{E_{z,x}} \Big|_{i+\frac{1}{2},j+\frac{1}{2},k}^{n-1} + c_x \Big|_{i+\frac{1}{2}} \left(\frac{H_y \Big|_{i+\frac{1}{2},j+\frac{1}{2},k}^n - H_y \Big|_{i,j+\frac{1}{2},k}^n}{\Delta x} \right) \quad \text{B-136}$$

$$\Psi_{E_{z,y}} \Big|_{i+\frac{1}{2},j+\frac{1}{2},k}^n = b_y \Big|_{j+\frac{1}{2}} \Psi_{E_{z,y}} \Big|_{i+\frac{1}{2},j+\frac{1}{2},k}^{n-1} + c_y \Big|_{j+\frac{1}{2}} \left(\frac{H_x \Big|_{i+\frac{1}{2},j+\frac{1}{2},k}^n - H_x \Big|_{i+\frac{1}{2},j,k}^n}{\Delta y} \right) \quad \text{B-137}$$

$$\Psi_{H_{x,z}} \Big|_{i+\frac{1}{2},j,k}^{n+\frac{1}{2}} = b_z \Big|_k \Psi_{H_{x,z}} \Big|_{i+\frac{1}{2},j,k}^{n-\frac{1}{2}} + c_z \Big|_k \left(\frac{E_y \Big|_{i+\frac{1}{2},j,k+\frac{1}{2}}^{n+\frac{1}{2}} - E_y \Big|_{i+\frac{1}{2},j,k-\frac{1}{2}}^{n+\frac{1}{2}}}{\Delta z} \right) \quad \text{B-138}$$

$$\Psi_{H_{x,y}} \Big|_{i+\frac{1}{2},j,k}^{n+\frac{1}{2}} = b_y \Big|_j \Psi_{H_{x,y}} \Big|_{i+\frac{1}{2},j,k}^{n-\frac{1}{2}} + c_y \Big|_j \left(\frac{E_z \Big|_{i+\frac{1}{2},j+\frac{1}{2},k}^{n+\frac{1}{2}} - E_z \Big|_{i+\frac{1}{2},j-\frac{1}{2},k}^{n+\frac{1}{2}}}{\Delta y} \right) \quad \text{B-139}$$

$$\Psi_{H_{y,x}} \Big|_{i,j+\frac{1}{2},k}^{n+\frac{1}{2}} = b_x \Big|_i \Psi_{H_{y,x}} \Big|_{i,j+\frac{1}{2},k}^{n-\frac{1}{2}} + c_x \Big|_i \left(\frac{E_z \Big|_{i+\frac{1}{2},j+\frac{1}{2},k}^{n+\frac{1}{2}} - E_z \Big|_{i-\frac{1}{2},j+\frac{1}{2},k}^{n+\frac{1}{2}}}{\Delta x} \right) \quad \text{B-140}$$

$$\Psi_{H_{y,z}} \Big|_{i,j+\frac{1}{2},k}^{n+\frac{1}{2}} = b_z \Big|_k \Psi_{H_{y,z}} \Big|_{i,j+\frac{1}{2},k}^{n-\frac{1}{2}} + c_z \Big|_k \left(\frac{E_x \Big|_{i,j+\frac{1}{2},k+\frac{1}{2}}^{n+\frac{1}{2}} - E_x \Big|_{i,j+\frac{1}{2},k-\frac{1}{2}}^{n+\frac{1}{2}}}{\Delta z} \right) \quad \text{B-141}$$

$$\Psi_{H_{z,y}} \Big|_{i,j,k+\frac{1}{2}}^{n+\frac{1}{2}} = b_y \Big|_j \Psi_{H_{z,y}} \Big|_{i,j,k+\frac{1}{2}}^{n-\frac{1}{2}} + c_y \Big|_j \left(\frac{E_x \Big|_{i,j+\frac{1}{2},k+\frac{1}{2}}^{n+\frac{1}{2}} - E_x \Big|_{i,j-\frac{1}{2},k+\frac{1}{2}}^{n+\frac{1}{2}}}{\Delta y} \right) \quad \text{B-142}$$

$$\Psi_{H_{z,x}} \Big|_{i,j,k+\frac{1}{2}}^{n+\frac{1}{2}} = b_x \Big|_i \Psi_{H_{z,x}} \Big|_{i,j,k+\frac{1}{2}}^{n-\frac{1}{2}} + c_x \Big|_i \left(\frac{E_y \Big|_{i+\frac{1}{2},j,k+\frac{1}{2}}^{n+\frac{1}{2}} - E_y \Big|_{i-\frac{1}{2},j,k+\frac{1}{2}}^{n+\frac{1}{2}}}{\Delta x} \right). \quad \text{B-143}$$

The coefficients b_w, c_w inside the PML are given by

$$b_w = e^{-\left(\frac{\sigma_w}{\varepsilon_0 \kappa_w} + \frac{a_w}{\varepsilon_0}\right) \Delta t} = e^{-\left(\frac{\sigma_w}{\kappa_w} + a_w\right) \frac{\Delta t}{\varepsilon_0}} \quad \text{B-144}$$

$$c_w = \frac{\sigma_w}{\sigma_w \kappa_w + \kappa_w^2 a_w} \left(e^{-\left(\frac{\sigma_w}{\epsilon_0 \kappa_w} + \frac{a_w}{\epsilon_0}\right) \Delta t} - 1 \right) = \frac{\sigma_w}{\sigma_w \kappa_w + \kappa_w^2 a_w} (b_w - 1) \quad \text{B-145}$$

where a_w is a scaling parameter that minimises reflections due to the discrete nature of the grid

$$a_w = a_{max} \left(\frac{d-w}{d} \right)^{m_a}, \quad \text{B-146}$$

d is the thickness of the PML, w is the distance into the PML for the axis of interest, a_{max} is the maximum value of the scaling parameter at the front of the PML and m_a is the scaling order. Outside the PML, b_w, c_w are always zero.

The conductivity parameters σ_w and κ_w take the value 0 and 1 respectively outside the PML, while inside the PML they are polynomially graded much like a_w :

$$\sigma_w = \left(\frac{w}{d} \right)^m \sigma_{w,max} \quad \text{B-147}$$

$$\kappa_w = 1 + \left(\frac{w}{d} \right)^m (\kappa_{w,max} - 1). \quad \text{B-148}$$

The values of $\sigma_{w,max}$ and $\kappa_{w,max}$ can be calculated from

$$\sigma_{w,max} = \kappa_{w,max} - 1 = \frac{(m+1) \ln(R)}{2\eta d} \quad \text{B-149}$$

where R is the desired reflection error and $\eta = \sqrt{\mu/\epsilon}$ is the wave impedance. Taflove and Hagness then go on to describe an equation for an optimal choice, found by experimentation:

$$\sigma_{w,max} = \frac{0.8(m+1)}{\eta \Delta w}. \quad \text{B-150}$$

B.6 Thin layers

The following treatment is expanded from Taflove and Hafness⁸² section 10.7.

In Figure 2.8 the thin material layer of thickness d , conductivity σ_s , electric permittivity ϵ_s and unchanged magnetic permeability resides at z location k^* . In the Yee cells that contain this layer, the electric field z component is split into two parts, one outside the layer, E_z and one inside, E_{zin} , as shown.

Starting from the integral form of Ampere's law to derive the electric field update equations:

$$\oint_C \mathbf{H} \cdot d\mathbf{l} = \iint_S \left(\epsilon \frac{\partial \mathbf{E}}{\partial t} + \mathbf{J} + \sigma \mathbf{E} \right) \cdot d\mathbf{S} \quad \text{B-151}$$

Consider first the outside component, which will continue to be referred to as E_z . The closed loop that surrounds the E_z component in an electric field cell consists of two occurrences each of H_x and H_y in adjacent magnetic field cells. Note that this loop does not cross into the thin sheet at all. The loop integral of Ampere's law can therefore be replaced by the sum of the magnetic fields around the loop, being careful to get the signs correct as the loop is traversed clockwise when looking in the direction of the E_z component:

$$\begin{aligned} H_y|_{i+1,j+\frac{1}{2},k}^n \Delta y + H_x|_{i+\frac{1}{2},j,k}^n \Delta x - H_y|_{i,j+\frac{1}{2},k}^n \Delta y - H_x|_{i+\frac{1}{2},j+1,k}^n \Delta x \\ = \iint_S \left(\epsilon \frac{\partial \mathbf{E}}{\partial t} + \mathbf{J} + \sigma \mathbf{E} \right) \cdot d\mathbf{S} \end{aligned} \quad \text{B-152}$$

Next, the surface enclosed by the loop only contains the E_z and the external current in the cell, therefore the surface integral can be replaced:

$$\begin{aligned} H_y|_{i+1,j+\frac{1}{2},k}^n \Delta y + H_x|_{i+\frac{1}{2},j,k}^n \Delta x - H_y|_{i,j+\frac{1}{2},k}^n \Delta y - H_x|_{i+\frac{1}{2},j+1,k}^n \Delta x \\ = \left(\epsilon \frac{\partial E_z|_{i+\frac{1}{2},j+\frac{1}{2},k}^n}{\partial t} + J_z|_{i+\frac{1}{2},j+\frac{1}{2},k}^n + \sigma E_z|_{i+\frac{1}{2},j+\frac{1}{2},k}^n \right) \Delta x \Delta y \end{aligned} \quad \text{B-153}$$

Now the time differential on the right-hand side is replaced with a finite difference approximation:

$$\begin{aligned} H_y|_{i+1,j+\frac{1}{2},k}^n \Delta y + H_x|_{i+\frac{1}{2},j,k}^n \Delta x - H_y|_{i,j+\frac{1}{2},k}^n \Delta y - H_x|_{i+\frac{1}{2},j+1,k}^n \Delta x \\ = \left(\epsilon \frac{E_z|_{i+\frac{1}{2},j+\frac{1}{2},k}^{n+\frac{1}{2}} - E_z|_{i+\frac{1}{2},j+\frac{1}{2},k}^{n-\frac{1}{2}}}{\Delta t} + J_z|_{i+\frac{1}{2},j+\frac{1}{2},k}^n + \sigma E_z|_{i+\frac{1}{2},j+\frac{1}{2},k}^n \right) \Delta x \Delta y \end{aligned} \quad \text{B-154}$$

Since the electric field components are not available on whole time steps, they are replaced by the average of the two adjacent half time steps.

$$\begin{aligned}
 H_y|_{i+1,j+\frac{1}{2},k}^n \Delta y + H_x|_{i+\frac{1}{2},j,k}^n \Delta x - H_y|_{i,j+\frac{1}{2},k}^n \Delta y - H_x|_{i+\frac{1}{2},j+1,k}^n \Delta x \\
 = \left(\varepsilon \frac{E_z|_{i+\frac{1}{2},j+\frac{1}{2},k}^{n+\frac{1}{2}} - E_z|_{i+\frac{1}{2},j+\frac{1}{2},k}^{n-\frac{1}{2}}}{\Delta t} + J_z|_{i+\frac{1}{2},j+\frac{1}{2},k}^n \right. \\
 \left. + \sigma \frac{E_z|_{i+\frac{1}{2},j+\frac{1}{2},k}^{n+\frac{1}{2}} + E_z|_{i+\frac{1}{2},j+\frac{1}{2},k}^{n-\frac{1}{2}}}{2} \right) \Delta x \Delta y
 \end{aligned} \tag{B-155}$$

Now rearrange to get the original time stepping equation:

$$\begin{aligned}
 E_z|_{i+\frac{1}{2},j+\frac{1}{2},k}^{n+\frac{1}{2}} = C_{ae}|_{i+\frac{1}{2},j+\frac{1}{2},k} \left(\frac{H_y|_{i+1,j+\frac{1}{2},k}^n - H_y|_{i,j+\frac{1}{2},k}^n}{\Delta x} \right. \\
 \left. - \frac{H_x|_{i+\frac{1}{2},j+1,k}^n - H_x|_{i+\frac{1}{2},j,k}^n}{\Delta y} - J_z|_{i+\frac{1}{2},j+\frac{1}{2},k}^n \right) \\
 + E_z|_{i+\frac{1}{2},j+\frac{1}{2},k}^{n-\frac{1}{2}} C_{be}|_{i+\frac{1}{2},j+\frac{1}{2},k}
 \end{aligned} \tag{B-156}$$

Where:

$$C_{ae} = \frac{\frac{\Delta t}{\varepsilon}}{\left(1 + \frac{\sigma \Delta t}{2\varepsilon}\right)} \quad C_{be} = \frac{\left(1 - \frac{\sigma \Delta t}{2\varepsilon}\right)}{\left(1 + \frac{\sigma \Delta t}{2\varepsilon}\right)} \tag{B-157}$$

For the extra component in the special cells, E_{zin} , the magnetic field components required are tangential to the sheet and therefore continuous over the sheet boundary. The loop integral is completely within the sheet and following the same procedure as above, the following expansion of Ampere's law can be written:

$$\begin{aligned}
 H_y|_{i+1,j+\frac{1}{2},k}^n \Delta y + H_x|_{i+\frac{1}{2},j,k}^n \Delta x - H_y|_{i,j+\frac{1}{2},k}^n \Delta y - H_x|_{i+\frac{1}{2},j+1,k}^n \Delta x \\
 = \left(\varepsilon_s \frac{E_{zin}|_{i+\frac{1}{2},j+\frac{1}{2},k}^{n+\frac{1}{2}} - E_{zin}|_{i+\frac{1}{2},j+\frac{1}{2},k}^{n-\frac{1}{2}}}{\Delta t} + J_z|_{i+\frac{1}{2},j+\frac{1}{2},k}^n \right. \\
 \left. + \sigma_s \frac{E_{zin}|_{i+\frac{1}{2},j+\frac{1}{2},k}^{n+\frac{1}{2}} + E_{zin}|_{i+\frac{1}{2},j+\frac{1}{2},k}^{n-\frac{1}{2}}}{2} \right) \Delta x \Delta y
 \end{aligned} \tag{B-158}$$

And rearranging to get the time stepping equation:

$$\begin{aligned}
 E_{zin}|_{i+\frac{1}{2},j+\frac{1}{2},k}^{n+\frac{1}{2}} &= C_{aein}|_{i+\frac{1}{2},j+\frac{1}{2},k}^* \left(\frac{H_y|_{i+1,j+\frac{1}{2},k}^n - H_y|_{i,j+\frac{1}{2},k}^n}{\Delta x} \right. \\
 &\quad \left. - \frac{H_x|_{i+\frac{1}{2},j+1,k}^n - H_x|_{i+\frac{1}{2},j,k}^n}{\Delta y} - J_z|_{i+\frac{1}{2},j+\frac{1}{2},k}^n \right) \\
 &\quad + E_{zin}|_{i+\frac{1}{2},j+\frac{1}{2},k}^{n-\frac{1}{2}} C_{bein}|_{i+\frac{1}{2},j+\frac{1}{2},k}^*
 \end{aligned} \tag{B-159}$$

Where

$$C_{aein} = \frac{\frac{\Delta t}{\epsilon_s}}{\left(1 + \frac{\sigma_s \Delta t}{2\epsilon_s}\right)} \quad C_{bein} = \frac{\left(1 - \frac{\sigma_s \Delta t}{2\epsilon_s}\right)}{\left(1 + \frac{\sigma_s \Delta t}{2\epsilon_s}\right)} \tag{B-160}$$

The remaining electric field components are tangential to the sheet and the loop crosses through it. For the E_x component the expansion of the loop integral of Ampere's law can be written in the same way as previously:

$$\begin{aligned}
 H_y|_{i,j+\frac{1}{2},k}^n \Delta y + H_z|_{i,j+1,k+\frac{1}{2}}^n \Delta z - H_y|_{i,j+\frac{1}{2},k+1}^n \Delta y - H_z|_{i,j,k+\frac{1}{2}}^n \Delta z \\
 = \iint_S \left(\epsilon \frac{\partial \mathbf{E}}{\partial t} + \mathbf{J} + \sigma \mathbf{E} \right) \cdot d\mathbf{S}
 \end{aligned} \tag{B-161}$$

For the surface integral, however, the enclosed surface contains the sheet which provides $d/\Delta z$ of the area, the remainder $1 - d/\Delta z$ being outside the sheet. The surface integral is therefore expanded with terms for each part:

$$\begin{aligned}
 H_y|_{i,j+\frac{1}{2},k}^n \Delta y + H_z|_{i,j+1,k+\frac{1}{2}}^n \Delta z - H_y|_{i,j+\frac{1}{2},k+1}^n \Delta y - H_z|_{i,j,k+\frac{1}{2}}^n \Delta z \\
 = \left(1 - \frac{d}{\Delta z}\right) \left(\epsilon \frac{\partial E_z|_{i+\frac{1}{2},j+\frac{1}{2},k}^n}{\partial t} + J_z|_{i+\frac{1}{2},j+\frac{1}{2},k}^n \right. \\
 \left. + \sigma E_z|_{i+\frac{1}{2},j+\frac{1}{2},k}^n \right) \Delta x \Delta y \\
 + \frac{d}{\Delta z} \left(\epsilon_s \frac{\partial E_z|_{i+\frac{1}{2},j+\frac{1}{2},k}^n}{\partial t} + J_z|_{i+\frac{1}{2},j+\frac{1}{2},k}^n + \sigma_s E_z|_{i+\frac{1}{2},j+\frac{1}{2},k}^n \right) \Delta x \Delta y
 \end{aligned} \tag{B-162}$$

Rearranging:

$$\begin{aligned}
 & H_y|_{i,j+\frac{1}{2},k}^n \Delta y + H_z|_{i,j+1,k+\frac{1}{2}}^n \Delta z - H_y|_{i,j+\frac{1}{2},k+1}^n \Delta y - H_z|_{i,j,k+\frac{1}{2}}^n \Delta z \\
 &= \left(\left(\left(1 - \frac{d}{\Delta z} \right) \varepsilon + \frac{d}{\Delta z} \varepsilon_s \right) \frac{\partial E_z|_{i+\frac{1}{2},j+\frac{1}{2},k}^n}{\partial t} + J_z|_{i+\frac{1}{2},j+\frac{1}{2},k}^n \right. \\
 & \quad \left. + \left(\left(1 - \frac{d}{\Delta z} \right) \sigma + \frac{d}{\Delta z} \sigma_s \right) E_z|_{i+\frac{1}{2},j+\frac{1}{2},k}^n \right) \Delta x \Delta y
 \end{aligned} \tag{B-163}$$

Defining ε_{av} and σ_{av} , the averages of the electric permittivity and conductivity, by

$$\varepsilon_{av} = \left(1 - \frac{d}{\Delta z} \right) \varepsilon + \frac{d}{\Delta z} \varepsilon_s \quad \sigma_{av} = \left(1 - \frac{d}{\Delta z} \right) \sigma + \frac{d}{\Delta z} \sigma_s \tag{B-164}$$

Using these leads to:

$$\begin{aligned}
 & H_y|_{i,j+\frac{1}{2},k}^n \Delta y + H_z|_{i,j+1,k+\frac{1}{2}}^n \Delta z - H_y|_{i,j+\frac{1}{2},k+1}^n \Delta y - H_z|_{i,j,k+\frac{1}{2}}^n \Delta z \\
 &= \left(\varepsilon_{av} \frac{\partial E_z|_{i+\frac{1}{2},j+\frac{1}{2},k}^n}{\partial t} + J_z|_{i+\frac{1}{2},j+\frac{1}{2},k}^n + \sigma_{av} E_z|_{i+\frac{1}{2},j+\frac{1}{2},k}^n \right) \Delta x \Delta y
 \end{aligned} \tag{B-165}$$

Then replacing the time differential with the finite difference equivalent and using the average for $E_z|_{i+\frac{1}{2},j+\frac{1}{2},k}^n$ as previously, followed by more rearranging, an update equation can be arrived at:

$$\begin{aligned}
 E_x|_{i,j+\frac{1}{2},k+\frac{1}{2}}^{n+\frac{1}{2}} &= C_{aeav} |_{i,j+\frac{1}{2},k+\frac{1}{2}} \left(\frac{H_z|_{i,j+1,k+\frac{1}{2}}^n - H_z|_{i,j,k+\frac{1}{2}}^n}{\Delta y} \right. \\
 & \quad \left. - \frac{H_y|_{i,j+\frac{1}{2},k+1}^n - H_y|_{i,j+\frac{1}{2},k}^n}{\Delta z} - J_x|_{i,j+\frac{1}{2},k+\frac{1}{2}}^n \right) \\
 & \quad + E_x|_{i,j+\frac{1}{2},k+\frac{1}{2}}^{n-\frac{1}{2}} C_{beav} |_{i,j+\frac{1}{2},k+\frac{1}{2}}
 \end{aligned} \tag{B-166}$$

Where

$$C_{aeav} = \frac{\frac{\Delta t}{\varepsilon_{av}}}{\left(1 + \frac{\sigma_{av} \Delta t}{2 \varepsilon_{av}} \right)} \quad C_{beav} = \frac{\left(1 - \frac{\sigma_{av} \Delta t}{2 \varepsilon_{av}} \right)}{\left(1 + \frac{\sigma_{av} \Delta t}{2 \varepsilon_{av}} \right)} \tag{B-167}$$

Using similar arguments for the E_y component, this update equation can be written:

$$\begin{aligned}
 E_y|_{i+\frac{1}{2},j,k+\frac{1}{2}}^{n+\frac{1}{2}} = & C_{aeav}|_{i+\frac{1}{2},j,k+\frac{1}{2}} \left(\frac{H_x|_{i+\frac{1}{2},j,k+1}^n - H_x|_{i+\frac{1}{2},j,k}^n}{\Delta z} \right. \\
 & \left. - \frac{H_z|_{i+1,j,k+\frac{1}{2}}^n - H_z|_{i,j,k+\frac{1}{2}}^n}{\Delta x} - J_y|_{i+\frac{1}{2},j,k+\frac{1}{2}}^n \right) \\
 & + E_y|_{i+\frac{1}{2},j,k+\frac{1}{2}}^{n-\frac{1}{2}} C_{beav}|_{i+\frac{1}{2},j,k+\frac{1}{2}}
 \end{aligned} \tag{B-168}$$

Moving to the consideration of the magnetic fields and starting from the integral form of Faraday's law:

$$\oint_C \mathbf{E} \cdot d\mathbf{l} = - \iint_S \left(\mu \frac{\partial \mathbf{H}}{\partial t} + \mathbf{M} + \sigma^* \mathbf{H} \right) \cdot d\mathbf{S} \tag{B-169}$$

Since the magnetic permeability and magnetic conductivity in the sheet required to be the same as outside the sheet there is no need for an extra magnetic field z component. In addition, the loop integral for the z component lies completely outside the sheet therefore the update equation is identical to the standard case:

$$\begin{aligned}
 H_z|_{i,j,k+\frac{1}{2}}^{n+1} = & C_{ah}|_{i,j,k+\frac{1}{2}} \left(- \frac{E_y|_{i+\frac{1}{2},j,k+\frac{1}{2}}^{n+\frac{1}{2}} - E_y|_{i-\frac{1}{2},j,k+\frac{1}{2}}^{n+\frac{1}{2}}}{\Delta x} \right. \\
 & \left. + \frac{E_x|_{i,j+\frac{1}{2},k+\frac{1}{2}}^{n+\frac{1}{2}} - E_x|_{i,j-\frac{1}{2},k+\frac{1}{2}}^{n+\frac{1}{2}}}{\Delta y} - M_z|_{i,j,k+\frac{1}{2}}^{n+\frac{1}{2}} \right) \\
 & + H_z|_{i,j,k+\frac{1}{2}}^n C_{bh}|_{i,j,k+\frac{1}{2}}
 \end{aligned} \tag{B-170}$$

Where:

$$C_{ah} = \frac{\frac{\Delta t}{\mu}}{\left(1 + \frac{\sigma^* \Delta t}{2\mu}\right)} \quad C_{bh} = \frac{\left(1 - \frac{\sigma^* \Delta t}{2\mu}\right)}{\left(1 + \frac{\sigma^* \Delta t}{2\mu}\right)} \tag{B-171}$$

For the x and y components that lie tangential to the sheet, the update equations can be shown to be as follows (essentially the required electric field z components become the average of the fields inside and outside the sheet):

$$\begin{aligned}
 H_x|_{i+\frac{1}{2},j,k}^{n+1} = & C_{ah}|_{i+\frac{1}{2},j,k} \left(- \frac{\left(1 - \frac{d}{\Delta Z}\right) \left(E_z|_{i+\frac{1}{2},j+\frac{1}{2},k}^{n+\frac{1}{2}} - E_z|_{i+\frac{1}{2},j-\frac{1}{2},k}^{n+\frac{1}{2}}\right)}{\Delta y} \right. \\
 & - \frac{\frac{d}{\Delta Z} \left(E_{zin}|_{i+\frac{1}{2},j+\frac{1}{2},k}^{n+\frac{1}{2}} - E_{zin}|_{i+\frac{1}{2},j-\frac{1}{2},k}^{n+\frac{1}{2}}\right)}{\Delta y} \\
 & \left. + \frac{E_y|_{i+\frac{1}{2},j,k+\frac{1}{2}}^{n+\frac{1}{2}} - E_y|_{i+\frac{1}{2},j,k-\frac{1}{2}}^{n+\frac{1}{2}}}{\Delta Z} - M_x|_{i+\frac{1}{2},j,k}^{n+\frac{1}{2}} \right) \\
 & + H_x|_{i+\frac{1}{2},j,k}^n C_{bh}|_{i+\frac{1}{2},j,k}
 \end{aligned}
 \tag{B-172}$$

And

$$\begin{aligned}
 H_y|_{i,j+\frac{1}{2},k}^{n+1} = & C_{ah}|_{i,j+\frac{1}{2},k} \left(- \frac{E_x|_{i,j+\frac{1}{2},k+\frac{1}{2}}^{n+\frac{1}{2}} - E_x|_{i,j+\frac{1}{2},k-\frac{1}{2}}^{n+\frac{1}{2}}}{\Delta Z} \right. \\
 & + \frac{\left(1 - \frac{d}{\Delta Z}\right) \left(E_z|_{i+\frac{1}{2},j+\frac{1}{2},k}^{n+\frac{1}{2}} - E_z|_{i-\frac{1}{2},j+\frac{1}{2},k}^{n+\frac{1}{2}}\right)}{\Delta x} \\
 & \left. + \frac{\frac{d}{\Delta Z} \left(E_{zin}|_{i+\frac{1}{2},j+\frac{1}{2},k}^{n+\frac{1}{2}} - E_{zin}|_{i-\frac{1}{2},j+\frac{1}{2},k}^{n+\frac{1}{2}}\right)}{\Delta x} - M_y|_{i,j+\frac{1}{2},k}^{n+\frac{1}{2}} \right) \\
 & + H_y|_{i,j+\frac{1}{2},k}^n C_{bh}|_{i,j+\frac{1}{2},k}
 \end{aligned}
 \tag{B-173}$$

Appendix C

The 10x10 pixelated pattern catalogues

The 10x10 four-fold catalogue containing the complex admittances of 32768 patterns is available at this URL:

<https://1drv.ms/u/s!AudHFjG9Wlmg5RbnIj6RZ4zR9Iriw?e=aS5TcW>

It is 50.7MB in zipped up XML format.

The 10x10 two-fold catalogue containing the complex admittances of both x and y components is available at this URL:

https://1drv.ms/u/s!AudHFjG9Wlmg5RcIC_zgv7NqpbJlQ?e=hmd5Jg

It is 11.25GB in zipped up XML format.

A tool for reading, displaying and searching these catalogues is provided with the modelling software described in section 2.5.

XML is a textual format consisting of nested named objects, indicated by <object> and </object> tags. The contents of the catalogue files are shown below.

```
<?xml encoding="UTF-8" version="1.0"?>
<binarycatalogue>
  <bitsperhalfside>5</bitsperhalfside>
  <fourfoldsymmetry>0</fourfoldsymmetry>
  <unitcell>0.0008</unitcell>
  <startfrequency>4e+09</startfrequency>
  <frequencystep>4e+09</frequencystep>
  <catalogueitem>
    <code>0</code>
    <pattern>0</pattern>
    <transmittance>...</transmittance>
    <phaseshift>...</phaseshift>
    <transmittancey>...</transmittancey>
    <phaseshifty>...</phaseshifty>
  </catalogueitem>
  <catalogueitem>...</catalogueitem>
</binarycatalogue>
```

The whole catalogue is the <binarycatalogue> object. This contains a number of global parameters:

<bitsperhalfside> Half of N in the NxN pixelated pattern. For a 10x10 pattern this value is 5.

<fourfoldsymmetry> A value of 1 indicates the catalogue is of four-fold symmetric patterns, a value of 0 indicates two-fold.

<unitcell> The size of the unit cell in metres.

<startfrequency> The frequency of the first sample in the transmittance and phase shift arrays, in Hertz.

<frequencystep> The frequency increment between samples, in Hertz.

There then follows a (large) number of <catalogueitem> objects. Each one represents a single pattern in the catalogue. These contain the following parameters:

<code> The code number of the pattern. For a two-fold pattern this is the same as the <pattern> parameter.

<pattern> The bit pattern of the top-left quadrant of the pattern.

<transmittance> A list of space separated floating-point values for the transmittance, one for each frequency step.

<phaseshift> A list of space separated floating-point values in degrees for the phase shift, one for each frequency step.

<transmittancey> In a two-fold symmetric catalogue, the y component of the transmittance (the <transmittance> object holds the x component). Not present in four -fold catalogues.

<phaseshifty> In a two-fold symmetric catalogue, the y component of the phase shift (the <phaseshift> object holds the x component). Not present in four -fold catalogues.

Appendix D

Modelling tool source code

The modelling tool source code is available in a public Git repository on BitBucket and may be cloned using this URL:

<https://jonthompson644@bitbucket.org/jonthompson644/fdtdlife.git>

It was developed using the CLion IDE from JetBrains and the build is cmake based.

The GUI libraries Qt or gtkmm3 are required to build many of the targets. The nvidia CUDA library is required to build the experimental GPU accelerated target.